

This item was submitted to Loughborough's Institutional Repository (<https://dspace.lboro.ac.uk/>) by the author and is made available under the following Creative Commons Licence conditions.



CC creative commons
COMMONS DEED

Attribution-NonCommercial-NoDerivs 2.5

You are free:

- to copy, distribute, display, and perform the work

Under the following conditions:

BY: **Attribution.** You must attribute the work in the manner specified by the author or licensor.

Noncommercial. You may not use this work for commercial purposes.

No Derivative Works. You may not alter, transform, or build upon this work.

- For any reuse or distribution, you must make clear to others the license terms of this work.
- Any of these conditions can be waived if you get permission from the copyright holder.

Your fair use and other rights are in no way affected by the above.

This is a human-readable summary of the [Legal Code \(the full license\)](#).

[Disclaimer](#) 

For the full text of this licence, please go to:
<http://creativecommons.org/licenses/by-nc-nd/2.5/>

**Hyperspectral Interferometry for Single-Shot
Profilometry and Depth-Resolved
Displacement Field Measurement**

by

Taufiq Widjanarko

**A Doctoral Thesis submitted in partial fulfilment of the
requirements for the award of Doctor of Philosophy of
Loughborough University**

May 2011

©by Taufiq Widjanarko 2011

Abstract

A new approach to the absolute measurement of two-dimensional optical path differences is presented in this thesis. The method, which incorporates a white light interferometer and a hyperspectral imaging system, is referred to as Hyperspectral Interferometry. A prototype of the Hyperspectral Interferometry (HSI) system has been designed, constructed and tested for two types of measurement: for surface profilometry and for depth-resolved displacement measurement, both of which have been implemented so as to achieve single shot data acquisition.

The prototype has been shown to be capable of performing a single-shot 3-D shape measurement of an optically-flat step-height sample, with less than 5% difference from the result obtained by a standard optical (microscope) based method. The HSI prototype has been demonstrated to be able to perform single-shot measurement with an unambiguous 352 μm depth range and a rms measurement error of around 80 nm. The prototype has also been tested to perform measurements on optically rough surfaces. The rms error of these measurements was found to increase to around 4 \times that of the smooth surface.

For the depth-resolved displacement field measurements, an experimental setup was designed and constructed in which a weakly-scattering sample underwent simple compression with a PZT actuator. Depth-resolved displacement fields were reconstructed from pairs of hyperspectral interferograms. However, the experimental results did not show the expected result of linear phase variation with depth. Analysis of several possible causes has been carried out with the most plausible reasons being excessive scattering particle density inside the sample and the possibility of insignificant deformation of the sample due to insufficient physical contact between the transducer and the sample.

Keywords: Hyperspectral interferometry, Single-shot measurement, Profilometry, Depth-resolved displacement field measurement, Absolute distance measurement, Phase measurement, Low Coherence Interferometry, Optical Coherence Tomography

Acknowledgment

*everything turns more expensive when they are rare
except knowledge
which becomes more precious when they are abundant
(hazrat ali bin thalib r.a.)*

I would like first to express my gratitude and thanks to Islamic Development Bank, which has generously awarded me The IDB Merit Scholarship that has enabled me to pursue my PhD research in Loughborough in optical interferometry – the subject that I have been long interested to, which back since my final years of my undergraduate education, I aspired one day to be able to pursue a research training in this field. Supplement funding from Research Scholarship from Wolfson School of Mechanical and Manufacturing Engineering is also acknowledged. Financial support for the extension period of my study from The Overseas Scholarship of Directorate General of Higher Education, Department of National Education Republic of Indonesia (Beasiswa Dikti LN Batch-3) is also acknowledged and appreciated.

It is such a great honour and pleasure to conduct this PhD research study under the supervision of Prof. Jonathan Huntley. Not merely has he trained me to be able to perform independent research, but I also learnt how to promote the research output to the industries. Also my thanks to my second supervisor Dr. Pablo Ruiz - from whom I learnt many things on the experimental works.

My thanks also goes to Dr. Manuel De la Torre-Ibarra, a visiting researcher from CIO Mexico, who really taught me on the real technical issues on the optical table. I can't imagine without his kind helps, cheerful and outgoing character that I would be able to cope the pressure that sometimes mounted during the experiments (especially when the result came out unexpected and I need to struggle to find the problems...). Also my appreciation goes to Dr. Russ Coggrave from Phase Vision Ltd who has assisted me a lot with his savvy knowledge in electronics and hardware programming.

Helps and stimulating discussions from the past and current lab cohorts are indeed also appreciated: Adel El-Mahdy - whom without his help the sample made from spin coating process would not be possible, Nadeem Shaikh who has helped me in providing the template from which this thesis is written on, and Bona Burlison – from whom I learnt organising things in the lab and the set-ups so it looks tidy and pleasant to work with, and indeed his sharing to alleviate the stress during the experiments on British comedy telly shows.. and Nguyen Truong Nam- my discussion pal on shape measurement and things I missed from Bandung...*kamé..terimakasih pak!* Without the support from my family and friends in Indonesia and in the UK, mainly East Midlands, this study will not be successful, to which I express my sincere thanks. My gratitude always for my teachers Dr. Hakim Malasan and Prof. Bambang Hidayat from Bosscha Observatory, Indonesia who constantly support and instill me with the spirit of performing scientific works, and finally Prof. Andrianto Handojo from Institute of Technology Bandung (ITB) Indonesia who has taught me that optics is much more interesting than simply the knowledge about mirrors, lens, and other transparent materials.

I wish not to thank my wife and daughter. For their continuous love, support, patience and understanding they deserve more than just the gratitude. They deserve dedication, to which this work is I dedicated to.

Loughborough, May 2011

*With every difficulty there comes an ease
Verily, with every hardship there always comes a relief
(Qur'an 94:5-6)*

This thesis is dedicated to

Ade dan Naila

My beloved wife and daughter

Ibuku

My beloved mother

Mas dan Mbakku

My brothers and sister

Almarhum Bapak

My late beloved father

who has opened all of these possibilities
the first person in my life who taught me logic and english...

Table of Contents

Abstract	ii
List of Nomenclature	8
Chapter 1 Introduction & Research Overview.....	15
1.1. Introduction	15
1.2. Goal of the research work.....	17
1.3. Relationship to past work	18
1.4. Organization of the thesis	19
Chapter 2 Literature Review & Novel Features of the Research	21
2.1. Single wavelength interferometry and its limitation	21
2.2. Low Coherence Interferometry	25
2.2.1. Time Domain LCI	28
2.2.2. Spectral-based LCI.....	33
2.2.3. Wavelength scanning LCI	42
2.2.4. Comparison between LCI configurations.....	45
2.3. Interference Microscope.....	46
2.4. Novel features and motivation behind the research goal.....	49
Chapter 3 Optical Configuration 1: Microlens-based Hyperspectral Interferometer.....	52
3.1. The concept of hyperspectral interferometry.....	52
3.2. The set-up	56
3.2.1. The generic design set-up	56
3.2.2. The light source	58
3.2.3. The grating	59
3.2.4. The microlens array.....	61
3.2.5. The sample	62
3.2.6. Practical design issues	63
3.2.6.1. Imaging path of the sample	64
3.2.6.2. Imaging path of the aperture.....	66
3.2.6.3. Fibre coupler.....	67
3.2.6.4. Spot imaging.....	68
3.3. Results and discussions	69
Chapter 4 Optical Configuration 2: Etalon-based Hyperspectral Interferometer	76
4.1. Introduction	76
4.2. Brief review of the previous design problems.....	76
4.2.1. Object imaging	76
4.2.2. Depth of field issue.....	77

4.2.3. Effect of non-collimated illumination of the grating.....	78
4.2.4. Diffraction grating non-linearity issues.....	78
4.2.5. Etalon for k -space linearization.....	80
4.3. HSI design.....	83
4.3.1. The diffraction grating.....	87
4.3.2. Imaging path and system magnification.....	88
4.3.3. Finesse.....	89
4.3.4. Object lens.....	90
4.4. The prototype.....	91
4.5. Defocusing the sample illumination.....	96
4.6. Effect of back reflections.....	98
4.7. System performance in brief.....	102
Chapter 5 Data Processing.....	104
5.1. Introduction.....	104
5.2. Interferogram spectrum.....	104
5.3. Implementation.....	106
5.4. Background pedestal removal.....	109
5.5. Derivation of system's parameters.....	112
5.6. Depth resolution improvement.....	114
Chapter 6 Experimental result 1: Single-shot opaque surface profilometry.....	116
6.1. Introduction.....	116
6.2. Reflective planar imaging.....	116
6.2.1. Depth range and resolution.....	116
6.2.2. Experimental verification of depth range.....	118
6.2.3. Error measurement.....	120
6.3. Smooth surface step height profiling.....	123
6.4. Rough surface measurement.....	125
6.4.1. Filtering the reconstructed height distribution.....	126
6.4.2. Reconstructed height map of the samples.....	129
6.5. Conclusion.....	132
Chapter 7 Experimental result 2: Depth (sub-surface)-resolved displacement measurement.....	134
7.1. Introduction.....	134
7.2. Signal analysis of scattering medium.....	135
7.3. Sample preparation.....	139
7.3.1. Plastic sheet 1 – deformed by electric field.....	140
7.3.2. Plastic sheet 2 – stretched by mechanical tension.....	142

7.3.3. Weakly scattering material	145
7.3.3.1. Sample preparation and testing	146
7.3.3.2. Grain requirements	150
7.4. Limiting the speckle pattern's spectral overlap	152
7.5. Improvements to the sub-image alignment method	154
7.6. PZT Calibration	159
7.7. The depth measurement experiment	161
7.8. Results and discussion	165
Chapter 8 Conclusions and Future Works	170
8.1. Summary of the research work	170
8.2. Further work	172
References	174
Appendices	183
A1. Hyperspectral Imager (Photon etc)	183
A2. Hyperspectral Imager (Teledyne-Dalsa)	184
A3. Hyperspectral Imager (Brimrose Corp)	185
A4. Imaging using Brimrose AOTF Hyperspectral Imager	186
A5. Hyperspectral Imager (Gilden Photonics)	187
A6. Hyperspectral Imager (Spectral Imaging Ltd)	188
A7. Hyperspectral Imager (Surface Optics)	189
A8. Grating efficiency plot	190
A9. Peak finding (Matlab) routine	191
A10. Low Density Polyethylene (LDPE) data	192
A11. Simple method for measuring the refractive index of a glass slab	193

List of Nomenclature

(x, y)	Spatial coordinate (2-D)
(x_c, y_c)	Offset (2-D) coordinates
a	CCD pixel size
A	cross section Area
A_e	Absorptance of the etalon
α	Incident beam angle of the grating
b	distance from grating to microlens array
β	Diffacted beam angle of the grating
c	speed of light
d	Distance from object to the scattered wave detector
D_1	Mass density of the resin
D_2	Mass density of the scattering particles
d_f	Depth of field
d_i	Image size
d_o	Object size (equiv.to field of view)
D_o	Effective aperture size of object lens
d_{sp}	speckle size at the image plane
D_{sp}	speckle size at the sample
$\delta\beta_1$	change in diffracted beam angle due to the change in wavelength $\delta\lambda$
$\delta\beta_2$	Angular deviation of the rays coming from two points on the object separated by d_o
δk	Free Spectral Range in k axis
$\Delta\lambda$	Bandwidth of the lightsource
$\delta\lambda$	Increment change in wavelength
$(\Delta\lambda_0)_{fsr}$	Free Spectral Range (expressed in wavelength)
$(\Delta\lambda_0)_{fwhm}$	Full Width Half Maximum (spectral width) of an etalon's transmission peak (expressed in wavelength)

$(\Delta\nu_0)_{fsr}$	Free Spectral Range (expressed in frequency)
$\Delta\phi$	phase shift of the interference signal due to the wavenumber shift Δk
$\Delta\phi_{i1}(z_n)$	Phase difference between the i^{th} and 1^{st} voltage image of the n^{th} depth layer
δ_e	Phase difference between two successive transmitted rays from the etalon
$\delta(z)$	Delta dirac function
Δz	Depth range
δz	Depth resolution
$\delta z'$	Depth resolution after windowing
Δk	Light source bandwidth in k axis
E	Applied electric field
ϵ_0	Electrostatic permittivity of air/vacuum
ϵ_r	Relative permittivity
η	Filtering constant (e.g. Hanning filter $\eta=2$)
F	Force
f	Focal length of a lens
\mathfrak{F}_e	Finesse of the etalon
$f_{\#}$	f-number of the lens
f_i	Focal length of imaging lens
f_k	Fringe frequency in k -axis
$f_{\mu L}$	Focal length of each microlens' lenslet
f_o	Focal length of object lens
$F_S(r, k)$	Scattering potential
\mathfrak{F}	Fourier transform operator
\mathfrak{F}_e	Finesse of the etalon
$f_{\mu L}$	Focal length of microlens

$G(k)$	Light source spectral distribution
g	Grating density (grooves/mm)
$G_H(r)$	Free space Green's function
$\tilde{G}(z)$	Fourier transform of $G(k)$
$\tilde{\gamma}_{12}(\tau)$	Complex degree of coherence between two lightwaves
$h(x, y)$	Height distribution
h_0	distance from the sample datum surface to the plane of zero OPD
h^{exp}	Experimental height distribution data
h^{fit}	Fitting plane to the height distribution
$H(k)$	Magnitude of Fourier transform of $I(x, y, k)$
$ H_p(x, y) $	Magnitude of the peak of Fourier transform of $I(x, y, k)$
h_s	Height distribution after smoothing operation
$I(x, y, z)$	Intensity (2-D) distribution
$I(x, y, k)$	Hyperspectral image volume
$I_D(k)$	Detector signal
$i_D(z)$	Fourier transform of $I_D(k)$
I_i	Incident intensity of the etalon
$I(k)$	Intensity in k axis
$I_o(x_m, y_n, k)$	Intensity of the object wave intensity along the k axis
$I_r(x_m, y_n, k)$	Intensity of the reference wave intensity along the k axis
I_t	Transmitted intensity of the etalon
$\tilde{I}_i(z_n)$	Fourier transform of the i^{th} voltage image of the n^{th} depth layer
$\tilde{I}(z)$	Fourier transform of $I(k)$
$\text{Im}[\dots]$	Imaginary part of $\tilde{I}(x, y, z)$

k	Wavenumber
\mathbf{K}	Backscattered wave vector
$\mathbf{k}^{(i)}$	Incident wave vector
$\mathbf{k}^{(s)}$	Scattered wave vector
k_c	Shift of k (for weighting function ($W(k)$))
L_C	Coherence length
$L_{coupling}$	Loss due to power coupling from the etalon back to the fiber
$L_{insertion}$	I insertion loss of the optical isolator
$L_{isolator}(\lambda)$	Wavelength-dependent loss of the optical isolator unit inside the SLED
λ	Wavelength
λ_0	Wavelength of light in air/vacuum
$\bar{\lambda}$	Mean wavelength
λ_C	Central wavelength
λ_{eq}	Equivalent synthetic wavelength
λ_L	Lower limit the lightsource's bandwidth
λ_U	Upper limit the lightsource's bandwidth
λ_W	Working wavelength of the component
m	Diffraction order
M_s	Magnification of the HSI system
m_1	Mass of the resin
m_2	Mass of the scattering particles
$N(x, y)$	Fringe number
N_f	Number of frames
N_k	Number of (spectral) sub-images
n_l	Refractive index of each microlens' lenslet
N_x	Number of pixels in a sub-image

N_y	Number of pixels along the CCD spectral axis
N_z	number of zero crossings occurring due to the wavenumber shift Δk
ν	Light frequency
$o(x, y)$	Smoothing (filter) kernel
P	Polarised charge per unit area
ϕ	Phase
ϕ_0	Initial phase distribution at depth $z = z_0$
ϕ_e	Phase shift due to the reflection of the light from the etalon surface
ϕ_e	phase shift due to the reflection of the light from the etalon surface
ϕ_j	Phase of the j^{th} layer inside the sample
ϕ_{j0}	phase change due to reflection at the j^{th} layer
ϕ_{j0}	Initial random phase of the j^{th} layer inside the sample
Φ	Applied voltage
\mathbf{r}	Coordinate of the illuminating lightwave
R_C	Radius of curvature of each microlens' lenslet
R_e	Reflectance of the etalon
\mathbf{r}'	Coordinate within the sample illuminated by the incident wave
r_R	Reflection coefficient of the reference mirror
R_R	Reflected power from reference mirror
r_{Sm}	Reflection coefficient of the m^{th} depth layer of the sample
R_{Sm}	Reflected power from the m^{th} depth layer of the sample
r_{sp}	Scattering particle radius
$\text{Re}[\dots]$	real part of $\tilde{I}(x, y, z)$
ρ	detector responsivity
$S(x, y)$	Optical path (2-D) distribution

s	Strain
$s_1(x_m, y_n)$	Sum of the interference intensity of the pixel at (x_m, y_n) along the k axis
$s_2(x_m, y_n)$	Sum of the object and reference intensities of the pixel at (x_m, y_n) along the k axis
s_x	Transversal strain (x -direction)
s_z	Axial Strain (z -direction)
σ	Standard deviation (rms error)
Σ	Stress (pressure/area)
T_e	Transmittance of the etalon
t_e	Thickness of the etalon
t_p	Thickness of the plastic
θ_B	blaze angle of the grating
θ_t	transmitted light angle relative to the etalon's normal
u	Amplitude of the complex lightwave
$U^{(i)}$	Complex incident lightwave function
$u^{(i)}$	Amplitude of the complex incident lightwave function
U_R	Reflected complex lightwave from reference mirror
U_S	Complex scattered lightwave function
u_S	Amplitude of the complex incident lightwave function
u_z	contraction in the axial direction
\bar{U}	Complex lightwave function
$W(k)$	Weighting function
w	width of the plastic
$\tilde{W}(z)$	Fourier transform of weighting function $W(k)$
Y	Young's (elasticity) modulus
z	Depth axis/ depth coordinate
z_0	The z (depth) location of the Fourier domain peak

z_j	optical depth of the j^{th} depth slice relative to the reference wavefront
z_M	Maximum allowed distance before fringe aliasing occurs
z_R	distance traversed by the reference wave
z_{Sm}	distance traversed by the object wave from the m^{th} depth layer of the sample

Chapter 1

Introduction & Research Overview

1.1. Introduction

Optical-based measurement methods have been indispensable techniques in the field of measurement technology. The non-contact nature of the methods avoids a significant problem in the measurement of responses of a component to applied loads - the fact that the gauging not only takes the reading but also potentially loads the object itself and thus adversely alters the measurement [1]. Of the wide range of optical-based measurement methods, interferometry offers advantages including full-field acquisition, accuracy to within a small fraction of the wavelength used [2,3] and the capability of performing both surface and depth-resolved (sub-surface) measurement.

In the field of surface profiling the conventional laser interferometer has been long used for three dimensional shape measurements. Shapes having a smooth surface, where height variations between adjacent measurement points are less than one quarter of the wavelength used, can be accurately measured using an interferometer that employs light of a single wavelength, such as a laser interferometer. There exist, however, objects possessing surface height gradients that are larger than this, for example rough objects or objects with surface steps. For these, conventional monochromatic interferometers have difficulty in determining the height distribution because the interference pattern becomes discontinuous and – in the case of rough surfaces - the reflected light is ‘speckled’ and the interference fringes may no longer be visible [2,4,5].

Another type of interferometry configuration, called low coherence interferometry (LCI), has been developed to avoid the problem of laser interferometry mentioned above. In LCI a broadband, polychromatic, and hence low (temporal) coherence light source is used in place of the conventional single wavelength light source such as a laser [6,7,8,9].

One of the most widely-used forms of LCI for surface measurement is the Scanning White Light Interferometer (SWLI) where a white light source is in use [2,7,10,11] to replace a laser as the probing light. This type of interferometer is now manufactured commercially by large optical metrology vendors such as Veeco and Zygo. In contrast to conventional laser interferometers, where the surface height distribution may be derived from a single recorded interference fringe pattern (or interferogram), generating the fringes in white light

interferometry may be a difficult task [12,13]. The fringes can only be observed when the optical path difference between the two interfering beams is within a small distance range called the coherence length or gate [2,14,15,16]. Instead of directly deriving the height distribution from the interferogram, in SWLI the height of a point on the object's surface is measured by how far the object or the optical component (usually a mirror) has been moved to achieve an OPD equal to zero. This is normally at the point where the fringe visibility becomes a maximum at the pixel of interest [11,12,17]. Height measurement in SWLI is sometimes also called absolute height measurement since it eliminates the ambiguity in surface profiling that is normally encountered in conventional laser interferometry [16,18,19].

In LCI, aside from using a broadband source where multiple wavelengths can be present at the same time, it is also possible to illuminate the object sequentially with light of different wavelengths [20]. This technique is called wavelength scanning interferometry (WSI) and it became possible due to the increasing availability of light sources capable of sequentially emitting a certain range of wavelengths, such as a tunable laser. Such light sources are, however, often very expensive and frequently undergo mode hops during operation [18,21]. Even if a mode-hop free laser is used, besides being expensive, such light sources tend also to be bulky and inconvenient for industrial applications [22].

Within the last 15 years, LCI-based methods have also been developed to provide measurements from under an object's surface, aimed particularly at scattering media. This class of LCI methods is called Optical Coherence Tomography (OCT) [23,24]. In OCT a broadband light source is used as in traditional LCI. Superluminescent LEDs have become a light source of choice in such applications because of their combination of high spatial coherence and low temporal coherence. The basic concepts underlying LCI and OCT are the same, although the terminology has become fragmented due to the different applications (engineering for LCI, medical for OCT). OCT also tends to be used as a point-wise measuring technique, with mechanical scanning used to provide volume information, although parallel versions similar to traditional LCI are also sometimes used [19].

The development of OCT, and therefore of LCI as well, in general followed two main paths: the time domain and Fourier domain [17,19,25] techniques. The later (Fourier-domain) technique removes the need to move a component (either the object or reference mirror), as usually encountered in the time-domain counterpart for depth detection [19,26]. In the time-domain technique, image frames at several different positions of the mirror or

object must be taken before processing can be performed to retrieve the sought depth information. In spectral OCT, instead of a moving mechanism, a spectral dispersing component, such as a diffraction grating, is employed. This becomes possible as the height information is not retrieved from the distance where fringes are detected, but from dispersed spectral components where the depth information is encoded [24,27,28]. Hence spectral OCT enables one to take only single frame [29] to measure the depth distribution along a line, provided that the detected spectral resolution is sufficient to retrieve the height to the desired precision.

Another feature of OCT is its spatial and depth resolution decoupling properties [19]. In conventional optical imaging, the improvement in lateral resolution comes at the expense of detail degradation along the longitudinal axis due to increasing defocus [30]. In OCT this capability can be used in microscopy to increase both resolutions at the same time. In fact, an OCT scanner itself can be considered as a combination of a single spatial mode confocal microscope, capable of performing optical sectioning, and range-gating instrument [23,31,19]. The term Optical Coherence Microscopy (OCM) is sometimes used to describe the implementation of OCT using high numerical aperture (NA) lenses [23]. The use of a high NA objective creates smaller lateral resolution that in turn decreases the focal volume to provide enhanced scatter rejection of out-of-focus light [23,32]. OCM is usually implemented using one of three interferometric microscopy set-ups [33]: Michelson, Mirau [34] and Linnik. Among these three set-ups, the Linnik uses the highest NA objective, thus offers the smallest lateral resolution among the three OCM configurations. The Linnik-based OCM however is more sensitivity to mechanical disturbance than the other two configurations [33].

1.2. Goal of the research work

The goal of this research work is to build an optical measurement prototype based on Low Coherence Interferometry (LCI) capable of measuring either (a) the three dimensional shape of an opaque object (i.e., surface measurements) or (b) depth-resolved (sub-surface) displacement fields of a weakly-scattering object within a single shot. The method represents the extension to an area-based sensor of an interferometric system which measures depth displacement along a line as proposed by Ibarra et al [35], and one dimensional shape measurement as proposed by Schwider and Zhou [36]. The LCI is

implemented using a Linnik interferometric microscope configuration with Fourier-based depth measurement, benefiting from the two advantages described in the previous section.

Details of the motivation behind this goal, as well as the novel features of this research, will be outlined following the report on the literature search presented in Chapter 2.

1.3. Relationship to past work

This research is the continuation of past work in depth-resolved 3-D measurement using LCI performed in the Optical Engineering Research Group of the Wolfson School of Mechanical & Manufacturing Engineering at Loughborough University. The first proof-of-principle experiments of the measurement of depth-resolved whole-field displacements by means of wavelength scanning interferometry were reported in Ref [6]. Details of the concept, and the theoretical and mathematical background of the system were presented in a subsequent article [24]. Recently a double shot Spectral Optical Coherence Tomography (SOCT) system to measure depth-resolved out-of-plane displacement fields through the thickness of a sample was described, with displacement sensitivity around two to three orders of magnitude better than the depth resolution of state-of-the-art OCT systems [35]. This was subsequently extended to the measurement of in-plane displacement fields [37].

In parallel to the successful experiments of LCI for sub-surface depth and displacement field measurements, another potential application of LCI for surface and 3D shape measurement is also being pursued. The current state-of-the-art for LCI profilometers is based on Scanning White Light Interferometry (SWLI), where the object must be scanned through the depth direction. Whilst moving, a number of interferogram frames must be captured in order to detect the occurrence of the peak in the fringe visibility that corresponds to the location of the depth. It will be a significant advance, for the reasons described in depth in the next chapter, if the need for the translation mechanism can be removed. Recognizing the ability of Fourier/spectral domain LCI or OCT to perform depth measurements without the necessity of mechanical scanning, this research is aimed at constructing a prototype of a spectral-based LCI setup capable of performing 3-D shape measurement in a single shot.

Part of the results of this research, on the single-shot profilometry application, has been published in May 2010 [38].

1.4. Organization of the thesis

This thesis is organized as follows:

a. Chapter 1: Introduction

A short description of the motivation behind the research, a brief summary of the pertinent past work carried out by other researchers, the goal of the research, relevancy and relationship to the past work conducted in the group.

b. Chapter 2: Literature review & novel features provided by the research

A more thorough description of the literature review which leads to the identification of the novel ideas underlying this work.

c. Chapter 3: Optical Configuration 1: Microlens-based Low Coherence Interferometer

Presentation of the first prototype, details of the design, the components, set-up construction & alignment, testing the set-up with real object and evaluation on the results leading to the new design set-up.

d. Chapter 4: Optical Configuration 2: Etalon-based Hyperspectral Interferometer

This chapter describes the current prototype which was developed to avoid the problems encountered by the previous design, identification of the possible causes of the first configuration failure, establishing the new design of the prototype, set-up construction and alignment.

e. Chapter 5: Data Analysis

Description of the steps to extract the information starting from the recorded interferogram, creating the 3-D stack of sub-images, Fourier transformation of the data, and a description of problems encountered in spectral peak detection along with a suitable suppression method.

f. Chapter 6: Experimental results 1: Opaque surface profilometry

This chapter analyses the performance of the current set-up in performing profilometry measurements of both a planar and a stepped object and analysis of the set-up leading to some important performance parameters, e.g. depth range, depth resolution and others.

g. Chapter 7: Experimental results 2: Diffuse object

A subsequent test of the prototype is the use of a diffuse/semi-transparent sample to evaluate the prototype performance for depth-resolved (sub-surface) measurements.

h. Conclusion and future work

This chapter concludes the thesis with a summary of the research work undertaken and suggestions and plans for future work.

Chapter 2

Literature Review & Novel Features of the Research

This chapter summarizes the results of a literature search carried out in order to identify other reported work in the field of interferometric profilometry and depth-resolved measurement. Following the exposition of the literature review the novel features of the research are formalized along with the motivation behind the research goal described in Chapter 1.

2.1. Single wavelength interferometry and its limitation

The interference of two or more waves can be utilized to investigate various properties of an object. In shape and depth measurement, interferometry normally involves measuring the phase differences between two waves. Therefore Briers defines interferometry as “the art of using the interference phenomenon to measure phase differences between two waves” [39].

An expression for the recorded interferogram is derived as follows [40]. If the two waves are assumed to be plane with single wavelength λ (monochromatic), they can be represented with complex notations \bar{U}_1 and \bar{U}_2 as follows:

$$\bar{U}_1 = u_1 \exp \left[i2\pi \left(-\omega t + \frac{\delta_1}{\lambda} \right) \right], \quad (2-1)$$

$$\bar{U}_2 = u_2 \exp \left[i2\pi \left(-\omega t + \frac{\delta_2}{\lambda} \right) \right], \quad (2-2)$$

where u_j and δ_j are respectively the amplitude and optical path length (from the source) of wave j ($j = 1,2$). In relation to two-beam interferometry in surface and depth measurements the subscripts $j = 1,2$ refer to the light waves from reference and sample arms, in which the properties of the light wave in the sample arm are altered due to the presence of the object whilst the wave in the reference arm undergoes no alteration.

The detector will record the time-average intensity I given by [41]

$$I = \frac{1}{2} \operatorname{Re}\{\overline{U_1} U_2^*\}, \quad (2-3)$$

where the superscripted asterisk denotes complex conjugate. The detected interferogram can thus be written as

$$I(x, y) = I_1 + I_2 + 2\sqrt{I_1 I_2} \cos[kS(x, y)], \quad (2-4)$$

where $S(x, y) = \delta_1 - \delta_2$ is the optical path length difference between two waves, $k = \frac{2\pi}{\lambda}$ is the wavenumber and $I_1 = \frac{u_1^2}{2}$, $I_2 = \frac{u_2^2}{2}$ are the intensities of waves 1 and 2, respectively.

In the case that both waves are derived from the same source such that $I_1 = I_2 = I_0$, Eq.2-4 can be written as

$$I(x, y) = 4I_0 \cos^2\left[\frac{k}{2}S(x, y)\right]. \quad (2-5)$$

As seen in Eq.2-5 the phase term of the interference pattern (the argument of the cosine term) is dependent on $S(x, y)$, the optical path length difference between the two waves.

If one of the beams is directed onto the object's surface while the other remains undisturbed, the quantity $S(x, y)$ in Eq.2-5 is proportional to the height distribution of the object's surface under investigation, $h(x, y)$, given by

$$S(x, y) = 2h(x, y) \cos \theta, \quad (2-6)$$

where θ is the angle between the two wavefronts. The height distribution is related to a variable called the (integer) fringe order $N(x, y)$ as

$$h(x, y) = \frac{\lambda}{2 \cos \theta} N(x, y). \quad (2-7)$$

Substituting Eqs.2-6 and 2-7 into Eq.2-4 yields

$$I(x, y) = I_1 + I_2 + 2\sqrt{I_1 I_2} \cos[2\pi N(x, y)]. \quad (2-8)$$

If the angle between the two waves, θ , is very small then $\cos \theta \approx 1$. Therefore if the fringe order information $N(x, y)$ can be extracted from interferogram $I(x, y)$ then the surface height distribution $h(x, y)$ can be calculated using Eq. 2-7.

The determination of surface profile using fringe order works well for continuous surfaces, i.e. surfaces with height variations less than $\lambda/4$ between adjacent pixels. There are surfaces however where the height gradient is larger than $\lambda/4 \text{ pixel}^{-1}$, usually called discontinuous surfaces, where the fringe order becomes discontinuous and can no longer be uniquely determined. This is illustrated in Fig.2.1.

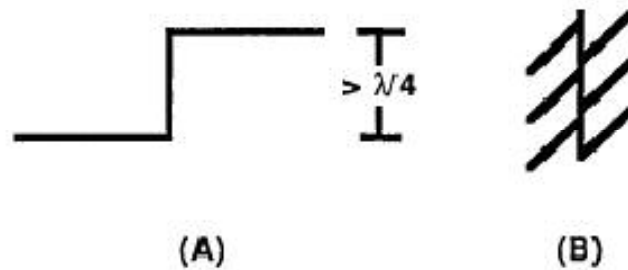


Figure 2.1. Fringe number ambiguity in single-wavelength interferometry when the step height is larger than $\lambda/4$ (figure taken from Ref [42])

This ambiguity problem is inherent in monochromatic interferometry, and can be seen directly from the expression for the interference pattern. As can be seen from Eq.2-8, the interferogram is essentially a cyclical function, so that the phase is wrapped within the interval $[-\pi, \pi]$. This leads to a 2π phase ambiguity problem [2,5,43]. Furthermore, *a priori* knowledge is required to identify the sign of the phase due to the even property of cosine function ($\cos \phi = \cos(-\phi)$) [4]. The wrapped phase interval $[-\pi, \pi]$ corresponds to a surface height range of $\pm\lambda/4$ [44], thus monochromatic interferometry is capable only of measuring height without ambiguity for surfaces where the height variation is less than a quarter of the wavelength [4,22,45,46] between any two adjacent pixels, as indicated in Fig.2.1.

A method called FDA (Frequency Domain Analysis) has been proposed by De Groot to analyse the phase ambiguity problems of the monochromatic interferometer [11,12,44]. The method stems from the fact that non-monochromatic, i.e. broadband or polychromatic, light waves can be decomposed into monochromatic components. Essentially FDA provides an alternative way to view the relation between OPD and wavenumber k . If the roundtrip optical path difference (OPD) between two beams, due to the surface profile, is S then the phase ϕ can be expressed as

$$\phi = kS + \phi_0, \quad (2-9)$$

where ϕ_0 is the phase offset. The linear relation between phase ϕ and wavenumber of the source light k in Eq.2-9 can be plotted and the sought OPD is equal to the gradient of the line

$$S = \frac{\phi - \phi_0}{k}. \quad (2-10)$$

The periodic characteristic of the interferogram phase, due to the cosine term as seen in Eq.2-4, implies that for a particular value of k there could exist more than one phase value. Consequently there will be more than just one line as well as the gradient value leading to ambiguity in determining the OPD.

The ambiguity situation above is interpreted in the method as *the insufficiency of k values to uniquely define the slope of the line*. This is depicted in Fig.2.2. If more k values are available in the frequency domain, then there would be only one possible line and consequently a unique gradient value can be obtained. This can also be interpreted as the more monochromatic waves that are available for measurement, the more accurate the resulting OPD or height measurement that can be expected.

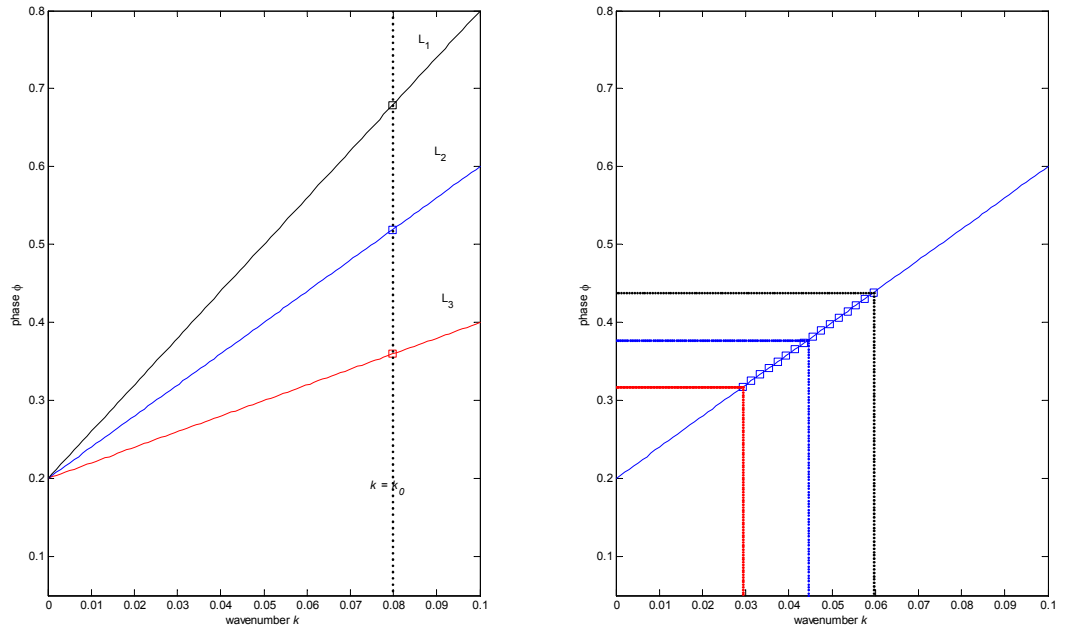


Figure 2.2. (a) height determination ambiguity in single wavelength interferometry, (b) multiple wavelength or k values can uniquely define a line and avoid phase ambiguity (figure adapted from Ref. [44])

Another issue that needs to be addressed in measurement of rough surfaces using a conventional laser interferometer is the speckle effect, as a consequence of the high temporal coherence property of lasers. Speckle is well known to degrade the measurement accuracy [47]. On the other hand incoherent illumination produces almost unnoticeable speckle [48], thus a broad-band based interferometer may be expected to suppress this shortcoming.

2.2. Low Coherence Interferometry

The previous illustration of frequency domain analysis suggests that for measurement of discontinuous surfaces, the use of more than one wavelength will be advantageous to some extent to alleviate the phase ambiguity problem.

Two wavelength interferometry has been used for many years [49,50,51], in which an equivalent wavelength synthesized by this set-up is much longer than that of a monochromatic interferometer. The equivalent synthetic wavelength λ_{eq} is given by [49,50,51]

$$\lambda_{eq} = \frac{\lambda_1 \lambda_2}{|\lambda_1 - \lambda_2|}, \quad (2-11)$$

where λ_1, λ_2 are the two monochromatic wavelengths. Typically the difference between λ_1 and λ_2 is chosen to be small to increase λ_{eq} . The range of unambiguous measurement can therefore be extended up to the height equal to the new synthetic wavelength [52]. Extension to more than two discrete wavelengths has been reported as well [53].

Rather than employing several discrete wavelengths, the use of a continuous, broadband light source has become the main alternative to monochromatic interferometry. In this type of interferometer, a low (temporal) coherence light source is used.

Since conventional monochromatic interferometry only involves a single wavelength, as seen in Eq. 2-4 the wavelength or wavenumber variable is merely a constant. The interferogram equation in Eq. 2-4 depends only on the optical path length difference (OPD) between reference and object arms. In LCI, however, as multiple wavelengths are involved, the integration over wavelength or wavenumber k values must be carried out for the wavelength-dependent variables. This includes the OPD which might be dependent on the wavelength for a dispersive medium [19,54]. Eq. 2-4 therefore becomes [54]

$$I(k) = \frac{c}{2\pi} \left[\int_{-\infty}^{\infty} G(k) dk + \int_{-\infty}^{\infty} G(k) \cos(kS(x, y, k)) dk \right], \quad (2-12)$$

where c is the speed of light in a vacuum. The relation between the two variables is $\nu = c/\lambda$ and $k = \frac{2\pi\nu}{c}$ where ν is the optical frequency. $G(k)$ is the spectral distribution of the light source. In Eq. 2-12 the OPD between reference and object arms $S(x, y)$, which is independent of optical frequency or wavelength in Eq. 2-4, is written as $S(x, y, k)$. This is to take into the account of the possibility of wavelength-dependent OPD if dispersive materials or components are in use.

White light, which is easy to generate and contains a continuous range of wavelengths, becomes one of the most suitable choices for LCI. Several references use the term “White Light Interferometry (WLI)” interchangeably with LCI (see, for example, refs [2,55,56]).

WLI has been used to increase the low resolution compact spectrograph (using a diffraction grating with density 600 lines/mm) by invoking the dispersion characteristics and thickness of a beam splitter or the object [57].

In recent years, however, the preferred light source for LCI has shifted to Superluminescent Light Emitting Diodes (SLD) in place of ordinary white light sources. Compared to ordinary thermal or white light sources of similar dimensions, SLDs typically offer a higher power output, up to tens of mW, compared to a fraction of μW for thermal or white light sources, as well as lower spectral width (see for example table 1 of Ref [19] for details). The smoother Gaussian spectra of SLDs compared to those of thermal or white light sources also offer lower noise [58]. The relatively low cost of SLDs currently makes this diode the preferred LCI light source option in many cases.

The illumination with broadband light in LCI can be carried out sequentially or in parallel. The sequential technique is also known as the wavelength scanning method [24,59]. Typically the parallel presence of broadband light is distinguished in two major schemes: time and frequency domain. As a scanning mechanism is required in a time-domain-based system to detect the fringes, sometimes the time-domain method is also called the scanning method [12,44]. Since frequency-domain-based LCI makes use of different spectral components for the analysis, the method is also referred to as Fourier-based [60] or spectral LCI [26,61].

In terms of the range of depth detection, LCI has been developed not only for surface but also for sub-surface measurement. This special class of LCI is called Optical Coherence Tomography (OCT) [19,24,62]. Lexically the word “Tomography” means *a method of producing a three-dimensional image of the internal structures of a solid object (as the human body or the earth) by the observation and recording of the differences in the effects on the passage of waves of energy impinging on those structures* [63]. It therefore implies that this device was developed mainly for detecting and measuring subsurface depth fields within a scattering medium, to distinguish somewhat from ‘ordinary’ LCI. It is not surprising that OCT has found rapid development for biological-related and medical diagnostic applications (for example: see a compendium of medical OCT applications in the last 13 chapters of ref [58]) since biological tissues usually are scattering media. OCT has been implemented in wavelength-scanning-based [6,24], time-based [64,65], and spectral-based [25,26,35,66,67] forms. Commercially available OCT scanners were initially time-based instruments and have been widely used as eye diagnostic tools in

ophthalmology [66], although spectral and wavelength scanning versions (sometimes called ‘swept source OCT’) are also now commercially available.

The generic designs of two major OCT configurations, the time and spectral-based set-ups, are shown in Fig.2.3.

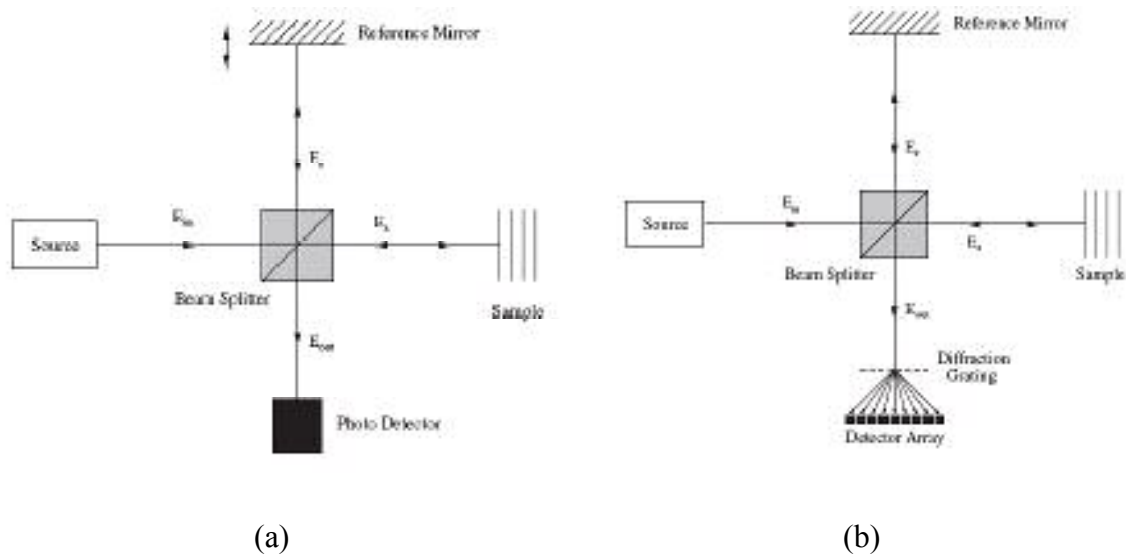


Figure 2.3. Generic OCT set-up in (a) Time domain, (b) Fourier domain. The parallel lines in the sample are to represent layers under the object’s surface. The light source is a broadband one (figures taken from Ref.[62])

Only a few articles have been found for non-medical or biological applications of OCT. These include, for example: (i) a new technique to read multilayer optical disks that can increase the data density storage [68], (ii) the study and non-destructive evaluation of Polymer Matrix Composite materials [69], and (iii) profiling of MEMS silicon V-grooves [70].

2.2.1. Time Domain LCI

Generating interference patterns using broadband light, however, is not an easy task. Interference fringes cannot be observed at all OPD values but only when the value is close to zero or when the OPD matches to within the coherence length of the light source [2,14,71,72,73]. In order to achieve zero or near-zero OPD, either the object or the reference mirrors are linearly scanned, or moved at a constant rate. This is the reason why several references call time domain LCI Scanning White Light Interferometry (see for example Refs [11,12,44,74]). The continuous high amplitude fringe signal for every OPD

value, normally observed in monochromatic interferometry, becomes enveloped around the zero OPD position in time domain LCI.

The envelope that modulates the fringes in WLI is due to the fact that white light can be considered to consist of a large number of monochromatic components. This is illustrated in Fig. 2.4. These components are normally out of phase with one another and hence tend to cancel each other out. Only at or near to zero OPD do the fringes from each spectral component align with respect to each other.

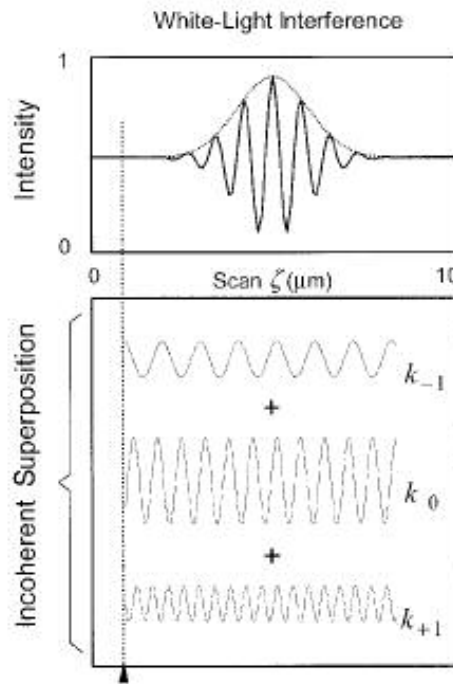


Figure 2.4. The white light fringe envelope can be considered as the incoherent sum of its components (figure taken from Ref [75])

This phenomenon can be explained mathematically as follows: the interferogram expression in Eq.2-4, can be also written as [2]

$$I(x, y) = I_0(x, y) \{1 + V(x, y, \phi) \cos(\Delta\phi)\}, \quad (2-13)$$

where $I_0(x, y) = I_1 + I_2$, and $\Delta\phi = \frac{2\pi}{\lambda} S(x, y)$. The quantity $V(x, y, \phi)$ in Eq.2-13 is called the visibility or fringe contrast. This quantity varies much more slowly with the OPD that,

in turn, acts as the envelope of the more rapidly varying cosine of the phase difference $\Delta\phi$.

Visibility is defined as [2]

$$V(x, y, \phi) = \frac{I_{\max}(x, y) - I_{\min}(x, y)}{I_{\max}(x, y) + I_{\min}(x, y)} = \frac{2\sqrt{I_1 I_2}}{I_1 + I_2} |\tilde{\gamma}_{12}(\tau)| \quad (2-14)$$

where $I_{\max} = I_1 + I_2 + 2\sqrt{I_1 I_2}$, $I_{\min} = I_1 + I_2 - 2\sqrt{I_1 I_2}$ and $\tilde{\gamma}_{12}(\tau)$ is the complex degree of coherence.

As seen in Eq.2-14 the visibility is dependent on a quantity called the complex degree of coherence $\tilde{\gamma}_{12}(\tau)$. It has been derived in various texts (e.g [72,76,48]) that the complex degree coherence $\tilde{\gamma}(\tau)$ is given by

$$\tilde{\gamma}_{12}(\tau) = \frac{\langle \bar{U}_1(t + \tau) \bar{U}_2^*(t + \tau) \rangle}{\sqrt{\langle |\bar{U}_1|^2 + |\bar{U}_2|^2 \rangle}}, \quad (2-15)$$

where $\bar{U}_1(t)$ and $\bar{U}_2(t)$ are the complex temporal amplitudes of the light waves from both interferometer arms, and τ is the coherence time given by

$$\tau = \frac{S(x, y)}{c}, \quad (2-16)$$

where c is the speed of light and $S(x, y)$ is the OPD between the two interferometer arms. For coherent light $|\tilde{\gamma}_{12}(\tau)| = 1$ [2,77], and setting $I_1 = I_2 = I_0$ in Eq.2-14, yields $V(x, y, \phi) = 1$. Eq.2-13 is then simplified to Eq. 2-4. But for partially coherent or incoherent light, such as white light, $|\gamma(\tau)|$ is less than unity. For a non-monochromatic light source it has been also derived in various standard optics texts [72,76,48,78] that the complex degree of coherence is related to the light source's power spectral density $G(k)$ as

$$\tilde{\gamma}(z) \xleftrightarrow{\mathfrak{F}} G(k), \quad (2-17)$$

where the notation \mathfrak{F} denotes Fourier transform.

Typically the broadband light source used in LCI has a Gaussian spectral density. Using Eq.2-17 and basic Fourier transform relation pairs the corresponding degree of coherence of the light source is also Gaussian. This is shown in Fig.2.5. Note that the corresponding wavenumber for the 840 nm centre wavelength is $k_C = 2\pi/\lambda_C = 7.4799 \times 10^{-3}$ rad/nm

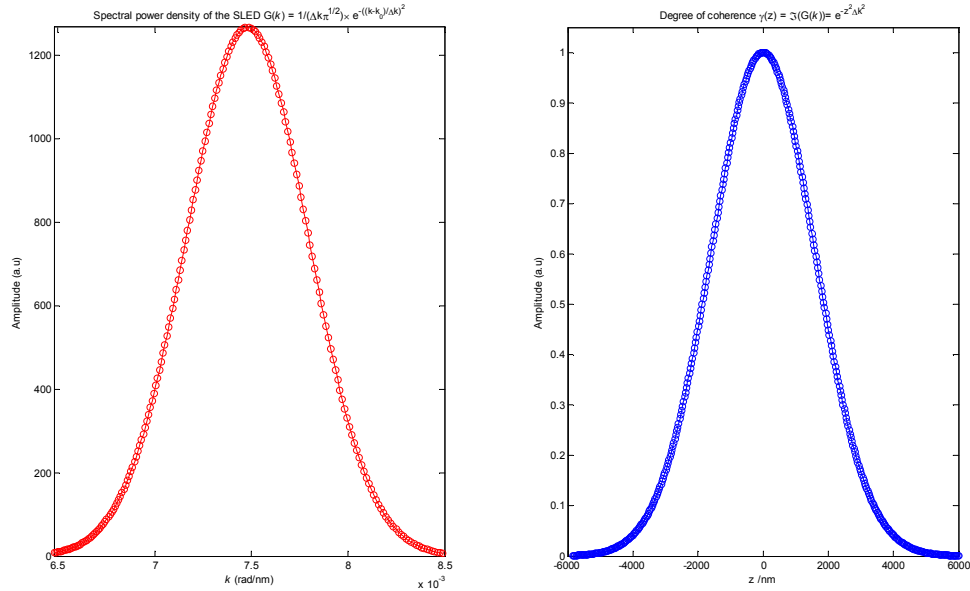


Figure 2.5. The Gaussian power spectral density $G(k)$ of a SLED with centre wavelength $\lambda_C=840$ nm and bandwidth $\Delta\lambda=50$ nm (left), and the corresponding Fourier transform (degree of coherence) (figure adapted from Ref [78])

It can be observed in Fig.2.5 (r.ight) that the peak of the coherence function occurs at the origin, i.e. when $z = 0$, or when OPD, is equal to zero. Hence in a low coherence or white light interferometer, zero OPD gives the highest visibility, and in turn the clearest observed fringes.

There exists, however, an OPD range called the coherence length L_C where reasonably high visibility fringes can still be acquired. The coherence length is related to the mean wavelength $\bar{\lambda}$ and spectral width of the light source $\Delta\lambda$ by [2]

$$L_C = \frac{c}{\Delta\nu} = \left| \frac{\bar{\lambda}^2}{\Delta\lambda} \right|, \quad (2-18)$$

where $\Delta\nu$ is the frequency width of the light source, and related to $\Delta\lambda$ through $\Delta\nu \approx \frac{\nu^2}{c}|\Delta\lambda|$. Coherence length in LCI determines the measurement parameter called depth resolution. This is because the measurement in an interferometric system is based on the occurrence of fringes, and a high fringe visibility occurs only when the magnitude of OPD is smaller than the coherence length.

As shown in Eq. 2-18, depth resolution is inversely proportional to the spectral width of the light used in the measurement. Thus the use of broadband or low coherence light can increase the depth measurement accuracy, as has been previously shown by the FDA method. The near-zero OPD requirement, however, stipulates the use of a high precision moving mechanism to scan the depth axis so as to detect the occurrence of the fringe with the highest contrast [22,79].

Despite this constraint, the use of scanning WLI (SWLI) has been widely reported to achieve very good accuracy in measurement and profilometry applications. A 30 μm thickness film measurement with resolution less than 1 μm has been achieved using white light as long ago as 1972 [14]. Using LCI, *in vivo* measurement of eye length [64] and eye cornea thickness [80] have been carried out. A technique called coherence radar, which is essentially a LCI set-up using white light, has been able to map the 3D surface profile with depth range of 90 μm [65]. In terms of precision, a measurement repeatability of 0.5 nm r.m.s for a surface height range of 100 μm has been achieved by De Groot & Deck [11]. Lower repeatability of 10 nm but for a lower step height of 20 μm was reported in spite of the insufficiently (sub-Nyquist) sampled data [11,74]. By using two AOM (Acousto-Optic Modulators) to produce a heterodyne signal and spherical mirrors, a tandem scanning WLI has been able to measure surfaces with reflectivity smaller than 10^{-4} [81]. Contrast variation or spectral density function based measurements have been also developed to solve the problem of inaccurate peak detection of the interferogram envelope [82]. This method is suitable if the desired depth resolution is not in the nanometer range. A WLI scanning microscope implemented in a Linnik set-up has been reported to measure deep grooves of depth 50 μm with resolution better than 1 nm after processing the phase information [33]. Reconstruction of the visibility function as an aid to detecting the highest contrast can be carried out by adding $\lambda/2$ and $\lambda/4$ plates and measuring the intensity at the center of fringe pattern corresponding to phase differences of $0, \frac{\pi}{4}, \frac{\pi}{2}$ and $\frac{3}{4}\pi$ radian [83].

Care must be taken, however, if the surface is covered by a thin transparent film. Each interface between layers will introduce an additional phase shift to the probing beam [27]. The interfaces can also introduce a change in the surface spectral reflectance that can shift the fringe visibility peak. As a result the peak visibility position no longer corresponds to the correct zero OPD [84]. This effect must be taken into consideration particularly when the layer thickness is in the order of, or less than, the coherence length of the white light source [84].

2.2.2. Spectral-based LCI

The need for a longitudinal moving mechanism can be avoided by utilizing the spectral information of the reflected light from the object. The terms SRWLI [85] and SAWLI [61,86], which stand for Spectrally Resolved and Spectroscopic Analysis White Light Interferometer, respectively, have been coined for this method.

This principle has been exploited by Schwider who used a dispersive grating to replace the moving mirror [36], as shown in Fig.2.6. The interference pattern of the light coming from reference and object surfaces was dispersed by the grating. For each of the white light's spectral components, a maximum intensity occurs when the OPD between the reflected light from the object's surface and the reference wave is an integral multiple of the wavelength, i.e.

$$2h = (m_0 + j)\lambda_j, \quad (2-19)$$

where j and m_0 are integers, λ_j is the wavelength of the corresponding maximum intensity and h is the surface depth. Without derivation, the surface depth h is given as [36]

$$h = \frac{n(n-1)(n+1)}{\frac{6}{\pi} \left[2 \sum_{j=1}^n j k_j - (n+1) \sum_{j=1}^n k_j \right]}, \quad (2-20)$$

where n the number of resolvable wavelengths by the detector and k_j is the corresponding wavenumber of the maximum intensity.

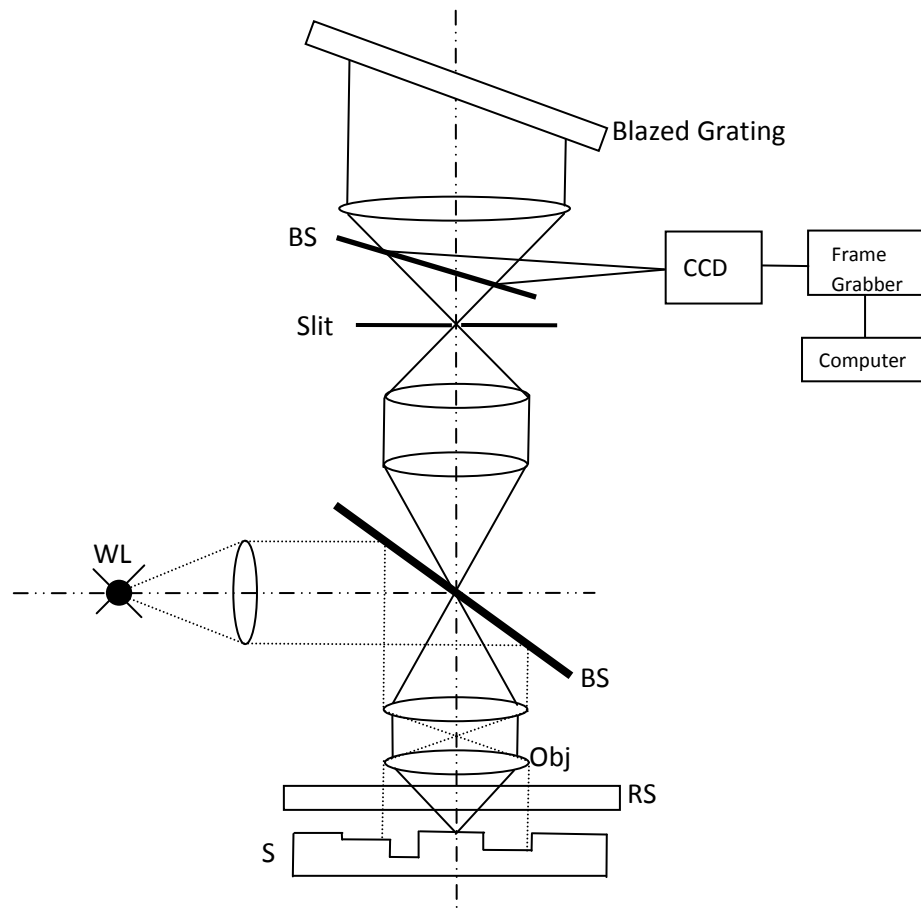


Figure 2.6.. Schematic components of a dispersive interferometric profilometer (figure adapted from ref. [36]). WL = White Light source, Obj = (microscope) objective, RS = Reference Surface, S = Sample, BS = Beam Splitter

Sandoz et.al used a prism, instead of a grating, as the dispersing element and realized the interferometer in a Mirau set-up. Instead of finding the maxima of each spectral component of the white light, the phase map was determined directly from the interferogram after performing phase unwrapping. A 1 nm resolution of a binary surface has been achieved using this set-up [86]. The other means to disperse the white light, apart from a grating or a prism, is a Diffractive Optical Element (DOE) where the object's profile can be determined from the detected chromatic wavelets [28]. Resolution of spectral detection was reported as 4 nm at a wavelength of 650 nm and an axial range of 30 μm has been measured. Combined with a Fourier Transform Spectroscopy module, a spectral LCI system is able to achieve 5 nm repeatability [61]. A so-called Dispersive Comb Spectrum Interferometer (DCSI) was proposed using a comb spectrum light source obtained from a low cost laser diode [87], and reported to have a maximum permissible working range of 1.2 cm, non ambiguous measuring range (NAR) of 1.6 mm, with an error of 1.2 μm . Limitations of the

system included thermal stability normally encountered in laser diodes, and the inverse proportionality relation of NAR to the sampling period of the comb spectrum. Increasing NAR can be achieved by lowering the sampling period but it can lead to aliasing of the spectrum.

Techniques using more than one grating have also been reported. The use of two gratings for surface profilometry has been proposed by [88]. The set-up is shown in Fig.2.7.

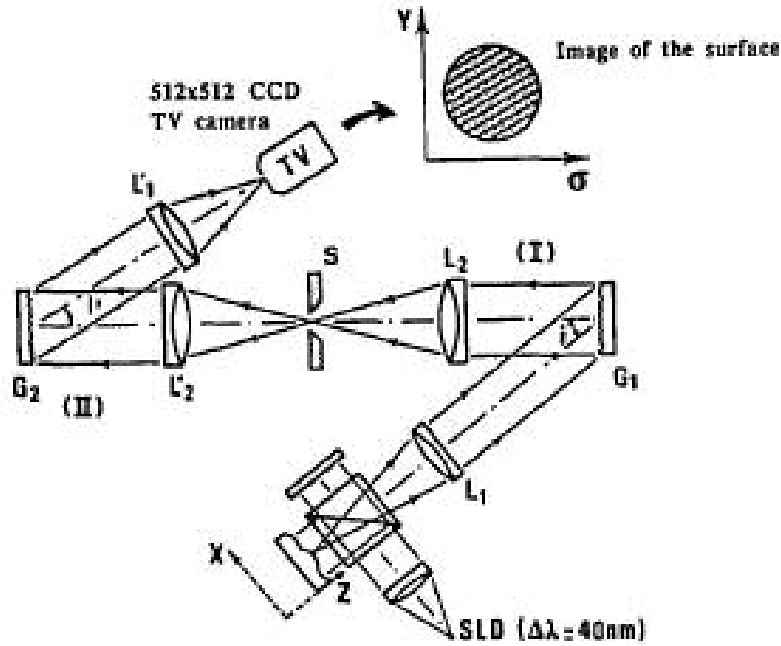


Figure 2.7. Double grating profilometer (figure taken from Ref [88])

The first grating is located after a broadband interferometric profilometer to disperse the interferometer output. The first grating subsequently ‘maps’ the spatial coordinate of the incoming beam to the ζ -domain, where $\zeta = \frac{1}{\lambda}$. The x -coordinate at the slit is chosen in this experiment such that $x = x(\zeta)$ and thus $h(x,y)$ becomes $h(\zeta,y)$. The slit, located after the first grating, is conjugate to the object and oriented in the y -direction. The second grating reverses the operation, i.e. splits the spectral superposition at the slit into the constituent spectral components. Without derivation the height distribution along y direction (x axis is for σ axis) at the exit plane of the system $h(y)$ is given as [88]

$$h(y) = \frac{1}{4\pi\sigma} \cos^{-1} \left\{ \frac{I(\zeta, y) - G(\zeta)[1 + T(\zeta, y)]}{V(\zeta, y)G(\zeta)[1 + T(\zeta, y)]} \right\} + C, \quad (2-21)$$

where $I(\zeta,y)$, $G(\zeta)$, $T(\zeta,y)$, $V(\zeta,y)$ are the recorded intensity at the CCD, the spectral distribution of the light source, the sample reflectivity and the fringe visibility, respectively. The constant C is to take into account the initial random phase, which can be calculated, for example, with *a priori* knowledge of the height at one point on the surface. The system indeed can only measure the height along a line, thus it requires a scanning mechanism to cover the entire sample. The proposed method was reported to be able to achieve lateral and depth resolutions of 3 and 10 μm , respectively, but for smooth surface measurements the resolution was found to be below that of a phase shifting interferometer.

A more thorough discussion on the principles of spectral or Fourier-based LCI has been presented by Fercher et al. [19], although the case developed in the paper is the measurement of the scattering potential inside the scattering medium. Suppose the sample under investigation is illuminated with a plane incident wave

$$U^{(i)}(\mathbf{r}, \mathbf{k}^{(i)}, t) = u^{(i)} \exp\{i(\mathbf{k}^{(i)} \cdot \mathbf{r} - \omega t)\}, \quad (2-22)$$

where $\mathbf{k}^{(i)}$, \mathbf{r} are the wave vector of the illuminating wave and the spatial coordinate of the propagating wave, respectively and $|\mathbf{k}^{(i)}| = \frac{2\pi}{\lambda}$ is the wave number of the incident light wave. The scattered wave can be expressed as a function of the incident wave as

$$U_S(\mathbf{r}, \mathbf{k}^{(s)}, t) = U^{(i)}(\mathbf{r}, \mathbf{k}^{(i)}, t) + \frac{1}{4\pi d} \int_{Vol(\mathbf{r}')} U^{(i)}(\mathbf{r}', \mathbf{k}^{(i)}, t) F_S(\mathbf{r}', \mathbf{k}) G_H(\mathbf{r}, \mathbf{r}') d^3 \mathbf{r}', \quad (2-23)$$

where $\mathbf{k}^{(s)}$ is the wave vector of the scattered wave, $Vol(\mathbf{r}')$ is the illuminated sample volume, \mathbf{r}' denotes a coordinate within the sample illuminated by the incident wave, and

$G_H(\mathbf{r}, \mathbf{r}') = \left(\frac{\exp(ik|\mathbf{r} - \mathbf{r}'|)}{|\mathbf{r} - \mathbf{r}'|} \right)$ is the free-space Green's function. The term $F_S(\mathbf{r}', \mathbf{k})$

represents the scattering potential of the sample which is given by [19]

$$F_S(\mathbf{r}, \mathbf{k}) = k^2 [m^2(\mathbf{r}, k) - 1], \quad (2-24)$$

with m is the complex refractive index distribution of the sample structure and given as

$$m(\mathbf{r}) = n(\mathbf{r})[1 + i\kappa(\mathbf{r})], \quad (2-25)$$

where $n(\mathbf{r})$ and $\kappa(\mathbf{r})$ are the phase refractive index and attenuation index, respectively. The scattering potential therefore can be physically viewed as the distribution of (complex) refractive index, as well as attenuation coefficient, inside the material to be probed [89], which in turn represents the sample's microstructure [90]. As shown in the Ewald sphere representation of OCT in Refs [19,90], LCI and OCT detect the high frequency components of the scattering potential. Using the Fourier transform, it can be seen that this property is related to the derivative of the scattering potential, which means that LCI or OCT is sensitive to the discontinuities or changes of the scattering potential [19]. Since the LCI parameter d -the distance from the object to the point where the scattered wave is detected- is much larger than the dimension of the coherently illuminated sample volume $\text{Vol}(\mathbf{r}')$, the amplitude of the illuminating wave $u^{(i)}$ can be assumed constant throughout the probe volume. The scattered wave expression of Eq.2-23 at distance d can be written as

$$U_s(\mathbf{r}, \mathbf{K}, t) = \frac{u^{(i)}}{4\pi d} \exp\{i(\mathbf{k}^{(s)} \cdot \mathbf{r} - \omega t)\} \int_{\text{Vol}(\mathbf{r}')} F_s(\mathbf{r}') \exp(-i\mathbf{K} \cdot \mathbf{r}') d^3\mathbf{r}'. \quad (2-26)$$

The quantity \mathbf{K} inside the integral in Eq.2-26 is the scattering vector and is related to the incident and scattered wave vectors $\mathbf{k}^{(i)}$ and $\mathbf{k}^{(s)}$, respectively as

$$\mathbf{K} = \mathbf{k}^{(s)} - \mathbf{k}^{(i)}. \quad (2-27)$$

From Eq.2-26 it can be seen that in the far field approximation the amplitude of the scattered wave U_s is proportional to the inverse Fourier transform of F_s . This can be found as follows: referring to Eq.2-22 the expression for the scattered wave is

$$U_s(\mathbf{r}, \mathbf{k}^{(s)}, t) = u_s \exp(i\mathbf{k}^{(s)} \cdot \mathbf{r} - i\omega t), \quad (2-28)$$

and by comparing with Eq.2-26 it can be seen that

$$u_S(\mathbf{r}', \mathbf{K}) = \frac{u^{(i)}}{4\pi d} \int_{Vol(\mathbf{r}')} F_S(\mathbf{r}') \exp(-i\mathbf{K} \cdot \mathbf{r}') d^3\mathbf{r}'. \quad (2-29)$$

Hence

$$u_S(\mathbf{r}') \propto \mathfrak{T}^{-1}\{F_S(\mathbf{r}')\}, \quad (2-30)$$

where \mathfrak{T}^{-1} denotes inverse Fourier transform. This relation serves as the basic theorem of diffraction tomography.

The detected signal in LCI is mostly the backscattered wave. Since the direction of the backscattered wave is the opposite of that of incident wave, i.e. $\mathbf{k}^{(s)} = -\mathbf{k}^{(i)}$, and by using Eq.2-27 the backscattered wave vector \mathbf{K} is

$$\mathbf{K}_j = -2\mathbf{k}_j^{(i)}, \quad (2-31)$$

where the magnitude of \mathbf{K}_j is given by $|\mathbf{K}_j| = \frac{4\pi}{\lambda_j}$, and subscript j refers to the j^{th} wavelength component of the broadband light.

In a LCI implementation, typically the sample is illuminated by a narrow beam and the only detected light is the backscattered beam. It is assumed that the scattering potential F_S inside the illuminated sample to be independent of the spatial coordinate \mathbf{r}' , which leads to the simplification of the integral in Eq.2-26 to be substituted by a constant factor. The expression for the backscattered light in Eq.2-26 at constant distance z which, again, is assumed to be much larger than the dimension of the coherently illuminated probe volume, can be further simplified as

$$U_S(z, K, t) = u_S(K) \exp[-i(kz - \omega t)], \quad (2-32)$$

with $K = 2k$ by invoking the relation in Eq.2-31. Setting the distance d in the denominator of Eq.2-29 as a constant, the wavelength dependent complex scattering field amplitude $U_s(K)$ becomes proportional to the inverse Fourier transform of the scattering potential F_s , or

$$u_s(K) = a_s(K) \exp(i\Phi_s(K)) \propto \mathfrak{F}^{-1}\{F_s(z)\}, \quad (2-33)$$

where $a_s(K)$ and $\Phi_s(K)$ are respectively the amplitude and phase of the complex scattering function $u_s(K)$.

Taking the Inverse Fourier Transform of the relation in Eq. 2-33 yields

$$F_s(z) = \mathfrak{F}\{u_s(K)\}. \quad (2-34)$$

The relation in Eq.2-34 serves as the physical basis of the Fourier domain LCI and OCT: *the scattering potential distribution can be constructed by taking a Fourier transform of the backscattered signal.*

The scattering potential $F_s(\mathbf{r})$ in the theory developed previously can be considered to represent particles or a layer that scatters the incident broadband light. In relation to the measurement of surface shape this scattering layer can be the surface of the object that reflects the incoming wave. Therefore the relation in Eq.2-34 can be also applied to shape measurement even though it was originally developed for sub-surface measurement.

A more ‘direct’ treatment to utilize spectral information to extract depth information is given as follows [24]: if the j^{th} layer is considered, the phase difference ϕ accrued between the reference beam and the depth-probing object beams of an LCI system back-scattered by that layer is given by

$$\phi_j(\lambda) = \phi_{j0} + \frac{4\pi}{\lambda} z_j = \phi_{j0} + 2kz, \quad (2-35)$$

where ϕ_{j_0} is the phase change due to reflection at the j^{th} layer, z_j is the optical depth of the j^{th} slice relative to the reference wavefront, and λ is the wavelength ranging from $\lambda_c - \Delta\lambda/2$ to $\lambda_c + \Delta\lambda/2$ where it is assumed that the LCI light source has a symmetrical distribution of spectral width $\Delta\lambda$ around centre wavelength λ_c . Similar to the definition developed in FDA [44,75], the frequency in this article was defined with respect to the wavenumber $k = \frac{2\pi}{\lambda}$. Referring to Eq.2-35, the frequency is given by

$$f_k = \frac{1}{2\pi} \frac{\partial \phi}{\partial k} = \frac{z_j}{\pi} \quad (2-36)$$

which is proportional to the optical depth of the j^{th} layer under observation. Information in the wavenumber (f_k) domain can be obtained following the Fourier transformation of the interferogram, where subsequently depth information can be extracted [24].

The depth-encoded spectral information enables Fourier-based LCI or OCT to eliminate the longitudinal (z -axis) scanning mechanism. Notwithstanding this, scanning along the lateral directions (x & y axes) is still required. Methods have been proposed to achieve unidirectional lateral scanning, either only in the x or y direction, typically by illuminating the sample with a line, instead of a point, of light. Endo et al. report the construction of a line-field spectral LCI profilometer system [91]. A line-shaped light beam, after passing through a cylindrical lens, is focused to the specimen so that a 2-D (depth and one lateral direction) shape can be measured from a single-shot image. The time taken to profile a volumetric sample of $2.6 \text{ mm} \times 2.6 \text{ mm} \times 0.8 \text{ mm}$ was 30 s, with lateral and depth resolution limited by the pixel size of $9 \text{ }\mu\text{m}$ and the coherence gate size of the light source of $13.5 \text{ }\mu\text{m}$, respectively [91]. The use of cylindrical lenses for a phase contrast version of spectral OCT to achieve depth range and depth resolution around 5 mm and $60 \text{ }\mu\text{m}$ has been also reported [35].

Applications of spectral-based WLI, apart from surfaces, include extension to profilometry of multilayer objects. One and two dielectric layers deposited upon a Si substrate have been measured to an accuracy in the order of 10 nm, provided the refractive indices are given, using 5 adjacent spectral samples on a linear photodetector array [27]. Thickness in a semitransparent dispersive media has also been measured where the spectral dispersing

module is realized by a spectrometer and a simple linear photo diode [92]. The apparatus was used to measure the effective refractive index of a silicone oil drop by separately measuring the OPD of the gap between two sapphire windows filled with air and oil. The value of refractive index was found to be 300 times more accurate as compared to the measurement using WLI. Sources of error may include incorrect determination of fringe maxima.

For multilayer depth profiles, the measurement inaccuracy problems due to the shift of the fringe visibility peak normally encountered in SWLI have been addressed by Kim et al. by using an Acousto-Optic Tunable Filter (AOTF) as a spectral scanning means in three methods. First is the detection of the peak in the spectral mode, achieving an error range of 20 nm for a thickness range of 4 μm [93]. Second is by the introduction of a spatial carrier to the wavelength-dependent phase function [16] followed by height calculation using Takeda's Fourier transform method for fringe analysis [60], to yield an average of 15 nm thickness difference with SEM measurements. Third is by performing a least square fitting on measured phase functions taken from 5 different wavelengths with the phase function model by assuming a known layer thickness. The third method was reported to give similar accuracy compared to the Fourier transform result but with approximately 5 times less calculation time [94].

In terms of algorithms, several methods to extract phase information from SRWLI interferograms have been reported. A method to recover phase by using a set of quadrature interferograms, obtained by a pair of $\lambda/4$ retarders, followed by phase shifting processing, has also been proposed [47], yielding an accuracy of $\bar{\lambda}/70$ where $\bar{\lambda}$ is the mean wavelength. A similar phase shifting technique but using half and quarter wave plates and a dispersing prism has been reported to achieve an error of a fraction of a nm when a five-step algorithm is used [85]. A method to determine the (integer) spectral order, in which its product with the corresponding wavelength equals the OPD between two beams, using 2 adjacent peak wavelengths in the interference spectrum, has also been reported [95]. The method is appropriate for a compact fiber optic sensor head for industrial applications where a low cost multimode fiber is used, and is only capable of resolving 2-5 peak wavelengths from the spectral interferogram. A method of illuminating one line profile on a large surface using a white light supercontinuum source (wide spectral width with peak at 532 nm) combined with a seven point phase calculation algorithm [96] has been reported to achieve a maximum deviation of 6 and 60 nm and spatial resolution 40 and 18 μm when

measuring plane mirrors with surface flatness of $\lambda/20$ and higher than $\lambda/2$, respectively [29].

The effect of the light source spectrum on the accuracy of height profile measurement has also been investigated for an LCI system working in phase shifting mode [55]. It has been derived that if the light source's spectrum is not symmetric the phase will no longer linear with the optical path difference. An additional phase correction factor is therefore needed and this parameter can be computed using knowledge of the source's spectral distribution. The accuracy improvement by using this correction factor has been shown by comparing the predicted (theoretical) and measured phase and visibility values, which yielded an average difference of less than 0.5% for both quantities.

Fourier-based LCI, however, is not without limitations. Problems are mainly associated with the inevitably wide spectral width, such as: spectral dispersion, absorption, attenuation and scattering. These disadvantages become more profound for non-uniformly transparent objects such as biological samples inside a liquid medium [56]. Experiments and simulations carried out by Pfötner et.al indicated that a small angular error of the beam splitter plate can shift the envelope of the interferogram and lead to a so-called 'ghost step' with a height of $\bar{\lambda}/2$ at the height step being measured ($\bar{\lambda}$ is the mean wavelength) [97]. The dispersion properties of piezoelectric transducer (PZT) phase shifters reported in SRWLI set-ups of Helen et al. [85] caused considerable phase shift variation across the detector pixels that must be compensated using an appropriate phase shifting algorithm.

2.2.3. Wavelength scanning LCI

Most of the reported profilometry work using broadband LCI or OCT came from Fourier based methods. As briefly described in the Introduction section the broadband spectrum can be delivered to the object simultaneously or sequentially. The latter method is usually called wavelength scanning interferometry (WSI).

One possible light source for WSI is a laser diode. In general the emitted wavelength does not vary linearly with the injection current. There is, however, often a small region in which the linear relation between injection current and emitted wavelength holds, thus allowing this type of device to serve as a WSI light source. Kikuta et al. reported the use of a laser diode and by varying the injection current produced a wavelength shift to measure rough surfaces [98]. A laser diode with 20 mW power output, 789 nm wavelength at 70

mA injection current was used to measure the phase change after being reflected from 2 different rough surfaces (aluminium and brass plates) and the results were compared with those obtained from a mirror. For a small OPD range of less than 6 mm the phase variations from both the rough surfaces and the mirror were found to be linear with changes in wavelength, in which the wavelength change itself is linear to the change of the injection current to the diode. Some systematic error problems using this technique include: optical feedback of light reflected back into the cavity, small longitudinal sub-modes (due to the fact that the laser not only oscillates on a single longitudinal mode, but is also accompanied with other side modes), and coherent noise due to reflected light from optical devices that interfere with the signal [99]. Attempts to suppress these shortcomings have been proposed by applying the FFT method initially developed for analysis of fringes with a spatial carrier [60], which gave a good agreement with the experimental results but with some limitations including the non-linear injection current-wavelength relation of the laser diode, influence of mechanical vibration, and separation of the frequency spectra [100]. The need for a Fourier transform can be avoided if the laser diode is driven with a certain waveform that produces in the coherence function a delta-function-like shape, yielding a selective depth extraction of the object [101]. This method, however, is essentially a holographic-based one in that the depth information can be retrieved after the reconstruction process. Similar problems in the previously reported works associated with non-linear characteristics of the laser diode were also encountered again in this experiment.

A frequency tunable laser diode has been also employed for profilometry using wavelength shifting speckle interferometry [79]. Combined with Takeda's FFT analysis the method has been able to measure objects with heights within the range of tens and hundreds of mm and resulting in an average difference of 0.2 mm with caliper measurements. The tunable laser diode operated at 670 nm, however, exhibited mode hops yielding a resolution of around 500 μm . This accuracy is thus far below the typical 1 μm depth resolution of SWLI, with depth range around 100 μm , using a white light source with center wavelength of 561 nm [12] and the coherence radar reported in [65] which had a depth range of around 20 mm. This speckle WSI technique does however eliminate the need for a depth scanning mechanism. Another tunable-laser-based broadband profilometer has been reported that for a 25 nm wavelength scanning width was able to achieve 1 μm resolution, comparable to that of SWLI and coherence radar [52]. The source of errors reported included dispersion effects, and speckle effects as coherent light is used to illuminate the rough surface, and

also zero crossing counting errors. The last factor becomes substantial since the height profile $h(x, y)$ is derived from the relation

$$h(x, y) = \frac{1}{2} \frac{\pi(N_z - 1)}{k_N - k_1}, \quad (2-37)$$

where $N_z(\Delta k; x, y)$ is the number of zero crossings occurring due to the wavenumber shift Δk and $k_i (i = 1 \sim N)$ is the wavenumber when the i^{th} zero crossing occurs. Eq.2-37 is in fact an approximation of the analytical relation between height profile $h(x, y)$ and the phase shift of the interference signal $\Delta\phi$ given by

$$h(x, y) = \frac{1}{2} \frac{\Delta\phi}{\Delta k}, \quad (2-38)$$

or

$$\Delta\phi(\Delta k; x, y) = 2h(x, y)\Delta k, \quad (2-39)$$

which shows the direct dependence of the phase change on the tuning range of the light source.

For diffuse surfaces the phase introduced after reflection can be assumed to be a random variable distributed in the range $[-\pi, \pi]$. Thus a π phase change can be identified by counting one zero crossing of the fringe, leading to the approximation in Eq.2-35.

The majority of the reported WSI profilometers were implemented in a Michelson configuration. Yamaguchi et al. experimentally tested an alternative implementation of the system in a Fizeau set-up, which has some benefits of compactness, simplification of the interferometer head (as only one interferometric arm is needed), and an increase of sample area compared to the Michelson counterpart [59]. The multiple reflections from the reference mirror and test surface in the Fizeau interferometer, however, must be taken into consideration. The Fourier transform of the fringes shows that the multiple reflections cause the presence of higher harmonics. For step and curved smooth surfaces, however, the

Fizeau profiler showed no noise spikes in the reconstructed height profile. In contrast to the Fizeau set-up, the Michelson set-up showed noise spikes, although the spikes were usually isolated or localized so that they could be removed by simple median filtering. These spikes were most likely coming from surface points with low reflectance or dark speckles. This advantage of the Fizeau set-up needs to be weighed against the difficulties in setting the sample under the reference plate since the gap must be of order 1 mm or less. Both set-ups exhibited more profound isolated spikes in height maps of milled or diffuse surface which increased with the amount of imaging system defocusing. The height resolution achieved by both set-ups was 39 μm by scanning the wavelength from 570.9 to 575.1 nm with tuning step of 0.016 nm.

The wavelength scanning mechanism in the system described by Sasaki et al. involved a sinusoidally-moving slit. The moving slit filtered the optical spectral distribution of the SLED light source obtained from a grating. The system was reported to measure OPD longer than a wavelength with an accuracy up to 2 nm [45]. This system however required a sinusoidal signal generator to drive the sinusoidal motion of the slit as well as the mirror. The use of a Liquid Crystal Fabry-Perot Interferometer (LC-FPI) as a wavelength scanning device has been reported by Kinoshita et al. and achieved an average step height profiling difference of 0.23 μm compared with the results obtained from a contact stylus measurement, with an average precision of 0.22 μm [18]. Mehta et.al has also used LC-FPI to construct a spectral interferometric microscope capable of performing 3-D step height surface measurement [22]. The system was also reported to be able to do optical depth sectioning by selectively filtering the temporal frequency components produced by the LC-FPI. The measurable range of the step height profiling was between 12.6 and 261 μm [22]. The resolution of these two LC-FPI based systems is strongly affected by the finesse of the Fabry-Perot etalon.

2.2.4. Comparison between LCI configurations

A summary of three main Low Coherence Interferometry configurations described in previous sections is presented in Table 2.1. The configurations presented in the table are Time-domain or Scanning Wavelength Interferometry (SWLI), Wavelength Scanning Interferometry (WSI) and Spectral-domain Optical Coherence Tomography (OCT).

Table 2.1. Comparison of three main LCI configurations

	SWLI	WSI	Spectral OCT
Depth resolution	$\sim \frac{\lambda_c^2}{\Delta\lambda}$	$\sim \frac{\lambda_c^2}{\Delta\lambda}$	$\sim \frac{\lambda_c^2}{\Delta\lambda}$
Depth range	∞ (limited by stage movement)	$\frac{N_f}{4} \frac{\lambda_c^2}{\Delta\lambda}$	$\frac{N_y}{4} \frac{\lambda_c^2}{\Delta\lambda}$
Acquisition time	$N_f \times \tau$	$N_f \times \tau$	τ
Advantage	Better spatial resolution	Better spatial resolution	Single-shot acquisition

N_f = number of recorded frames

τ = exposure time

N_y = number of pixels along the CCD spectral axis

As shown in Table 2.1, despite lower spatial resolution, the spectral-based LCI/OCT offers higher data acquisition rates compared to the other two configurations. In order to extract the depth information a spectral-based set-up requires only one frame, whilst the other configurations need N_f frames. The current spectral configuration set-ups however are point or line imaging based system, thus to create a full 3-D depth image an additional scanning mechanism is required. The subsequent chapters (chapters 3 and 4) will report on designs of LCI systems capable of performing full-field 3-D surface and depth measurement in a single shot (without scanning mechanism) based on the spectral configuration set-ups.

2.3. Interference Microscope

The Interference microscope is briefly described in this section since most of the LCI profilometers nowadays are based on this optical arrangement. Furthermore the interferometer part of the first prototype design in this thesis is also based on this configuration. Frequently appearing terms are also to be briefly explained here.

Essentially the idea of an interferometric microscope came from the fact that any LCI, either white light or broadband, is capable of localizing measurement or imaging at a particular depth range, a similar capability to the optical sectioning ability of a confocal scanning microscope [102,103]. In the first interference microscope system reported in the literature, a Michelson SWLI module was attached to the microscope under the objective lens to image a 4 μm step target, that could otherwise confuse the measurement by a standard laser interferometric profilometer [12]. The vertical resolution obtained from this first prototype was 10 nm. A diagram of the prototype is shown in Fig.2.8.a.

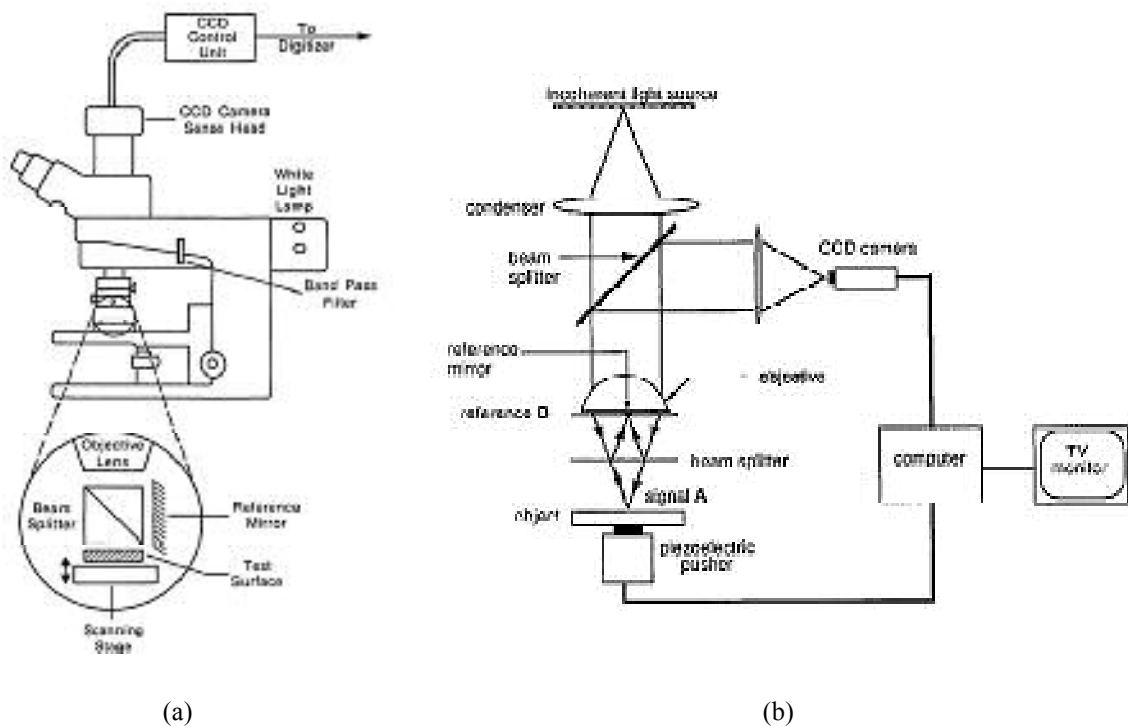


Figure 2.8. First practical prototype of (a) interference (figure taken from [103]) and (b) correlation microscopic profilometer (figure taken from Ref [104]).

Another term frequently found in several papers from the literature is the correlation microscope. Once again, this type of microscope is physically an LCI attachment to a microscope and located under the objective. The term correlation comes from the fact that the interferometer essentially measures the correlation signal between the objective beam and reference beam. Although in LCI the light is temporally incoherent, or partially incoherent, as usually both object and reference beams are derived from the same source their spatial coherence properties can be maintained so that the interference between two waves can still take place [104]. This is the reason that sometimes an interference microscope is also called a coherence microscope. The first prototype of a correlation

microscope was based on a Mirau set-up, and was also developed by the same researchers Kino and Chim [34]. The 3-D image realization using a Mirau correlation microscope was reported 2 years later [105]. A diagram of a correlation microscope is shown in Fig.2.8.b.

Another occasionally-found related term is optical coherence microscopy (OCM). OCM can be considered to be a combination of a confocal microscope with a low coherence interferometer [31]. The lateral and longitudinal resolution decoupling property of OCT [19] enables one to increase the resolution in one direction without affecting it in the other. Improving resolution along the lateral axes, using a high NA microscope objective, results in a smaller illumination area. This in turn creates a smaller probing volume. Scatter rejection of out-of-focus light can therefore be enhanced to yield lower noise in the signal detection stage [23].

Generally there are 3 main geometries to implement a low coherence interference microscope: Michelson, Mirau and Linnik (see Fig. 2.9). The Linnik set-up provides the highest lateral resolution [33,106] but is more sensitive to mechanical noise [33].

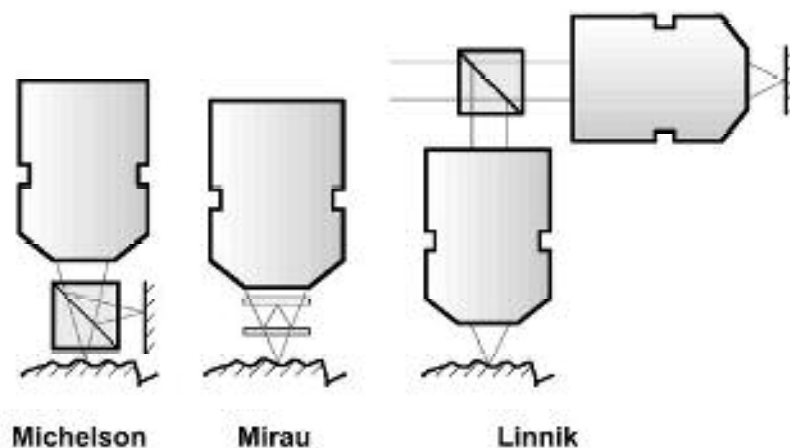


Figure 2.9..Three main types of LCI microscope (figure taken from reference [33])

Several profilometers cited in the previous sections, both in the time [12,33,55,97] or the spectral domains [16,22,27,28,86,94], have now been realized in one of these interference microscope geometries.

2.4. Novel features and motivation behind the research goal

As previously described in Section 1.2, the aim of this research is to be able to build a low-coherence interferometer capable of performing 3D shape and depth measurement within only a single shot. This short term goal can be regarded as a stepping stone to the more ambitious objective of measuring scattering potential and displacement fields within a weakly scattering media, again with a single shot acquisition for each of the deformation states of the object.

In the preparation of this thesis, a literature search of around 500 abstracts was undertaken, and over 100 of these were subjected to a more detailed reading. Although by the time of the preparation of this thesis a number of publications pertinent to shape and depth measurement have appeared and claim the similar capability of single shot measurement, none of the reported methods bear a strong resemblance to the prototypes developed in this research work. Baker and Stappaerts constructed a Liquid Crystal Spatial Light Modulator (LC-SLM) combined with linear polarizers to construct a pixellated phase shifting interferometer – a laser interferometer where several phase shifted interferograms are spatially multiplexed within a single frame to achieve single-shot recording [107]. Sugiyama et.al proposed a new algorithm called local model fitting (LMF) to estimate the phase of a point of interest (x_0, y_0) from the recorded (laser) interferogram value $I(x, y)$ at nearby points (x, y) [108]. A single interferogram is sufficient as the input to the algorithm. It locally analyses the phase at (x_0, y_0) by least squares fitting of the model to the measured data. This approach however requires a strict assumption that the phase is constant in the vicinity of (x_0, y_0) and in practice must be followed by a median filtering to remove sharp jumps in the vicinity of a height discontinuity region. Assumptions underlying the algorithm were later re-analysed and an improved version called interpolated local model fitting (iLMF) was proposed [109]. Another single-shot surface profiling technique has also been reported by Su and Liu in which fringe patterns of two different spatial frequencies, recorded in a single frame, are projected onto the surface of an object [110]. A single-shot version of a radial-shearing laser interferometer with phase-shifting mechanism has been reported by Toto-Arellano et al. [111]. The same authors also developed the lateral-shear version of the apparatus [112]. In a similar way to the previous authors, in which multiple interferograms of different polarisation states are multiplexed into a single frame, Hrebesch et al built a profilometer using a (broadband) LED of central wavelength $\lambda_C = 846$ nm and Full Width Half Maximum (FWHM) = 46 nm, with each interferogram phase-shifted with respect to the others [113]. Despite their claim to produce the

volumetric image in a single shot, however, the reference mirror must be scanned in the axial direction. They demonstrated that their proposed system is capable of producing $4\text{ mm} \times 4\text{ mm} \times 160\text{ }\mu\text{m}$ (depth) volumetric images with a $1\text{ }\mu\text{m}$ interval depth scan.

A system to record four phase-shifted interferograms in one frame, produced by a fringe projection system and a Digital Micromirror Device (DMD) camera, has been reported by Ri, Fujigaki and Morimoto to obtain 3-D shape (surface) measurement in a single shot [114]. Lago and Fuente proposed a method of reconstructing amplitude and phase from a single frame from a modified laser Mach-Zehnder interferometer [115]. Despite the single-shot claim the proposed system still has a moving part, i.e. one of the interferometer's mirrors must be translated to introduce a spatial frequency carrier to the interferogram. A single-shot low-coherence interferometric contouring set-up has been described by [116]. Similarly this apparatus still needs a movable part to translate the delay stage on one of the interferometer arms. Witte et al. achieve single-shot depth measurement by numerically compensating for the dispersion [117], however this approach only provides 2-D depth images. For industrial inspection application, Bosch GmbH and the Universities of Heidelberg and Stuttgart have developed a white-light-based single-shot profilometer using spatial phase shifting [118]. The prototype however only images a 1-D line profile. Possibly the closest of the other reported work to the prototype developed in this research is the system proposed by Koukourakis et al, in which a similar 3-D stack of spectral interferograms is also required to be constructed to obtain depth information [119]. The main difference is that their set-up employs a wavelength scanning tunable laser as the light source and the use of a photorefractive medium to holographically store the spectral interferograms obtained by scanning the wavelength. Digital-holography-based depth imaging has also been reported by Javidi et al by codifying the reference beam using the fractional Talbot effect [120].

Single shot profilometry offers various advantages over techniques dependent on scanning, mainly the substantial reduction in the constraint on the object's stability during the profiling. There are objects that are always in constant motion or only able to maintain a stationary position for a very short time. For example, in *in-vivo* ophthalmic measurement of the saccadic eye movement, with typical duration between 20 and 200 ms, can cause displacement between two consecutive measurements to be much larger than a fraction of wavelength and thus wash out the interference signal, especially in SWLI [67]. Therefore a single shot capability can be expected to suppress the problems associated with vibration-sensitive measurements [108].

In this thesis a system is proposed that will allow one to measure the shape of an opaque object, or the subsurface structure and displacement fields within weakly scattering media, in a single shot. The method is related to developments described in the current chapter, most notably the work by Schwider et al. [36] and de la Torre-Ibarra et al. [35]. The key feature that distinguishes the current work from its predecessors is that the need to scan mechanically along the last remaining axis is removed. This is achieved through spatial multiplexing of spectral images onto separate regions of a high resolution two-dimensional photodetector array.

One of the novel features of the work is the use of an etalon to create spectrally separated transmission peaks of the broadband beam prior to being launched into the interferometer. From each of these transmission peaks, a set of spectral sub-images are created on a single final detector frame. Subsequently these sub-images are aligned and stacked to create the so-called ‘3-D hyperspectral cube’ from which the depth information is extracted. The construction and the use of this type of 3-D spectral image stack, have been widely known and implemented in the other fields, particularly in imaging and biomedical. For example Harvey et.al have been working extensively on the development of hyperspectral image processing techniques for applications on retinal imaging as well as pattern recognition [121,122]. The design of an etalon-based broadband interferometer set-up, that produces a set of spatially separated spectral sub-images across a single frame of the detector, is described in detail in Chapter 4. This chapter is preceded by Chapter 3, which describes an ultimately unsuccessful attempt to perform the similar spectral separation of the sub-images by means of a microlens array. Despite the unsuccessful result, the design reported in this chapter has not been found in any previously reported work. Chapter 5 describes the algorithms and methods for processing the interferogram data acquired by the etalon-based hyperspectral interferometer and derivation of the system’s parameters from the recorded data. Application of the prototype described in Chapter 4 for single-shot height profiling of smooth and rough surfaces is presented in Chapter 6. The second application of the etalon-based hyperspectral interferometer for single-shot full-field depth resolved and strain measurement is presented in Chapter 7. Chapter 8 concludes this thesis by summarising the research results and recommendations for further work.

Chapter 3

Optical Configuration 1:

Microlens-based Hyperspectral Interferometer

3.1. The concept of hyperspectral interferometry

It has been described in detail in the first section of Chapter 2 (Section 2.1) that the inherent problem in single wavelength (monochromatic/laser) interferometry of phase (whence height) ambiguity can be alleviated by using more wavelengths. It has been demonstrated in a simple graphical analysis, such as the FDA method from de Groot [44] as shown in Fig.2.2, that the additional wavelengths produce a single line, rather than multiple lines, relating phase and wavenumber k . The unique linear relation of the phase and wavenumber therefore provides unambiguous height information (from knowledge of the line's slope) of the object.

The multiple-wavelength interferometric system can be considered as the extension to the conventional counterpart principle, i.e. light of multiple, instead of single, wavelengths is launched into the interferometer. In order to realise a single-shot capability, however, not only should the system be able to inject broadband light, but also at the other end, the system's detector should also be able to provide simultaneously the spectral 'bins' for every wavelength component of the light. In other words, the detector must be able to record all the spectral sub-images (bins) in a single frame. In each narrow-band bin the interferogram of the corresponding wavelength is stored. Another requirement is that these narrow-band sub-images must be spatially well-separated, i.e. there must be a spatial gap between two adjacent spectral sub-images. Otherwise, sub-images will overlap and the spectral range of each sub-image is no longer well defined.

Due to the narrow-band range of one sub-image, the fringe structure inside can serve as a means to determine the state of the object's surface (for profilometry) or depth-resolved structure and deformation state (for sub-surface measurement). If the fringes appear well defined, as shown in each disjointed region inside one box in Fig.3.1, then the surface of the object at that region is smooth or having height difference between two adjacent pixels less than $\lambda/4$ – as previously described in Sect.2.1. If the height difference is more than a quarter of the wavelength, the fringes appear to be discontinuous, either because the surface is smooth and contains global discontinuities, or because the surface is optically rough, in which case the fringes appear speckled as the starting phase at a given pixel is

random. For all cases, however, the phase at a given pixel changes from one sub-image to the next by an amount proportional to the z (depth) value for that particular pixel. The disjointed regions R_1 and R_2 within the sub-image in Fig.3.1 are to show the general situation where the object is smooth over one small region but not throughout the surface. As described in Sect.2.1 in conventional narrow-band interferometry, such separated areas create problems in phase unwrapping since they create ambiguities in determining the fringe order. The use of broadband illumination avoids these difficulties since the unwrapping takes place not along the spatial axes but along the k axis, or, – if the Fourier transform based approach used here is adopted, – phase unwrapping is avoided altogether.

This concept can be better illustrated in Fig.3.1. Each box inside the larger frame represents the ‘spectral bin’ for a single wavelength (or, strictly, narrowband range of wavelengths). It is depicted in the figure as the $(p-1)^{\text{th}}$, p^{th} and $(p+1)^{\text{th}}$ spectral bins, where each bin is centred at wavenumbers $k = k_{p-1}$, $k = k_p$ and $k = k_{p+1}$, respectively.

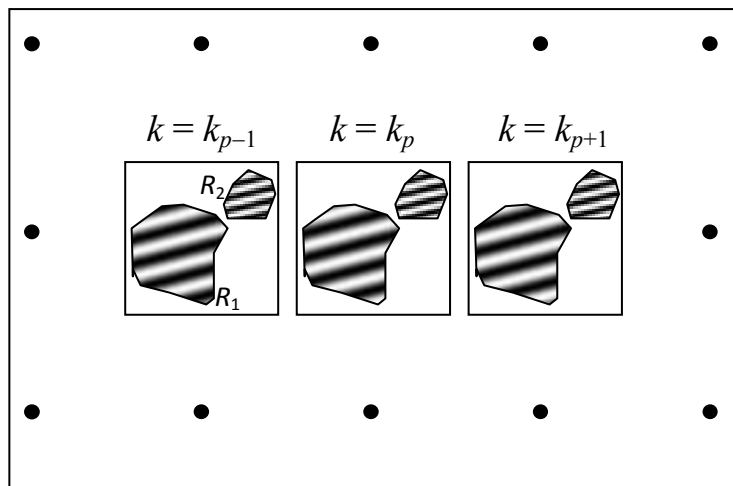


Figure 3.1. Spectral ‘bins’ (sub-images) of a multi-spectral interferometric system. The dots indicate the centre coordinate of the spectral sub-image (figure taken from [38])

These spectral sub-images are subsequently stacked to create a 3-D spectral volume data as shown in Fig.3.2. The process for extracting the unambiguous height/depth information from the 3-D spectral volume data stack, including the essential parameters in broadband interferometry of depth resolution and depth range, will be described in detail in Chapter 5.

One alternative to the approach suggested so far, i.e. of splitting the white-light interferogram into a set of spatially-separated narrowband interferograms, is to create a mosaic of the spectra of small regions of the interferogram. This technique is popular in the

astronomical literature, where it is known as ‘Integral Field Spectroscopy’ [123]. Optically efficient solutions have been developed including techniques based on lenslet arrays in the image plane – each lenslet producing a line spectrum – and ‘microslicer’ systems in which diamond-turned mirror facets are used to redirect different portions of the dispersed image into different relay lenses. Due to time constraints, this class of techniques has not been investigated further, however they offer an interesting alternative to the two prototypes investigated in the next two chapters of this thesis.

The construction of a 3-D spectral volume dataset from a set of 2-D spectral images in Fig.3.2 is similar to the data acquisition process in an imaging technology called hyperspectral imaging. This technology has been widely used, particularly in remote sensing applications (see for example Refs [124,125]). Other applications have been investigated extensively by Harvey et.al in retinal imaging [122,126,127], and also in automatic object classification’s pattern recognition [128,129]. Therefore an interferometric system capable of performing unambiguous depth measurement can be constructed by combining a broadband interferometer and a hyperspectral imager module. As a result, we call the technique ‘hyperspectral interferometry’.

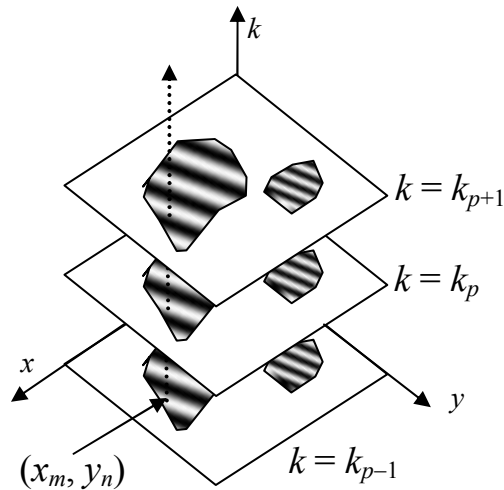


Figure 3.2. The formation of a 3-D spectral data volume from the spectral sub-images in Fig.3.1 (figure taken from Ref [38])

As a relatively well established technology, various hyperspectral imaging systems are commercially available nowadays. The single-shot feature however stipulates that the system should be able to simultaneously record the spectral sub-images, such as those illustrated in Fig.3.1. A survey was carried out to search for a hyperspectral imaging

system with such capability. The result indicated that most of the currently available hyperspectral imaging systems record the spectral band images sequentially in time. The wide-field hyperspectral imager from Photon Etc, for example, despite the elimination of x-y scanning to speed up the acquisition of a 2-D spectral image, involves sequential capture of narrowband images by means of a tunable filter (with a filter bandwidth as low as 0.3 nm) (see Appendix A1). Similarly the imager from Teledyne employs tunable filter-based technology (see appendix A2) but detailed information on the filter is unavailable. A hyperspectral imager from another major vendor, Brimrose, uses an acousto-optic tunable filter to perform a similar task with spectral resolution of 5 – 20 nm in the near IR band, and 2 – 6 nm in the visible and UV regions (see Ref.[130] and appendix A3), and can typically record 100 frames within 30 seconds (see appendix A4). Another company, Gilden Photonics, distributes a line of hyperspectral cameras from Spectral Imaging Ltd of Finland (see appendix A5). The products however are not (2-D) image-based but rather 1-D line, push-broom scanning-based, or multipoint-based (like that of the multiple point spectrometer products) (see appendix A6). Surface Optics Ltd has claimed to launch the fastest hyperspectral camera, with line scan speed up to 6,700 lines per second which is equivalent to 12 hyperspectral cubes per second at spectral resolution down to 2.8 nm (see appendix A7). The imager, as with the preceding system, is based on line-scanning technology. Possibly the closest hyperspectral camera system working in single-shot mode is the imager developed by Ocean Optics, which employs a dichroic filter array to record different spectral images on a CCD single frame [131]. The filters are arranged in a mosaic pattern so that a spectral component of the incoming light can be spatially registered into a particular pixel group (such as that of the Bayer pattern, the spatial arrangement of RGB filters commonly found in commercial electronic colour imagers). The number of spectral bands can be tailored depending on the customer. With the current technology, however, the number of spectral bins can go up only to 8 bands. A higher number of bands increases the complexity of pixel registration and alignment, as well as the complexity of dichroic coating of adjacent filter, and reduces the overall optical efficiency of the imaging system.

With all of the limitations previously described, it is therefore unfeasible to construct a single-shot hyperspectral interferometer by combining a broadband interferometer with a current state-of-the-art hyperspectral imager. The hyperspectral imaging sub-system of the interferometer should therefore be constructed. This chapter reports the first attempt to design and construct a hyperspectral interferometer which employs a microlens array to simultaneously record the spectral sub-images in a single frame.

3.2. The set-up

As described in Chapters 1 and 2, the system proposed in this research is designed to be capable of measuring full field height and depth field distributions in a single shot. The previous section shows how the single shot capability may be realized by combining a full-field imaging system with spectral decomposition of the acquired interference image. The optical layout described in this chapter was ultimately unsuccessful and was superseded by the design presented in Chapter 4, but it is described here for reasons of the completeness of the system's design process. Further development could potentially see this approach being used in the future.

3.2.1. The generic design set-up

A high level overview of the system is presented in the form of a block diagram in Fig. 3.3.

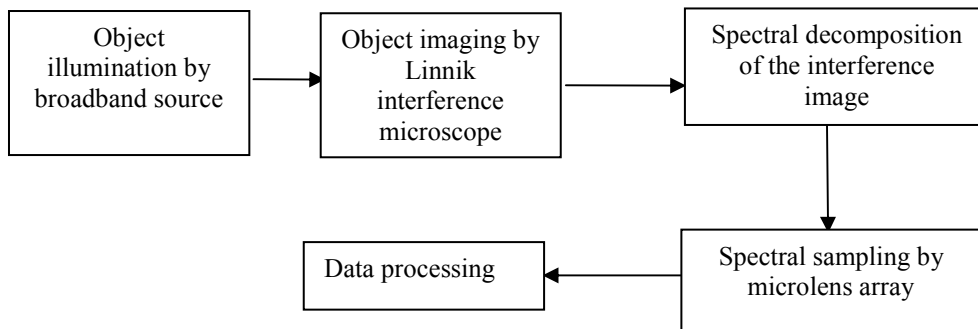


Figure 3.3. Block diagram of the proposed system

The interference set-up is based on a Linnik configuration. This type of set-up, compared to other interference microscope configurations, such as the Michelson or Mirau types, offers one important advantage, i.e. the decoupling of object and reference interferometer arms. The reference and object arms are separated but otherwise identical to one another. The fact that the optical path of each arm can be adjusted independently from the other [132] means that analysis of the optical path for one of the arms is sufficient to analyse the optical path of the entire interferometer. A further advantage of the Linnik setup is that a high lateral resolution can be achieved by employing a high numerical aperture objective [133].

Briefly, the object is illuminated by a broadband source. The reflected light from the illuminated area is collected by one of an identical pair of microscope objectives in a Linnik interference microscope, while the other objective provides the reference beam. Both beams recombine and interfere, and an intermediate image of the object is formed on or close to a diffraction grating. The diffraction grating spatially spreads the spectral content of the interference image, which is sampled by a microlens array such that each microlens will occupy approximately the same spectral width. Each lens images the intermediate image of the grating onto the CCD array, as shown in Fig.3.4 where N spectral sub-images are formed on the focal plane of the microlens array by N lenslets. Finally, following recording of the sub-images by a digital camera, data processing is performed to extract the height distribution information contained in the images sampled by the microlens array.

The selection of the components to build the set-up was primarily based on two considerations. The first was the availability of off-the-shelf components from commercial suppliers, and the second was the re-use of components from previous work on Spectral OCT (SOCT).

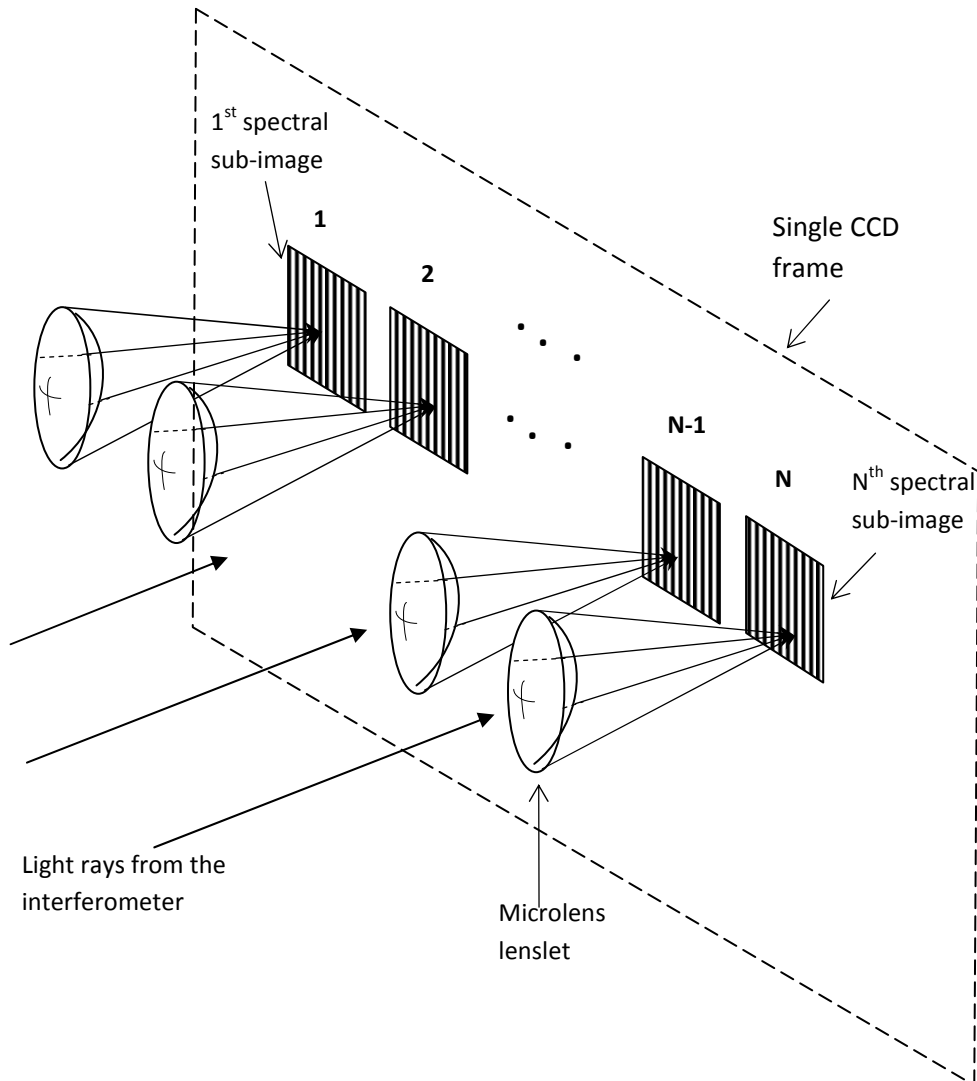


Figure 3.4. The formation of N spectral sub-images by means of N lenslets of the microlens array

3.2.2. The light source

The light source used in this set-up is similar to that from the previous SOCT set-up, a Superlum broadband superluminescent LED (SLED) light source Superlum S840-HP-I (Superlum Diodes Ltd, Moscow). The specification sheet details the nominal values of the equipment as 15 mW optical output power, centre wavelength of 840 nm, and a full width half maximum (FWHM) bandwidth of 50 nm. The manufacturer's final test prior to the light source's delivery, as shown in Fig.3.5, indicates that the spectral profile is not uniform but rather that there are two approximately Gaussian peaks, with a mean wavelength of ~ 840 nm and with a FWHM bandwidth of 50 nm (i.e., from ~ 815 nm to ~ 865 nm) [134].

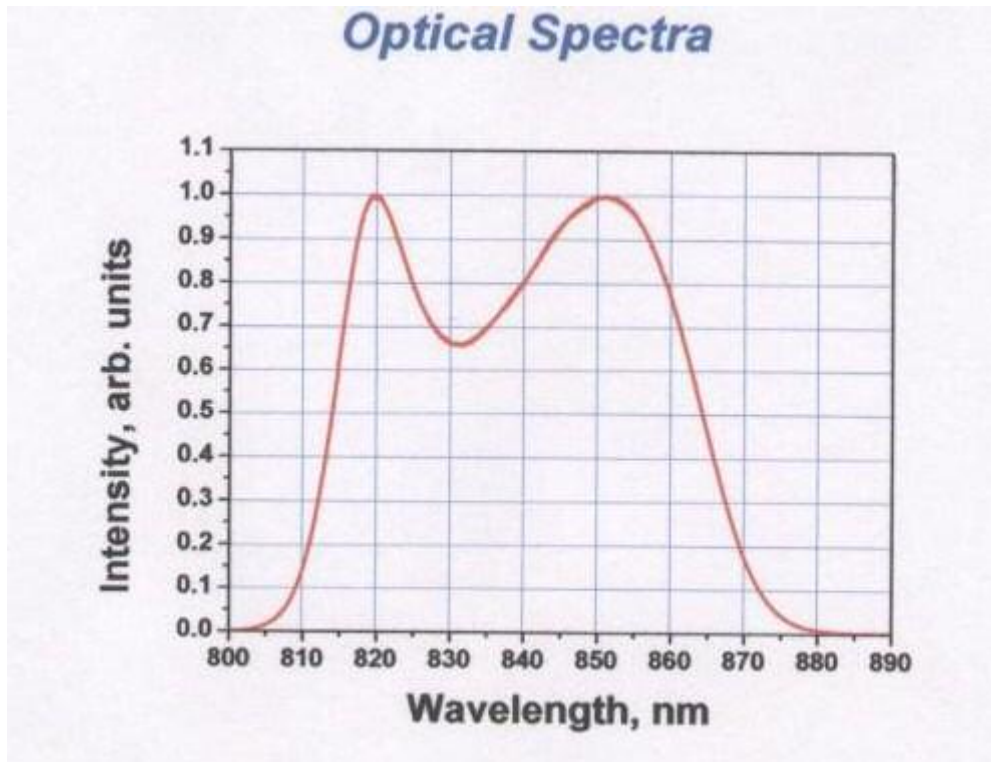


Figure 3.5. The spectrum of the light from the SLED light source used in the set-up (figure taken from [134])

3.2.3. The grating

The spectral decomposition block in Fig.3.3, which functions as the hyperspectral subsystem of the set-up, is performed by a diffraction grating plus microlens array. As with the light source, the same grating from the previous SOCT work was employed in this set-up. The grating is a reflective type, with a line density of 1,200 lines/mm. In the set-up another camera was used to monitor the alignment during the set-up's construction (this will be shown in the next section of the set-up layout). In order to accommodate this placement, the grating is oriented in the Littrow configuration in which the grating normal is angled such that the first order light beam is diffracted back along the same path as the incoming beam [135].

At this so-called Littrow blaze condition the grating facets are tilted with respect to the grating normal at the blaze angle θ_B given by

$$\theta_B = \sin^{-1} \left[\frac{gm\lambda}{2} \right], \quad (3-1)$$

where λ is the wavelength of the light, m is the diffraction order and g is the grating density in lines/mm. With the central wavelength of the SLD used in this set-up of 840 nm, a grating frequency of 1200 lines/mm and setting the grating to maximize the first

diffraction order, the blaze angle θ_B is found to be $\sin^{-1}\left[\frac{1200 \times 10^3 \times 1 \times 840 \times 10^{-9}}{2}\right] =$

30.28°.

The angular spectral spread due to the grating for light of spectral width $\Delta\lambda$ can be calculated using the standard grating equation as follows, where all angles are measured relative to the grating's normal:

$$gm\lambda = \sin \alpha + \sin \beta, \quad (3-2)$$

and where α and β are the angles of the incident and diffracted beams, respectively, with $\alpha = 30.2^\circ$ due to the Littrow blaze configuration, and $m = 1$ since only the first diffraction order will be used.

With the spectral width of the light source $\Delta\lambda$ and centred at λ_c , the lower and upper wavelengths λ_L and λ_U are $\lambda_c - \frac{\Delta\lambda}{2}$ and $\lambda_c + \frac{\Delta\lambda}{2}$, respectively. Therefore for the broadband source with $\Delta\lambda = 50$ nm and centre wavelength λ_c at 840 nm used in this setup, λ_L and λ_U values of the source are 815 and 865 nm, which respectively yield the following diffracted beam angles:

$$\lambda_L = 815 \text{ nm} \rightarrow \beta = 28.26^\circ$$

$$\lambda_U = 865 \text{ nm} \rightarrow \beta = 32.24^\circ.$$

With respect to the optical axis, the diffracted angles for λ_L and λ_U are found as $+2.02^\circ$ and -1.96° , respectively. Therefore, approximately a $\pm 2^\circ$ beam spread with respect to the optical axis will occur after dispersion takes place. As shown in Fig.3.6 in order for the diffracted beam to occupy the full width of the microlens array, the distance between the grating and the array is $b = \frac{5 \text{ mm}}{\tan 2^\circ}$ or approximately 145 mm. This distance dictates the

focal length requirement of lens F – one of the aperture imaging components described later in Sect.3.2.6.2.

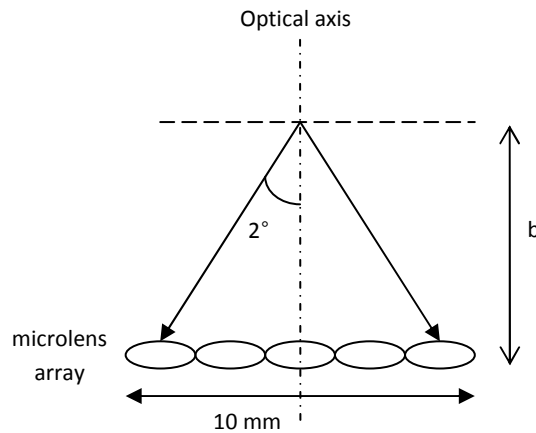


Figure 3.6. Calculation of the distance from grating to microlens array to fully sample the object spectrum.

In practice, the distance b can be longer than this value if the full 50 nm bandwidth is not required.

One consequence of orienting the grating in the Littrow arrangement is the need to insert a beamsplitter. Although this results in a decrease of overall system efficiency by at least 75%, the high diffraction efficiency of the blazed grating in the Littrow configuration more than compensates for such losses when compared to most other grating configurations. Furthermore, the beamsplitter serves the dual purpose of allowing a separate camera (the webcam) to assist in the alignment of the optical set-up.

3.2.4. The microlens array

The microlens array used to sample the spectral images in this setup is a Linos FC-Q-100 device with a 10 mm x 10 mm square array of plano-convex lenses. Each lenslet has a clear aperture of 95 μm , radius of curvature R_C of 140 μm and center-to-center spacing between two adjacent lenslets of 100 μm . The plano-convex focal length of each lenslet can be estimated using the relation [136]

$$f_{\mu L} = \frac{R_C}{n_l - 1}, \quad (3-3)$$

where n_l is the material index of refraction. The array is made of quartz with $n_l=1.45$, giving each lenslet a focal length of 311 μm .

With this particular microlens array, the gap between lenslets is transparent. This gap is part of the transparent planar substrate and light passing through these regions does not contribute to the images. Rather, it creates an unwanted intensity background to the final recorded image, as will be shown in the later sections on the performance of the set-up.

3.2.5. The sample

An object with a step height profile, as a simplest type of discontinuous 3-D shape, was used as the sample to verify the performance of this proof-of-principle system for shape measurement. The sample was realized by attaching a glass cover slip on top of a glass substrate and to create a reflective surface, a layer of aluminium was deposited on the top with a surface thickness of around 1,000 \AA in order to achieve a mirror type coating (90-100% reflectivity).

The supplied product specification indicates that the thicknesses of the glass substrate and cover slips are 10 mm and between 90-150 μm , respectively. From microscope inspection, by focusing the light on the upper side of the step followed by the lower side and finding the difference in focusing distance from the objective's micrometer, the height difference of the profile was found as 120 μm . The height uncertainty of this inspection is 10 μm due to the uncertainty of the objective micrometer.

The step height of the sample should not exceed the expected depth range of the system, which is given by [24,37]

$$\Delta z = \frac{N_f \lambda_c^2}{4\Delta\lambda}, \quad (3-4)$$

where Δz , N_f , $\Delta\lambda$ and λ_c are the depth range, number of object frames, bandwidth of the source and centre wavelength of the source, respectively.

From Eq.3-4 the depth range is linearly proportional to the number of object frames, which in this case is the number of sub-images. Increasing N_f however involves a corresponding reduction in the number of pixels in a sub-image, and hence the object's field of view. In the previous work on (Phase Contrast) Spectral OCT the entire 640 pixel horizontal width of the 640 × 480 webcam was used to record the spectral interference pattern [35]. As a consequence, however, each spectral image only contained a single line, not a 2-D image. In other research on wavelength scanning interferometry, the entire frame of 1024 × 1024 pixels of the camera was used but the spectral images must be captured sequentially [24]. From the experience of the previous works above, a reasonable number of N should be selected such that the field of view is not too small whilst allowing the sub-images to be acquired in a single-shot, and not sequentially. With this consideration it was decided to acquire around 100 sub-images in a single frame acquisition or $N \approx 100$. With the camera used in the set-up with 1024 × 1024 pixels each sub-image has around 10 × 10 pixels, or equivalently 64.5 × 64.5 μm since the pixel size is 6.45 μm. Using this number ($N=100$) with $\Delta\lambda= 50$ nm and $\lambda_C = 840$ nm, the maximum step height is found to be 352.8 μm. The 120 μm step height difference of the sample therefore meets the measurement condition.

3.2.6. Practical design issues

Several issues needed to be addressed prior to designing the set-up. By referring to the block diagram in Fig 3.3, the minimum configuration to implement the system must comprise at least two elements: the microscope objective (of the Linnik set-up) for imaging the object; and the microlens array to sample the spectral images. These two optical elements, however, are vastly different in size, i.e. the effective aperture diameter of the objective is of the order of millimetres, whilst that of each lenslet of the microlens array is a hundred times smaller (of the order of tens of μm). An additional set of lenses between these two components is required so that the light rays captured by the objective can pass through the aperture of the lenslets in the microlens array. This set of lenses is known as the (lens) relay system [137]. The relay system images one lens aperture onto the other in order to achieve the maximum light transfer efficiency. In parallel with imaging the object, the set-up design therefore must also perform correct imaging of the apertures. The layout of the system is shown schematically in Fig 3.7.

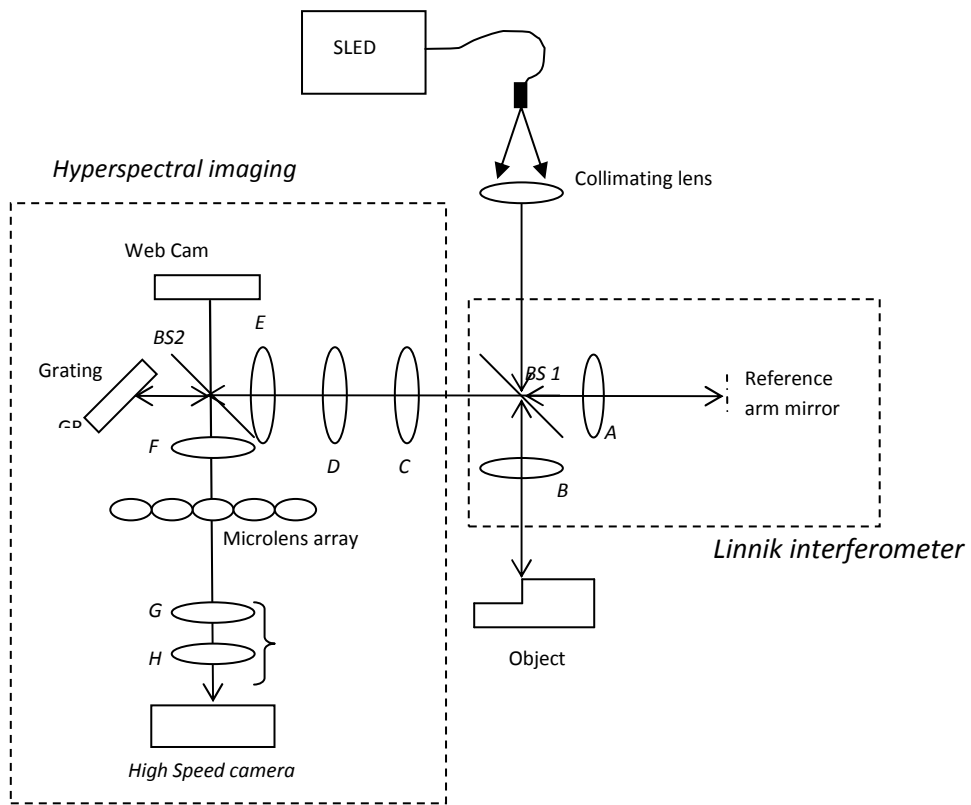


Figure 3.7. Microlens-based system layout

3.2.6.1. Imaging path of the sample

The imaging path for the object arm is shown in Fig 3.8. Referring to the system layout diagram in Fig.3.7, the object imaging task is performed by lenses *B*, *D*, one of the microlenses, and lenses *G* and *H*.

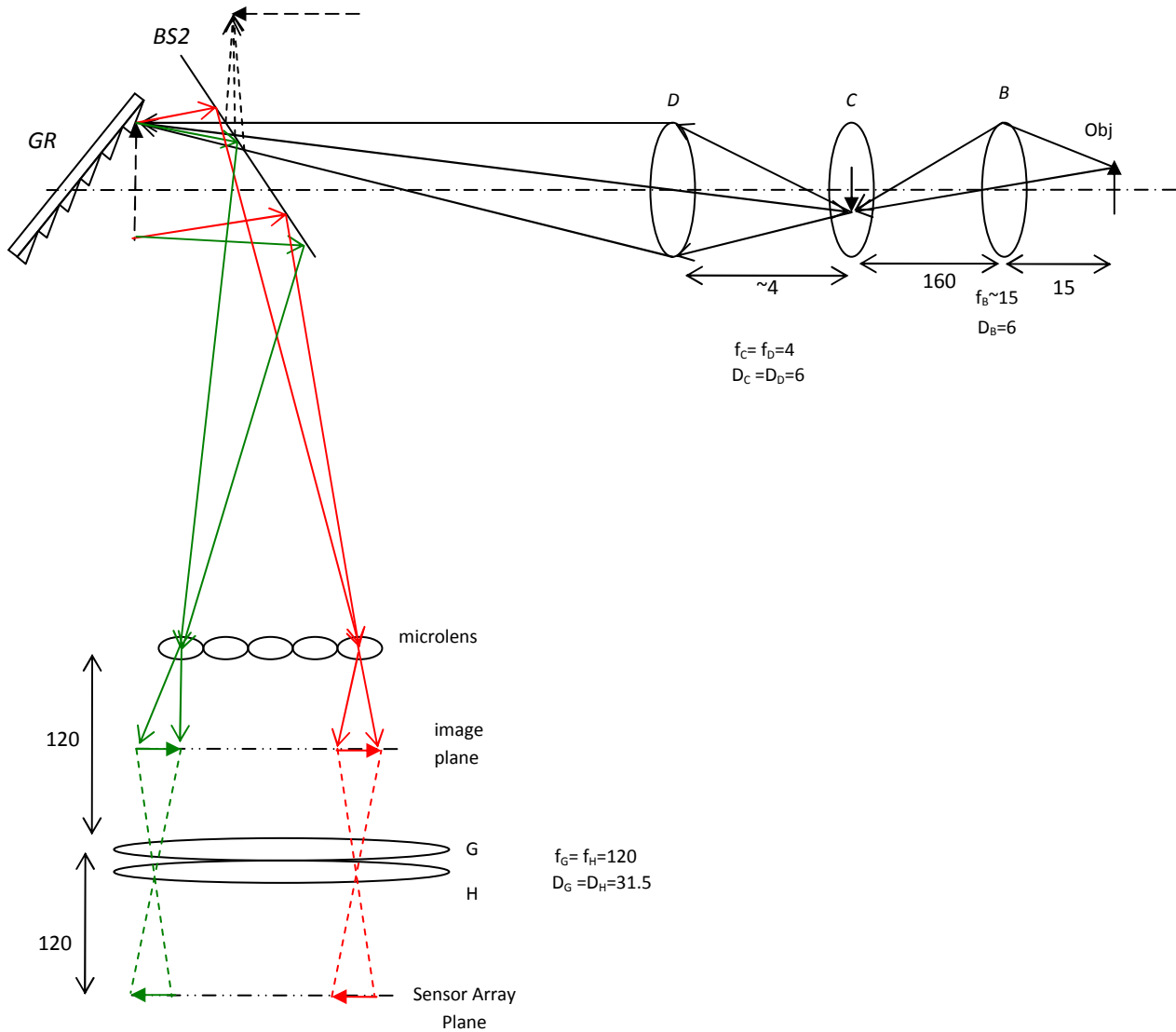


Figure 3.8. Complete imaging path for object. Units in mm.

The design of the imaging path of the set-up is based on the imaging path of a high-speed rotating camera system [138] where the (intermediate) image of the sample is formed on the surface of a rotating mirror. The mirror rotates to successively direct the cone of rays from the objective lens onto an array of relay lenses in the subsequent imaging stage. In the current set-up, the grating acts as the rotating mirror of the high-speed camera, but where the deflection angle of the beam is now related to wavelength rather than to time. The intermediate image of the sample is formed in front of the grating and subsequently diffracted through different angles onto the microlens array lenslets, depending on the wavelength of the light. The size of the intermediate image is made to be as close as

possible to the area of the grating's surface, since the maximum attainable resolving power of the grating is proportional to the grating's illuminated area [135]. Furthermore, whereas a spectrometer would normally be set up to diffract plane waves, in this case the wavefront associated with a given point on the sample surface will be a spherical wave, and the diffracted wave of a spherical wave is a distorted spherical wave. To reduce these distortions as much as possible, the radius of curvature of the spherical waves should be as large as possible, and this in turn implies maximizing the size of the diffraction grating.

Details of the object's imaging sequence is as follows: lens *B* (Linnik sample objective of 10× magnification, focal length 15.5 mm, numerical aperture 0.3 and diameter = 6 mm) images a region of the sample onto the aperture of lens *C* (focal length = 4 mm, diameter = 6 mm). Using an objective with a larger NA will increase the resolution as well as the magnification. Since however the image due to this objective will be imaged by another objective and magnified, due to the aperture imaging configuration of the system, it will be an advantage if the first intermediate image (the image due to the sample's objective) does not undergo a large magnification. The location of lens *C* is close to the focal length distance of lens *D* (focal length=4 mm, diameter=6 mm), so that the first intermediate image will be imaged in front of the grating to create the second intermediate image. Since the second intermediate image is formed by a microscope objective (lens *D*), the separation between lens *D* and the grating is around the tube length distance of objective *D*, which is 160 mm. Upon dispersion by the grating the second intermediate object image is imaged again by a horizontal row of lenslets in the microlens array and subsequently imaged onto the camera detector array through the combination of relay lenses *G* and *H*. This pair of lenses is needed since the location of the image due to the microlens array is very close (around 300 μm) to the array itself so that a camera cannot easily be placed at that image plane.

3.2.6.2. Imaging path of the aperture

The imaging path of the aperture from the first 10× objective to the aperture of the microlens array is shown in Fig.3.9. The aperture of lens *B* (10× objective) is imaged by lens *C* (40× objective) onto lens *D* (40× objective). Lens *B* and its image at lens *D* are a conjugate pair with magnification of $4/160=0.025\times$. Therefore lens *B* with an effective aperture of 6 mm is imaged onto lens *D* which has a diameter of $6\text{ mm} \times 0.025 = 0.15\text{ mm}$.

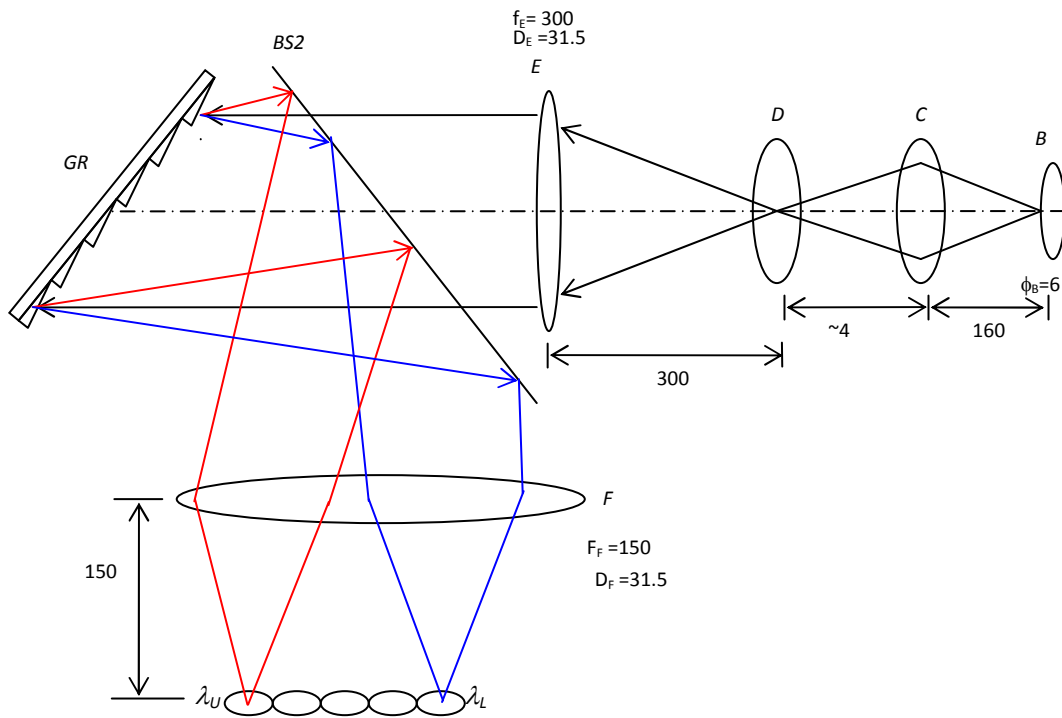


Figure 3.9. Aperture imaging path from objective to microlens array. Units in mm.

Lens D is located at the focal length distance of lens E (focal length = 300 mm and diameter 25.4 mm), so that the combination of lenses E and F (focal length = 150 mm and diameter 25.4 mm) form a telescope system (SmithOptEngText2000) [131] with magnification of $-150/300$ or $-0.5\times$. Therefore the 0.15 mm effective aperture diameter of lens D will be imaged by the telescope onto the microlens array with a size of 0.5×0.15 mm = 75 μm , which is within the size of each individual lenslet pupil of around 100 μm [136].

3.2.6.3. Fibre coupler

Although the system is designed to employ an SLED as the light source, performing the alignment of the set-up using near IR light is not very easy. The need for an IR card to see the location of the spot and the further additional need for an IR viewer when the intensity is not strong enough to cause visible fluorescence of the card makes alignment using the SLED light rather laborious.

Laser light, for example from a He-Ne laser, on the other hand is visible and is easier to form fringes with when interfered with the reference beam due its long coherence length, so offers significant benefits when performing the alignment. This light must however be launched into the system at exactly the same position and orientation as that of the SLED. The solution to this requirement is to employ a (fibre) beam coupler, in which two beams are launched into two different ports of the apparatus and the output ports are the combination of both input beams at a different ratio. The beam ratio of the coupler is shown in Fig.3.10. In this set-up, the light from output port 2 was used since it was found that the detector became saturated with the other ratio from port 1.

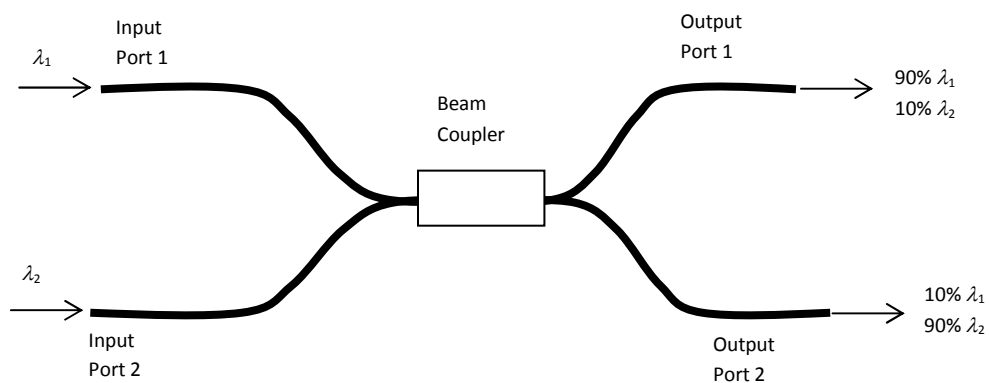


Figure 3.10. Beam coupler used in the set-up to launch two different wavelengths into the system co-axially. λ_1 is the SLED light (840 nm) and λ_2 is the He-Ne light (632.8 nm).

3.2.6.4. Spot imaging

Spot imaging refers to the method developed to create spots across the image plane of the microlens array, which are used to check whether the object is in focus. Due to the small area of a sub-image (10 pixels or around 65 μm) in practice it is very difficult to find whether the object is properly focused on the final CCD camera. This situation is worsened by the fact that the space between lenslets is not opaque but transparent, giving rise to additional unfocused background light.

It is therefore an advantage if a small focused and higher intensity spot appears in each lenslet image plane. Furthermore, these focused spots will be of use as the reference for alignment of the spectral sub-images in the CCD camera to create a 3-D spectral stack. The latter process is described in detail in Chapter 5 (Data Analysis). An individual spot itself however does not necessarily occupy a single pixel but can be more.

The spot imaging mode is realized by altering the distance between the fiber tip to the objective/lens B (see Figs.3.7 and 3.11), whilst maintaining the distance from sample to objective until the spot is observed in the webcam. This corresponds to the case where the illuminating beam is focused to as small a spot as possible on the sample surface. In the spot imaging mode the collimating lens is removed so that the spot on the sample surface is only due to the objective, thus the fiber tip and the spot are conjugate.

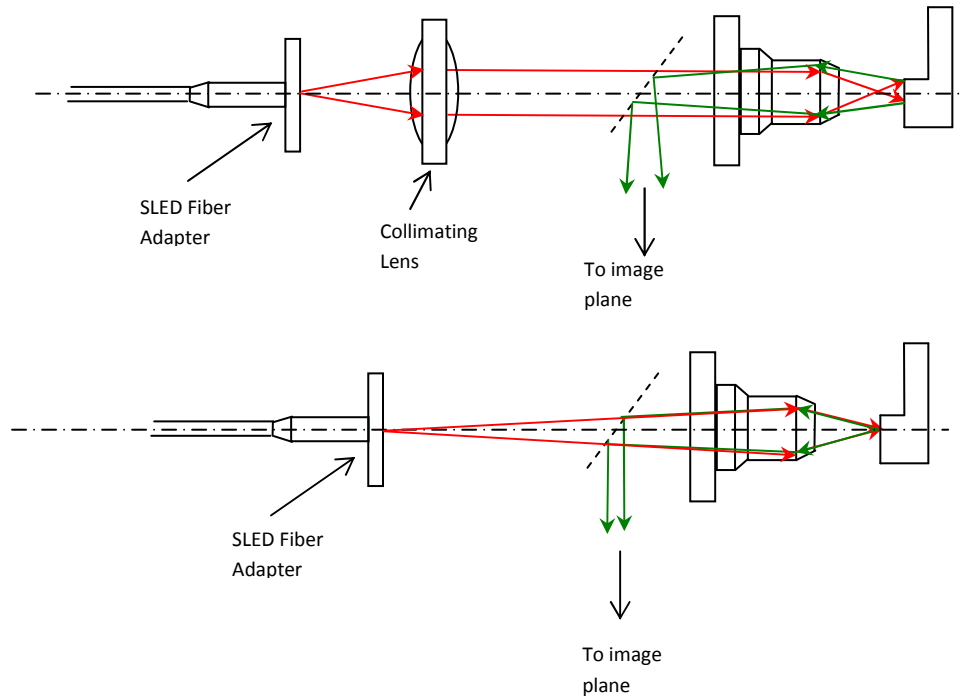


Figure 3.11. The difference between full field and spot imaging modes. (a) Full field imaging - the beam is collimated before entering the objective. (b) Spot imaging mode – in this mode the sample-to-objective distance is maintained while the distance of the fiber tip to objective is altered until a spot is observed at the 2nd intermediate image plane. In this configuration the collimating lens is removed.

3.3. Results and discussions

Typical output images of the set-up are shown in Figs. 3.12 and 3.13. In both Figures 3.12 and 3.13 the light came only from the object (the reference beam was blocked), but the first image was captured in spot imaging mode whilst the second was in full-field mode. The stepped sample was used as the sample for both images.

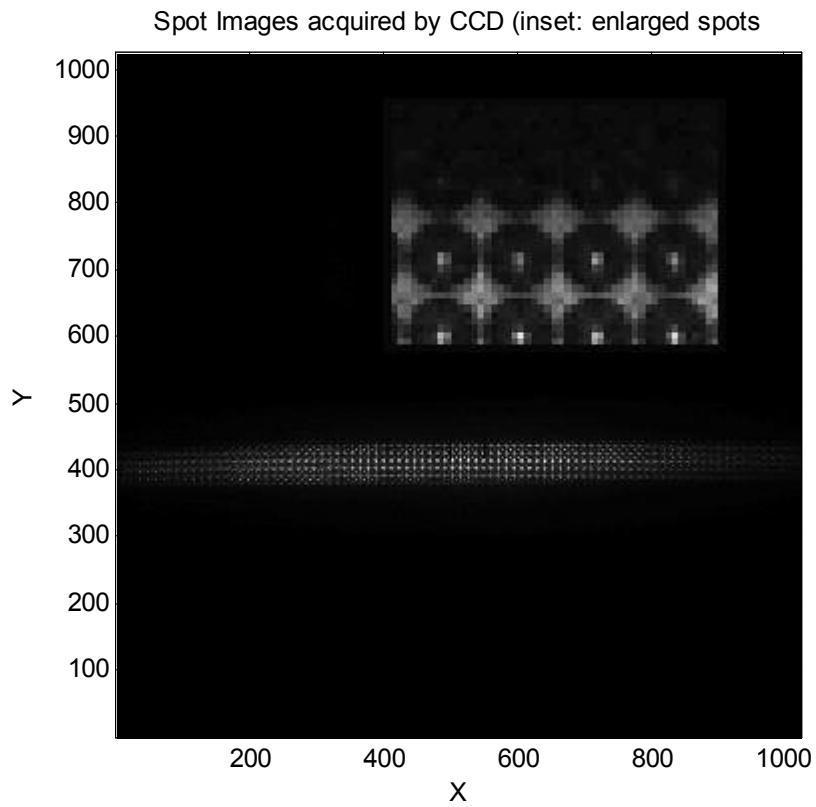


Figure 3.12. Spot image acquired by the CCD camera

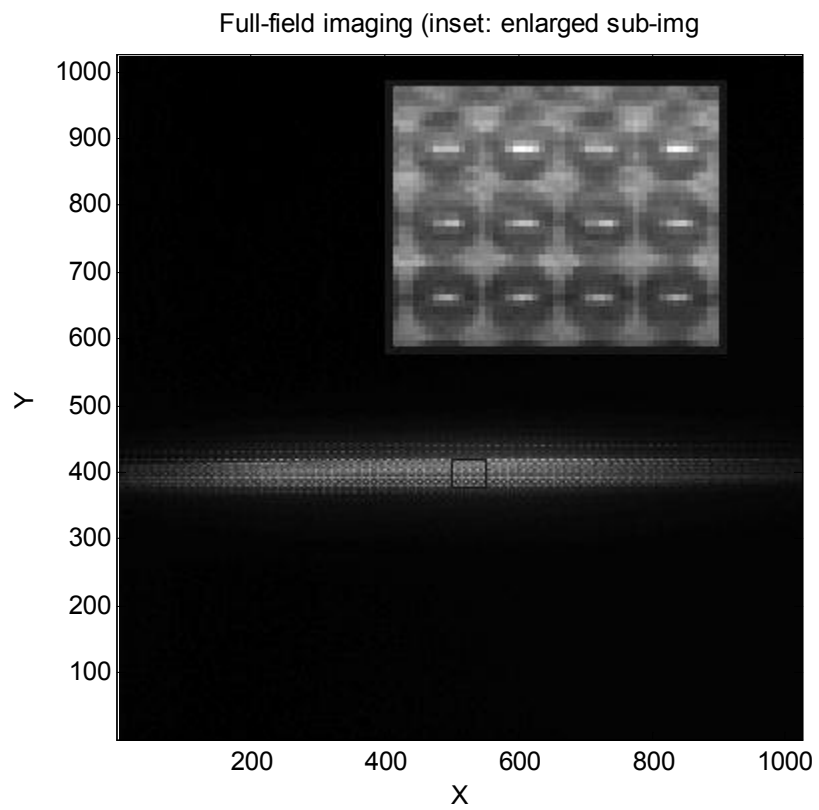


Figure 3.13. Image of the object acquired by the CCD camera in full-field imaging mode.

Both the spot and full-field imaging results show that the aperture and object imaging do not work as expected. Ideally only a single row of lenslets is illuminated if the aperture imaging path is correct, but both figures show more (around 5 rows). Also as shown in the inset of Fig.3.13, the pattern inside each lenslet does not show any resemblance with the image of a step profile.

The remainder of this section is devoted to a discussion of the most likely reasons for the setup not to perform as expected. None of these are fundamental obstacles and given time it should be possible to overcome them. This has not been done so far because a more successful prototype was developed instead that is described in the next chapter.

Firstly, it was found from the experiments that one of the most difficult tasks in constructing this set-up was to adjust the gap between (objective) lenses C & D in Fig.3.9. As described in Sect.3.2.6.2 the gap between the two lenses should be equal to the focal length of objective D, which is 4 mm. This gap must be indeed measured between the principal planes of the two lenses. The information on the principal plane locations of the objective used as lens D unfortunately was unavailable from the manufacturer. A data sheet from a similar type of objective, but from a different manufacturer, however showed that the location of the principal plane is typically 3.5 mm from the vertex of the first lens element. This means that even if objectives C and D were in contact, the distance between their principal planes is more than 4 mm. In fact, the images in Figs.3.12 and 3.13 are those with the least number of rows illuminated.

A second problem related to the finite size of the image of the step. The combined magnification of objectives B and D yielded a total magnification of $400\times$. A simple test was performed as shown in Fig.3.14. The webcam was located at the tube length of the $10\times$ objective B, so that the correct magnification was obtained. The captured image is shown in Fig.3.15.a, where the middle stripe is the image of the step transition and occupies around 55 pixels. The pixel size of the webcam was not exactly known, however with the physical dimension of the sensor array of around 6×4 mm, made of 640×480 pixels and assuming no dead pixels, the pixel size of the webcam is around $9\ \mu\text{m}$. The 55 pixel width of the step height in the first intermediate image therefore corresponds to roughly $495\ \mu\text{m}$. This image was subsequently magnified by the $40\times$ objective D, to yield a width of $400\times 55 = 2,200$ (webcam) pixels, equivalent to 19.8 mm. The image of the step transition therefore almost filled the grating surface and hence each of the sub-images.

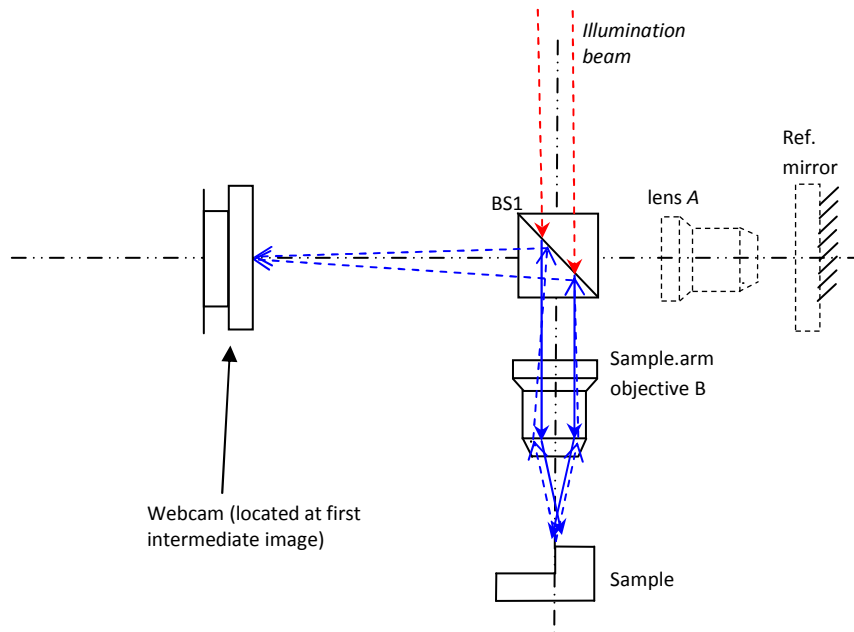


Figure 3.14. Optical setup to record first intermediate image.

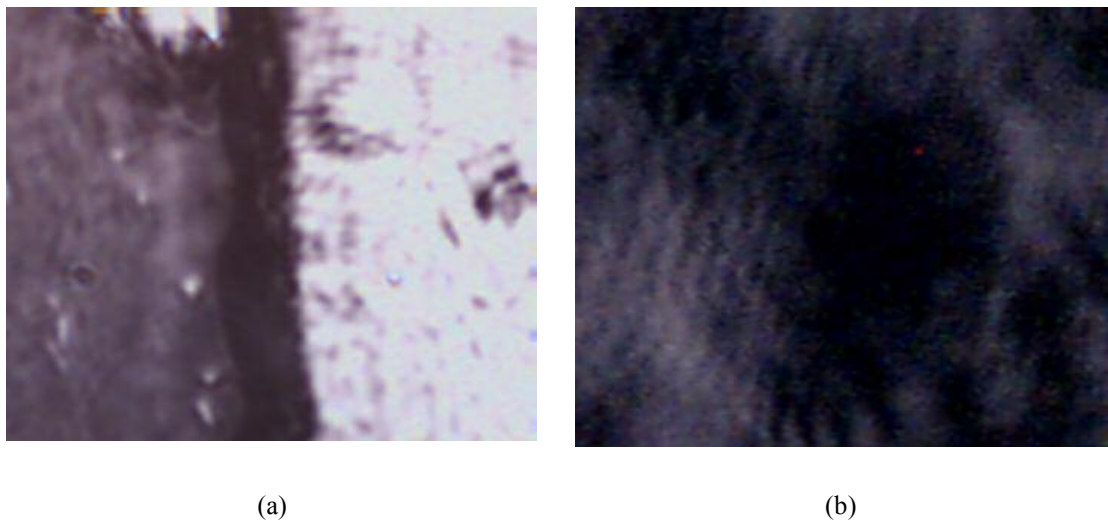


Figure 3.15. Intermediate images. (a) First intermediate image, (b) second intermediate image (after 400X magnification).

A closer inspection at each lenslet sub-image revealed that the sub-images are not square, nor occupying around 10×10 pixels as expected, but a rectangular shape where the image is wider than its height. This is shown schematically in Figs.3.16.a and b. As shown in Fig.3.16.b one sub-image occupies ~ 5 pixels in the horizontal direction and $\sim 2-3$ pixels in the vertical direction and bears no obvious resemblance to a step object. From the previous analysis, however, it is clear that each lenslet does not image correctly the second intermediate image.

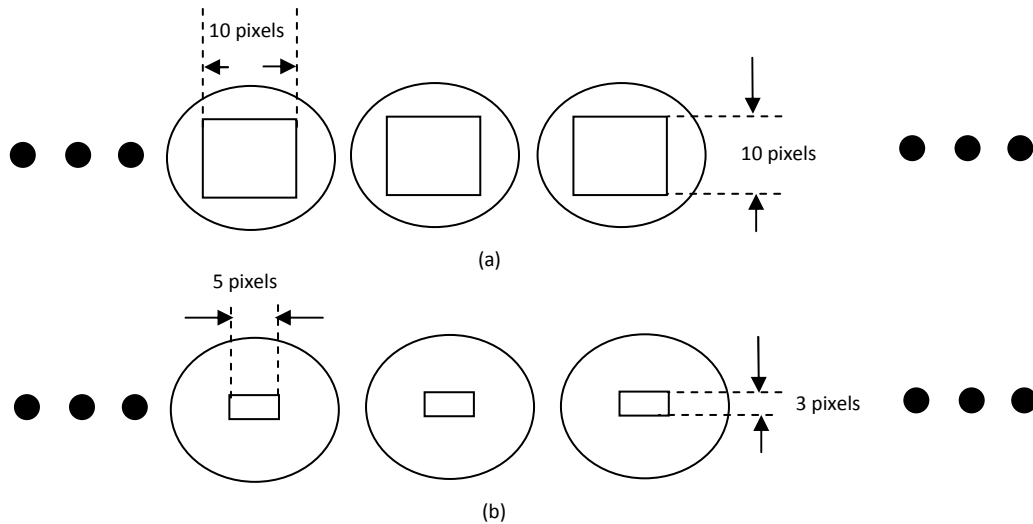


Figure 3.16. Graphical depiction of full-field imaging: (a) ideal result – the sub-image occupies roughly 10×10 pixels with a sufficiently sharp edges to define the image border; (b) the actual result of the system – each sub-image is only around 5×3 pixels with blurred and unfocused edges

Another possible cause of the sub-image clipping problem was misalignment of the back-to-back 40× objectives (Lenses C & D in Fig.3.9). This is because the lens components of the objectives are located in the front barrel and the resultant torque may cause a small angular offset between the optical axes of the objectives and the optical axis of the system, as illustrated in Fig.3.17.

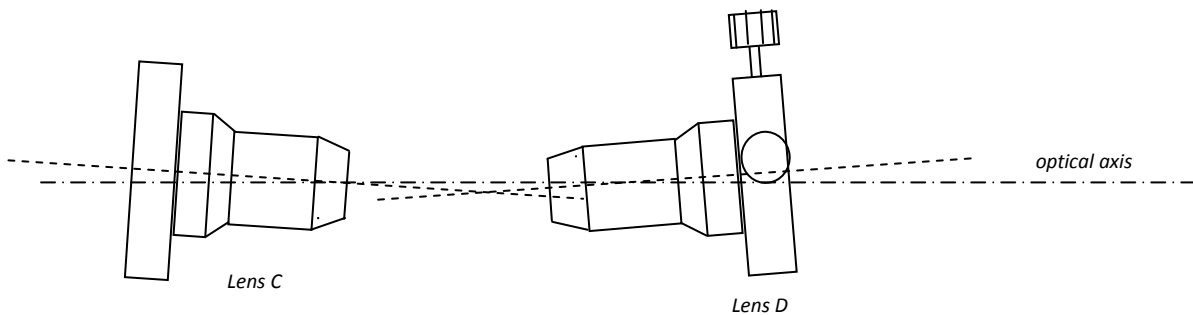


Figure 3.17. Non-parallel optical axes of the back-to-back 40X objectives. Scale is exaggerated for the sake of clarity.

A third problem found from the tests of this set-up was that, during the spot imaging mode (using the SLED light source), when one of the arms was blocked, a single spot was never observed but there was always another one of lower intensity. This is shown in Fig.3.18 which is the images of the spot recorded by the webcam during the alignment stage. Fig.3.18.a shows the twin image of the spot from the reference arm (the sample arm was blocked). Although in Fig.3.18.b there is only one spot from the sample arm (the reference

arm was blocked), this image was actually recorded after adjusting the sample prism support so that the twin image of the sample was outside the field of view. The concentric pattern surrounding the twin spot can still be clearly seen in the field of view as marked by the arrow.

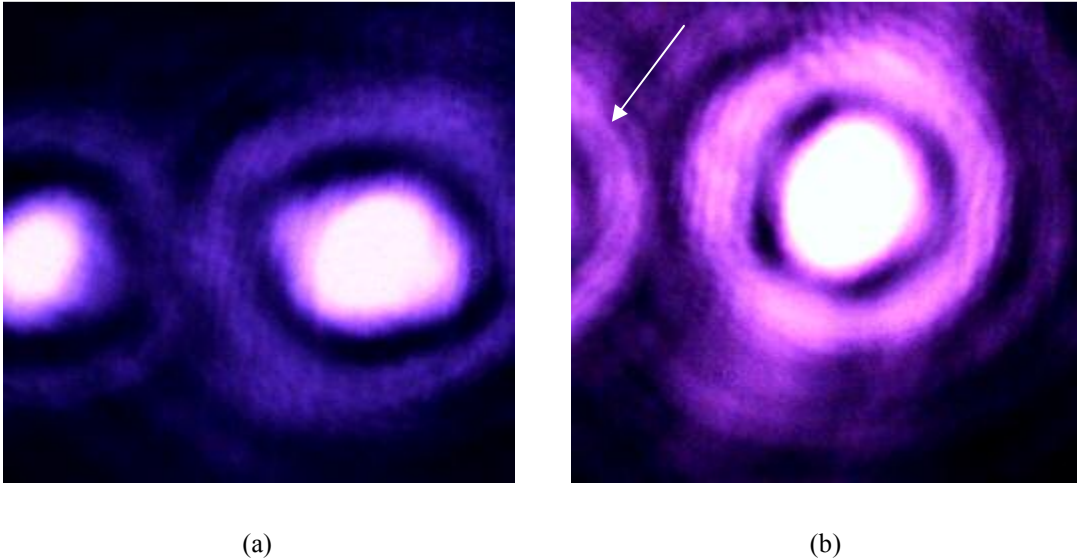


Figure 3.18. Twin images of spots. (a) From reference arm, (b) from object arm.

The twin images of sample and reference spots are due to the reflection of the spot being reflected by the system back into the camera. The cause of the reflection is not clearly identified, but most likely one of beam splitters has imperfect anti-reflection coating in the near IR region.

It was also found in the experiment that the z translation of the sample and reference mirrors is not purely axial, but also came with an angular movement. A gimbal mount, instead of the prism support on which the current sample and reference mirror are attached, can be an alternative solution to this problem. A gimbal mount allows pure rotational motion since the axis of rotation of this mount is in the same plane as the mirror surface. This property prevents the common beam walk-off typically found in rotating mirror mounts thus eliminating the need to constantly readjust the mount position in the optical table.

Considering the various aforementioned factors, a new design of hyperspectral interferometer was investigated alongside the microlens array design. Ultimately this new design, based on an etalon to generate a frequency comb from a broadband SLED source, proved to be more successful and therefore the microlens design was not pursued further.

Details of the etalon-based system are given in the next chapter (Chapter 4). In brief the new design eliminates the need for an intermediate image on the grating surface, but uses collimated beams instead. The spectral sampling of the light in the new design is not performed by the microlens array, but using an etalon, which removes the problem of non-uniform wavenumber shifts between adjacent sub-images. This approach and sample results will be discussed further in Chapter 4.

Chapter 4

Optical Configuration 2:

Etalon-based Hyperspectral Interferometer

4.1. Introduction

The inability of the microlens-based set-up, described in detail in Chapter 3, to produce the required spectral sub-images required further investigation. After changing all the optical components of the set-up from the visible to the near IR band to match the SLED light spectrum, the recorded interferogram images both at the webcam and the final CCD camera remained essentially unchanged and still did not show the expected output. A completely new design to overcome the problems encountered in the previous microlens-based set-up is presented in this chapter. The new design is called an etalon-based Hyperspectral Interferometer (HSI).

4.2. Brief review of the previous design problems

A discussion of the possible causes of problems of the previous design in Section 3.3 is briefly revisited in this section.

4.2.1. Object imaging

As shown in Fig.3.7, the previous set-up consists of two major blocks, i.e. the Linnik interferometer and the spectrometer. In between these two sub-systems a webcam is located to check whether the correct image magnification is achieved. Rather than using the large (final) CCD camera, during the set-up construction the webcam was also used to quickly check the interferogram due to its small size and flexibility.

The webcam image in Fig.3.15.b shows that the total 400× magnification of the sample has produced an image that occupies almost the entire frame and leaving almost nothing for the lower and upper side of the step. The final image at the CCD however indicates a more serious problem, i.e. the expected image of the step object did not fully appear across the aperture but merely as a tiny vertical slit on a ‘letter box’ size rectangle as shown in Fig. 3.16. This indicates that the object imaging path of the set-up did not work as expected,

and neither did the aperture imaging since more than one row of lenslets were illuminated as shown in Figs.3.12 and 3.13.

4.2.2. Depth of field issue

As described in Section 1.3 one of the goals of this research is the continuation of previous work on Phase-contrast Spectral Optical Coherence Tomography (PS-OCT) for sub-surface depth measurement [35]. The depth of field of the imaging sub-system is therefore a crucial issue since if the system's depth of field is less than the depth of the object, the system will not be able to image with good lateral resolution the whole axial span (depth) of the object. The system's depth of field should be larger than, or at least equal to, the desired depth of the object to be imaged.

The depth of field d_f is given as [139,140]

$$d_f = \frac{4\lambda f_o^2}{D_o^2}, \quad (4-1)$$

where f_o and D_o are the focal length and aperture diameter of the object lens, respectively. Eq. 4.1 shows the proportional and reciprocal relation of depth of field to the square of the focal length and the imaging lens aperture, respectively. From this relation, despite the small aperture, the use of a microscope objective will not normally result in a large depth of field since microscope objectives typically have short focal lengths. This can be shown in the following calculation: the object used in the previous PC-SOCT experiments has a depth of around 0.5 mm. Rearranging Eq. 4.1 for the focal length of the lens gives

$$f_o = \frac{D_o}{2} \sqrt{\frac{d_f}{\lambda}}. \quad (4-2)$$

The microscope objective used in the previous design to image the sample has $NA = 0.3$. Rearranging Eq.4-1 in terms of the lens's numerical aperture NA (with $NA \approx D_o/(2f_o)$) the depth of field of the objective is $9.3 \mu\text{m}$, which is less than 2% of the required 0.5 mm depth of field mentioned above. If however a standard microbench 1 inch diameter lens is used, using Eq.4-2 and substituting the expected depth of field of 0.5 mm above, the

required focal length of the lens is around 300 mm. It is not difficult to obtain such lens since the standard focal lengths of the microbench lens set ranges widely from 25 to more than 800 mm. As mentioned in the section on the redesign of the interferometer, a 500 mm focal length lens is used to obtain an extended depth of field of more than 1 mm.

4.2.3. Effect of non-collimated illumination of the grating

Another issue with the microlens design is related to the incoming beam to the grating. In this set-up a convergent beam from the interferometer forms the intermediate image in the plane of the grating. However, several publications on imaging spectrometers (e.g. Ref [141,142,143]) point out that standard imaging spectrometers use a (planar) diffraction grating always illuminated by a collimated beam. The main reason for this is that spherical wavefronts are not diffracted as perfect spherical wavefronts. The standard grating equation is derived on the assumption of parallel incident rays [135]. Although the approach used here can be thought of as a non-standard configuration, one can nevertheless consider the aperture plane of the imaging lenses to consist of a set of light emitters, with each of these emitters producing a separate collimated beam incident on the diffraction grating.

4.2.4. Diffraction grating non-linearity issues

The use of a diffraction grating in the set-up introduces non-linearity issues. The first non-linearity aspect to be considered is the non-linear relation between wavenumber k and wavelength λ . As shown in the interferogram equation Eq.2-4, the sought path length difference between reference and sample arms, $S(x,y)$, is embodied inside the phase term i.e. the argument of the cosine function. The phase of the recorded fringe is

$$\phi = 2kS(x, y). \quad (4-3)$$

The phase however cannot be directly measured from the interferogram. The measurable quantity is the fringe frequency, which is proportional to the rate of change of phase with respect to wavenumber:

$$f_k = \frac{1}{2\pi} \frac{\partial \phi}{\partial k} = \frac{S(x, y)}{\pi}. \quad (4-4)$$

Once the fringe frequency is measured, the sought depth z can be extracted from the interferogram.

The frequency variable in Eq. 4-4 however is derived from k instead of from λ . By the same token, the phase in Eq.4-3 is also linear in k , not in λ . Therefore it is desirable and more convenient for further analysis to express all the measurements in terms of k rather than λ . The recorded interferogram at the final camera is however, due to the grating diffraction, that spans across the wavelength λ but not k -axis. In most spectral-based interferometric systems, such as the set-up in this research, the interference pattern (diffracted by the grating) will be recorded by a spatially discrete detector array such as a CCD camera. It is therefore necessary to investigate further the relation between the grating's diffracted angle and k . If the two quantities are linearly related then it is safe to conclude that the sensor array pixels uniformly sample the k axis, otherwise some form of compensation method may be required. The grating equation in Eq.3-2 can be rearranged to express the relation between k and β as follows:

$$k = \frac{2\pi mg}{\sin \alpha + \sin \beta}. \quad (4-5)$$

It has been described in Sect.3.2.3 that the grating used in the previous design is a blazed type to maximise the efficiency for the 1st diffraction order ($m = 1$) and has a grating density $g = 1,200$ lines/mm. The grating's blaze angle is 36.87° , which also means $\alpha = 36.87^\circ$. To simplify the analysis it is assumed that a collimated beam is incident on the grating (at incoming angle $\alpha = 36.87^\circ$), which is different from the configuration in the previous design where the incoming light to the grating was convergent. Substituting these values into Eq.4-5 allows the diffracted angle β to be plotted as a function of k as shown in Fig.4.1.

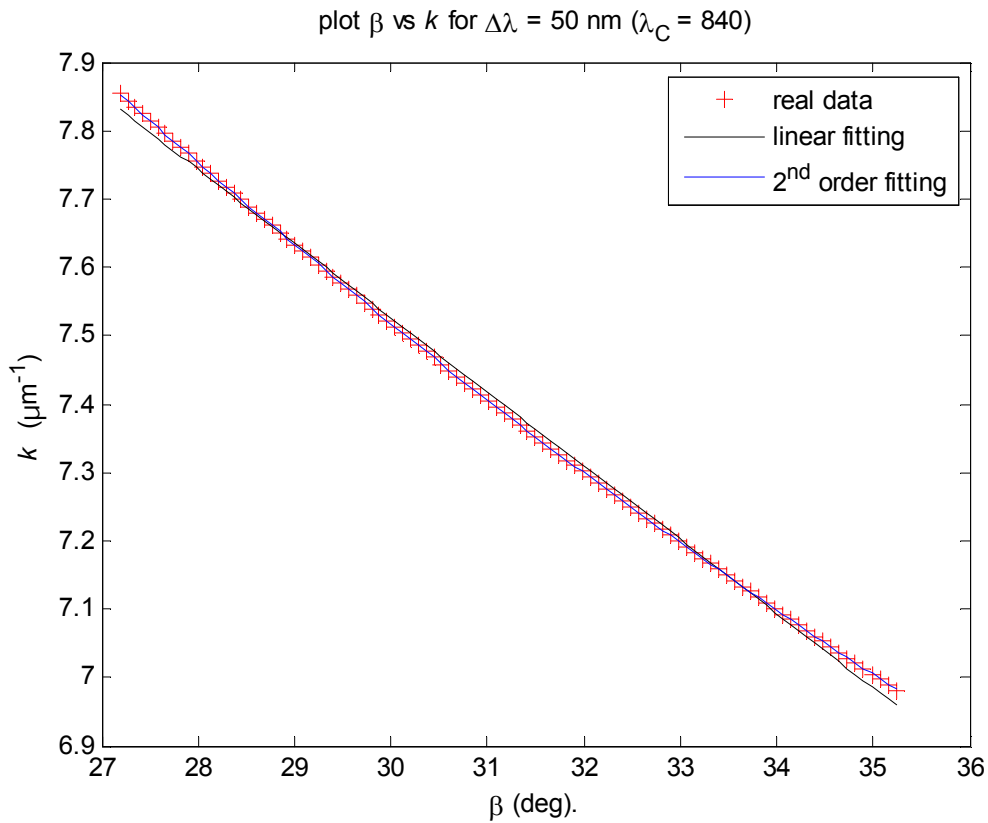


Figure 4.1. Plot of diffracted angle β as a function of k

Although the plot looks approximately linear, a 2nd order polynomial fit was found to give significantly lower errors than those produced by a linear fit. The mean deviation from the quadratic fitting is $3.0 \times 10^{-4} \text{ mm}^{-1}$ which is 1/30 of the figure from the linear fit. Also the maximum deviation of the original plot from the quadratic fitting is $8.9 \times 10^{-4} \text{ mm}^{-1}$, which is less than 4% from that obtained by the linear fitting. The results clearly show the relation between the diffracted angle β and k cannot be assumed to be linear, thus the depth information therefore cannot be directly derived from the recorded interferogram without some form of linearization. A convenient method to provide the linear relation between the recorded spectral interferogram and k is described in the next section.

4.2.5. Etalon for k -space linearization

To overcome the grating non-linearity problem, Bajraszewski et al suggested a solution employing an optical frequency comb (OFC) component that samples the continuous spectral content of the broadband light to produce discrete spectral transmission peaks prior to launching into the interferometer [144]. In the current set-up, an etalon is used as

an optical filter to implement the OFC function. Also as reported by Lee et.al, the use of a tandem OFC generator enabled an increase in the scanning speed and repetition rate by a factor of the order of ten to hundred as compared to conventional OCT [145].

The uniform k -space sampling properties of an etalon can be shown as follows. The transmitted intensity of an etalon is given by [72]

$$\frac{I_t}{I_i} = \left(\frac{T_e}{1-R_e} \right)^2 \frac{1}{1 + \left[\frac{4R_e}{(1-R_e)^2} \right] \sin^2(\delta_e/2)}, \quad (4-6)$$

where I_t and I_i are the transmitted and incident intensity of the light passing through the etalon, respectively. T_e and R_e are the etalon's transmittance and reflectance, respectively which are related by [72]

$$T_e + R_e + A_e = 1, \quad (4-7)$$

where A_e is the etalon's absorptance, i.e. the fraction of the incoming energy that is absorbed by the etalon's material. Finally, the term δ_e is the phase difference between two successive transmitted rays from the etalon and is given by

$$\delta_e = 2kn_e t_e \cos \theta_t + 2\phi_e, \quad (4-8)$$

where $k = \frac{2\pi}{\lambda_0}$ with λ_0 the wavelength of the light in vacuum/air, n_e is the refractive index

of the etalon's material, θ_t is the transmitted light angle relative to the etalon's normal, t_e is the etalon's thickness and ϕ_e is a phase shift due to the reflection of the light from the etalon surface. The product $n_e t_e$ is usually called optical thickness.

Further simplifications can be made to Eq.4-7 by assuming that an ideal etalon is used. An ideal etalon should only reflect and transmit the incoming light without absorbing it. The absorptance A in Eqn.4-7 can therefore be set to zero. Furthermore in the set-up the etalon is placed in the path of a collimated beam so that the transmitted light angle θ_t can be assumed to be close to zero. Also, as pointed out in Ref. [72], in general the etalon

thickness t_e is much larger than the light wavelength λ_0 so that the phase shift ϕ can be neglected. With these simplifications Eq.4-8 can be rewritten as

$$\delta_e \approx 2kn_e t_e, \quad (4-9)$$

and hence Eqn.4-6 becomes

$$\frac{I_t}{I_i}(k) \approx \frac{1}{1 + [4R_e / (1 - R_e)^2] \sin^2(kn_e t_e)}. \quad (4-10)$$

Eq.4-10 shows that the transmitted intensity has peaks uniformly separated in k -space, thus eliminating the non-uniform sampling problem of the grating described in the previous section. The sampling interval between transmission peaks can be calculated as follows. Using Eq.4-10 a peak in the transmitted intensity occurs when $kn_e t_e = \pi m$, where m is an integer. Therefore the distance between transmission peaks in k -space, known as the Free Spectral Range (FSR) δk can be calculated as

$$\delta k = \frac{\pi}{n_e t_e}. \quad (4-11)$$

Since the etalon's refractive index n_e and thickness t_e are constant, then so is the k -space FSR, which explains the uniform spectral sampling properties of an etalon in k -space. Aside from the inherent k -space linearization benefit, OFC has been also reported to suppress signal drop [144].

An example of an etalon's transmission plot is illustrated in Fig.4.2. Parameters to generate the plot are similar to those of the etalon used in the set-up, i.e. $R = 0.81$ at 840 nm, working wavelength $\lambda_W = 840$ nm, optical thickness $n_e t_e = 0.7056$ mm and FSR (expressed in wavelength terms) is 0.5 nm. For the sake of the plot's clarity only 10% of the 50 nm SLED total bandwidth is used to generate the plot.

Etalon transmission function for $\lambda_w=840$ nm, $\Delta\lambda=5$ nm & optical thickness $n_e t_e=0.7056$ mm

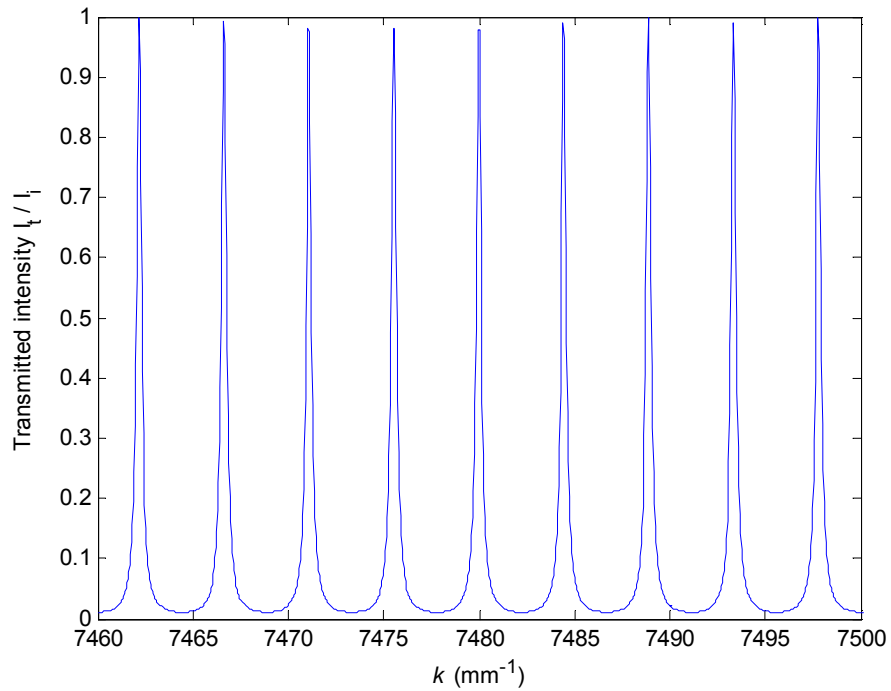


Figure 4.2. Plot of etalon's transmitted intensity in k -space (note that the working wavelength $\lambda_w = 840$ nm corresponds to $k= 7,480 \text{ mm}^{-1}$ - located in the centre of the horizontal axis of the plot).

4.3. HSI design

Based on the issues pointed out in Sect.4.2 the design of the previous set-up was revised. The design of the new set-up, called an etalon-based Hyperspectral Interferometer, is described in this subsection. The generic design of the system is shown in Fig.4.3.

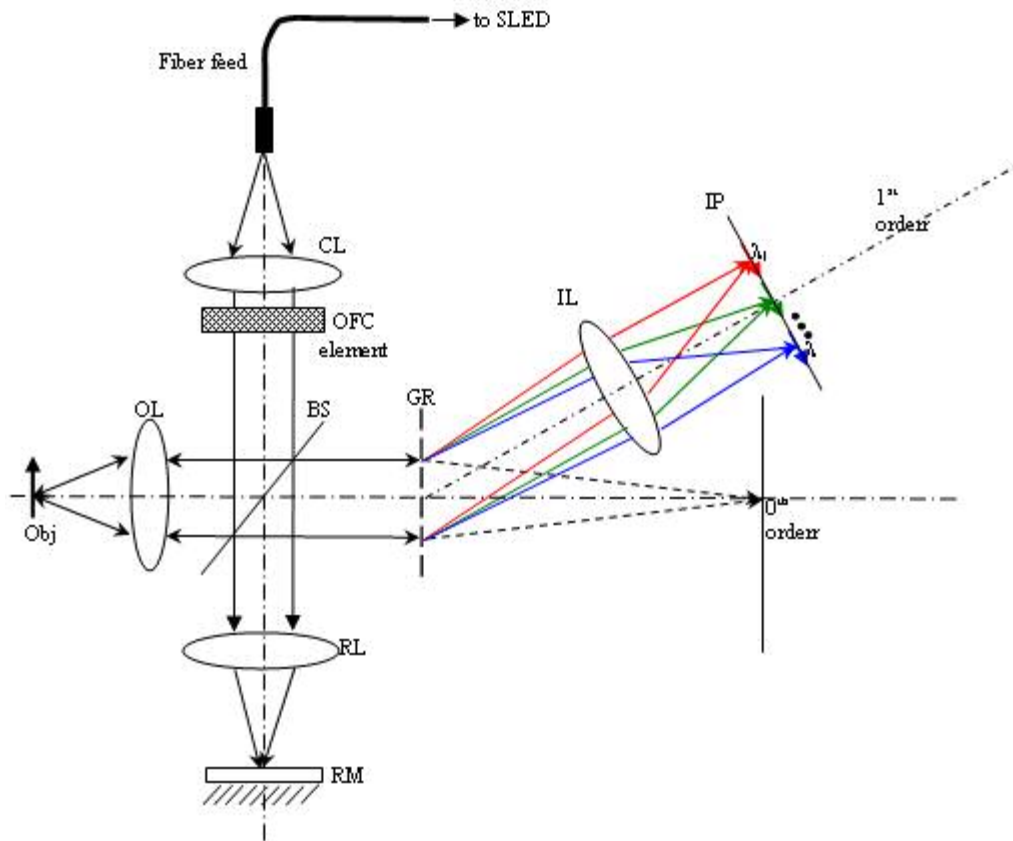


Figure 4.3. Generic design of an etalon-based HSI system. CL=Collimating Lens, OL=Object arm Lens, RL=Reference arm Lens, RM=Reference arm Mirror, BS=Beam Splitter, GR=Grating, IL= (Spectral) Imaging Lens, IP= (Spectral) Image Plane.

Compared to the previous set-up, the new design is simpler with fewer optical components. This is due to the elimination of the previously-necessary intermediate image formation in the system i.e. the object now is directly imaged onto the final detector at different wavelengths. Also, the aperture imaging path in the previous design is removed. The current design however still employs the Linnik-like interferometer configuration. It is described as ‘Linnik-like’ since long focal length lenses are used instead of a pair of identical short focal length or microscope objectives as are used in most Linnik interferometers- see for example Refs [97,132]. In the new design the microscope objectives for both interferometer arms are replaced by larger 1 inch diameter lenses. All lenses in the set-up were chosen to transmit the spectrum of the SLED light. Although it has several advantages, one drawback of this approach is that it is inefficient in its use of the available light, in that most of the incident illumination on the OFC filter does not enter the interferometer.

The principle of the new HSI design is as follows. First, the broadband light is sent into the interferometer after passing through an OFC element. Upon reflection from both interferometer arms, the beams are recombined and fall upon a diffraction grating. Subsequently the broadband light is decomposed into its spectral components by diffraction at different angles depending on the component wavelengths. The diffracted beams are finally focused onto a sensor array to be recorded. As the final camera records the grating output, the horizontal axis of the camera frame therefore corresponds to the wavelength axis of the broadband light input of the interferometer.

The optical frequency comb element in this set-up is realized by a Fabry-Perot etalon. Details on this type of passive spectral comb filter have been described in the previous section and only three essential parameters to specify the etalon are mentioned here. First is the Free Spectral Range (FSR) which is the (spectral) separation between two adjacent (spectral) transmission peaks. Each peak has a finite width. The width is measured at half of the maximum power, and thus is called the Full Width Half Maximum (FWHM) value. Finally a parameter called Finesse indicates the sharpness of the transmission peak which is expressed as the ratio of FSR to FWHM. In this research these etalon parameters, i.e. Free Spectral Range, Full Width Half Maximum and Finesse, are represented by the symbols used in Ref [72] as $(\Delta\lambda_0)_{fsr}$, $(\Delta\lambda_0)_{fwhm}$ and \mathfrak{F} , respectively. Details on the derivation of the required etalon's parameters for the set-up, including the corresponding spectral image formation are described in sub-sections 4.3.1 and 4.3.2.

Although the etalon approach has the benefit of simplicity over the microlens-based set-up, it has a drawback of reduced light efficiency. This can be illustrated as follows: the relation between Finesse \mathfrak{F}_e and reflectance R of the etalon is given by [72]

$$\mathfrak{F}_e = \frac{4R_e}{(1-R_e)^2}. \quad (4-12)$$

The etalon used in this set-up has finesse $\mathfrak{F}_e = 15$. This finesse figure is obtained by the design consideration explained later in Sect.4.3.3. Substituting the finesse $\mathfrak{F}_e = 15$ of the etalon used in this set-up (at working wavelength $\lambda_w = 840$ nm) the resulting reflectance R is 0.81, or only less than one-fifth of the incoming light energy is transmitted by the etalon. The reflectance plot of the etalon can be generated by invoking Eq.4-7 by, again, assuming an ideal etalon is used so that no absorption takes place ($A_e = 0$). The plot is shown in

Fig.4.4. The high back-reflected light intensity from the etalon is potentially harmful to the light source. A detailed description of the methods to avoid this adverse effect will be given later, including the reasons why finally an etalon was used to implement the OFC functionalities despite the other available types of wavelength selective filters, in Sect.4.7.

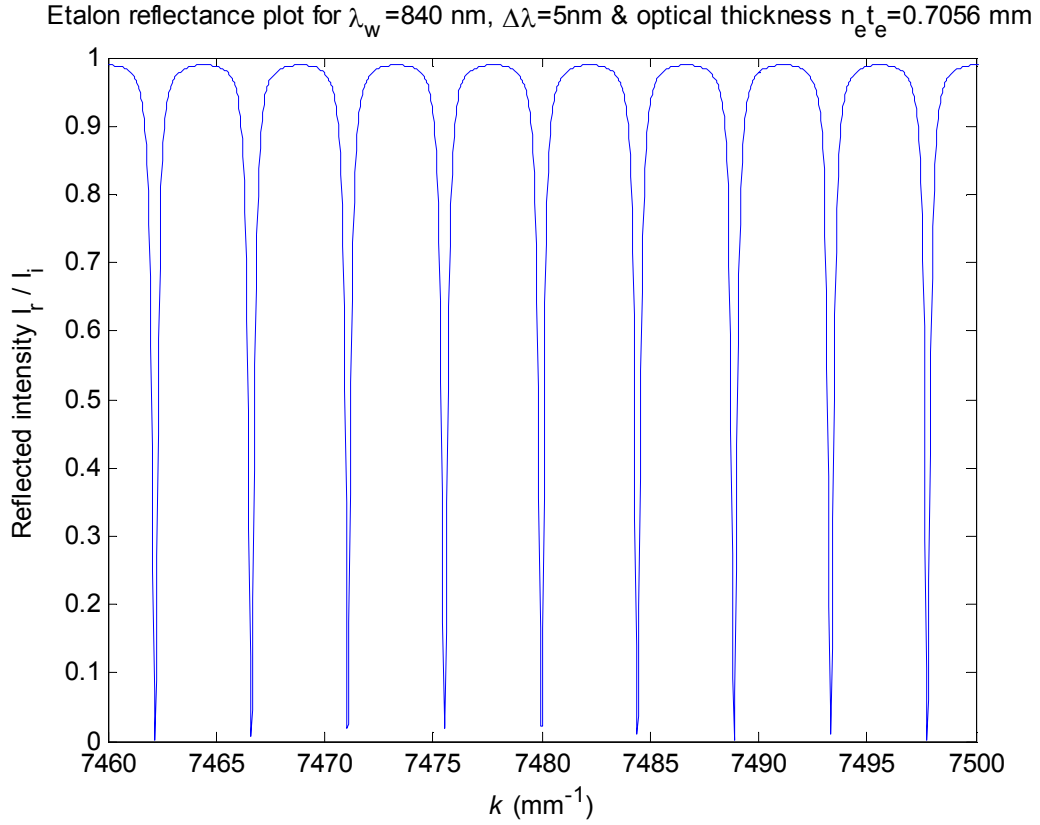


Figure 4.4. Plot of the etalon's reflected intensity as a function of wavenumber of the incident illumination.

Other pertinent relations to be considered are the relation between FSR $(\Delta\lambda_0)_{fsr}$, the etalon's refractive index n_e and the thickness of the etalon t_e

$$(\Delta\lambda_0)_{fsr} = \frac{\lambda_w^2}{2n_e t_e} \quad (\text{in wavelength}) \quad (4-13a)$$

$$(\Delta\nu_0)_{fsr} = \frac{c}{2n_e t_e} \quad (\text{in frequency}). \quad (4-13b)$$

Similar to the previous design, despite the later change described in Sect.4.5, the new design was also chosen to have 100 sub-images across the k axis. With the same SLED

light source with working wavelength ($\lambda_w = \lambda_c = 840$ nm) and bandwidth $\Delta\lambda = 50$ nm, the 100 sub-images requirement implies the gap between two adjacent sub-images is $50/100 = 0.5$ nm. Therefore the etalon's FSR $(\Delta\lambda_0)_{fsr}$ is also equal to 0.5 nm since the sub-image gap is equivalent to the gap between two adjacent transmission peaks. Using these figures the optical thickness (the product of refractive index n_e and material thickness t_e) with the assumption of an air-gap etalon ($n = 1$) is calculated using Eq.4-13a as 705.6 μm .

The corresponding FSR in frequency is 212.6 GHz. These calculated figures, the optical thickness and the FSR expressed in frequency, were the main parameters for the fabrication of the etalon by the selected manufacturer (Optarius).

4.3.1. The diffraction grating

The diffraction grating decomposes the incoming interferometer signal into its spectral constituents, which can be expressed by the standard grating equation as given in Eq. 3-2.

Using small angle approximations by only using the first order ($m=1$), and incident beam angle at (constant) Littrow angle ($\alpha = \alpha_L = 30.26^\circ$), with taking into account small increments of wavelength, Eq.3-2 can be simplified as

$$g \frac{d\lambda}{d\beta} = \cos \beta, \quad (4-14)$$

where g is the grating frequency (grooves/mm) and $\delta\beta_1$ is the change in diffracted beam angle resulting from a change in wavelength $\delta\lambda$. Since the grating is oriented in Littrow configuration, then $\beta = \alpha = 30.26^\circ$, and Eq.4-14 can be approximated as

$$g\delta\lambda \approx \delta\beta_1, \quad (4-15)$$

since the cosine term in the right hand side of Eq.4-14 is close to unity. The use of subscript '1' in the diffracted angle will be clarified later in the subsequent section.

The relation in Eq.4-15 will be used further in determining other system parameters including the system magnification M_s , etalon's FWHM $(\Delta\lambda_0)_{fwhm}$ and Finesse \mathfrak{F}_e .

4.3.2. Imaging path and system magnification

The system's imaging path is shown in Fig 4.5, which is similar to Fig.4.3 after removing the reference arm, the zeroth order light path and taking into consideration only one k value.

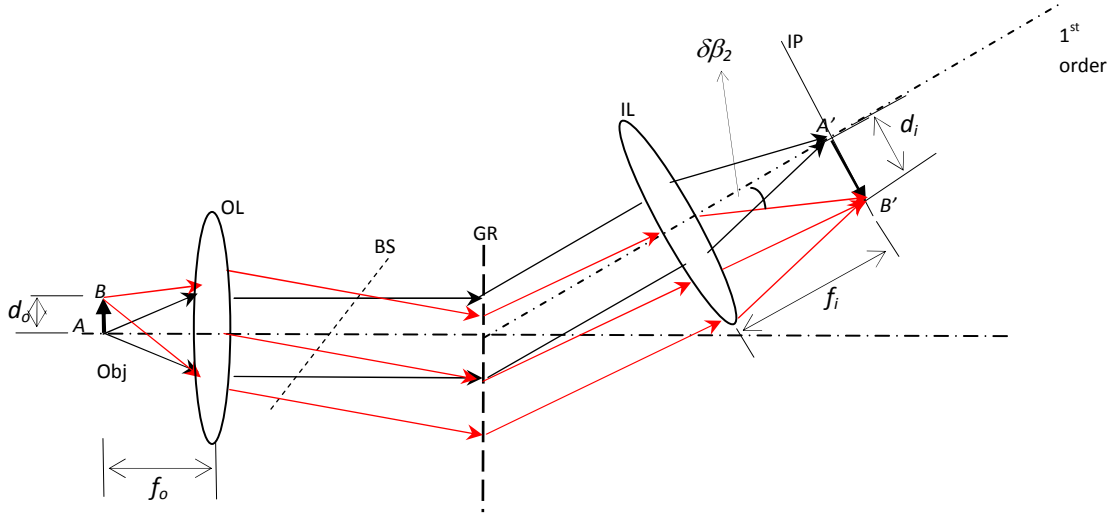


Figure 4.5. Object imaging path of the generic design (Fig.4.3).

The system magnification M_s is found as

$$M_s = \frac{d_i}{d_o} = \frac{f_i}{f_o}, \quad (4-16)$$

where f_o and f_i are the focal lengths of object and imaging lenses, respectively and d_o and d_i correspond to the object's FOV (Field Of View) and the width of the sub-image, respectively. It can be seen also from Fig.4.5 that

$$d_i \approx f_i \delta\beta_2, \quad (4-17)$$

where $\delta\beta_2$ is the angular deviation of the rays coming from two points on the object separated by d_o . By equating $\delta\beta_1$ from Eqn.4-15 and $\delta\beta_2$ from Eqn.4-17, the maximum field of view before an overlap of two adjacent spectral images occurs can be obtained as

$$d_i \approx f_i g \delta\lambda. \quad (4-18)$$

where $\delta\lambda$ is the etalon's FSR $(\Delta\lambda_0)_{fsr}$. If one sub-image occupies N_x pixels and the dimension of one CCD pixel is a μm , the width of sub-image d_i is then equal to $N_x \times a$. The imaging lens focal length f_i can be found as

$$f_i = \frac{N_x a}{g(\Delta\lambda_0)_{fsr}} . \quad (4-19)$$

4.3.3. Finesse

Eq.4-19 can be used again to determine the maximum allowable etalon FWHM. Spectral spread of one transmission peak, or the *FWHM*, of the etalon causes spatial spread at the CCD. If this spread is to be limited to 1 pixel then by substituting the etalon's FWHM $(\Delta\lambda_0)_{fwhm}$ for $\delta\lambda$, Eq.4-18 becomes

$$a \approx f_i g (\Delta\lambda_0)_{fwhm} . \quad (4-20)$$

Rearranging Eqns.4-19 and 4-20 for the FSR $(\Delta\lambda_0)_{fsr}$ and FWHM $(\Delta\lambda_0)_{fwhm}$, respectively, yields

$$\begin{aligned} (\Delta\lambda_0)_{fsr} &= \frac{N_x a}{f_i g} \\ (\Delta\lambda_0)_{fwhm} &\approx \frac{a}{f_i g} , \end{aligned} \quad (4-21)$$

from which the expression for the etalon's Finesse \mathfrak{F} is given as

$$\mathfrak{F}_e = \frac{(\Delta\lambda_0)_{fsr}}{(\Delta\lambda_0)_{fwhm}} \approx N_x . \quad (4-22)$$

This simple result states that if the spectral spread is to be limited to a single pixel only, then the required Finesse of the etalon is simply equal to the number of pixels of one sub-image.

4.3.4. Object lens

As the purpose of the interferometer is for depth measurement, it is reasonable to expect the system to have a sufficiently large depth of field d_f . From Eq.4-1, the depth of field d_f is proportional to the squared focal length of the object lens f_o . However, since the size of the illumination spot on the object d_o is proportional to focal length (Airy spot size relation $d \sim \lambda f/D$), a long focal length will increase the spot size and hence reduce the lateral resolution.

For the purpose of the initial system design, the spot image size at the CCD is set to be equal to or less than the size of a single pixel. It can be seen later, in Section 4.6 on the practical aspects of the system's design, that this single-pixel constraint can be eased as the size of the sub-image is deliberately enlarged to assist the alignment as well as to increase the field of view of the object.

Using the single-pixel constraint Eq.4-16 becomes

$$M_s = \frac{f_i}{f_o} = \frac{a}{d_o}$$

or

$$d_o = a \frac{f_o}{f_i}, \quad (4-23)$$

where d_o and a are the object illumination spot and pixel size, respectively. The illumination spot size is given by

$$d_o = 2.44 \frac{\lambda f_o}{D_o}, \quad (4-24)$$

where f_o and D_o are the focal length and the effective aperture (or the beam diameter) of the object lens, respectively. Combining Eq.4-23 with Eq.4-24 and Eq. 4-19 to find the imaging lens focal length f_i , the beam diameter of the object lens D_o can be calculated as

$$D_o = 2.44 \frac{N_x \lambda}{g(\Delta\lambda_0)_{fsr}}. \quad (4-25)$$

By combining Eqs.4-25 & 4-2, once the depth of field is determined in advance, the required focal length of the object lens can be calculated as

$$f_o = 1.22 \frac{N_x \sqrt{\lambda d_f}}{g(\Delta\lambda_0)_{fsr}}. \quad (4-26)$$

4.4. The prototype

As with the previous design, as noted in Section 3.2.5, it was initially decided that the new set-up should record around 100 spectral sub-images across the CCD or $N_k = 100$. As described also later in Section 4.5, however, the number of sub-images across the CCD frame was subsequently reduced in order to increase the number of pixels in each sub-image. As a starting point for the initial set-up design, however the 100 sub-image value was used.

The CCD has 1024×1024 square pixels, with the dimension a of each pixel equal to $6.45 \mu\text{m}$. The number of pixels in each sub-image N_x is therefore around 10×10 pixels. Using Eq. 4-22 the required Finesse is therefore also 10. In the implementation, however, the etalon was manufactured with a higher finesse (>15) to reduce the spectral blurring of the images.

Etalons are in most cases not available as an off-the-shelf optical component. In the preparation stage of ordering this component around 40 suppliers worldwide were approached. With the required technical specification tendered, only 25% gave a positive response. Taking into consideration the lead time and cost finally only 5 suppliers were shortlisted. Two types of etalon were offered: glass-based (both air spaced or solid), and a fiber-based etalon from one supplier. This is summarised in Table 4-1.

Table 4.1. Shortlisted etalon suppliers (entries are ordered from the least to the most costly product)

	<i>Supplier</i>	<i>UK rep.</i> <i>(if avail)</i>	<i>Product</i>	<i>Delivery time</i>	<i>Remarks</i>
1	Optarius Ltd, Malmesbury		Solid etalon	Approx. 6 weeks	- Ave. reflectance 815 - 865 nm approx. 77.3% - Theoretical wavelength drift approx. 13 nm/°C
2	CVI Melles Griot	BFi Optilas Ltd, Milton Keynes	Air gap etalon	3-4 weeks	Solid etalon costs approximately the same
3	IC Optical System Ltd, Kent		Solid etalon	3-4 weeks	Air gap etalon costs more
4	Micron Optics, Atlanta,GA	Smart Fibers Ltd, Bracknell	Fiber Fabry- Perot Interferometer FFP-I (Fixed filter)	n/a	-temperature stability available - reflected power between -8 to - 25 dB -operating range: 820-860nm -bandwidth: 7.1 GHz +/- 20% -finesse: ~ 30 -free spectral range: 213 GHz ± 10% -max. loss < 3.0 dB
5	Light Machinery, Ontario, Canada	n/a	Solid etalon	Approx. 8 weeks	Air space costs more

As later described in Section 4.6 the fiber-based Fabry Perot Interferometer option (from Micron Optics Inc.) was finally dropped due to the power back-reflection issue. This left the option of solid glass-based etalons. Among the three that had local suppliers, the item offered by Optarius Ltd was finally chosen. The final etalon specifications are: solid etalon of UV fused silica, optical thickness $486 \pm 10 \mu\text{m}$, Free Spectral Range 0.5 nm (at 840 nm), finesse > 15 , reflective coating approximately 81% (at 840 nm), parallelism < 5 arcsec and clear aperture > 8 mm.

The light source of the HSI prototype system is similar to that of the previous set-up, i.e. a 15 mW broadband SLED Superlum S840-HP-I (Superlum Diodes Ltd, Moscow) with centre wavelength $\lambda_c = 840$ nm and bandwidth $\Delta\lambda=50$ nm. The diffraction grating used in the set-up is a reflective ruled grating, blazed at 1 μm wavelength with grating frequency g

of 1,200 lines/mm. Despite the fact that the maximum efficiency is supposed to be achieved at the blaze wavelength, the grating efficiency (for the average of both orthogonal polarization modes) remains flat down to the range of the light source's FWHM (825 to 865 nm). This is shown in Fig.4.6.

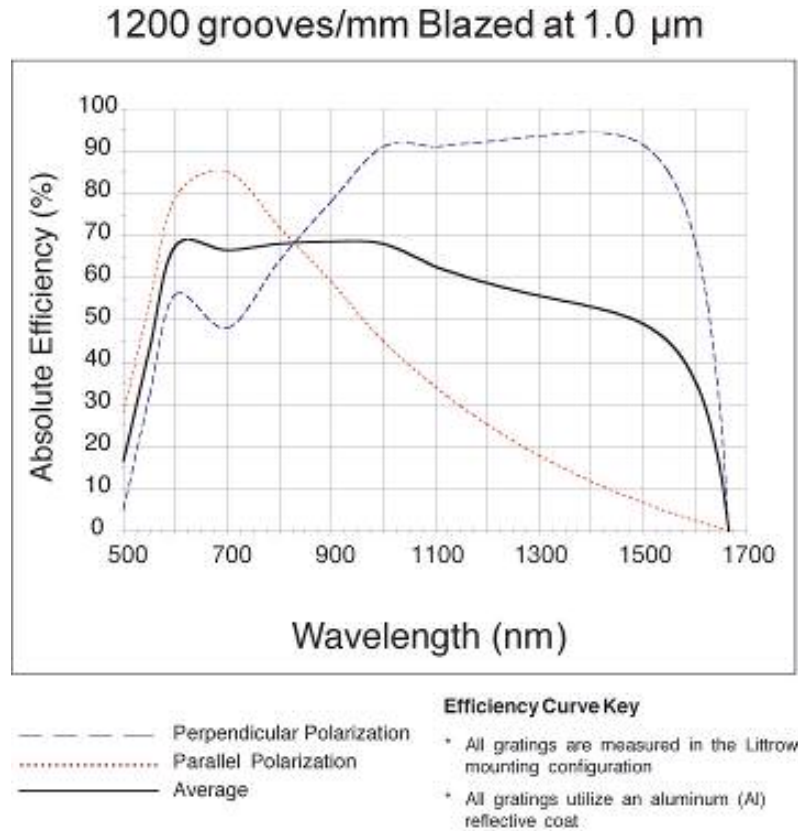


Figure 4.6. The diffraction grating spectral efficiency curve (source: Thorlabs website, see Appendix A8)

By using Eq.4-19 with the values $N_x = 10$ pixels, $a = 6.45 \mu\text{m}/\text{pixel}$, $g = 1,200$ lines/mm and $(\Delta\lambda_0)_{fsr} = 0.5$ nm, the required focal length of the imaging lens f_i is found to be 107.5 mm. No off-the-shelf lens was available with this exact value, thus for the imaging lens the focal length was selected to be the nearest available value of 100 mm. The final selected lens was a biconvex design, AR coated for the near IR.

For the application of the system to sub-surface measurement, the required depth of field of the system is expected to be in the range of a few millimetres. A 25.4-mm diameter lens with focal length 500 mm was selected as the object lens to give a 1.3 mm depth of field according to Eq.4-1. Using Eq.4-16, the system magnification can be calculated to be 0.2. Finally using again Eq.4-16 and setting the image size d_i of 10 pixels wide or $10 \text{ pixels} \times 6.45 \mu\text{m}/\text{pixel} = 64.5 \mu\text{m}$, the object's field of view is found to be $64.5 \mu\text{m}/0.2 = 322.5 \mu\text{m}$.

It will be shown later in the subsequent section that this choice of lens brings some alterations in the initial design, including the situation encountered in the experiment that the 10 pixel width of each sub-image brought difficulties in the system's alignment and construction, as well a limited field of view of the object.

Figure 4.7 shows the complete set-up of the new etalon-based hyperspectral interferometer system. The nomenclature is given in the figure caption. In comparison with the generic design in Fig.4.3 and the object imaging path in Fig.4.7, lenses L_3 and L_4 serve as the object and imaging lenses, respectively. Details of each component of the prototype are as follows (several components have been described previously, but reiterated here for completeness): LS_1 is the light source 1 – Superlum broadband superluminescent LED (SLED) light source Superlum S840-HP-I (Superlum Diodes Ltd, Moscow) 15 mW optical output power with a centre wavelength 840 nm, and a full width half maximum 50 nm. LS_2 is a narrowband source (He–Ne laser; wavelength 632.8 nm), used in the set-up for alignment purposes only and which contributes nothing to the final detected interferogram. Both beams are injected into a fiber coupler FC which splits the output into two power ratios, one with $LS_1: LS_2 = 90:10$ and the other $LS_1: LS_2 = 10:90$. The second power ratio ($LS_1: LS_2 = 10:90$) was chosen, as 10% of the total SLED light power was sufficient to produce a detectable signal without the use of any attenuating filter.

The fibre to deliver the light from the fiber coupler has a numerical aperture $NA = 0.12$ with mode field diameter $MFD = 5.6 \mu\text{m}$. The fiber end face is located at the focal length distance of lens L_1 so that light is collimated after leaving the lens. Lens L_1 is an aspheric lens with a focal length f_1 of 7.5 mm and clear aperture diameter D_1 of 4.5 mm, and is optimized to work at 830 nm. The collimated light subsequently passes through the etalon with FSR (Free Spectral Range) $(\Delta\lambda_0)_{fsr}$ of 0.5 nm and finesse $\mathcal{F}_e > 15$ to produce a frequency comb as depicted in Fig.4.2.

The light then enters the interferometer, split by beamsplitter BS_1 which is a pellicle type with membrane thickness $2 \mu\text{m}$ and splitting ratio 55:45 within the wavelength range 700-900 nm. One part (the 55%) goes to the reference arm in which the beam is focused by reference arm lens L_2 to the reference mirror RM . The mirror is placed at the focal length distance of lens L_2 . The other part (the 45%) is focused onto the sample by object arm lens L_3 . For surface profilometry applications, the sample's surface is located nearby the focal distance of lens L_3 . For the depth/sub-surface measurements, however, the sample surface can be located in front of the focal point of lens L_3 to allow the light to be focused under

the surface of the sample. This will be discussed further in Chapter 7 on depth resolved measurements of weakly scattering samples. The reflected light from the reference mirror and sample are recombined by BS_1 and subsequently divided by BS_2 into two other paths. One is focused onto webcam C_2 by lens L_5 for alignment monitoring and the other goes unfocused (collimated) onto the diffraction grating G . Beamsplitter BS_2 is identical to BS_1 , the webcam C_2 is a Trust webcam with 640×480 pixels, and the grating G is a reflective ruled grating, blazed at wavelength $1 \mu\text{m}$ with grating frequency g of 1,200 lines/mm. The diffracted light from the grating G is directed by BS_2 to imaging lens L_4 where it is subsequently focused onto the final CCD camera C_1 . Across the sensor area of camera C_1 are the sub-images due to the focused diffracted light, with each sub-image occupying a certain width and spatially separated from one another according to its wavelength range.

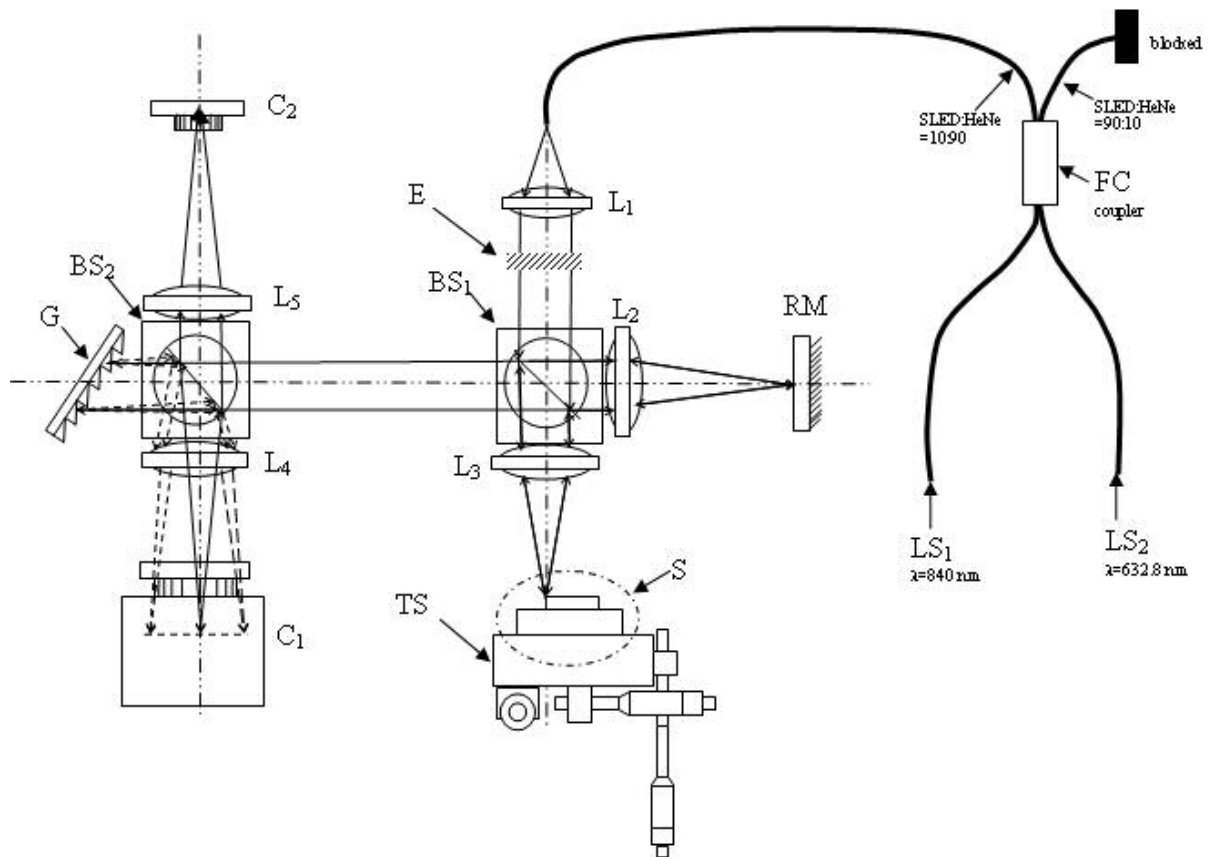


Figure 4.7. The HSI prototype. L_1 , L_2 , L_3 , L_4 and L_5 are collimating, reference, object, CCD (alignment monitoring) and imaging lens, respectively; BS_1 and BS_2 are beamsplitters 1 and 2, respectively; LS_1 and LS_2 and FC are light source 1 (SLED 840 nm), light source 1 (SLED 840 nm), light source 2 (He-Ne laser 632.8 nm) and fiber coupler, respectively; C_1 and C_2 are camera 1 (final spectral imaging camera CCD) and camera 2 (webcam for alignment monitoring), respectively, E , TS , S , G , RM are etalon, translation stage, sample object, diffraction grating and reference mirror, respectively (figure taken from Ref.[38])

4.5. Defocusing the sample illumination

It was later found experimentally that the initial 10-pixel width of each sub-image was not readily interpretable. As a result, the sub-image width was increased, although this comes at the expense of a reduction in the total number of sub-images. As indicated in Eq.3-4, the system's depth range depends on the total number of sub-images. Also, fewer sub-images implied a reduction of the effective light source bandwidth that will further affect the depth resolution.

According to Eq.4-16, enlarging the sub-image width can be achieved by shortening or increasing the object or imaging lens focal length, respectively. It was decided to keep the object lens L_3 unchanged in order to maintain the same depth of focus. The imaging lens L_4 was modified by increasing the focal length from 100 to 150 mm. The system magnification was therefore raised from 0.2 to 0.3. As the magnification became 1.5 times larger the sub-image size was also expected to increase from 10 to 15 pixels, or occupying $15 \text{ pixels} \times 6.45 \text{ } \mu\text{m/pixel} = 96.75 \text{ } \mu\text{m}$. The number of sub-images across the frame therefore drops from 100 to around 67

Another issue to be considered was the size of the illuminating spot on the sample. In the previous section it was calculated that in order to obtain a 10 pixel-wide sub-image with a combination of the focal lengths of object and imaging lenses of 500 mm and 100 mm, respectively, the illuminating spot diameter should be 322 μm . However, by using Eq.4-24, with an object lens of 500 mm focal length and 25.4 mm diameter, the resulting illuminating spot size is only 40.35 μm , or only 12.5% of the required spot size.

The spot size calculation in Eq.4-24 however is based on the assumption that a collimated beam fully fills the entire lens aperture area D_o . In reality, due to the light delivery by fiber with small numerical aperture, the incoming light does not entirely fill the aperture of the collimating lens L_1 . This is schematically shown in Fig.4.8. The (half) launch angle θ_L is given as $\theta_L = \sin^{-1}(\text{NA})$, where NA is the numerical aperture of the fiber. The fiber used in the set-up has NA=0.12 which gives $\theta_L = 6.89^\circ$. The collimating lens L_1 is an aspheric type with focal length 7.5 mm and aperture diameter, D_1 , of 4.5 mm. It is located a focal length from the fiber end face to produce a collimated beam after leaving the lens. Compared with the imaging lens L_2 , it is clear that the diameter of collimating lens L_1 is smaller than that of lens L_2 .

This implies that, even if a full aperture collimated beam is output by L_1 , it will only illuminate 4.5 mm out of the full 25.4 mm diameter, i.e. less than 20% of the full aperture of imaging lens L_2 . This is illustrated in Fig.4.8.

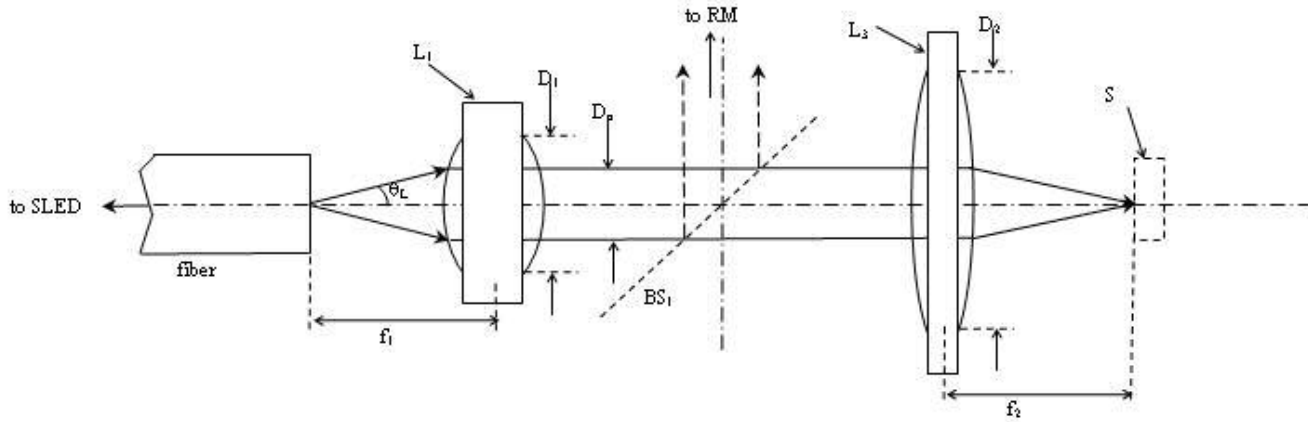


Figure 4.8. Light path of sample illumination from the fiber (drawing not to scale)

As can be seen in Fig.4.8, the collimated output beam diameter $D_0 = 2 \times f_1 \times \tan(\theta_L) = 1.81$ mm, which is even less than the aperture of the collimating lens L_1 . This collimated beam, as shown in the light path of Fig.4.8, will be focused by L_3 onto the sample. The focused beam diameter at the sample, d_o , calculated using Eq.4-24 with f_o equal to f_3 (the focal length of lens L_3) = 500 mm, and using the centre wavelength of the SLED light of 840 nm, gives $d_o = 565 \mu\text{m}$, which is larger than the initially expected illuminating spot size of $322.5 \mu\text{m}$. With the new magnification of 0.3, the sub-image size would be $169 \mu\text{m}$ or around 27 pixels – almost twice as much as the initially expected 15 pixels/sub-image. This will give only $1024/27 = 38$ sub-images, which less than a half of the initial plan of 100 sub-images across the CCD frame.

Another method was therefore needed to increase the number of sub-images again whilst keeping the configuration unchanged. One alternative way to achieve this is instead of producing a spot illumination, the sample is illuminated with a larger width beam. With a larger illuminated sample whilst keeping the imaging lenses unchanged to keep the same magnification (using Eq.4-16) a wider sub-image can be obtained. In the real set-up construction the aspheric lens L_1 is mounted on a micrometer z and location of the lens was gradually adjusted by micrometer until the expected 16 to 17 pixel width of a sub-image was observed in the CCD.

This adjustment has two minor consequences for the subsequent optical path. Firstly the beam passing through the etalon is no longer collimated, and this will broaden slightly the frequency comb. However, at close to normal incidence the effect is second order in the angle of a given ray to the optical axis and therefore has negligible effect in practice. Secondly, the wavefront illuminating the sample surface is now curved which at first sight may seem undesirable in view of the small number of pixels spanning the field of view. In practice, however, high frequency fringe patterns are avoided because the reference wave will have the same radius of curvature due to the symmetrical layout of the Linnik interferometer head.

4.6. Effect of back reflections

The use of an etalon comes at the price of power reduction due to back-reflected light. High-finesse etalons require highly-reflective mirrors, which inevitably creates strong light reflections back to the light source. An important issue that has to be taken into consideration is that this reflected power must not exceed the limit of the ability of the light source to handle back reflections. This acceptable limit of back reflection of the SLED light source is given by [146,147]

$$R - L_{coupling} - L_{isolator}(\lambda) - L_{insertion} < -30 \text{ dB} \quad (4-27)$$

where R is the fraction of the reflected incident power from the etalon (or the etalon reflectivity), $L_{coupling}$ is the loss due to power coupling from the etalon back to the fiber, $L_{isolator}(\lambda)$ is the wavelength-dependent loss of the optical isolator unit inside the SLED unit, and $L_{insertion}$ is the insertion loss of the optical isolator. All the quantities must be expressed in decibels (dB). Eq.4-27 essentially states that the total light reflected before entering back the SLED light module unit must be attenuated by more than 30 dB.

Of all the variables in Eq.4-27 only one is wavelength-dependent, i.e the power loss of the isolator $L_{isolator}(\lambda)$. The spectral plot of the isolator loss of the SLED is shown in Fig.4.9.

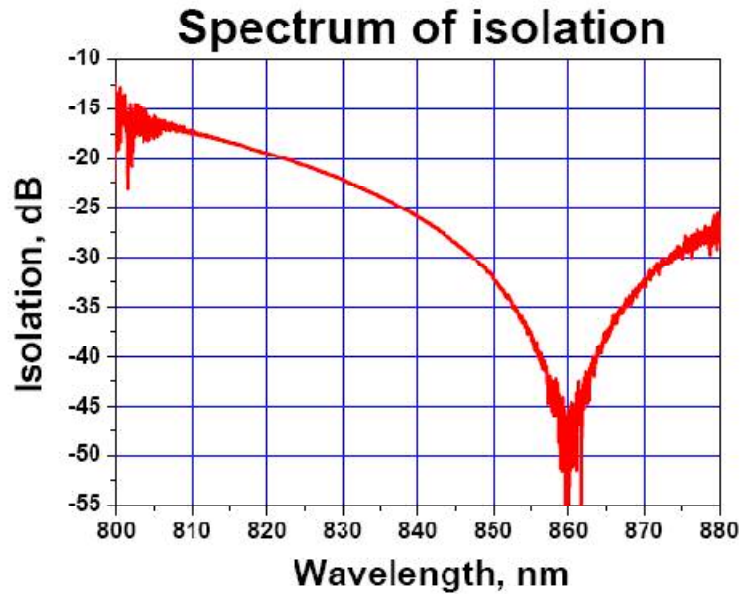


Figure 4.9 .Spectrum of loss of isolator module in the SLED unit (from Ref [148,149]).

Three wavelengths were selected to represent the SLED spectrum (50 nm bandwidth centred at 840 nm) in order to calculate the wavelength-dependent isolator loss $L_{\text{isolator}}(\lambda)$. The wavelengths are: 815 nm (lower end of the bandwidth), 840 nm (centre wavelength) and 865 nm (upper end of the bandwidth). From the spectrum loss plot in Fig.4.20 the isolation loss at 815 nm is approximately -18 dB, whilst the corresponding figures for the centre wavelength 840 nm and upper end of the bandwidth (865 nm) are -26 dB and -55 dB, respectively.

As described in Section 4.4, the surveyed etalons included the fiber-based Fabry-Perot Interferometer (FPI) from Micron-Optics (Atlanta, GA). This type of device offers simplicity in constructing the set-up, since both ends of the device are terminated by fiber connectors that can be directly connected to the SLED output and lens L_1 adapter input terminals. However, the back reflections are fed straight back down the fibre and therefore this type of device has a much greater risk of damaging the light source than do non-fibre etalons.

The configuration using a fiber-based etalon (Fabry-Perot interferometer) is shown in Fig.4.10. Since the etalon is integrated with the fiber in this kind of device the fiber power coupling loss L_{coupling} can be assumed to be very small or neglected ($L_{\text{coupling}} \approx 0$).

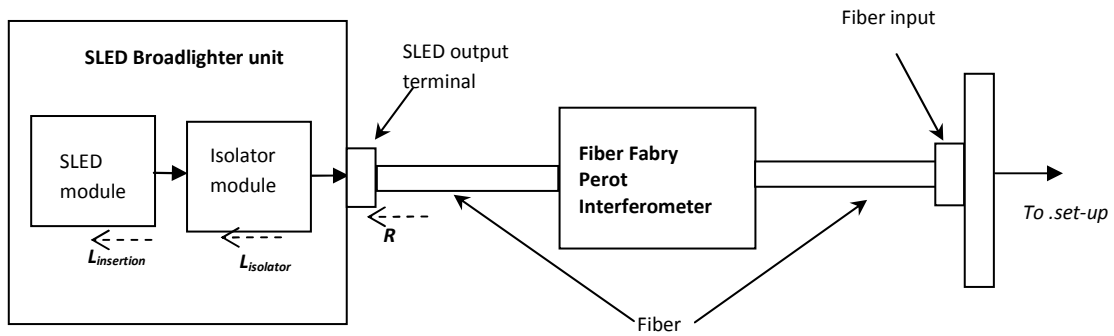


Figure 4.10. Fiber etalon (Fabry-Perot Interferometer) placement between SLED and lens L1 adapter and the corresponding loss components.

The insertion loss of the isolator $L_{insertion}$ according to SLED manufacturer (Superlum Didoes Ltd) is 1.2 dB. As indicated in the table of shortlisted etalon suppliers the fiber FPI reflected power varies between -8 to -25 dB. The total loss of this device calculated using Eqn.4-27 is shown in Table 4-2 for the maximum and minimum reflected power values at the three selected wavelengths

Table 4.2. Loss/reflected power calculation for Fiber Fabry-Perot Interferometer type etalon

Reflected power level	wavelength	Total loss calculated using Eqn.4-27	Is total loss above -30 dB threshold?
-8 dB	815 nm	-27.2 dB	<u>yes</u>
	840 nm	-35.2 dB	no
	865 nm	-64.2 dB	no
-25 dB	815 nm	-44.2 dB	no
	840 nm	-52.2 dB	no
	865 nm	-81.2 dB	no

From the table, despite the fact that only one wavelength causes the total loss to rise above the threshold, it is not safe to assume that the entire spectrum of the back reflection power will not harm the SLED unit. The fiber Fabry-Perot interferometer arrangement was therefore dropped, and the only alternative was to use the glass-based etalon.

In comparison to the fiber-based device, the glass-based etalon was not as simple to install. It could not be directly connected to the SLED in the same way as the fiber-based device.

This disadvantage however is also a benefit in that it offers a degree of freedom in adjustment so that the back reflection power can be significantly suppressed.

This was achieved by mounting the etalon on a gimbal mount so that instead of being perpendicular to the incident beam, the mount enables oblique incidence of the light onto the etalon. The reflected beam can in this way be directed away from the fiber end. The configuration and loss factors of the glass etalon in the set-up are shown in Fig.4.11.

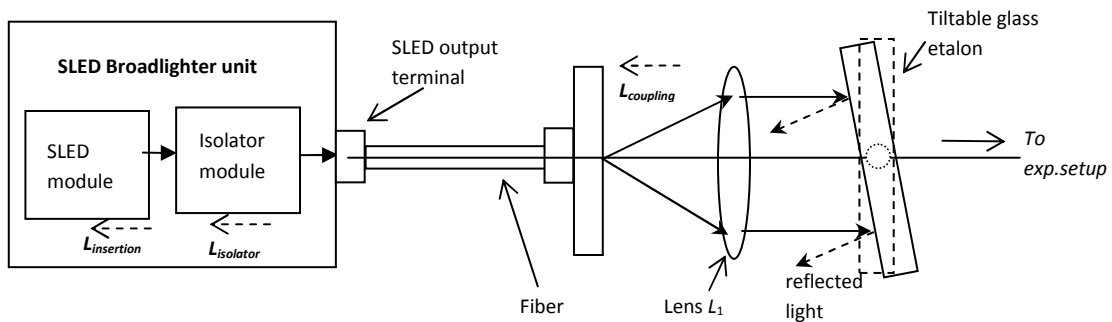


Figure 4.11. Glass etalon in the gimbal mount to SLED and lens L_1 adapter, and the corresponding loss components.

We assume the worst-case situation in which the power reflected by the etalon exactly traces its path back to a spot at the fiber end. In order to completely miss the fiber end, the beam must be reflected from the tilted etalon such that the spot so produced is shifted by the fiber end width. This situation is illustrated in Fig.4.12 where line AB is equal to the fiber's beam width MFD and line AC is the distance between the fiber tip and the etalon (tilting axis). The width of the fibre's core can be assumed to be similar to the fiber's MFD of $5.46 \mu\text{m}$. Lens L_1 is mounted in a mounting plate with 10 mm thickness. The gimbal mount also has roughly the same thickness thus the minimum distance between the lens and the etalon (tilting axis) is roughly 10 mm. Thus the total minimum distance between the fiber tip and the etalon is 17.5 mm since the focal length of lens L_1 is 7.5 mm. The angle θ in triangle ABC is equal to $\tan^{-1}(0.0546/17.5) = 0.018^\circ$ or around 1/60 of a degree. This means by tilting the etalon by only 0.5 arc minutes, the reflected power from the etalon can be safely assumed to be almost nil. In fact, for the convenience of constructing the set-up, lens L_1 and the etalon are not placed touching each other, but rather are separated by a larger gap, making the required tilt angle of the etalon even smaller.

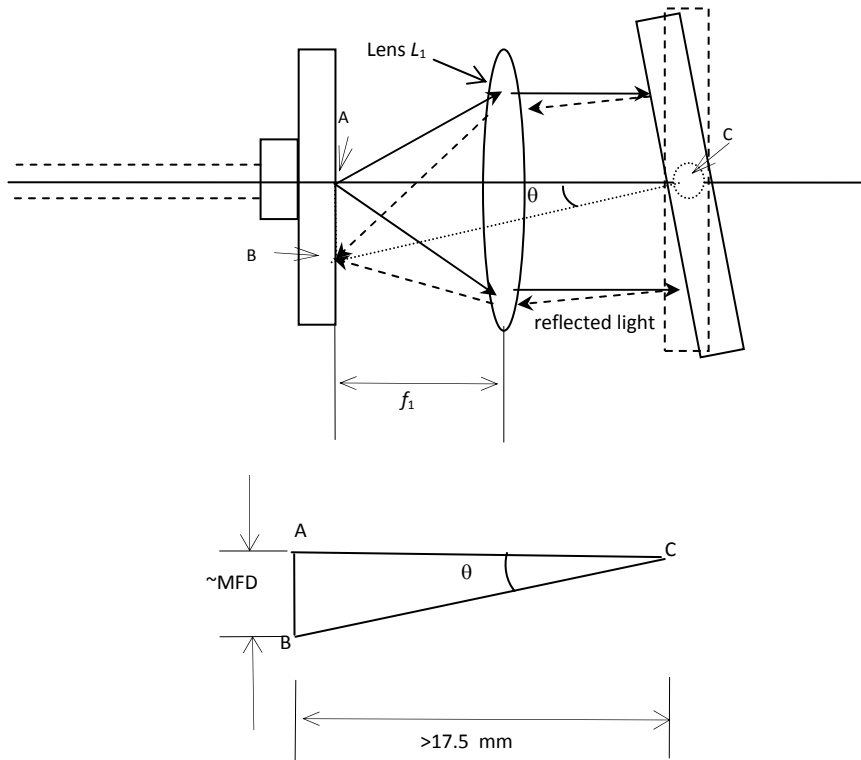
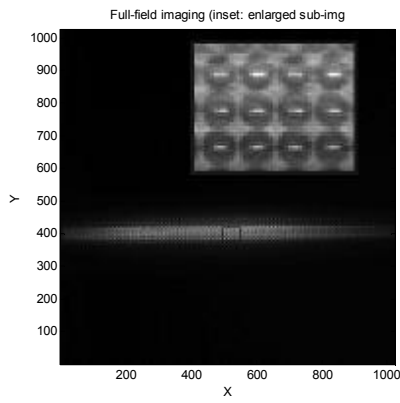


Figure 4.12. Diagram of reflected light from the etalon to calculate the required tilt to eliminate the back reflected power (drawn not to scale).

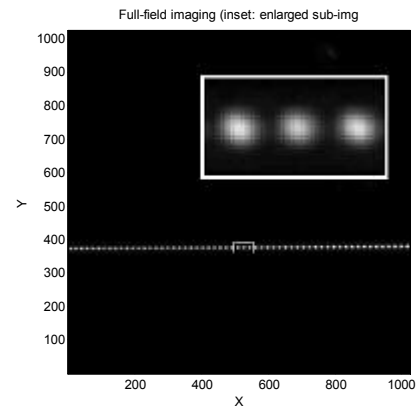
4.7. System performance in brief

The performance of the new etalon-based hyperspectral interferometer is only briefly discussed in this section. The details, particularly in the sample imaging, will be presented in Chapter 6 on surface profilometry. This sub-section just describes the noticeable improvement in imaging performance compared to the previous microlens-based system.

Fig.4.13 shows the output image from the reference arm recorded by the final CCD camera for both systems. It is clear that the etalon-based system produces distinct sub-images across the frame compared to the previous design. Although there are more sub-images in the image produced by the microlens-based system (100 sub-images in Fig.4.13.a) compared to 62 sub-images in Fig.4.13.b, there is more than one row of sub-images produced by the previous design. Furthermore, since the gaps between lenslets were transparent the unwanted background light was also included during the image acquisition and in effect added noise to the required signal. This noise is not observed on the image produced by the new design set-up.



(a)



(b)

Figure 4.13. Comparison of the performance of both systems: (a) microlens-based, (b) etalon-based HSI taken at stage position 28.50 mm.

The difference between the two system's outputs becomes more profound when evaluating the sample imaging performance. This will be shown in Chapter 6 next chapter as part of the surface profilometry application.

Chapter 5

Data Processing

5.1. Introduction

Once the single frame multiple spectral interferogram has been recorded by the final CCD camera (as shown in Fig.3.1 in Chapter 3), the next task is to perform data analysis. This chapter presents the steps to be performed to analyse the data, methods to filter out unwanted signal and to extract the sought information. The sought information is essentially the optical path difference between sample and reference arms. Background theories pertinent to data processing and analysis will be discussed first.

5.2. Interferogram spectrum

In section 2.2.2 the principles of spectral low-coherence interferometry have been described in detail based on the derivation from Ref [19]. In particular, Eq.2-32 which states that the scattering potential distribution can be reconstructed by taking the Fourier transform of the backscattered interferometric signal. The derivation however is quite long and complex. A rather shorter version of analysis is normally used in the field of experimental mechanics where typically only two interfering beams are involved. The interferogram due to any two-beam interferometric process in general can be represented by [38]

$$I(x_m, y_n, k) = \{I_0(x_m, y_n) + I_1(x_m, y_n) \cos[kz_0(x_m, y_n) + \phi_0]\}W(k - k_c), \quad (5-1)$$

where $z_0(x_m, y_n)$ and ϕ_0 is the optical path difference distribution at $z = z_0(x_m, y_n)$ and phase shift between the reference and sample light waves, respectively. I_0 and I_1 are respectively the dc and modulation intensities. In comparison with the standard single-wavelength interferogram expression in Eq.2-4, there are additional two terms included in Eq.5-1. The first is the weighting function $W(k)$, which is assumed to be an even function to take account of a spectral windowing function or non-uniform spectral distribution of the light source. Also, the wavenumber k becomes the variable in Eq.5-1 to take account of the non-monochromatic lightwaves, whilst it was only a constant in Eq.2-4. Finally, the term k_c in

Eq.5-1 is to account for the shift of the weighting function $W(k)$ in k space. The subscripts m,n denote the pixel 2-D indices.

The Fourier transform of Eq.5-1 with respect to k yields [38]

$$\tilde{I}(z) = \left[I_0 \delta(z) + \frac{I_1}{2} \delta(z - z_0) \exp(i\phi_0) + \frac{I_1}{2} \delta(z + z_0) \exp(-i\phi_0) \right] \otimes \left[\tilde{W}(z) \exp(-ik_c z) \right], \quad (5-2)$$

where $\delta(z)$ is the Dirac delta function, $\tilde{W}(z)$ is the Fourier transform of $W(k)$, and where \otimes represents convolution. It can be observed from Eq.5-2 that the Fourier transform operation transforms the variable k (of the recorded interferogram domain) to optical path distribution z .

If the 1-D version of Eq.5-2 is plotted, with the phase terms $\exp(\pm i\phi_0)$ and $\exp(\pm ik_c z)$ dropped, the result is shown in Fig.5.1. The figure shows how $\tilde{W}(z)$ is convolved with the delta function located $z=0$, along with the copies centred at the side peaks of $z=\pm z_0$. As mentioned briefly in the introduction, the goal of the data analysis stage is to extract the optical path difference distribution z from the recorded interferogram. In Eq.5-1 this term is part of the argument of the cosine function that cannot be immediately extracted. In the Fourier domain (Eq.5-2), however, this term is transformed into a pair of peaks whose shift z_0 (see Fig.5.1) is proportional to optical path difference on a pixel-wise basis. Detecting the location of the shifted peak at each pixel is therefore the crucial part of the data processing stage.

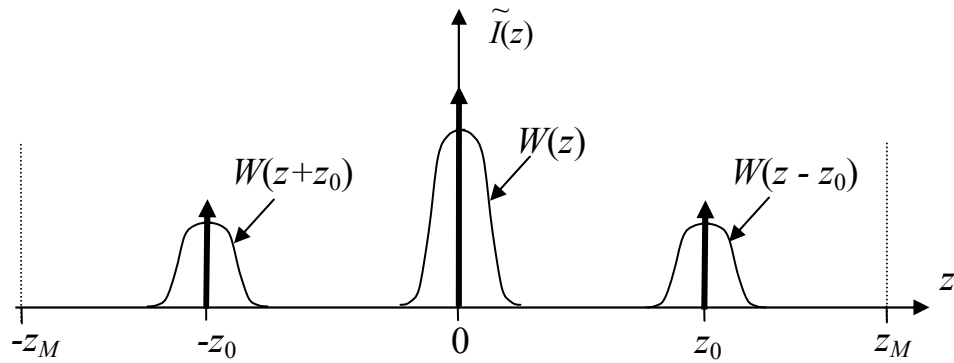


Figure 5.1. Fourier transform of Eq.5-1 with respect to k . The location of the side peak corresponds to the optical path distribution z_0 at the pixel of interest (figure taken from Ref [38]).

The fact that original data is real rather than complex means that the magnitude of the spectrum is symmetric about the origin. One sided peak detection (e.g., the region of the transform $z > 0$) is therefore sufficient in determining the peak shift. Accurate measurement of the peak position however requires negligible leakage from any adjacent peaks, which in this case is normally the peak centred at $z=0$. It is therefore useful to suppress the DC term (centre peak) to reduce the possibility of error in determining the peak shift.

5.3. Implementation

As briefly discussed in Sect.3.1 on the concept of hyperspectral interferometry the subsequent step after acquiring the single frame in Fig.3.1 is to stack the sub-images in the frame to construct the Hyperspectral image volume. This 3-D data volume is denoted as $I(x, y, k)$.

In order to perform the stacking, there must be a pixel in every sub-image, to serve as a reference, onto which other reference pixels from other sub-images are aligned so that the corresponding 2-D sub-images can be assembled to form the 3-D hyperspectral image volume. These reference spots are acquired by means of the spot imaging method. The spot profile ideally should be a (2-D) Gaussian profile, thus the function to fit the data was therefore also a Gaussian.

The fitting is carried out by means of Matlab built function `fminsearch` – a multidimensional non-linear minimization function. The Gaussian function to fit the spot takes the form of

$$I(x, y) = DC + I_0 \exp\left\{-\frac{(x - x_c)^2 + (y - y_c)^2}{2\sigma^2}\right\}, \quad (5-3)$$

where DC , I_0 , x_c , y_c and σ are the DC/constant term, peak intensity of the Gaussian, x and y coordinate offsets and standard deviation of the peak width, respectively.

The location of the spots were is automatically identified by a modified Matlab script initially developed by T. O’Haver to detect peaks in absorption spectroscopy data (see Appendix A9). It will be shown later in Chapter 7 on depth measurement of weakly scattering object that some more steps following the Gaussian fitting must be carried out to improve the accuracy of finding these reference pixels.

The coordinates of these reference pixels are then stored in the table and every table entry serves as the centre point to segment the interferogram in Fig.3.1 into regions of a user-defined number of pixels along both spatial axes. The segmented area becomes the sub-image corresponding to that reference pixel. After all sub-images are formed, these reference coordinates are aligned, acting as the axis onto which the 2-D sub-images are stacked to create the 3-D hyperspectral image volume $I(x, y, k)$. Each pixel in the hyperspectral image volume can therefore be denoted as $I(x_m, y_n, k_p)$ where subscripts m , n and p take the values $m = 0, 1, 2, \dots, N_x - 1$, $n = 0, 1, 2, \dots, N_y - 1$, and $p = 0, 1, 2, \dots, N_k - 1$, respectively, and N_x , N_y and N_k are the number of sample points along the respective axes.

The next step of the processing is to extract the sampled points along the k axis on the hyperspectral image volume $I(x, y, k)$ for a given pixel. The diagram of $I(x, y, k)$ in Fig.3.2 is presented again in Fig.5.2 for clarity, on which a dotted line in Fig.5.2.(a) shows the path where the intensity signal $I(x_m, y_n, k)$ is sampled along the k direction.

The example of the sampled intensity $I(x_m, y_n, k)$ extraction from the hyperspectral image volume $I(x, y, k)$ is shown in Fig.5.2.(b). The data was taken from the reflective planar surface experiment described in Section 6.2 of Chapter 6. It was extracted from the pixel at the centre of field of view of the sub-images (which later were stacked to create the 3-D hyperspectral image volume $I(x, y, k)$) at the known stage position of 30.88 mm. The

number of sampled points in $I(x_m, y_n, k)$ is equal to N_k - the number of sub-images across the full-frame interferogram shown in Fig.3.1.

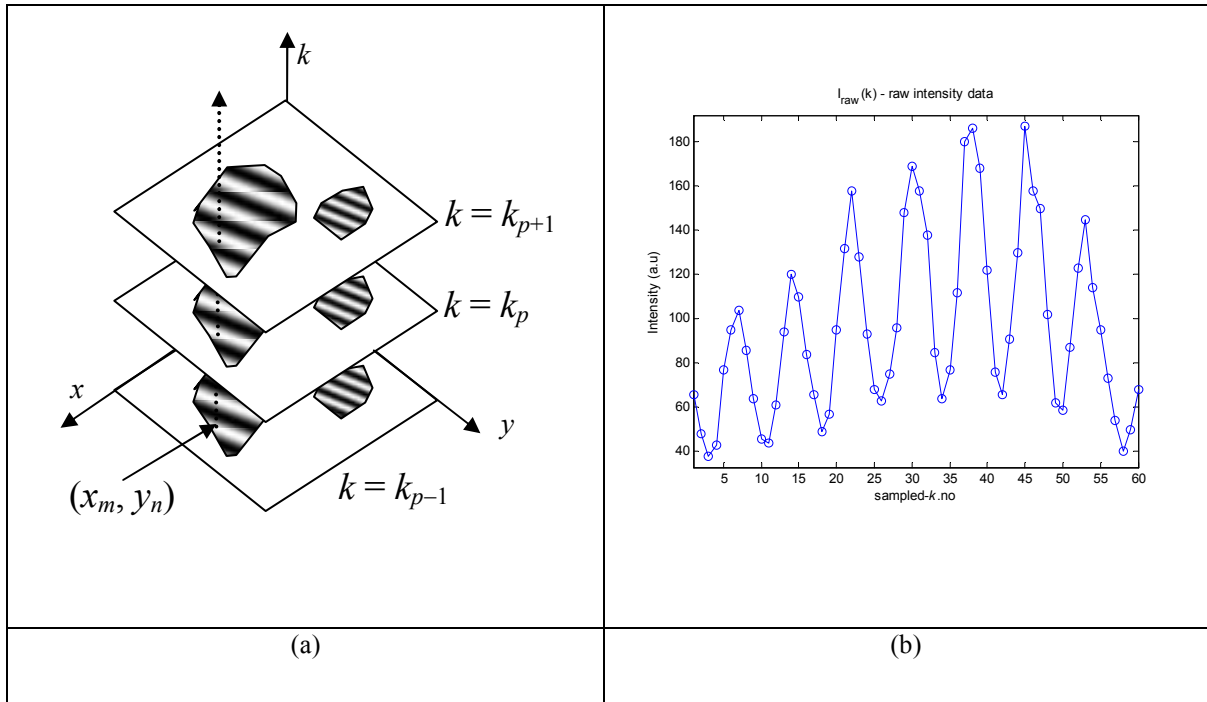


Figure 5.2.(a) Hyperspectral image volume $I(x, y, k)$ as shown in formed by stacking spectral sub-images across the frame shown in Fig. 3.1. The dotted line represents the path from which the sampled 1-D signal $I(x_m, y_n, k_p)$ ($p = 0, 1, \dots, N_k - 1$) is extracted, (b) Example of the extracted sampled points along the dotted path in the left diagram (figure 5.2(a) taken from Ref [38])

Next the sampled intensity signal $I(x_m, y_n, k)$ first has its mean value subtracted to remove the DC term and is subsequently Fourier-transformed. The operation transforms $I(x_m, y_n, k)$ in the k domain to $\tilde{I}(z)$ in the depth (z) domain. The transformation produces a peak, and the peak location $z = z_0(x_m, y_n)$ corresponds to the depth of pixel (x_m, y_n) . This is illustrated in Fig.5.3.(b). Note that if subtraction of the average signal is not performed prior to carrying out the transformation, the DC term will appear as a peak along with the others as shown in Fig.5.3.(b). The presence of the dc peak is undesirable, particularly when the Fourier transformation produces more than one peak. Multiple peaks might not be encountered in shape profilometry but will in general be more obvious when measuring semi-transparent scattering media in which the sample can be modelled as a stack of multiple depth layers. Furthermore, the peak due to the DC term usually has higher amplitude than the others that can potentially mislead the peak finding function from finding the sought peak.

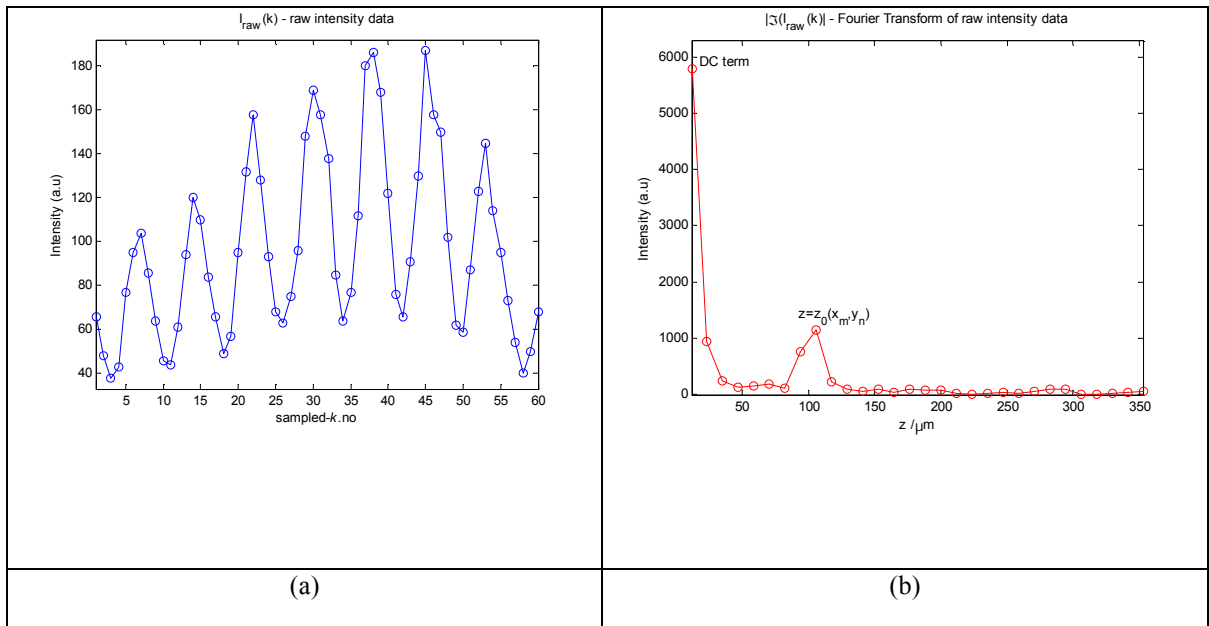


Figure 5.3.(a) The (raw) data of intensity at sampled points of k transform of $I(x_m, y_n, k)$ as shown in Fig.5.2.(b), (b) The Fourier transform result of $I(x_m, y_n, k)$ to extract $z_0(x_m, y_n)$, the depth information of pixel (x_m, y_n) in the sub-image. Only the positive part of the depth axis is shown. The high amplitude of DC peak can mislead the peak detection algorithm to identify the desired peak (from depth $z = z_0(x, y)$)

The process of extracting the 1-D intensity signal $I(x_m, y_n, k)$ is repeated for all the other pixels in the sub-image until the map of optical path length for every pixel in the sub-image has been constructed.

5.4. Background pedestal removal

During the data processing of real data it was later found that not only the DC term needed to be removed, but also other low frequency components that are systematically present in the interferogram signal. These components arise from the spectral distribution of the SLED, which varies slowly across the k -axis and appears as a peak located close to the DC location in Fourier domain.

As an illustration, the intensity data at sampled point of k of a pixel $I(x_m, y_n, k)$ shown in Fig.5.3.(a) is presented again in Fig.5.4.(a), and Fig.5.4.(b) is the Fourier transform output of $I(x_m, y_n, k)$ after the DC term removed. Compared to Fig.5.3.(b) the DC term removal eliminates the zero frequency peak, yet an undesired peak still appears nearby the zero frequency location (shown as the first peak in the left in Fig.5.4.(b)). In this example the undesired peak has lower amplitude than the desired peak at $z = z_0(x_m, y_n)$. This situation,

however, cannot be guaranteed to exist in every measurement, which can mislead the peak detection algorithm in locating the correct depth peak.

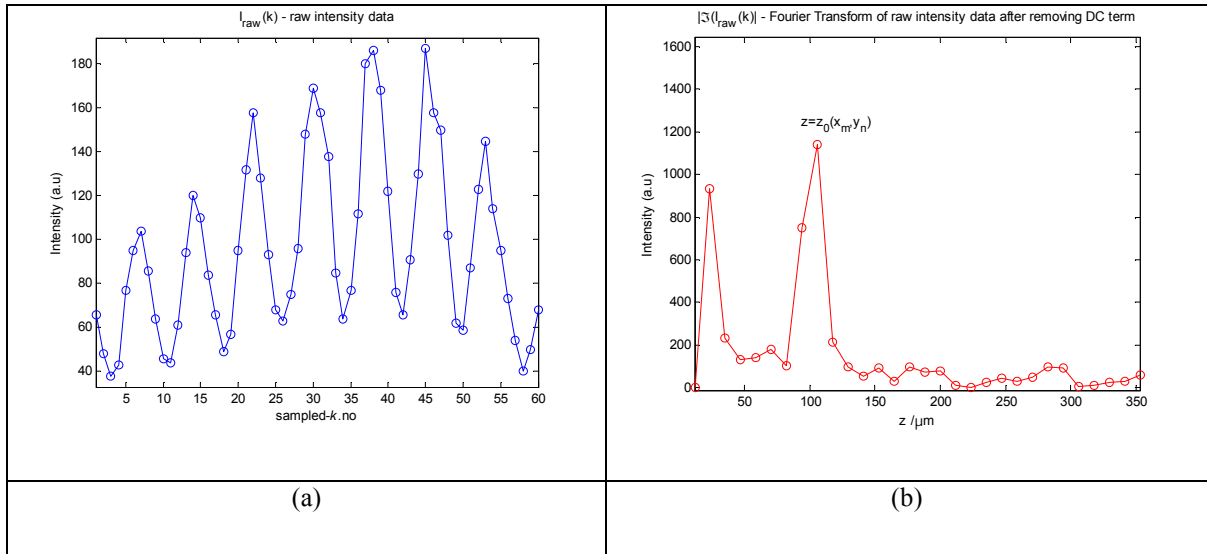


Figure 5.4.(a) The (raw) data of intensity at sampled points of k transform of $I(x_m, y_n, k)$ as shown in Fig.5.3.(a), (b) The Fourier transform result of $I(x_m, y_n, k)$ after removing the DC term still leaves another low frequency peak due to the spectral distribution of the light source (left peak), which can mislead the peak detection algorithm in locating the desired peak (right peak)

To alleviate this problem an algorithm proposed by Huntley [150] was applied. The algorithm requires separate intensity data for object and reference. A separate hyperspectral image volume of the object wave and reference intensity, denoted by $I_o(x, y, k)$ and $I_r(x, y, k)$, respectively were recorded. The next stage is to carry out sums of both intensity data defined as

$$s_1(x_m, y_n) = \sum_{p=0}^{N_k-1} I(x_m, y_n, k_p)$$

$$s_2(x_m, y_n) = \sum_{p=0}^{N_k-1} [I_o(x_m, y_n, k_p) + I_r(x_m, y_n, k_p)], \quad (5-4)$$

where N is the number of sub-images in the hyperspectral volume stack. The sums are the zero-frequency Fourier components of the sampled interference signal and dc pedestal, respectively. The new intensity data, called the mean-free signal $I_2(x_m, y_n, k_p)$ with signal pedestal removed, can be obtained by using the same separate hyperspectral intensity volume of both reference and object and the sums defined in Eq.5-4 as follows:

$$I_2(x_m, y_n, k_p) = I(x_m, y_n, k_p) - (s_1 / s_2) [I_o(x_m, y_n, k_p) + I_r(x_m, y_n, k_p)] \quad (5-5)$$

The result of applying the correction method above to the recorded interferogram is shown in Fig. 5.5. The left column of Fig.5.5 is the interferogram signal before the correction took place, which contains the plots from Fig.5.4. The plots are re-displayed to show the comparison of the result after the correction method was applied in the right column.

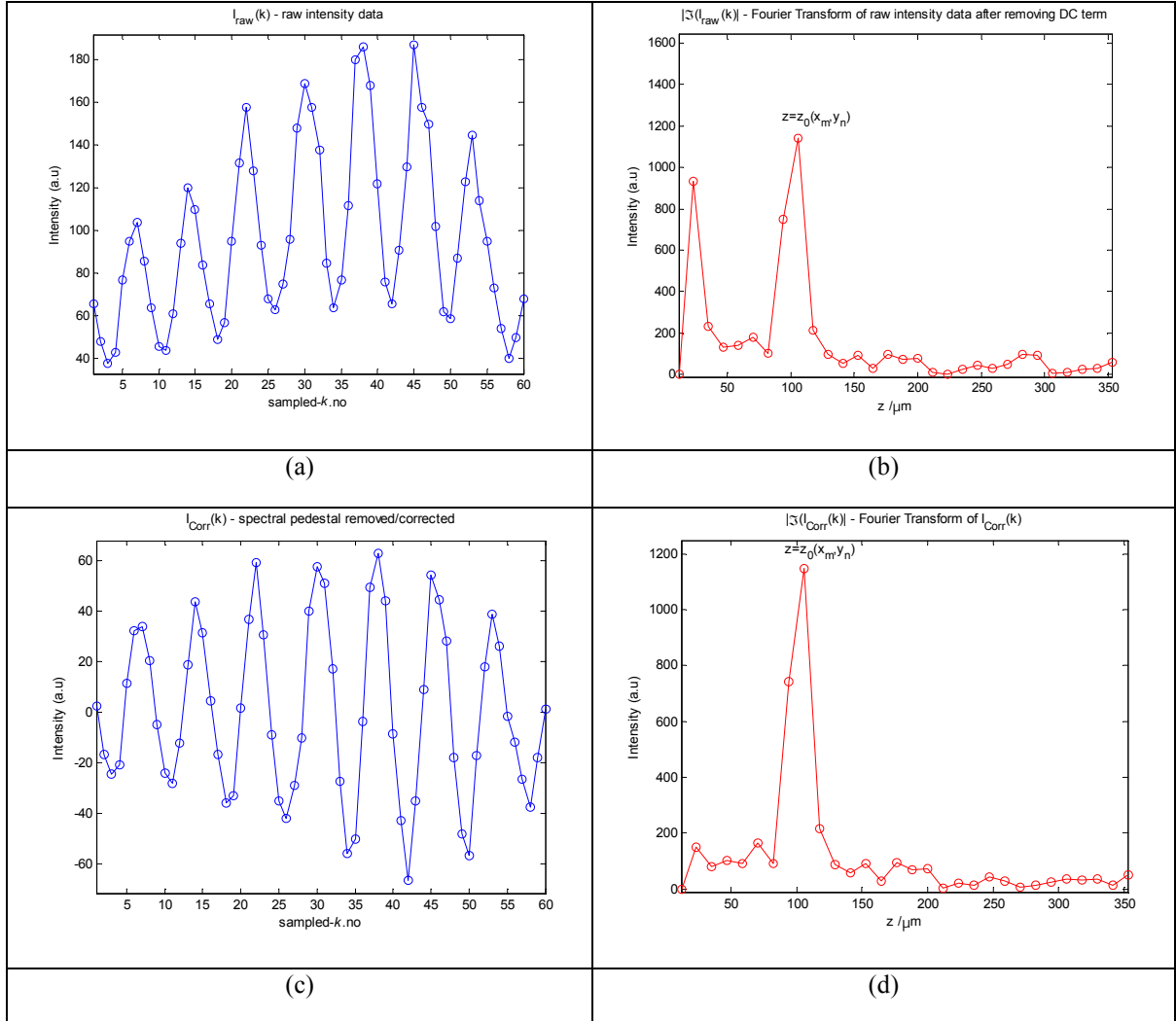


Figure 5.5..(a) and (b) are $I(x_m, y_n, k)$ and its Fourier transform as shown in Fig.5.4 which are re-displayed for comparison purpose, (c) $I_2(x_m, y_n, k)$ – the corrected $I(x_m, y_n, k)$ after the DC and spectral pedestal terms removed and (d) the corresponding Fourier transform of $I_2(x_m, y_n, k)$ which shows only one expected depth peak at $z = z_0(x_m, y_n)$

Comparison of the Fourier transform (lower row plots) shows that after the correction, the first peak was almost completely removed. As there was only one peak after the correction the peak detection routine now will detect the correct frequency peak.

5.5. Derivation of system's parameters

In any surface or depth profilometer system, depth range along with depth resolution are two of the most important parameters to indicate the system's performance. Depth range can be derived by applying Shannon's sampling theorem to the interferometer signal of Eq.5-1. The theorem sets the condition of adequate sampling of the $I(x_m, y_n, k)$ signal by stating that the change of the phase $\phi = kz(x, y)$ should not exceed π between two adjacent k samples. This leads to the maximum allowed value z_M

$$z_M = \frac{\pi}{\delta k}, \quad (5-6)$$

where δk is the separation between sample points along the k axis (which is also equal to the etalon's FSR in k axis). Using the relation $k = \frac{2\pi}{\lambda}$, the (absolute) value of δk can be

found as $\delta k = \left| \frac{2\pi}{\lambda^2} \right| \delta \lambda$. Substituting the values of λ and $\delta \lambda$ with the center wavelength of the

SLED light of 840 nm and etalon's FSR of 0.5 nm, respectively, δk is found to be $4.45 \times 10^{-3} \mu\text{m}^{-1}$. Using Eq.5-6, the calculated value of z_M is 705.6 μm . Since the beam travels the path twice due to the reflection from the surface, the depth range of the set-up is $z_M/2 = 352.8 \mu\text{m}$.

Values larger than z_M will be aliased onto lower z values thereby creating an under-sampling artefact. Due to the use of half of the z axis, the minimum allowable value of z is $z=0$. The depth range or the allowable path difference range is thus

$$0 \leq z \leq z_M. \quad (5-7)$$

Simulations have been carried out to illustrate the sampled $I(x_m, y_n, k)$ distribution at two z values $z = 0.23z_M$ and $z = 0.65z_M$ for a given $N_k = 16$ and a total k bandwidth Δk equal to 20% of the centre k value. The simulation results are shown in Fig.5.6. The corresponding Fourier transforms $\tilde{I}(x_m, y_n, z)$ are shown in Figs 5.7 (upper and lower), respectively.

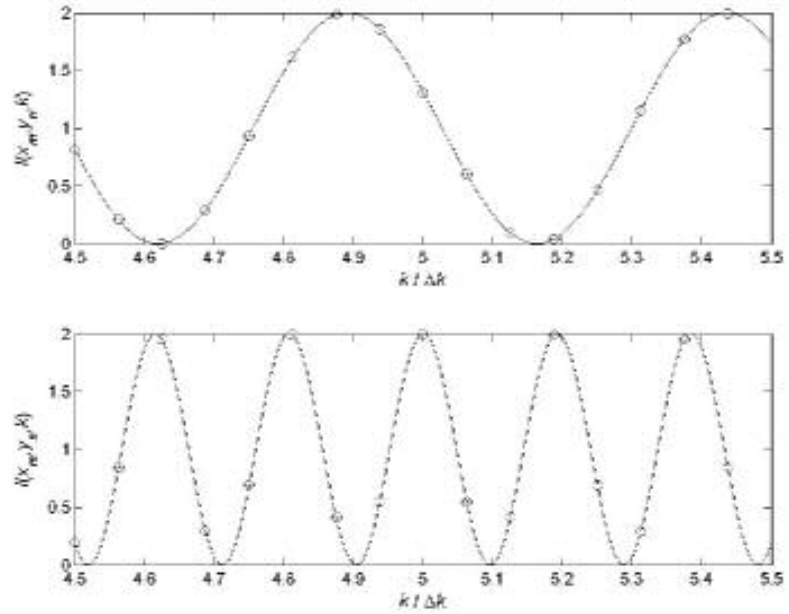


Figure 5.6. Simulation result of 1-D signal $I(x_m, y_n, k)$ from Fig. 5.2 for the two cases $z = 0.23z_M$ (top) and $z = 0.65z_M$ (bottom). Open circles indicate the sampled values $k = k_p$. (figure taken from Ref [38])

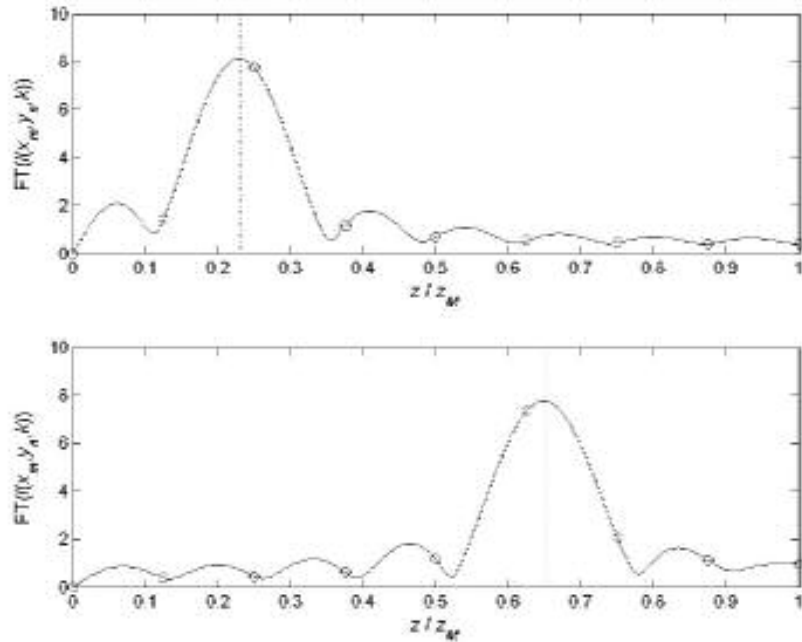


Figure 5.7. Fourier transform $\tilde{I}(x_m, y_n, z)$ of the two 1-D signals $I(x_m, y_n, k)$ from Fig. 5.6. Open circles indicate the sampled z values, and the vertical dotted lines indicate the position of the true z values used to generate the signals in Fig. 5.7 (figure taken from Ref [38])

As shown in Sect.5.3, $I(x_m, y_n, k)$ is sampled from N_k sub-images. From the sampling theorem the corresponding number of frequency points is $N_k/2$. When the fringe frequency

reaches $N_k/2$, the maximum frequency before aliasing occurs, the optical path is equal to z_M . Thus $N_k/2$ frequency points correspond to optical path $z=z_M$. Therefore the depth or optical path resolution δz is the separation between sample points

$$\delta z = \frac{(\pi / \delta k)}{(N_k / 2)} = \frac{2\pi}{N_k \delta k} . \quad (5-8)$$

If the spectral profile of the light source is uniform with the width of $N_k \delta k$ then the width of the spectral peak (i.e., separation between zero crossing points) is $2\delta z$. In the case of a non-uniform spectral distribution with a profile of $W(k)$, then the width of the peak is the width of $\tilde{W}(k)$. In general the width of the spectral peak can be written as

$$\delta z' = \eta \delta z , \quad (5-9)$$

where η is a constant that takes the value 2 for a rectangular window, and 4 for a Hanning window for example. Using Eq.5-8 the HSI system has depth resolution of 11.4 μm , or with the assumption $\eta=2$ using Eq.5-9 yields $\delta z' = 22.8 \mu\text{m}$.

5.6. Depth resolution improvement

The depth resolution however can be improved over the values given by Eqs.5-8 and 5-9. This has been illustrated in Fig. 5.7. The continuous line is the value of the Fourier transform evaluated at a much finer set of k values than the discrete set provided by the fast Fourier transform (shown as circles). Clearly, in the absence of noise, the peak lies much closer to the true z value (shown as dotted lines) than the value of δz (the distance between two adjacent discrete sample points) would suggest. The improvement in resolution could be carried out for example by zero padding the intensity line $I(x_m, y_n, k)$ so that sub-pixel resolution can be achieved in the frequency domain. However, better methods exist as will be described here.

In this research the algorithm to detect the peak to sub-pixel precision was based on the method from Huntley [150]. which was a 2-D version of the sub-pixel peak detection algorithm proposed by Kaufmann et al. [151]. Details of the algorithm are given in Ref

[150] but in general the algorithm improves the precision of the peak location using the Newton-Raphson method. This numerical method is widely used to find roots of a function by using the first derivative of the function, which can be expressed as

$$x_{n+1} = x_n - \frac{f(x_n)}{f'(x_n)}, \quad (5-10)$$

where x is the approximate location at which $f(x)=0$, $f'(x)$ is the first derivative and the subscript of x refers to the iteration index [152]. Since the extreme points such as a peak in a function has first derivative equal to zero the problem becomes finding the roots of the first derivative. The iteration in Eq.5-10 becomes

$$x_{n+1} = x_n - \frac{f'(x_n)}{f''(x_n)}, \quad (5-11)$$

where $f''(x)$ is the second derivative of the function.

In this problem the function is $|H(k)|^2$ - the squared magnitude of the Fourier transform of $I(x_m, y_n, k)$, and k is the Fourier domain variable. Eq.5-11 therefore becomes

$$k_{n+1} = k_n - \frac{\frac{\partial}{\partial k_x} |H(k_n)|^2}{\frac{\partial^2}{\partial k_x^2} |H(k_n)|^2}, \quad (5-12)$$

where subscript n refers to the n^{th} iterations. The details of the derivation of the first and second derivative of $|H(k)|^2$ are given in the appendix of Ref [150]. The iteration in Eq.5-12 continues until the change of k_x is less than a given tolerance.

The probability of the Newton-Raphson method's convergence however will improve if the inputted initial value is close to the real root of the function [152]. In this peak search case, the convergence is almost guaranteed since the initial value is already the peak location of lower accuracy.

Chapter 6

Experimental result 1:

Single-shot opaque surface profilometry

6.1. Introduction

The first test to evaluate the performance of the etalon-based hyperspectral interferometry prototype was to perform a 3-D shape measurement of an opaque object. The prototype was first tested using the reflective step profile similar to that described in detail in Sect.3.2.5. With a step height of 120 μm , the object height is within the system's depth of range of 353 μm (calculated in Section 5.5). The prototype was subsequently tested to measure the height distribution of a rough flat (non-step) surface.

6.2. Reflective planar imaging

In order to experimentally verify the two main system parameters calculated in Chapter 5, the depth range and depth resolution, the HSI prototype was tested using a reflective planar surface described in Sect.3.2.5. This flat surface was obtained using the step height sample by transversally shifting the object until the abrupt height change of the step was out from field of view and the interferometer now only imaged one of the planar sides of the sample. In this experiment the lower side of the sample was used

6.2.1. Depth range and resolution

Fig.6.1 shows the coordinate reference system for the profilometry measurements. The analysis developed in Sect.5.5 will be used again here. As described in Section 2.1, an optical path distribution measurement using a hyperspectral interferometry system provides an absolute height distribution, thereby resolving the height ambiguity problem commonly encountered in the single wavelength counterpart. In Fig.6.1 the surface (local) height distribution $h(x,y)$ is illuminated and observed from above. The optical path difference is therefore twice the local distance of the sample from the surface of zero optical path difference L (see Fig.6.1). In order to be consistent with Ref [38], the paper to which this section refers to, the optical path difference is denoted by z , instead of S as shown in Chapter 2, and given as

$$z = 2[h_0 - h(x, y)], \quad (6-1)$$

where h_0 is the known distance from the sample datum surface to the plane of zero optical path difference. The local sample height $h(x, y)$ is measured relative to the datum.

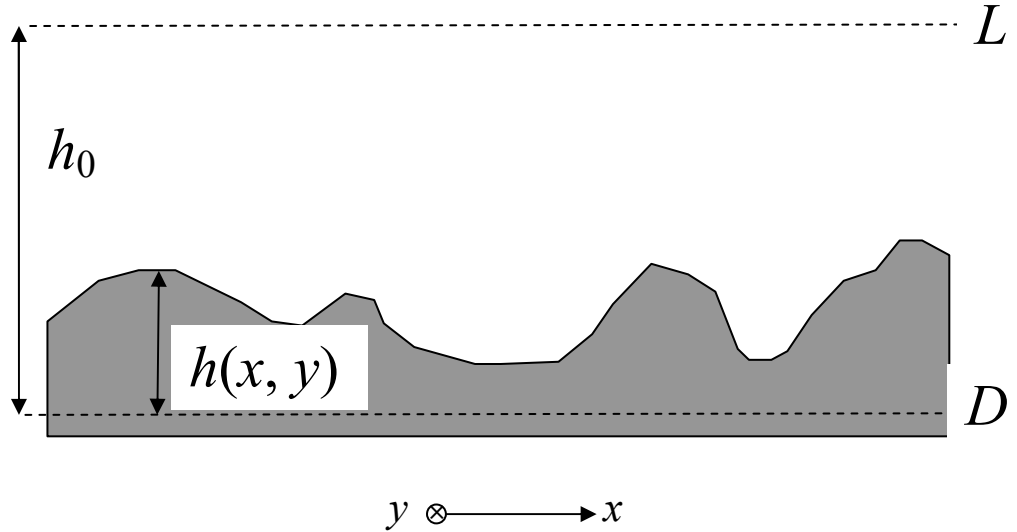


Figure 6.1 .Cross-section of a sample with height distribution $h = h(x, y)$. Lines L and D are cross-sections through the zero path difference and sample datum surfaces respectively (figure taken from Ref [38])

The condition to be met to obtain the absolute optical path difference is that the object surface lies within the height measurement range, Δh . This can be derived by substituting the depth range expression in Eq.5-6 into Eq.6-1 to yield

$$\Delta h = \frac{z_M}{2} = \frac{\pi}{2\delta k}. \quad (6-2)$$

Similarly the expression for depth resolution follows from Eqs. 5-8 and 5-9 as

$$\delta h' = \eta \delta h, \quad (6-3)$$

with

$$\delta h = \frac{\pi}{N_k \delta k} . \quad (6-4)$$

6.2.2. Experimental verification of depth range

The system's depth range was verified experimentally using the planar surface object. The sample was moved along the optical axis of the interferometer with an increment of 50 μm using a translation stage. A hyperspectral image volume was recorded at each position and analysed using the algorithm described in Chapter 5 on data processing. Fig. 6.2 shows an example of a 1-D plot of the interferogram signal $I(x_m, y_n, k)$ from one pixel. In the figure is the $I(x_m, y_n, k)$ signal from the centre of the field of view (centre pixel of a sub-image) taken at different (increasing) optical path differences from plot (a) to (c). The plots in the figure, however, are before undergoing the background pedestal removal as detailed in Section 5.4. Fig.6.3 shows the signal plots of Fig.6.2 after background pedestal removal. Note that on both Figs.6-2 and 6-3 the oscillation frequency increases as the optical path difference increases as well, which has been derived in Eq.2-34.

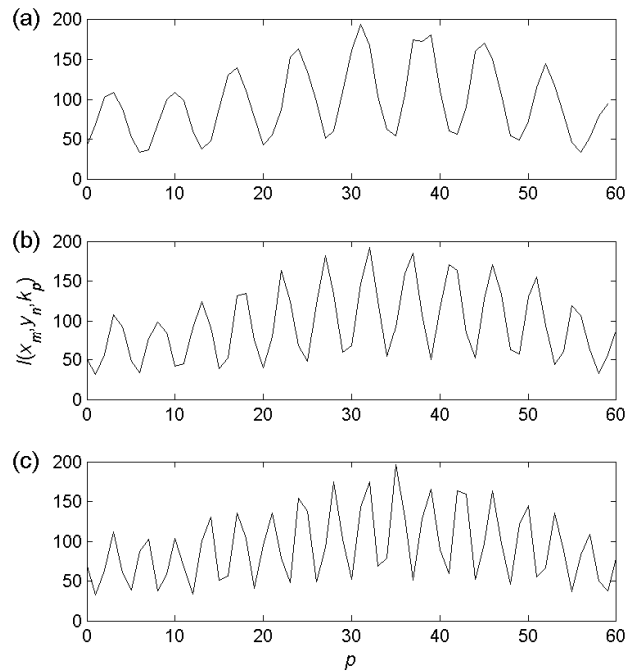


Figure 6.2. Plots of 1-D interferogram signal $I(x_m, y_n, k)$ of the centre pixel in a sub-image taken at three different (increasing) optical path differences (figure taken from Ref [38])

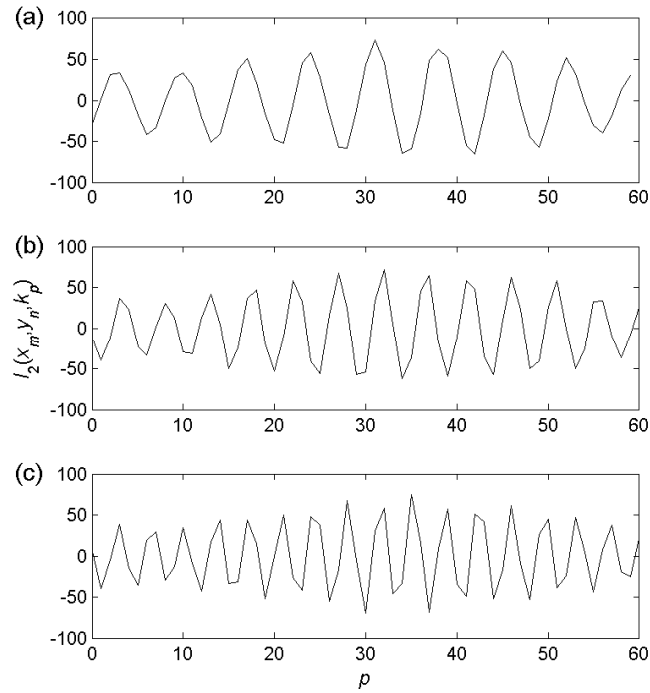


Figure 6.3. Plots of 1-D interferogram signal $I(x_m, y_n, k)$ of Fig.6.2 after background pedestal removal (figure taken from Ref [38])

Figure 6-4 shows the plot of the computed height from $I(x_m, y_n, k)$ of a pixel at the centre of the field of view (centre pixel of a sub-image) versus the known position of the translation stage. Positions denoted by (a), (b) and (c) correspond, respectively, to the three parts (a), (b) and (c) of the plots in both Figs.6-2 and 6-3.

As the stage moves away from the zero OPD position, the fringe frequency increases. When the frequency reaches the Nyquist limit, however, further movement causes aliasing and the apparent fringe frequency starts to drop until a uniform intensity appears across the sub-images, indicating that the zero frequency point has been reached. If the stage is translated further the fringe frequency starts to climb again and the same fringe appearance repeats itself. This results in a ‘saw tooth’ characteristic of the plot.

The proportionality of fringe frequency to optical path difference gives the same plot appearance when the data is converted to height variables. Similarly, as the object moves outside the range $0 < (h_0 - h) < \Delta h$, the peak in the spectrum is aliased giving rise to an erroneous position estimate. The linear response over the range $0 < (h_0 - h) < \Delta h$ is therefore modified outside this range to give a characteristic ‘saw tooth’ shaped response curve that is apparent in Fig. 6.4. It can be clearly seen that the height span in which the

reading reaches the upper and lower inflection points is around $350 \mu\text{m}$. This span is equal to the depth range which is the experimental result close to the calculated depth of range of $353 \mu\text{m}$ as derived in Sect.5.5.

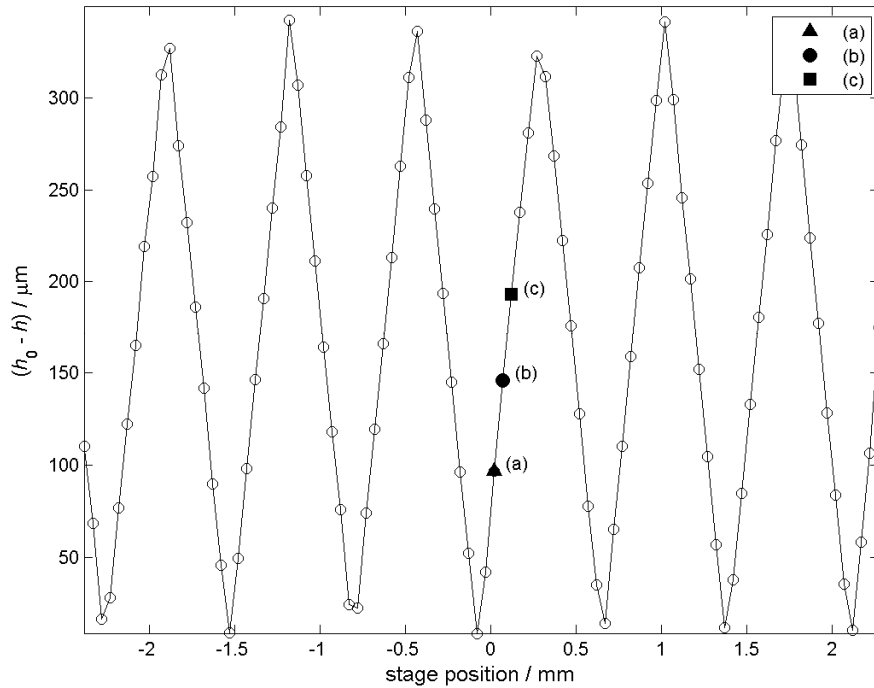


Figure 6.4. Measured position of one point on planar sample versus known sample position. Points (a) – (c) correspond to the locations of the plots displayed in Figs 6.2 and 6.3 (figure taken from Ref [38])

6.2.3. Error measurement

At three locations marked by (a) – (c) in Fig.6.4 the height distribution of the surface is shown in Fig.6.5. Each point in the plot has been obtained completely independently from the other points, without any data smoothing.

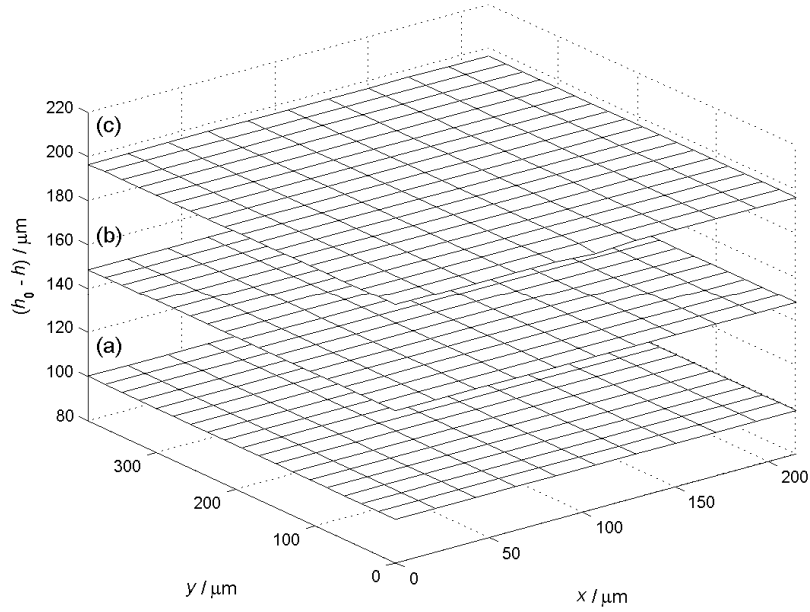


Figure 6.5. Measured surface profile for the planar sample when at locations marked as (a)-(c) of Fig. 6-4 (figure taken from Ref [38])

Measurement noise was estimated by fitting a plane to each of these three surfaces by

$$\sigma = \sqrt{\frac{(h^{\text{exp}} - h^{\text{fit}})^2}{N_k}}, \quad (6-5)$$

where σ is the rms noise, h^{exp} , h^{fit} and N_k is the experimental height distribution, the fitting plane and the number of sub-images, respectively. The root mean square (rms) of the residual about the best fit planes was 111, 73 and 119 nm for locations (a) – (c) respectively, with an overall rms residual of 103 nm. The results are shown in Fig.6.6.

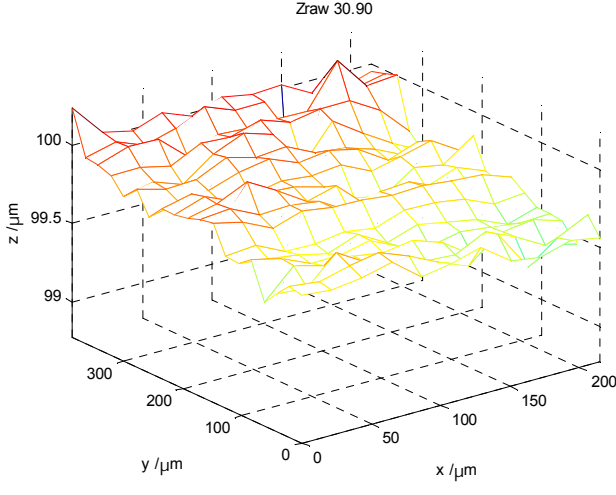
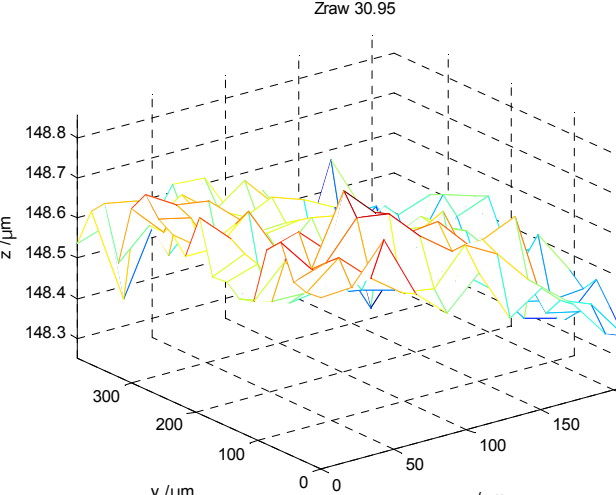
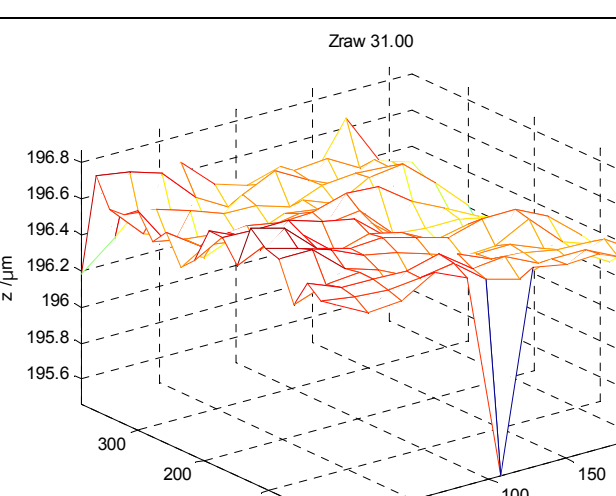
	Stage Pos. (mm)	h^{exp}	rms value (nm)
(a)	30.90		110.8
(b)	30.95		72.9
(c)	31.00		118.8

Figure 6.6. The height distribution measurement result and the corresponding fitting planes for the planar sample when located at positions marked (a)-(c) of Fig. 6.4.

The data however has one outlier for locations (a) and (c). After removing these outliers the rms residual drops to 78 and 92 nm, respectively, with an overall rms for the three planes of 81 nm.

This figure is higher than the values of order 1 nm (or less) typically achieved by SWLI. There are several reasons for this which may be summarized as follows. Firstly, not all the SLED bandwidth is used in the measurement. With average of 60 sub-images in which each occupies 0.5 nm, the total used bandwidth is only $60 \times 0.5 = 30$ nm, or only 60% of the total SLED bandwidth of 50 nm. This bandwidth is around an order of magnitude lower than that typically used in SWLI. Depth resolution scales inversely with bandwidth so one can expect a factor of $10\times$ worse performance due to this factor alone. Secondly, spatial variations in photodetector sensitivity have not been taken into account so far. These variations will introduce apparent noise in the measured profiles in the case of hyperspectral interferometry, but not for SWLI, because in the latter case the same pixel provides all the data for a given point on the sample. This effect could be significantly reduced by appropriate calibration of the image sensor.

6.3. Smooth surface step height profiling

The HSI set-up was subsequently used to measure the smooth surface step height sample. The sample is similar to the object described in Sect.3.2.5. An interferogram of the object is shown in Fig.6.7. A set of 62 sub-images of 11×19 pixels each are formed across the horizontal axis of the CCD camera C_1 (see Fig.4.7). Three selected sub-images are shown magnified as in inset to Fig. 6.7. The step is visible as a vertical discontinuity in the fringe patterns passing approximately through the centre of the field of view. The presence of the discontinuity causes a relative shift of the fringes with changing k , which is clearly visible in these three sub-images. To the right of the step, there are around three fringes that remain almost stationary from sub-image to sub-image indicating that this part of the sample surface is close to the zero OPD position. To the left of the step, there is one broad diagonal fringe that moves downwards as one moves from one sub-image to the next.

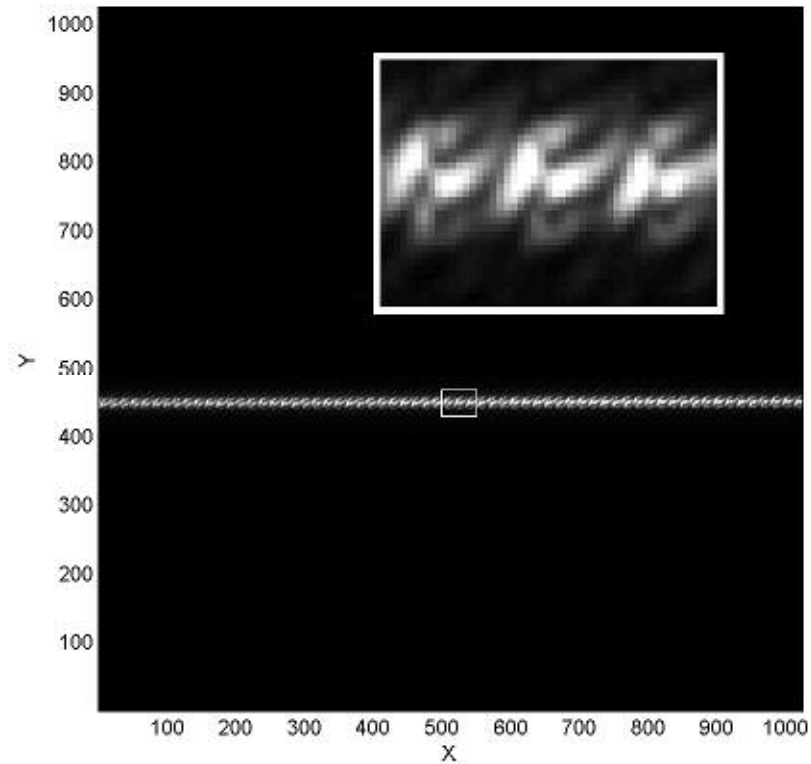


Figure 6.7. Interferogram of a step height surface spread across the horizontal axis of camera C1 (see Fig.4.8 for set-up details), containing 62 hyperspectral images within a single frame. Inset: three of the hyperspectral images within the central white box enlarged by a factor of 10× (figure taken from Ref [38])

After analysis of the raw data using the calculations described in Chapter 5, the height distribution of the step height sample is shown in Fig.6.8. The height difference between the two sides of the step can be clearly seen. The calculated height difference was 115 μm , which is close to the true value of 120 μm found from the microscope inspection method described in Section 3.2.5.

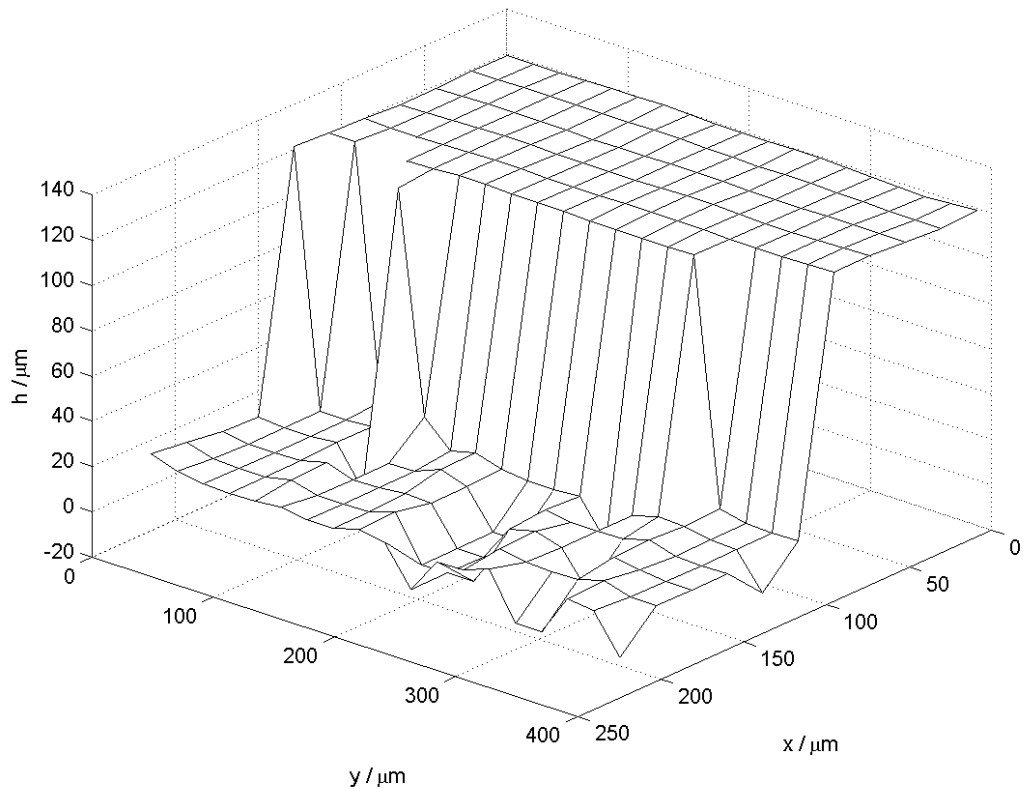


Figure 6.8. Surface profile of the step height sample on a 11×19 pixel grid measured in a single shot using the etalon-based HSI system (figure taken from Ref [38]).

6.4. Rough surface measurement

The next test of the prototype for profilometry application was to measure height distributions of rough surfaces. As opposed to the smooth surfaces considered earlier, the random height distribution of this type of surface will produce speckles in the image if the height fluctuations are a significant fraction of the wavelength or more. Compared to the reflective surface case, it can therefore be predicted that the rms values of this type of surface will be higher.

The sample used in this test was an aluminium block spray painted with white metallic paint. This type of paint contains very fine scattering particles. The surface finish of the sample is shown in Fig. 6.9.



Figure 6.9. The sample used for the rough surface measurement test consisting of an aluminium block spray painted with white metallic paint

6.4.1. Filtering the reconstructed height distribution

The speckles produced by the random height distribution from a rough surface result in a non-uniform amplitude distribution across the wavefront, resulting in non-uniform intensity response across the photosensitive area. In turn the height distribution, which was the output of the Fourier transform operation of the detected $I(x,y,k)$, will also be non-uniform. It can be expected that some form of spatial ‘speckle averaging’ will be needed to provide useful data at pixels whose object beam amplitude is close to zero.

The filtering was carried out by a weighted averaging of the original height distribution. If the output of the filtering operation and the original height distribution are denoted by $h_s(x,y)$ and $h(x,y)$, respectively, both distributions are related by

$$h_s(x,y) = \frac{\left(|H_p(x,y)|^2 h(x,y) \right) \otimes o(x,y)}{|H_p(x,y)|^2 \otimes o(x,y)}, \quad (6-6)$$

where notation \otimes denotes the convolution operation, $o(x,y)$ is the smoothing kernel (which in this work was a 3×3 matrix with each matrix entry equal to one) and $|H_p(x,y)|$ is the *magnitude* of the peak (peak height) from the Fourier transform of $I(x,y,k)$. As described in section 5.2 of Chapter 5, $z(x,y)$ is proportional to the *location* of the peak in the Fourier transform of $I(x,y,k)$, and the magnitude of the peak $|H_p(x,y)|$ is proportional to the *height* of the peak. The smoothing kernel $o(x,y)$ was convolved with both the

weighted height map and the peak magnitude (the nominator and denominator of Eq.6-6, respectively) to obtain spatial smoothing of both terms prior to calculating the smoothed height distribution. Data points with higher modulation are therefore given greater weight than those with lower modulation. The reason for this choice of weight is that theoretically one should weight the data inversely with the variance of the quantity being averaged. In this case the signal strength is proportional to $|H_p(x,y)|$ and therefore it seems a reasonable assumption that the variance of a given z value scales inversely with $|H_p(x,y)|^2$.

The result of the smoothing process from one height map of the painted surface is shown in Fig.6.10. The filtered result is presented along with the original height distribution prior to smoothing for comparison. The rms values before and after filtering are also shown, which shows the decrease of rms value after the smoothing process by more than 25% of the initial value. The rms values were calculated using the same method for the smooth surface as described Sect.6.2.3.

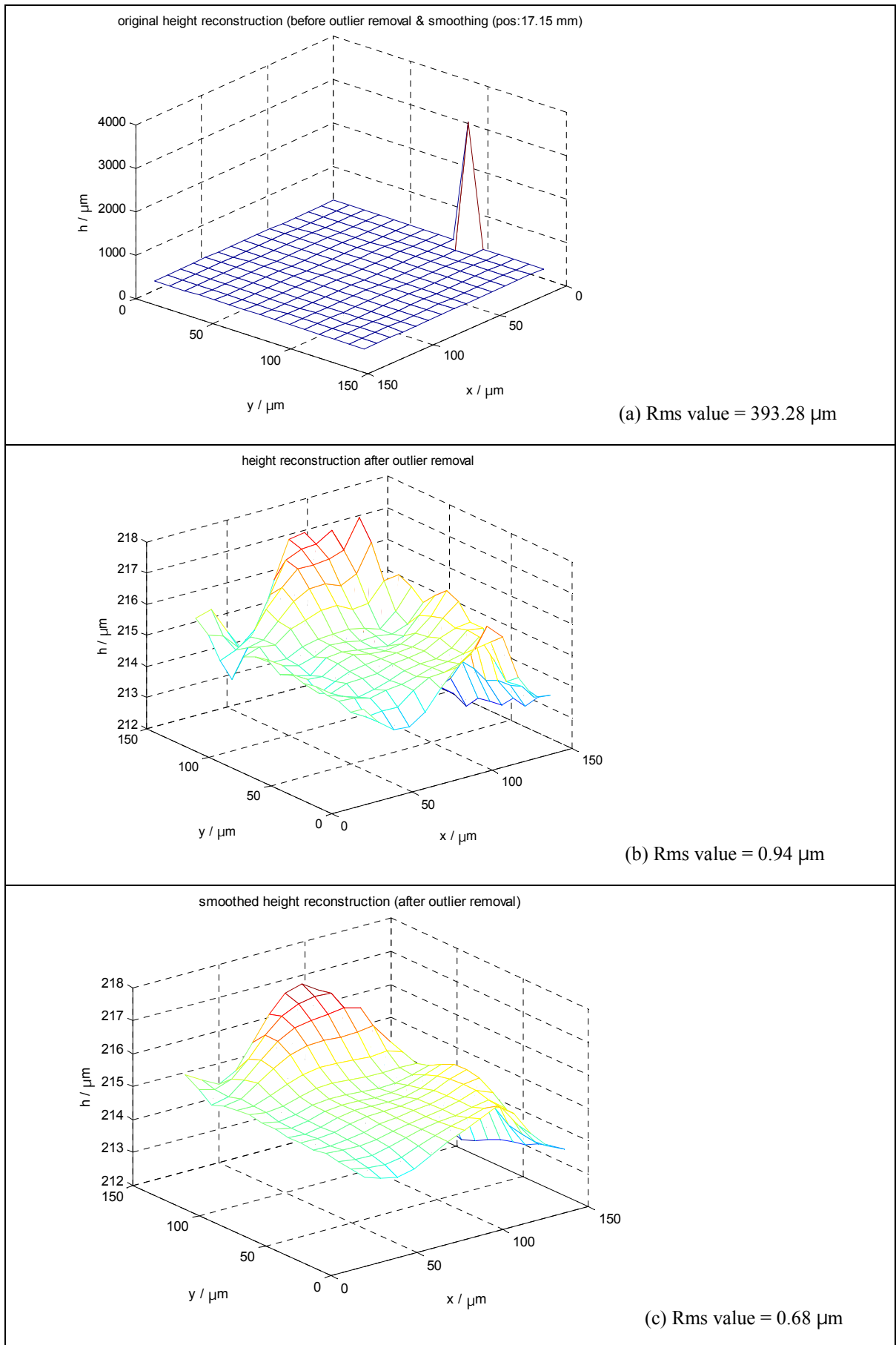


Figure 6.10.(a) Original height map reconstruction with data outliers, (b) height map with data outliers removed and (c) height map after removal of outliers followed by smoothing

6.4.2. Reconstructed height map of the samples

Similar to the smooth surface in Sect.6.2.3, the rough surface object was also measured at three known stage positions. The positions were 17.05, 17.10 and 17.15 mm. One example of the recorded interferogram and object image is shown in Fig.6.11. These images were taken at the stage position of 17.15 mm.

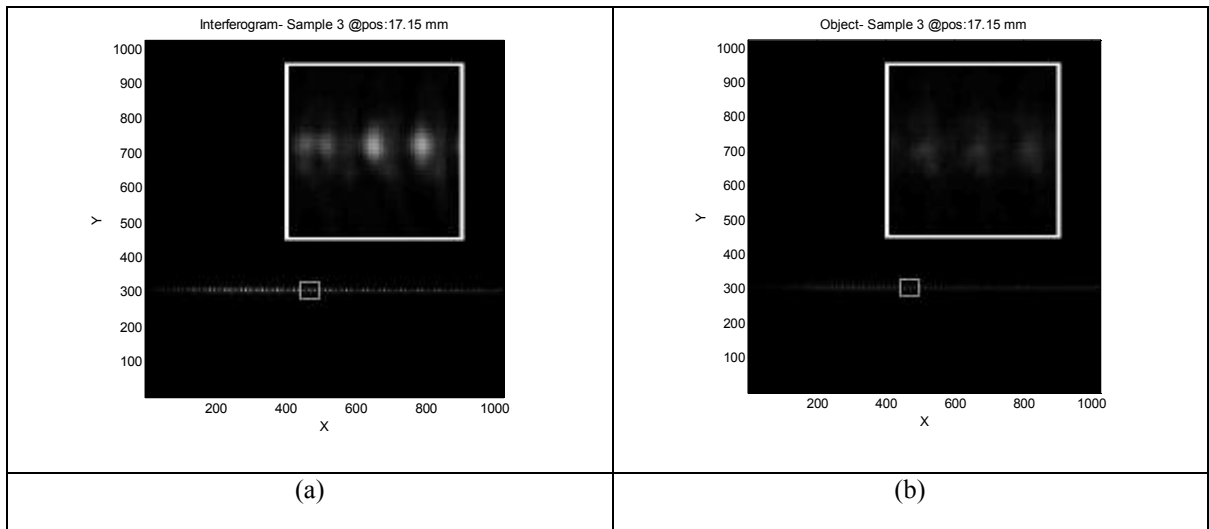


Figure 6.11. Example of the (a) interferogram and (b) object wave of the rough surface sample. Both images were recorded at the same stage position of 17.15 mm

Outlier data was also found in the reconstructed height at position 17.10 mm. After removal of this data and filtering (data smoothing) the reconstructed height at 3 stage position was constructed and shown in Fig.6.12. The rms values improved significantly, from 0.59, 3.67 and 77.31 μm (with average of 27.19 μm) prior to outliers removal, down to 0.59, 0.71, 0.69 μm (average value = 0.66 μm) after the outlier removal for positions 17.05, 17.10 and 17.15 mm, respectively.

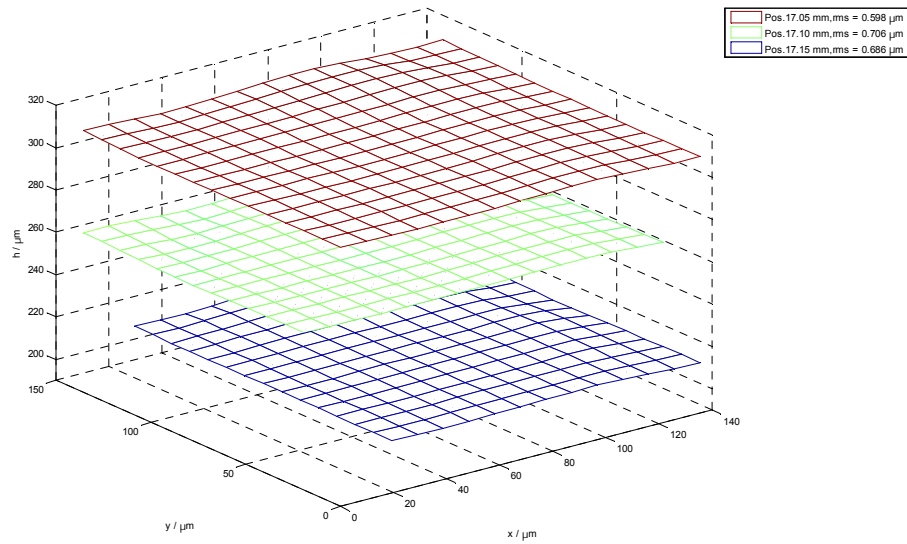


Figure 6.12. The smoothed height distribution of the painted sample at Fig. 6.9 after removing the data outliers (figure taken from Ref.[153])

The rms values from the painted surface are almost an order of magnitude higher than from the smooth surface described earlier. The possibility that this is due to the sample having significant deviations from a non-planar geometry over the field of view was therefore investigated. This was carried by subtracting the mean value for each surface, leaving only the height variation across the surface as shown in Fig.6.13. For the purpose of clarity in displaying the result, the height variation in Fig.6.13 is limited only from -1 to 2 μm . A noticeable group of pixels is present in the top right of the image recorded at position 17.05 mm (roughly spanning the region between 70 – 110 μm and 100 – 120 μm in the x and y directions, respectively). The height of this group of pixels spans roughly the same range of between 1.5 and 2 μm for all stage positions, confirming these pixels as a feature on the surface of the sample. The location of this feature however moves slightly with the change of stage position, suggesting that an unwanted lateral shift occurred during the axial translation of the stage.

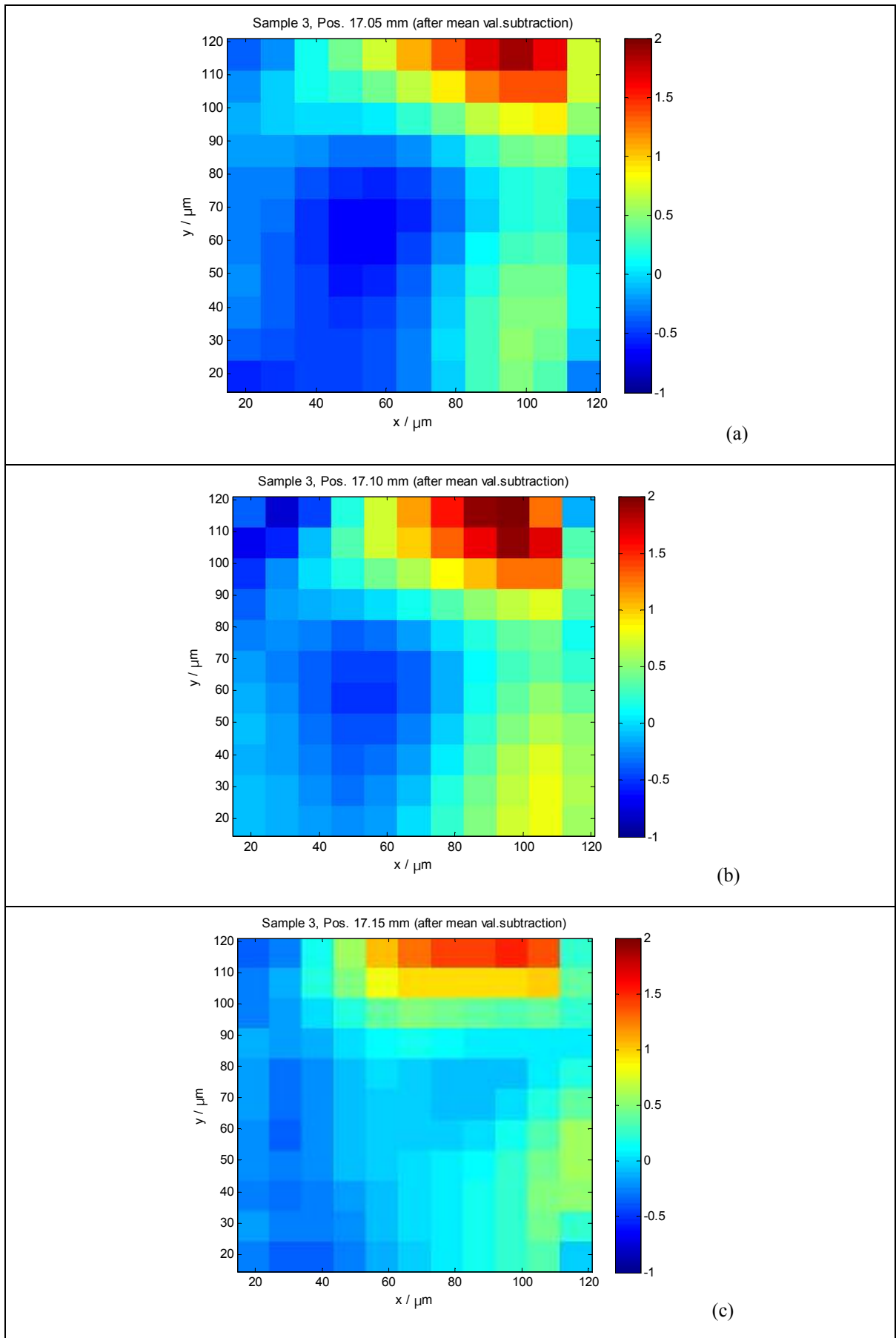


Figure 6.13. The reconstructed height maps of the painted sample after subtraction of the mean height value for stage positions (a) 17.05, (b) 17.10 and (c) 17.15 mm (figure taken from (figure taken from Ref.[153])

6.5. Conclusion

The hyperspectral interferometer prototype system has been constructed and experimentally verified to be able to perform the surface profilometry measurement in a single-shot on both optically smooth/reflective surfaces and on optically rough surfaces.

From the test using smooth surfaces, it has been demonstrated that the system is able to perform measurements with an unambiguous depth range of $\sim 350 \mu\text{m}$ and a depth resolution around 80 nm (1 part in 4,000 of the depth range), using a light source with bandwidth of 30 nm and centre wavelength of 840 nm. The experimental unambiguous depth range compares well with the predicted value of $353 \mu\text{m}$.

On the test using the rough sample, the rms height values from imaging flat planes were found experimentally to be significantly larger than the value obtained from the smooth surfaces. The rms of the difference of two height maps (i.e. the difference between maps at positions 17.05 and 17.10 mm, and 17.10 with 17.15 mm, after subtracted with mean value of each surface) is $0.30 \mu\text{m}$. This figure is almost $4\times$ larger than the ~ 80 - nm rms value for optically smooth surface calculated in Sect.6.2.3. Apart from the fact that a rough surface has higher random height fluctuations than the smooth flats, one of the plausible causes of this deviation is the lateral drift of the sample, the fact that the paint to coat the sample is not infinitesimally thin but has a finite thickness so that this layer can act as a volume scatterer, and also the lower amplitude signal due to the ‘dark speckles’ in the object wave [153]. The first factor is possibly due to the angular separation between the lead-screw of the micrometer (that translates the stage) and the optical axis. If this factor is included in the re-alignment of the datasets from two surface positions the error due to this factor can be expected to decrease.

Turning to future improvements, the observation of the recorded frame immediately indicates that the use of the sensor area is very inefficient, i.e. out of a total 1024×1024 ($=1,048,576$) pixels of the array only $62 \times 20 \times 20$ ($=24,800$) pixels are used. This means only less than 2.5% of the total area of the CCD is in use. Further work should therefore include a more efficient use of the sensor array area so that more spectral sub-images (or a similar number but with higher spatial resolution) are recorded in a single frame. Techniques for spatially multiplexing images have been reported, for example a technique proposed by Subhash et.al by using a combination of polarized beams and 4 channel polarization phase stepper optics [113]. Such a method could be applied to improve the

spatially efficiency that can increase the number of sub-images recorded on a frame, which in turn would increase the system's depth of range. The depth measurement precision of 80 nm on smooth surfaces could also be improved through the use of light with a greater bandwidth, and by calibrating the sensor to account for spatial variations in pixel sensitivity. Such improvements would be beneficial in order to help close the gap with SWLI systems, which can have sub-pixel depth-resolution. Despite the currently lower accuracy value compared to SWLI, the proposed approach does have the important benefit of single-shot data acquisition, thereby offering the potential to reduce vibration-induced artefacts given a sufficiently short exposure duration.

Chapter 7

Experimental result 2:

Depth (sub-surface)-resolved displacement measurement

7.1. Introduction

The next test to evaluate the performance of the (etalon-based) hyperspectral interferometry set-up is to perform single-shot depth (sub-surface)-resolved 3-D displacement measurement within a weakly-scattering medium.

Compared to the previous application to surface profilometry this experiment was more challenging and difficult. Despite the use of the same optical set-up, the sample and data processing techniques for this experiment are different.

The sample for the profilometry test reported in the preceding chapter was a smooth surface covered with an aluminium coating to create a reflective surface. Instead of reflection only at the surface, for this experiment the sample should be made to be translucent: penetrable by light yet also scattering some of the incoming light. Media such as gels are transparent but do not scatter enough light to be detected by the system. A certain amount of a scattering material must be embedded into the transparent sample to increase the amplitude of the back-scattered light. There is a further requirement that the sample must also be thin enough to meet the one-third to one-half of the depth range requirement. This criterion will be discussed in the upcoming section on the object specification.

In relation to the sample, the rig onto which the sample is mounted must also be modified. Whilst in the previous experiment the purpose of the rig was simply to hold the sample firmly so that it can be illuminated perpendicularly to its surface, for this experiment it must also have a mechanism to provide the deformation to the sample. The deformation was needed to alter the internal structure of the sample which will subsequently be detected by the system.

The different characteristics of the sample subsequently modify the data processing techniques. The highly reflective surface sample in the previous experiment enabled the interferometer to detect more than enough light to saturate the camera even at short exposure durations. The weakly-scattering medium of this experiment implies the detected signal is lower and the data is more prone to be corrupted by noise.

This chapter starts with the brief background theory on the frequency components of the detected signal from a scattering medium. It is an extension to the theory described in Section 5.2 on the interferogram signal for a single scattering surface. Following the description of the theory is a summary of the attempts to manufacture a suitable sample that provides a detectable scattering signal for the experiment, and the corresponding loading rigs. Additional methods, to reduce some of the problems due to the low-level signal, developed from the techniques to process data in Chapter 5, are subsequently described. The chapter concludes with some preliminary single-shot measurements of depth-resolved displacement fields using the etalon-based hyperspectral interferometer.

7.2. Signal analysis of scattering medium

The profilometry experiment reported in Chapter 6 measured the surface of the sample. The surface can be considered as the ‘upper’ layer of the sample on which the light falls and is reflected back to the interferometer. In this case the sample can be assumed to be a ‘single scattering layer’ object.

For depth-resolved measurements, however, where the detected light not only is reflected from the surface but also from under the surface material, it is easier to consider this type of sample as a ‘multi layer’ object, as illustrated in Fig.7.1. The internal structure of the sample can be modelled as a stack of layers where the light beam first hits the surface and fraction of the light energy goes further under the surface. Light is scattered by each successive layer and the interferometer captures these back-scattered light waves. In this simplified beam travelling model, the light is assumed to be scattered only once, and then travels back to the interferometer with no further scattering. In fact, inside the material the light can undergo more than one scattering event before reaching the surface again, however a more complicated model is needed to portray such multiple-scattering phenomena. Most of the LCI-based systems such as OCT and WSI are based on a single scattering model where all the light detected by the interferometer is assumed to be due only to a (single) backscattering process [19].

The multiple layer model of a deep object will be now used to analyse the interferometric signal from a scattering sample. The analysis presented in this section is adapted from the derivation of the theory of OCT developed by Izatt and Choma [78]. Assume a semi-transparent sample having N multilayers, with the m^{th} layer with discrete reflection coefficient $r_s(z_{sm})$ located at distance $z = z_{sm}$ from a reference point. For this derivation

the beamsplitter is set as the reference point $z = 0$ for convenience. Assume the incoming electric field of the light has amplitude $\bar{U}_i = u_i(k, \omega)e^{i(\omega t - kz)}$ with $u(k, \omega)$ the amplitude as a function of k and ω , the light reflected from the reference mirror RM expressed as $U_R = \frac{u_i}{\sqrt{2}} r_R e^{-i2kz_R}$ where r_R is the reflection coefficient of the reference mirror and the light from all layers in the sample is the sum of all reflected signal inside the material $U_S = \frac{u_i}{\sqrt{2}} \sum_{m=1}^N r_S(z_{S_m}) e^{-i2kz_{S_m}}$. The detected signal at the detector I_D is with ρ the detector responsivity (in Amperes/Watts).

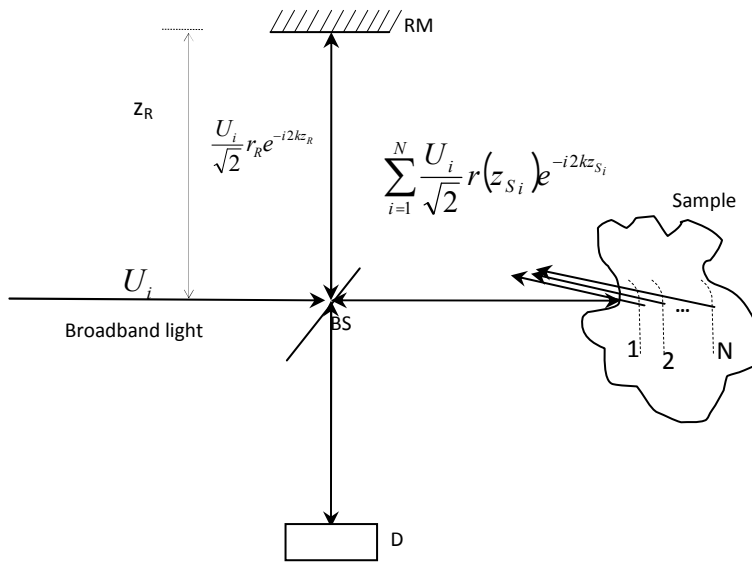


Figure 7.1. Schematic diagram of a finite-depth object measured using LCI system. The finite-depth object is illustrated to be constructed of multiple layers, each of which has reflection coefficient r . D, RM and BS are the detector, reference mirror and beamsplitter, respectively (figure adapted from Ref.[78]).

After substituting the reference and sample fields the expansion of the detector signal reads as

$$I_D(k, \omega) = \frac{\rho}{2} \left\langle \left| \frac{u(k, \omega)}{\sqrt{2}} r_R e^{j(2kz_R - \omega t)} + \frac{u(k, \omega)}{\sqrt{2}} \sum_{m=1}^N r_{S_m}(z_{S_m}) e^{j(2kz_{S_m} - \omega t)} \right|^2 \right\rangle. \quad (7-1)$$

The time averaging operation in Eq.7-1 will drop the temporal component of the field $e^{-i\omega t}$. After expanding the quadratic expression inside the time average parentheses, and using the identity $\cos(x) = 1/2(e^{ix} + e^{-ix})$, Eq.7-1 becomes

$$\begin{aligned}
I_D(k) &= \frac{\rho}{4} [G(k)(R_R + R_{S1} + R_{S2} + \dots)] \\
&+ \frac{\rho}{2} \left[G(k) \sum_{m=1}^N \sqrt{R_R R_{S_m}} \cos[2k(z_R - z_{S_m})] \right] , \\
&+ \frac{\rho}{4} \left[G(k) \sum_{m \neq n=1}^N \sqrt{R_{S_m} R_{S_n}} \cos[2k(z_{S_m} - z_{S_n})] \right]
\end{aligned} \tag{7-2}$$

with $G(k)$ is the spectral distribution of the light ($G(k) = \langle |u(k, \omega)|^2 \rangle$), and R_R is the reflectivity of the reference mirror RM which is related to the reflection coefficient r_R as $R_R = |r_R|^2$. Similarly the reflectivity of the m^{th} layer is $R_{S_m} = |r_S(z_m)|^2$.

As described in Section 5.2 the next step is the Fourier transformation of the interferogram along the k axis. Using Fourier transform relation pairs $\cos(kz) \xleftrightarrow{\mathfrak{F}} \frac{1}{2} [\delta(z - z_0) + \delta(z + z_0)]$ and $x(z) \otimes y(z) \xleftrightarrow{\mathfrak{F}} X(k)Y(k)$, the Fourier transform of the interferogram of Eq.7-2 is

$$\begin{aligned}
i_D(z) &= \mathfrak{F}\{I_D(k)\} \\
&= \frac{\rho}{8} [\tilde{G}(z)(R_R + R_{S1} + R_{S2} + \dots)] \\
&+ \frac{\rho}{4} \left\{ \tilde{G}(z) \otimes \sum_{m=1}^N \sqrt{R_R R_{S_m}} [\delta(z \pm 2(z_R - z_{S_m}))] \right\} , \\
&+ \frac{\rho}{8} \left\{ \tilde{G}(z) \otimes \sum_{m \neq n=1}^N \sqrt{R_{S_n} R_{S_m}} [\delta(z \pm 2(z_{S_m} - z_{S_n}))] \right\}
\end{aligned} \tag{7-3}$$

with $\tilde{G}(z) = \mathfrak{F}\{G(k)\}$ and \otimes denotes the convolution operation.

Using the sifting property of the delta function, Eq.7-3 reads as

$$\begin{aligned}
i_D(z) = & \frac{\rho}{8} \left[\tilde{G}(z)(R_R + R_{S1} + R_{S2} + \dots) \right] \text{"DC terms"} \\
& + \frac{\rho}{4} \sum_{m=1}^N \sqrt{R_R R_{S_m}} \left[\tilde{G}[2(z_R - z_{S_m})] + \tilde{G}[-2(z_R - z_{S_m})] \right] \text{"Cross-correlation term"} \\
& + \frac{\rho}{8} \left[\sum_{m \neq n=1}^N \sqrt{R_{S_n} R_{S_m}} \left[\tilde{G}[2k(z_{S_n} - z_{S_m})] + \tilde{G}[-2(z_{S_n} - z_{S_m})] \right] \right] \text{"Auto-correlation term"}
\end{aligned} \tag{7-4}$$

The first, second and third terms of Eq.7-4 are called the DC, cross-correlation and auto-correlation terms, respectively. Each term contains $\tilde{G}(z)$ -the Fourier transform of the light spectral density $G(k)$ - located at different positions along the depth (z) axis. The quantity $\tilde{G}(z)$ appears as individual peaks in depth z axis, in which the peak positions correspond to the depth of the layer. The location of the first term is at the centre of the axis ($z=0$), and since it corresponds to zero frequency is often called the ‘DC’ component. The second term is due to the interference of the reference beam and the light waves scattered from various layers inside the material. It is the information from this term which is useful for reconstructing the internal displacement map of the sample. The last term is due to the interference between scattered light waves from inside the sample. The separation of the last two terms in Eq.7-4 can be achieved by requiring that the distance between layers inside the sample is small compared to the optical path difference between the reference beam and the light from a layer inside the sample. With this assumption then $(z_{S_n} - z_{S_1}) < (z_R - z_{S_1})$ and therefore the location of $\tilde{G}(z)$ due to second term is farther to the right (with respect to the DC term) than that from the auto-correlation term.

A simpler illustration of the peak distribution along the z axis as derived in Eq.7-4 is shown in Fig.7.2 where it is assumed there were only two layers inside the sample. The desired component (the cross-correlation term) is shown in the figure to be located towards the end of the z axis whilst the DC and autocorrelation occupy the opposite front part of the axis close to $z = 0$. Also Fig.7.2 only shows the positive part of the spectrum whereas in Eq.7-4 both positive- z and negative- z peaks are present. However, as noted in Section 5.2, the negative components are mirror images of the positive ones due to the symmetrical properties of the cosinusoidal nature of the fringes, and thus one side of the axis is sufficient to provide the required information for peak detection. Note that the analysis developed in Eq.7-4 contains no phase information. This is due to the assumption that each depth layer has no initial phase distribution, which is different from other analysis, for

example, from Ruiz et al that the phase difference $\phi_j(x,y)$ between the reference wave and the speckled wavefront from j^{th} depth layer contains also the term $\phi_{0j}(x,y)$ – the random phase term responsible for the speckle coming from the j^{th} depth layer [24].

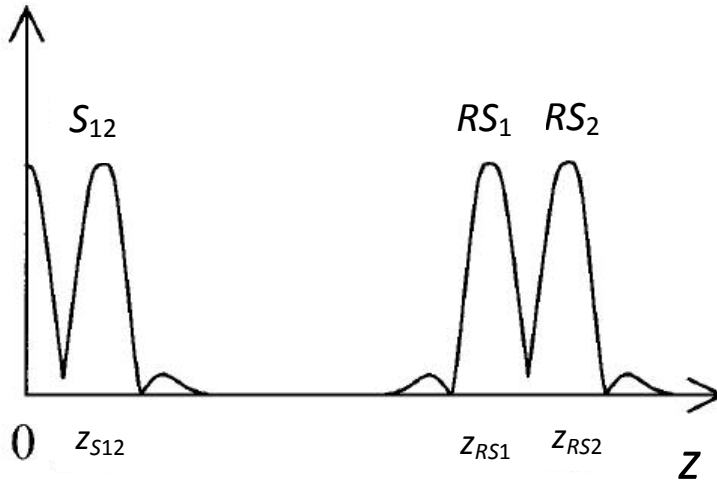


Figure 7.2. Peak distribution along the depth z axis for two layer depth object. S_{12} is the autocorrelation peak (due to self-interference between layers inside the sample) and its location is z_{S12} , RS_1 and RS_2 are the cross-correlation peaks due to interference between the reference beam and layers 1 and 2 inside the sample and located at z_{RS1} and z_{RS2} , respectively (figure taken from Ref [24])

On proper arrangement, all terms in Eq.7-4 should appear across the depth range span of the interferometer ($0 < z \leq z_M$). It can therefore be inferred that the depth span occupied by the desired cross-correlation term (between the reference and the sample's depth layer only) is one half of the whole depth range span of the system. Some past works put a stricter limit of only one-third of the total depth range. This in turn dictates the necessary optical thickness of the sample i.e the sample thickness is expected be equal to or less than one-third (or half) of the system's depth range. As derived in Sect.5.5 the etalon-based HSI system has a depth range of around $350 \mu\text{m}$ (assuming a refractive index of unity), thus it is expected that the maximum thickness of the sample is $115 \mu\text{m}$ (or less than $175 \mu\text{m}$ if half of the depth range criterion is used).

7.3. Sample preparation

Preparation of the sample that can provide scattering signal and meet the thickness requirement above is not a straightforward task. The other main requirement is that the

sample must be able to deform in the through-thickness direction due to the applied force. This section presents the attempts to manufacture the sample, and suitable loading device, to meet all requirements above.

7.3.1. Plastic sheet 1 – deformed by electric field

The first attempt to prepare a sample for this experiment was to use a plastic sheet with thickness between 100 to 125 μm , loaded by means of an applied electric field. This type of plastic is widely known as (thin) conductive plastic. The reason of using this type of material is because it is penetrable with light but not totally transparent, which indicates the material is to some extent capable of scattering the light. The resulting force due to the applied field will deform the sample, which is subsequently detected by the interferometer. The arrangement for providing the electric field to the sheet is illustrated in Fig.7.3.

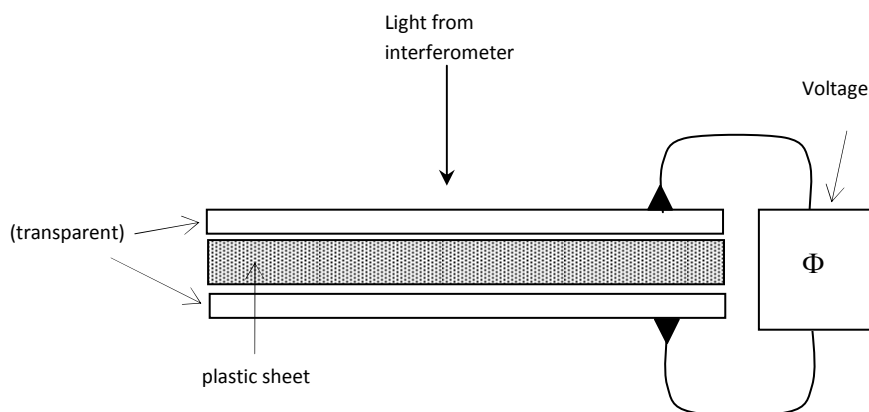


Figure 7.3. Applied electric field to provide deformation of the plastic sheet.

In a survey for suitable plastics it was found that this type of material is widely available in the market but unfortunately none was with the specified thickness above. The thinnest available was 0.5 mm or almost $5\times$ thicker than expected. With this limitation ordinary thin plastic, overhead projector transparency sheet, which has typical thickness 120 μm was considered next. This type of sheet is made from LDPE (Low Density Polyethylene) and has a relative permittivity $\epsilon_r = 2.25$ [154]. The electric field E that produces the force to deform the sheet however comes from the supplied voltage Φ , which is related to the

sample (plastic) thickness t_p by $E = \Phi/t_p$. According to electricstatic field theory an applied electric field will create polarised charge distribution (per unit area) P [155]

$$P = \varepsilon_0 (\varepsilon_r - 1)E = \varepsilon_0 (\varepsilon_r - 1) \frac{\Phi}{t_p}, \quad (7-5)$$

with ε_0 is the permittivity of vacuum ($\varepsilon_0 = 8.85 \text{ pF/m}$) and the unit of P is C/m^2 .

Since in the presence of electric field E a charge q will experience a force F related by $F=qE$, the charge density (per unit area) P under electric field E will therefore undergo force per unit area (or stress Σ) or using Eq.7.5

$$\Sigma = PE = \varepsilon_0 (\varepsilon_r - 1) \left(\frac{\Phi}{t_p} \right)^2. \quad (7-6)$$

The resulting stress should however sufficiently deform the sample so that the produced strain is detectable by the interferometer. Assuming the sheet is in the linear elastic region then the strain s is related to the stress Σ and Young's modulus Y by $s = \Sigma/Y$. Note that despite the common symbols of ε , σ and E to represent strain, stress and Young's modulus found in standard textbooks on the strength of materials (for example Ref [156]), in this thesis strain is symbolised by s since the symbol ε has been used for representing electric permittivity, σ for rms error, and Y for Young's modulus. Eq.7.6 now becomes

$$sY = \varepsilon_0 (\varepsilon_r - 1) \left(\frac{\Phi}{t_p} \right)^2. \quad (7-7)$$

Rearranging Eq.7-7 to find the required voltage to deform the sheet yields

$$\Phi = \sqrt{\frac{sY}{\varepsilon_0 (\varepsilon_r - 1)}} t_p. \quad (7-8)$$

If it is aimed to detect a 2π phase change across the sheet, corresponding to a relative displacement of $\lambda/2 = 0.42 \mu\text{m}$, the through-thickness strain of a $125 \mu\text{m}$ thick sheet can be calculated as $s = 0.42/125 = 3.4 \times 10^{-3}$. The Young's modulus of LDPE sheet Y is between $200 - 400 \text{ MPa}$ (see Appendix A10). Substituting these values into Eq.7-8 by assuming $Y_{\text{LDPE}} = 200 \text{ MPa}$ the required voltage Φ is found to be around 29.7 kV . It was therefore very inefficient with such a large voltage only to produce a deformation of only a small fraction of a micron. Another issue was compliance with the safety regulations of using such a high voltage. On these grounds, the original plan of using an electric field to deform the semi transparent material was not considered viable and a more feasible technique was therefore required.

7.3.2. Plastic sheet 2 – stretched by mechanical tension

For the second attempt to produce a suitable sample, a similar type of material (plastic sheet) was used, but this time the deformation was provided by means of mechanical force. The arrangement is shown in Fig.7.4.

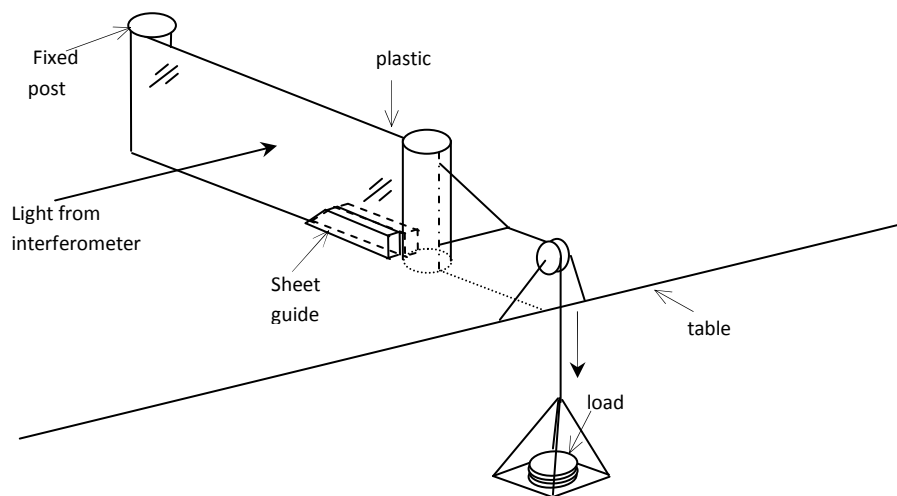


Figure 7.4. Deformation of the plastic sheet by means of mechanical tension.

According to the linear elasticity theory, stretching the sheet in one direction will cause a shrinkage in the direction perpendicular to the stretching force. The axes convention of the deformation arrangement Fig.7.4 is shown in Fig.7.5. As normally adopted in an optical set-up, the direction of the incoming light is taken as the axial direction. Therefore the

stretching force is in the transverse direction and the shrinkage therefore takes place in the axial direction parallel to the direction of the incoming light.

The longitudinal and transverse strains are related by Poisson's ratio ν (with reference to Fig.7.5) as

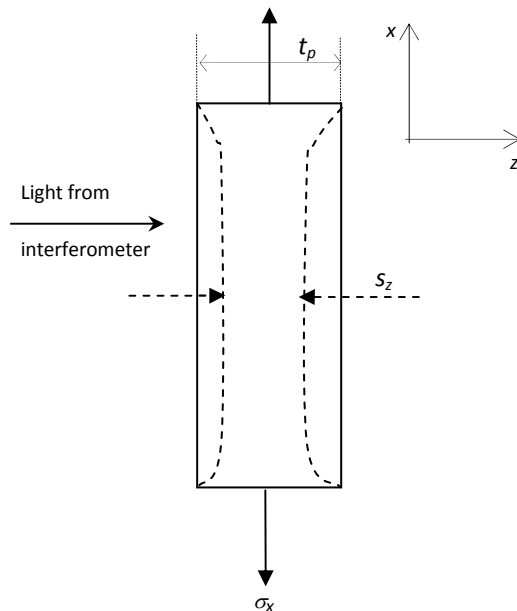


Figure 7.5. Contraction in the axial direction due to transversal stress (z is taken as axial direction)

$$\nu \approx -\frac{s_z}{s_x}, \quad (7-9)$$

The weight of the loads acts as the force P working on the sheet's cross section with area of $w \times t_p$, as shown in Fig.7.6.

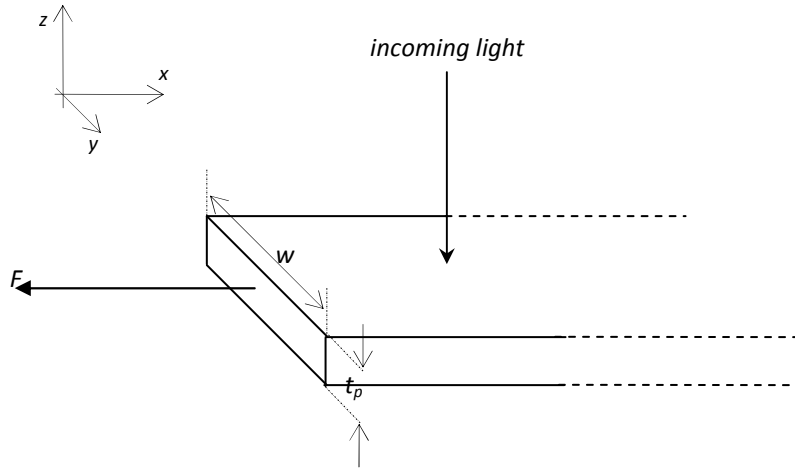


Figure 7.6. Contraction in the axial direction due to transversal stress (z is taken as axial direction)

Thus the stress on the sheet cross section is

$$\Sigma = \frac{F}{A} = \frac{F}{wt_p} . \quad (7-10)$$

But from the relation $s_x = \frac{\Sigma}{Y}$ and Eq.7-9 the strain in axial direction

$$s_z \approx \nu s_x = \frac{\nu F}{wt_p Y} . \quad (7-11)$$

The contraction in the axial direction, u_z is then given by

$$u_z = t_p s_z = \frac{\nu F}{wY} . \quad (7-12)$$

The sheet used for this experiment was cellulose acetate which has Poisson's ratio $\nu = 0.44$ and Young's modulus $Y = 1.6$ GPa with width $w = 1$ cm. The weight of the loads, which acts as the pulling force F that creates the stress Σ on the sheet cross section area, was gradually increased. The load and the resulting contraction are plotted in Fig.7.7.

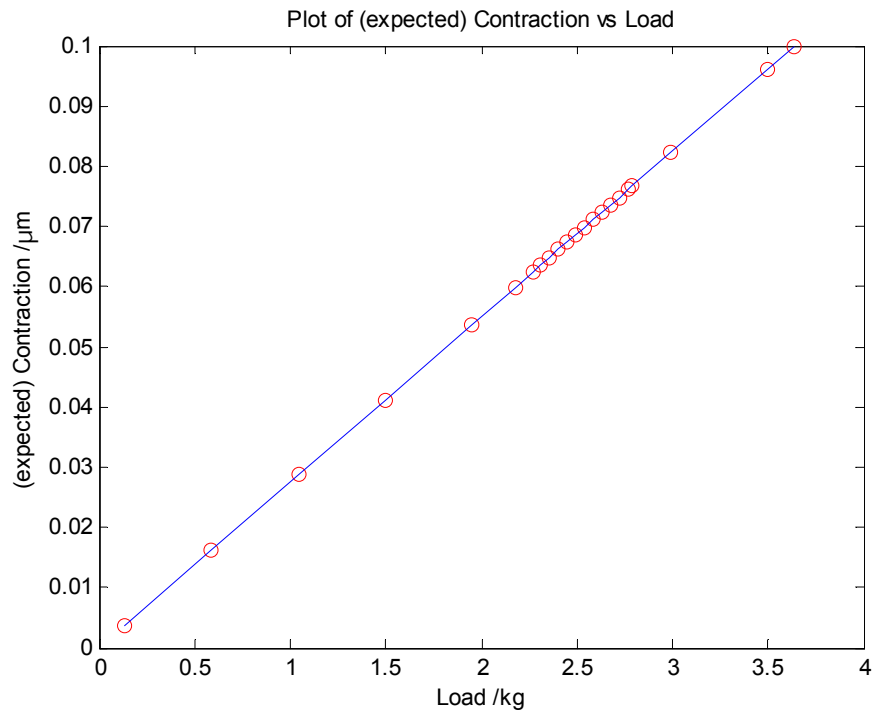


Figure 7.7. Plot of the data of contraction vs load.

Although some data was obtained from this sample, rigid body translation of the sample in the axial direction was a significant problem. Another problem with the sheet was that the material is almost purely transparent. No small particles are present between the front and back surfaces that can scatter the light. Therefore even if the HSI system can detect the contraction of sheet, the signal comes only from the Fresnel reflections from front and back surfaces due to the difference between the refractive index of the material and air. Negligible light was found to be scattered from inside the material. With this consideration, the next attempt involved the use of a semi-transparent/weakly scattering material which was made of a transparent material, such as resin, with small scattering particles embedded inside to increase the amount of scattered light.

7.3.3. Weakly scattering material

The next attempt to provide the sample to test the depth measurement capabilities of the HSI system was to prepare a weakly scattering material, and with a more controlled method for creating the mechanical deflection. Whilst the axial strain of the previously proposed methods was altered by electrical and mechanical means, for this sample it will be deformed by a combination of the two using a high voltage piezoelectric transducer

(PZT). This type of transducer is able to produce a very fine, highly repeatable movement, controllable to within fraction of μm .

For the main experiment the sample was sandwiched between two glass plates, one of which was held fixed and the other was in contact with the PZT thus compressing the sample when electrical voltage was applied to the transducer. For this purpose the sample was housed in the structure with side view shown in Fig.7.8. The PZT (grey), held fixed to the structure by a screw, provides the push to the sample which is in contact with the two glass plates.

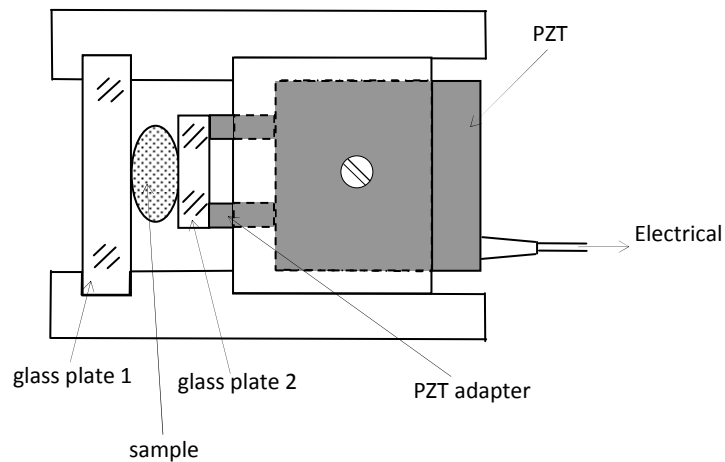


Figure 7.8. The weakly scattering sample arrangement for PZT compression.

7.3.3.1. Sample preparation and testing

The samples used for these studies were a mixture of a transparent material, such as gel or resin, embedded with small scattering particles. Past work conducted in the research group on application of Phase Contrast Spectral OCT (PC-SOCT) for simultaneous in and out of plane depth measurement [37] involved a test of several types of scattering grains [157]. The test result became the reference in selecting among varieties of commercially available scattering grains. The grains tested in this study are tabulated in Table 7.1. Some of the materials used in the preparation, however, have no available information on their physical properties.

Table 7.1.Types of scatterer used in the test

	Material	Physical properties	Remarks
1	Talcum powder	n/a	n/a
2	Glitter (gold) grain	n/a	glitter grain for decoration/toys, size ~ 0.5 – 1 mm
3	Glitter (silver) grain	n/a	glitter grain for decoration/toys, size ~ 0.5 – 1 mm
4	Copper	grain size $\leq 10 \mu\text{m}$	
5	Nickel	n/a	
6	Glass beads in suspension	grain sizes ~ 3 μm and 5 μm	
7	Window sealant	n/a	resin is not needed (the material is already a gel)

In total, during this study sixteen samples have been prepared from the grains listed in Table 7.1, mixed with the resin on different (mass) ratios. One of the samples included a mixture of two metals (Cu & Ni), which from previous study was found increasing the scattering signal. which was expected to improve the scattering.

The mixture of resin and scattering grains was subsequently placed in the sample arm of the interferometer and illuminated. Initially, the HSI was in the configuration state of surface profilometry. The distance from the sample to the object lens (the lens at the sample arm) is large (~500 mm) due to the use of long focal length ($f = 500 \text{ mm}$) lens. The reference arm of the interferometer was blocked so that the detected signal came only from the sample. The CCD barely showed any scattering signal for all sample types. If some grain types scatter more the others then the dark recorded frame, irrespective of the sample type, indicated that the light was too weak to be detected by the camera. To increase the intensity, the object lens was replaced with shorter focal length so that the sample can be moved closer to the interferometer. The 500 mm focal length lens (diameter = 25.4 mm) was replaced by a 100 mm focal length one with the same diameter. Scattering signals became stronger as the wave amplitude is inversely proportional to the distance. The CCD now could detect signal with the same exposure time previously employed to record the sample at longer distance.

As previously observed in the PC-SOCT work, the metallic grains showed stronger (scattering) signal than the others. For example, to produce roughly similar signal strength talcum powder and sealant required an exposure time 4 times longer than that for metallic grain. Nickel produced a stronger scattering signal than Copper, but in this experiment most of the Nickel grains were found to be lumped together, thus giving much larger effective scattering particles than the Copper. Most likely moisture absorption had taken place due to imperfect sealing of the packaging. Such a signal was also found for the gold and silver decoration glitter, however due to the very large grain size these grains were not investigated further. The mixture of Cu & Ni apparently did not improve much the signal compared to the samples made from the individual grains. The glass beads, with diameter 3 and 5 μm , showed a good scattering signal. It was found from the experiment that the 5 μm beads produced a stronger signal. This type of scatterer, however, was not embedded well in the resin when tested because it is a water suspension particle. From the experiment it is apparently difficult to mix this particle into the resin. With all of the above findings, Copper powder finally was chosen as the scattering material. It was also found from the experiment that there was a good correlation between stronger signal with higher concentration of the powder, particularly on Cu and Ni. Higher concentration however comes with the trade-off of the penetration depth of the light.

To achieve a thin sample ($\sim 115 \mu\text{m}$) the mixture of resin and scattering particles were subsequently spin-coated at a speed of 3,000 rpm for a period of 2 minutes in the case of Copper and resin mixture. The mixture was placed on top of glass plate 1 (Fig.7.10) and spun. The thickness was checked from time to time with a swept source OCT system (Thorlabs Swept Source OCM-1300SS) several times until the thickness requirement was met, and the sample then left to cure. An example of the thickness check using the OCT system is shown in Fig.7.9, where the sample has mass ratio of resin to Cu of 2:1 and the thickness was found to be 120 μm . Visual observation under the light showed that the layer of resin-Cu mixture appeared 'milky', indicating that the grains were distributed reasonably uniformly.

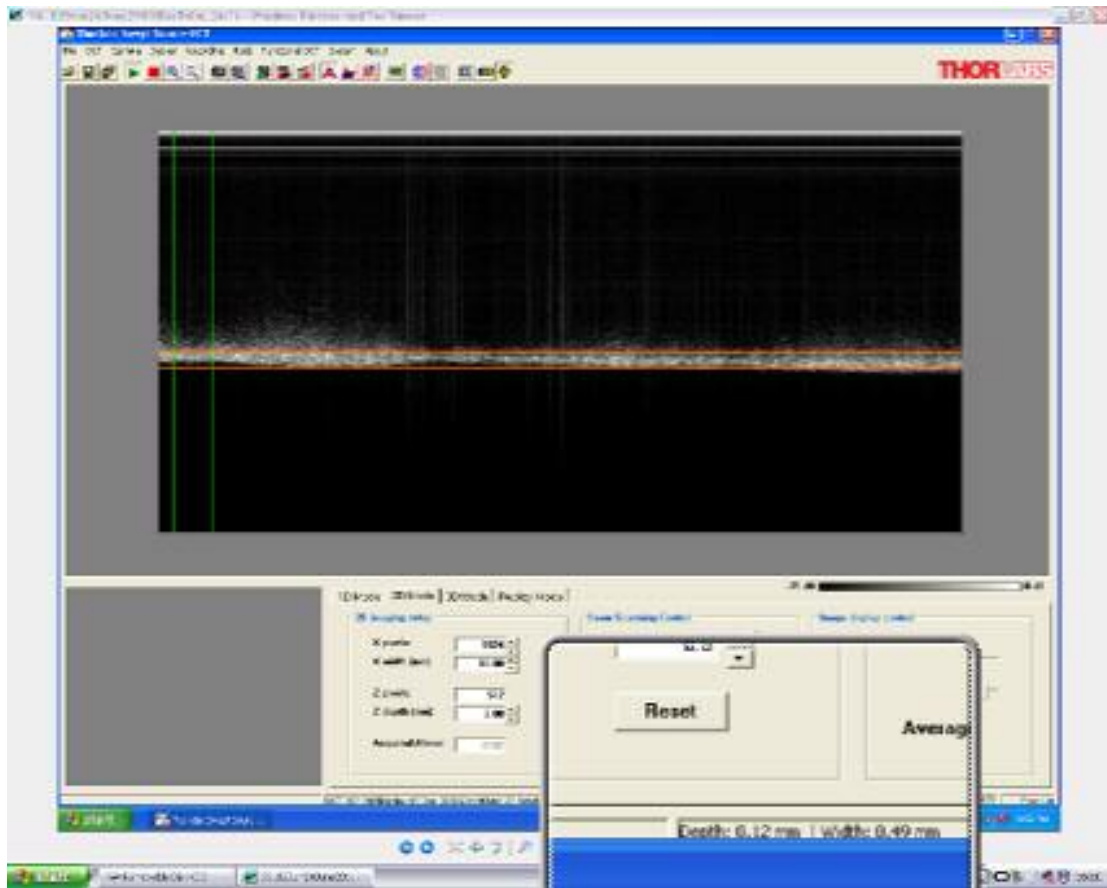


Figure 7.9. Sample thickness measurement result using swept source OCT system. Measurement result is shown in the enlarged image.

After the desired thickness was obtained and the sample was fully cured, glass plate 1 (with the sample layer) was inserted into its slot and glass plate 2 and the PZT were pressed against the sample. Another observation under the light of the sandwiched sample was carried out, but this time it was found some voids and patches on the contact surface between sample and glass plate 2. This might indicate that the sample was not in full contact with the pushing glass plate.

A modification to the method above was carried out. The mixture of resin and grain was layered on top glass plate 1, and then rather than being spun the sample was pressed from the top. Between the glass plates was placed a metal shim with thickness similar to the required sample thickness. To ensure full contact of the sample and glass plate 2, a load was applied on top of the glass plate 2. The metal shim acted as the spacer to keep the correct gap between the two glass plates until the mixture was fully cured. When the sample has been fully cured, these spacers were removed. The arrangement of this modified method is shown in Fig.7.10.

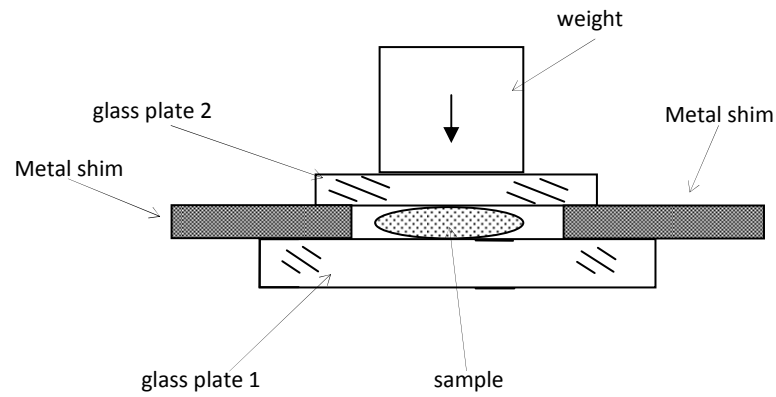


Figure 7.10. Side view of the configuration of the modified method for sandwiching the sample.

Visual checking under the light after the sample was cured showed improvement on the contact between the sample and the pushing glass, i.e. voids were still found but with much smaller area compared with the previous method and also fewer of them. The problem with this approach however was that there was a slight displacement between the PZT adapter and glass plate 2 when they were put into contact. This is due to the difficulties in keeping glass plate 2 stationary when the load was placed on top of it. Another problem was an accurate sample thickness measurement can no longer be done using the OCT system. The sample now has been already sandwiched between two glass plates with each having thickness around 3.5 - 4 mm, whilst the OCT system has a maximum measurement depth range of 3 mm. Therefore before preparing the sample the thickness of each glass plate was measured (using micrometer) and the thickness of two glass plates when in contact were measured. Later after the sample was cured the thickness of the stack of two glass plates and the sample was measured. Subtracted with the previous measurement with no sample, the difference was roughly equal to the sample thickness. The uncertainty of the measurement was of the order of the micrometer uncertainty, which is $\pm 10 \mu\text{m}$.

7.3.3.2. Grain requirements

Two main aspects must be considered in selecting the type of grain as the scattering particle. The first is the grain size. Interference between light from randomly positioned grains of the object produce the speckle pattern on the image plane. If the lens to image the sample has a f-number $f_{\#}$ (which is the ratio of the lens focal length f and effective lens

diameter D), magnification M and the illuminating wavelength is λ , then the (subjective) speckle size at the image plane d_{sp} can be approximated with [158]

$$d_{sp} \approx 1.22(1 + M)\lambda f_{\#}. \quad (7-13)$$

The ‘physical’ speckle size at the sample D_{sp} is therefore [158]

$$D_{sp} \approx \frac{d_{sp}}{M}. \quad (7-14)$$

Using the similar profilometry configuration outlined in Sect.4.4 (Chapter 4), with the imaging lens focal length $f = 100$ mm, the illuminating wavelength taken as $\lambda_C = 840$ nm, and the system magnification as the ratio of focal lengths of lenses L_4 and L_3 in Fig.4.7 to yield $M = 1.5$, the image speckle size using Eq.7-13 is found to be $5.76 \mu\text{m}$. The effective speckle size on the object using Eq.7-14 is $28.82 \mu\text{m}$.

The pixel size of the CCD, $6.45 \mu\text{m}/\text{pixel}$, is smaller than the size of the speckle on the object. Ideally one should match the speckle size to the pixel size to achieve good signal modulation depth without ‘wasting’ pixels through oversampling of the speckle field. The intensity at one pixel at the detector, due to the random walk statistical property of speckle [159], is due to averaging of the scattered light from many particles. The particle size must therefore be smaller than the pixel dimension. With a system magnification of 1.5 the effective speckle size (and hence maximum particle size) on the sample should be less than $6.45/1.5 = 4.3 \mu\text{m}$.

The other aspect to consider is the density of the grains inside the resin. The required density can be estimated as follows. Suppose the mass and the density of the resin and the scattering particles are denoted by m_1 and m_2 , and D_1 and D_2 , respectively (where subscript 1 and 2 refers to resin and scattering particle as shown in Fig.7.11). A scattering particle with radius r_{sp} is confined in a typical cube volume with side l . The volume of the cube v_C is given by

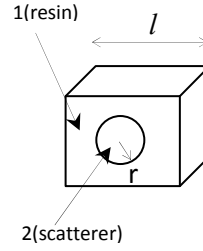


Figure 7.11. Diagram of a scattering particle confined in a cube of volume L^3 for grain density calculations.

$$v_C = l^3 = \frac{4}{3} \pi \frac{D_2}{D_1} \left(\frac{m_1 + m_2}{m_2} \right) r_{sp}^3 \quad (7-15)$$

For example, the resin used to prepare the sample (ACC Silicone MM 240TV) consists of base material (A) and the hardener (B) each with 1.08 g/ml. To prepare the resin the ratio of A to B is 10:1, which gives the resin density of 1.08 g/ml. The Copper powder (Sigma Aldrich, 99% Cu) has a density of 8.94 g/ml. For the calculation the Cu grain size was assumed to be 10 μm , despite the powder's technical data which indicated that particle size can also be smaller than the nominal value. The ratio of mass of resin to Cu powder was chosen as 2:1. Using Eq.7-15 the cube volume v_C is found as $7.06 \times 10^4 \mu\text{m}^3$.

This volume must be 'confined' inside the 'volume' of the imaging pixel V_p , which is equal to the product of pixel area and the depth resolution of the HSI. The depth resolution has been calculated in Sect.7.2 to be around 22.77 μm . Therefore the volume of the voxel V_p can be approximated as $6.45 \times 6.45 \times 22.7 = 947.43 \mu\text{m}^3$. The number of scattering points 'inside' a voxel therefore can be approximated as the ratio of V_p to V_C , which equals to $947.43/7.06 \times 10^4 \approx 0.013$.

7.4. Limiting the speckle pattern's spectral overlap

The observed speckle field was typically found to be larger than that encountered in the surface imaging of optical flats. It was decided to reduce the amount of cross-talk from one spectral image to the next by placing a field stop in the interferometer beam path.

Two lenses were therefore placed in between BS_1 and BS_2 in Fig.4.7 and a vertical slit was placed at the common focal length distance of both lenses. To simplify the design, the two lenses were chosen to be identical. This additional configuration is shown in Fig.7.12. The light from the sample (red arrows) will be blocked by the slit, unless the scattering point is sufficiently close to the optical axis.

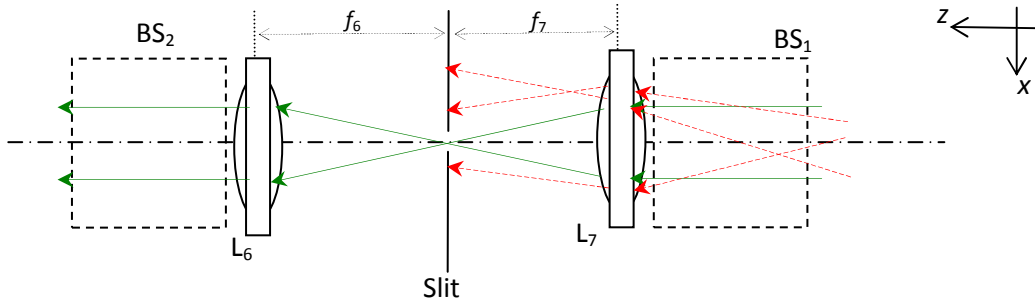


Figure 7.12. Top view of the vertical slit (drawn not to scale).

The slit is imaged to each spectral sub-image through a combination of two lenses L_6 and L_4 (in Fig.4.7). The focal length of lens L_4 , is 150 mm. After considering the factors in determining the two identical lenses L_6 and L_7 including the space between BS_1 and BS_2 and the optical component availability, the lenses were realised by two 50 mm focal length lenses. Observing the paths of light from the slit to the sub-image in the CCD as shown in Fig.7.13 the slit undergoes magnification of $f_4/f_6 = 150/50 = 3 \times$.

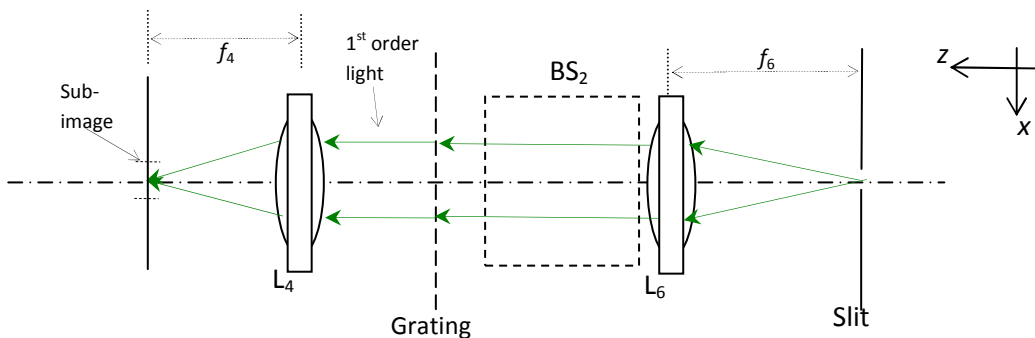


Figure 7.13. Geometry of imaging from the slit to the CCD.

If one sub-image at the CCD is 20 pixels wide or $130 \mu\text{m}$ (the CCD's pixel size is $6.45 \mu\text{m}$) then the required size of the slit is the sub-image width divided by the magnification

or $130/3 \approx 43.33 \mu\text{m}$. The nearest available size of the slit was $40 \mu\text{m}$ (Thorlabs model number S40R). The result of the image without and with the slit filtering is shown in Fig.7.14. The slit filtered image shows a distinct gap between adjacent sub-images, indicating a clear spectral separation between two sub-images.

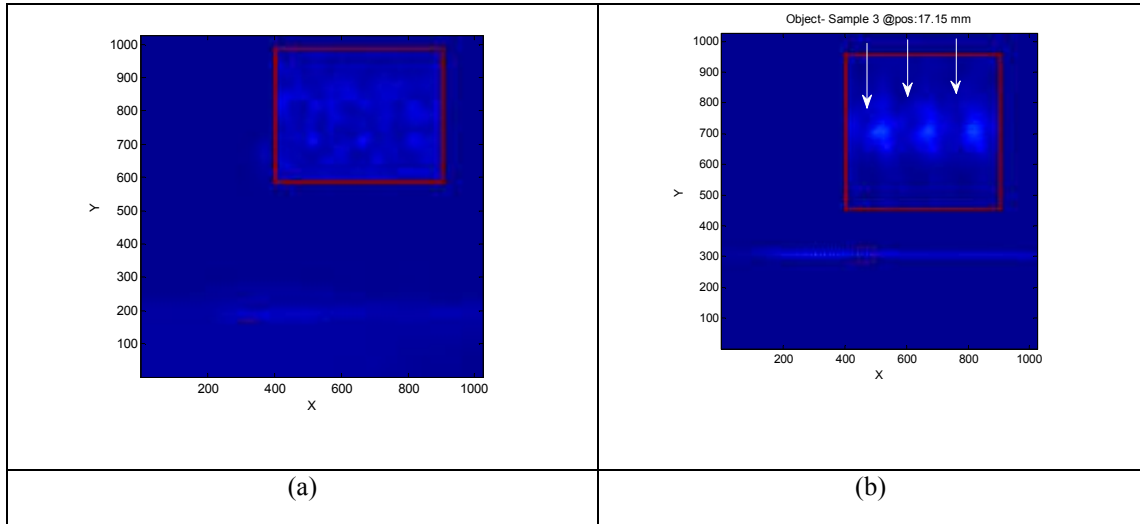


Figure 7.14. The sub-images in a recorded frame (a) before and (b) after vertical slit filtering (arrows indicate the gaps)

7.5. Improvements to the sub-image alignment method

The sub-images in the (single-shot) frame are stacked to form a hyperspectral image volume as shown in Figs. 3.2 and 5.2. The technique to stack the sub-images has been described in Sect. 5.3.

During the processing of the depth measurement images it was observed that the sub-images from the reference arm were not entirely aligned. This was identified when a set of sub-images were played back, from the first to the last, the Gaussian profile inside several sub-images appeared shifted, as shown in Fig.7.15. The shift of the centre pixel coordinate in this example appeared subtle (around 1 – 3 pixel drift). In the cases when the peak detection algorithm could not normally detect the peak accurately (for example when a spot is almost of the same intensity to the adjacent or even with the gap between two spots) however the drift will be clearer and can produce a larger shift. The alignment method previously described in Section 5.3 was therefore modified to reduce this effect.

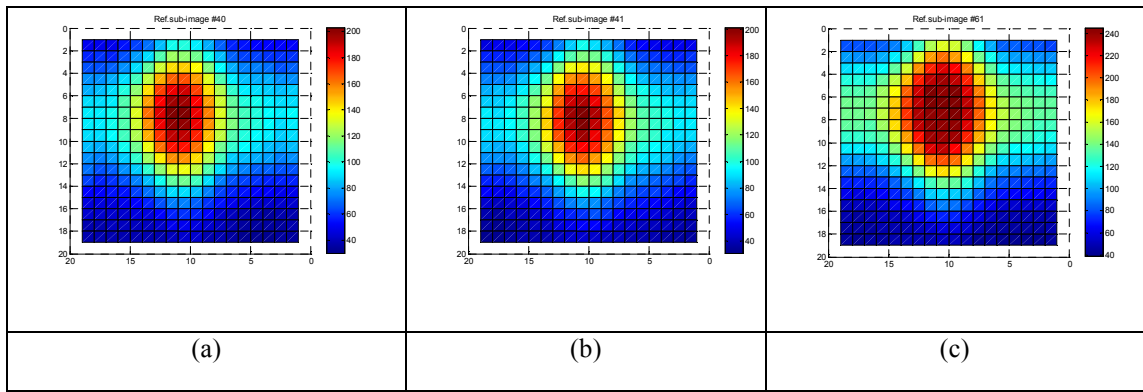


Figure 7.15. The drift of Gaussian (contour) profile inside some of the sub-images from reference arm.

The pixel coordinates of the sub-images was then examined. When plotted against the sub-image index the plot should look linear. The plot of sub-image coordinates as a function of sub-image index is shown in Fig.7.16 as two separate graphs - for x and y coordinates.

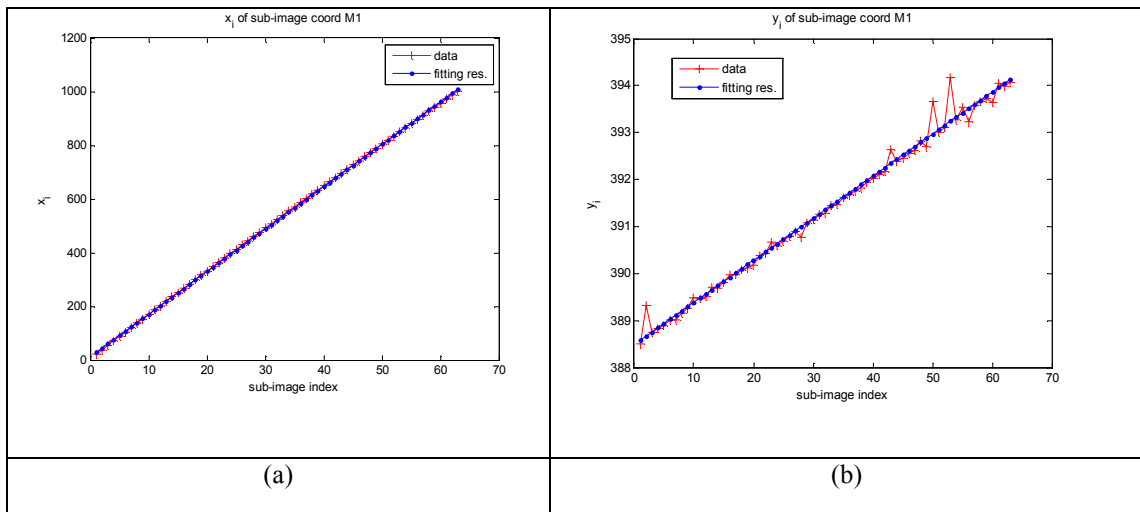


Figure 7.16. Plot of (a) x -coordinate, (b) y -coordinate of the sub-images' centre pixels. Each graph is fitted with a linear line to estimate the drift.

Comparing both graphs, it appears that more data points are outside the linear fitting line in Fig.7.16.b (y -coordinate) than in the x -coordinate (Fig.7.16.a). The average deviation (difference between the data and the fitting line), however, is larger for the x -coordinate than for the y -coordinate, as is the maximum deviation from the fitting line. The average deviation and maximum deviation of the x -coordinates from the best-fit line are 3.124 and 7.885 pixels, respectively whilst for the y -coordinate the corresponding values are 0.099 and 0.928 pixels, respectively.

Fig.7.17.a shows the intensity plot of one row of the reference image, which passes through the set of spectral images. The envelope of this intensity plot is equal to the SLED spectral profile. If the centre pixels of the sub-images from the reference light are correctly aligned, then the sampled points should resemble the ‘smooth’ SLED spectrum profile either in full or in part (depending on the portion of the spectrum used to illuminate the interferometer). Fig.7.17.b is the plot of reference intensity sampled at the centre pixel of the sub-images obtained from Gaussian fitting only, as previously described in Sect. 5.3. The intensity fluctuates, indicating the presence of jitter in the alignment of the sub-images.

The spectral profile of the light source can be estimated as the envelope of the plot in Fig.7.17.a. The envelope of the signal was obtained by fitting by a 6th degree polynomial to the intensity. The fitting result is as shown by the red curve in the same plot.

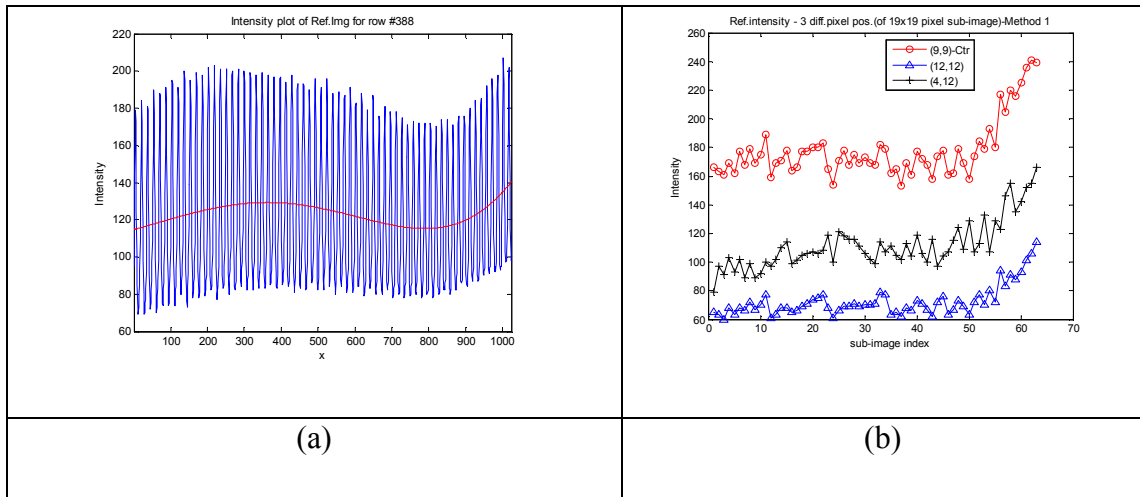


Figure 7.17. Plot of (a) Reference intensity of a single row and , (b) reference intensity sampled at the sub-images’ centre pixels fitted with Gaussian function only

The modified method includes several additional steps from the previous Gaussian fitting, i.e. the sub-images’ centre pixel coordinates is fitted with a polynomial function. The modified coordinates, which are now no longer integral, are then used to re-sample each spectral image by a 2-D interpolation on the original image data. The improved algorithm is summarized in Table 7.2, with both the original and modified algorithms listed for comparison.

Table 7.2. Improvement of the sub-images' centre pixel detection

Original method	Modified method
<ol style="list-style-type: none"> 1. Use the original 2-D reference image 2. Manually click on two endpoints of the sub-image row 3. Extract a 1-D intensity profile line 4. Feed the line obtained from step 3 to the peak detection algorithm 5. Create sub-image using the centre pixel coordinates from the detected peak positions in step 4 6. Each sub-image from step 5 is fitted with 2-D Gaussian function 7. The outputs from step 6 are the new centre pixels of the sub-images 8. Create the hyperspectral image volume by stacking the sub-images centred at the new coordinates obtained in step 7. 	<ol style="list-style-type: none"> 1. Use the original 2-D reference image 2. Manually click on two endpoints of the sub-image row 3. Extract a 1-D intensity profile line 4. Feed the line obtained from step 3 to the peak detection algorithm 5. Create sub-image using the centre pixel coordinates from the detected peak positions in step 4 6. Each sub-image from step 5 is fitted with 2-D Gaussian function 7. The outputs from step 6 are the new centre pixels of the sub-images 8. Fit the centre pixel coordinate in step 7 with polynomial function 9. Stack the sub-images centred at the modified coordinates obtained in step 8 10. Create the hyperspectral image volume by performing 2-D interpolation to the sub-image stack obtained in Step 9

For the implementation of the sub-image fitting with a 2-D Gaussian profile the Matlab function `fminsearch` was used, whilst the 2-D interpolation was by means of another Matlab function `interp2`.

The result of the improved algorithm is illustrated in Fig.7.18. Fig.7.17 is re-displayed for comparison. After applying the modified method the intensity jitter is reduced indicating significantly improved alignment of the sub-images.

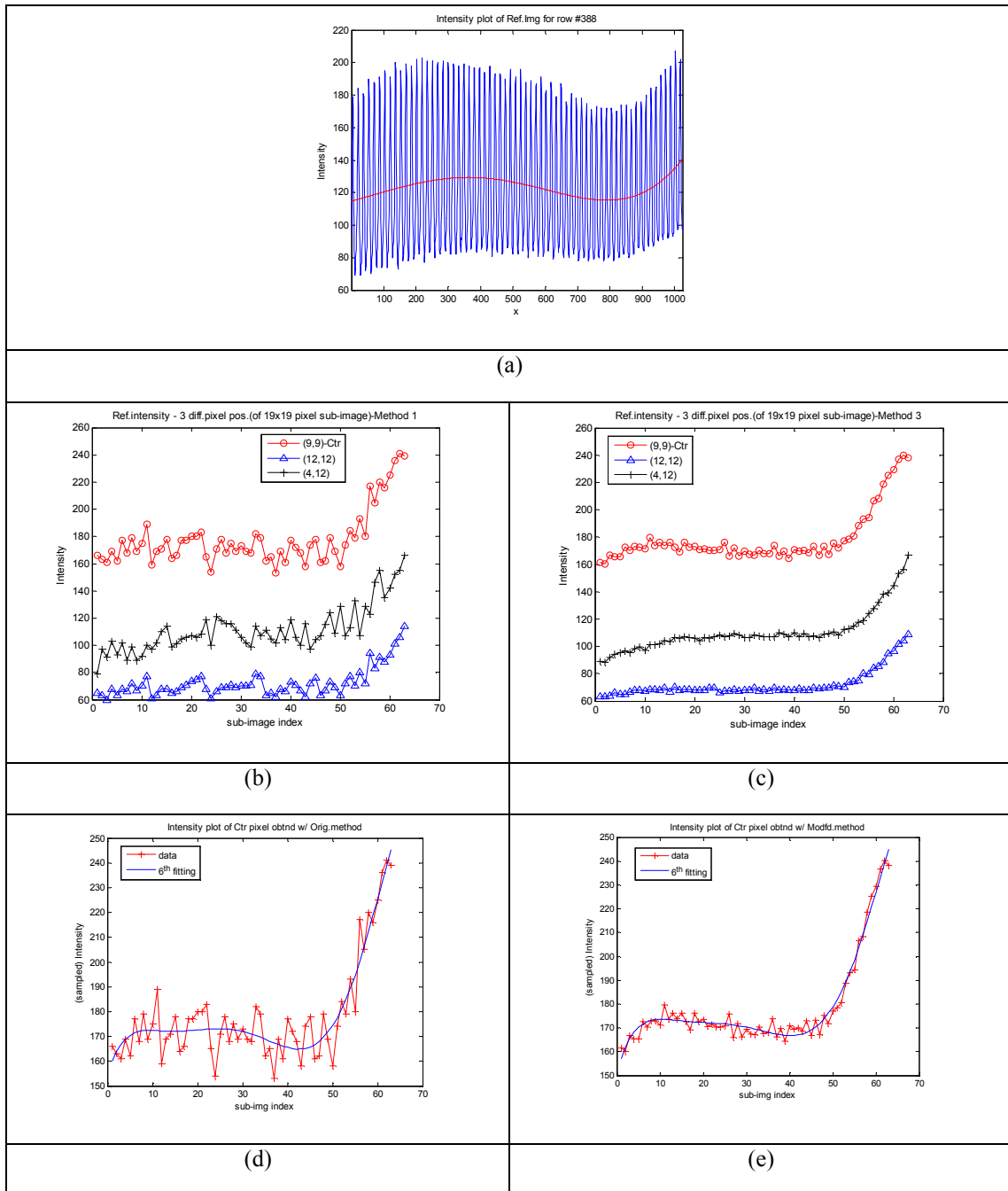


Figure 7.18. Plot of (a) Reference intensity of a single row, reference intensity sampled at the sub-images' centre pixels obtained by (b) original, (c) modified methods; the intensity of the centre pixel of the sub-image obtained (d) original and (e) modified methods

The sampled reference intensity of the sub-images' centre pixel (the red graphs in Fig.7.18.c and d) were further analysed. Both the reference intensity plots are fitted by a 6th order polynomial function. The modified method clearly shows smaller difference from the

fitting polynomial than the original counterparts. The maximum deviation from the fitting function for the modified method is less than the original algorithm (the original method is 19.04 whilst the modified method is 6.90). The average deviation of the entire datapoints has also dropped after the modified method was applied: using the original method the average deviation is 6.30, whilst the modified algorithm results in an average deviation of 2.50.

7.6. PZT Calibration

Prior to the use for compressing the sample, the Piezoelectric Transducer (PZT) was tested in a simple 2 beam laser interferometer. The purpose of the test was to evaluate whether the PZT can produce linear motion and to calibrate its voltage-displacement response.. This property can be examined from the resulting phase difference between the two arms since the OPD is proportional to the phase. In this test, the PZT was attached to a mirror thus constructing a two mirror interferometer with one kept fixed (the reference mirror) and the other displaced by the transducer (the object mirror). The configuration is shown in Fig.7.19, which is a simplification of the full HSI configuration.

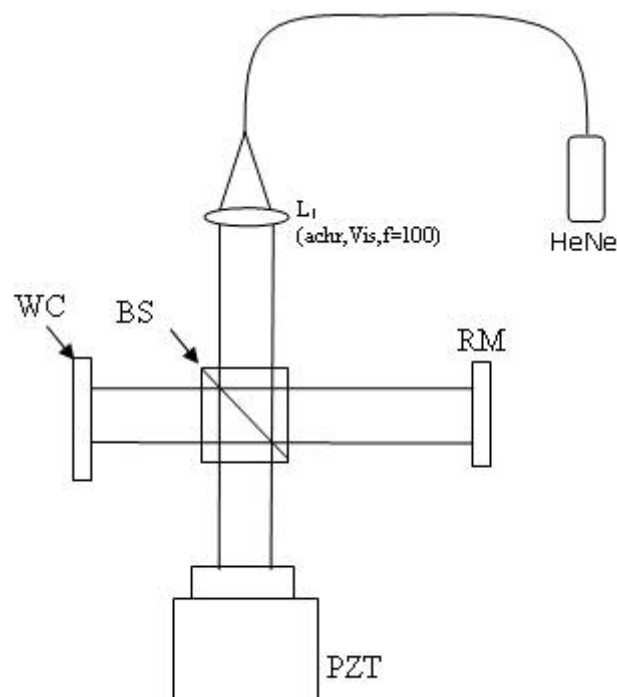


Figure 7.19. The configuration for PZT calibration. HeNe=HeNe laser source, RM=reference mirror, BS= beamsplitter and WC=Webcam

The PZT employed in this experiment is a Burleigh PZ-81, driven by a high DC voltage source from Burleigh ramp generator RG-9. In this calibration the transducer was supplied with ramp voltage range approximately from 157 to 824 V with ramp signal duration of 10 sec. The acquired data was a movie of 209 frames with duration of 42 seconds. Data analysis consisted of extracting the phase from the peak of the 2-D Fourier transform of each image. The resulting wrapped phase as a function of supplied voltage is shown in Fig.7.20.a, whilst the unwrapped version is displayed in part b.

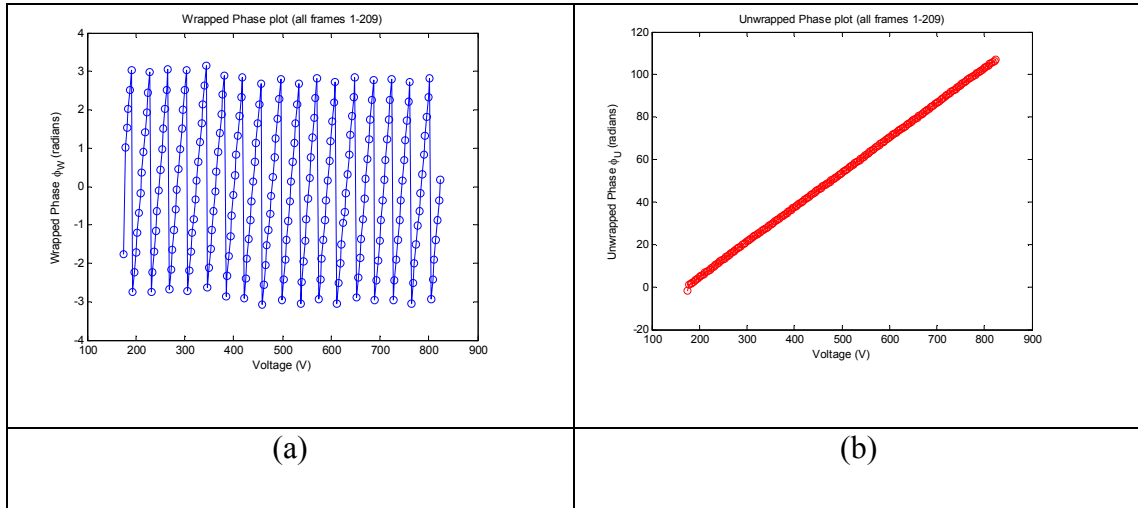


Figure 7.20. The calibration result of the PZT – (a) wrapped, and (b) unwrapped phase as a function of supplied voltage.

A linear fitting was performed to the unwrapped phase from within the supplied voltage range of 230 – 330 Volts. The fitting result is shown in Fig.7.21. The average rms value about the best-fit curve was found to be 0.08 radian. The slope of the fitting line was found to be 0.18 rad/V. Using this figure with the 632.83 nm He-Ne laser light used in this calibration 1 V voltage change applied to the transducer will displace the mirror by 0.18 rad or equivalent to $(0.18 \text{ rad} \times 632.83 \text{ nm}) / (4\pi) = 9.07 \text{ nm}$ or $0.0091 \mu\text{m}$. This means when the transducer is biased with the maximum voltage 1 kV it will displace by 9 μm . This figure however does not match with the transducer specification which states a displacement of 2 μm at 1 kV, and thus requires further investigation. Nevertheless the calibration result shows the expected linear relation between phase (displacement) and the supplied voltage of the transducer. In the calibration however the PZT was in contact with no sample and free to move. In the real data acquisition the situation will be different, however the calibration parameters may still be valid if the sample compliance is much higher than that of the PZT crystal.

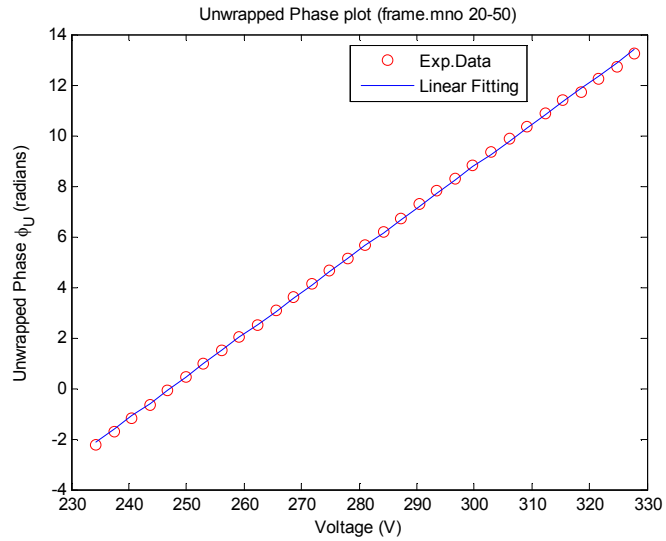


Figure 7.21. Linear fitting to the unwrapped phase from the PZT calibration

7.7. The depth measurement experiment

The configuration of the HSI system for depth measurement is shown in Fig.7.22. The symbols in Fig.7.22 are identical to those of the configuration for surface profilometry shown in Fig.4.7. Some additional changes include the slit and two identical lenses L_6 and L_7 , located between BS_1 and BS_2 , to limit the spectral overlap as described in Sect.7.4, and the test object.

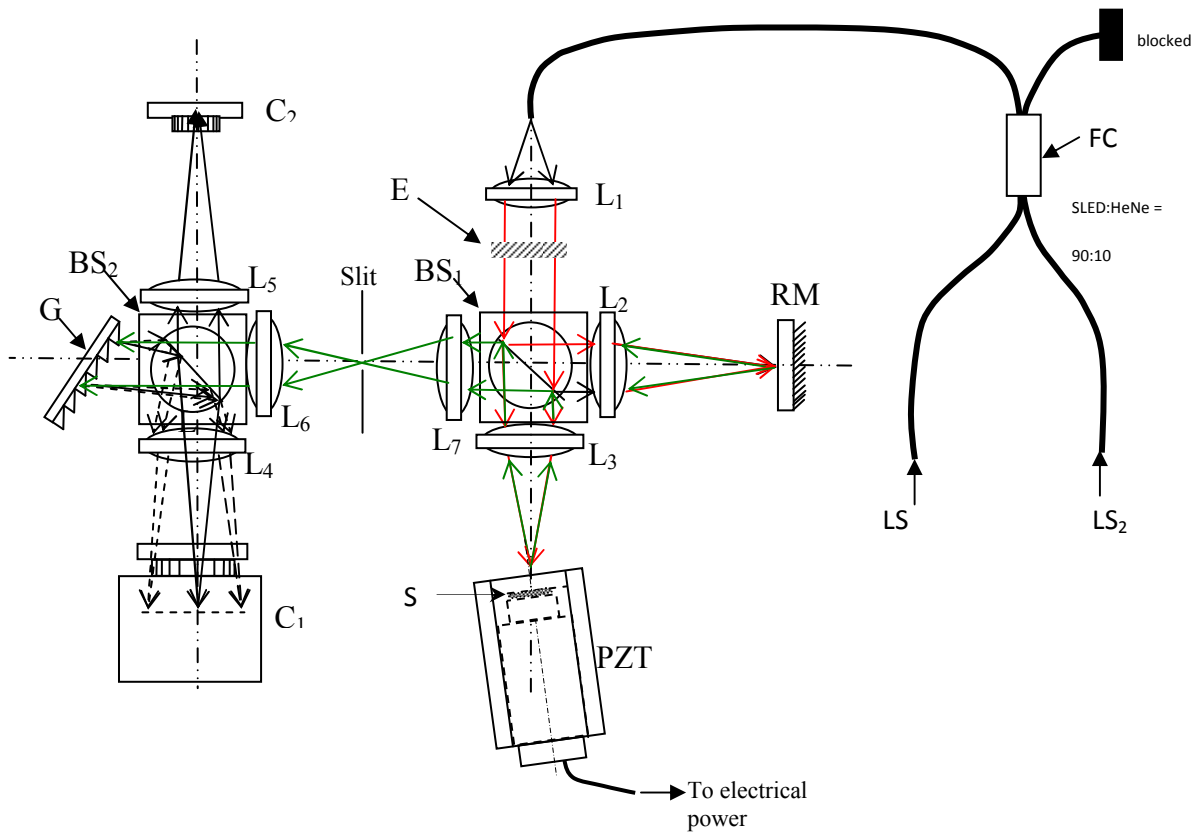


Figure 7.22. The diagram of the HSI system for depth measurement

The sample was confined in a structure so that it can be compressed by the PZT as described in Sect.7.3.3.1 and Fig.7.8. The test object was not oriented perpendicular to the optical axis that goes through lenses L_1 and L_3 but slightly tilted to avoid the strong specular reflection when the light hits glass plate 1. Besides the specular reflection, the front glass plate will add optical length in the object arm which must be taken into account to maintain zero OPD between the reference and object arms. Using a simple measurement technique, for example method described in (see Appendix A11), the refractive index of the front fixed glass plate was found as 1.44. With a thickness of 3.83 mm this glass plate, if oriented perpendicular to the incoming beam, adds optical path $1.44 \times 3.83 \times 2 = 11.03$ mm. The titled plate in this experiment to avert the specular reflection will therefore produce a further increase in optical path.

The positioning of the sample in front of the imaging lens L_3 will also affect the distribution of interferometric terms such as shown in Fig.7.2. The intensity (depth) signal obtained at various stage positions is shown in Fig.7.23. The sample here was Copper particles in a matrix of resin (mass ratio = Cu : resin = 2: 1). The 1-D spectra through all

the images have been averaged to create a one-dimensional signal with improved SNR. The stage (and sample) position was initially at 27.21 mm and only one peak is observed which is in the ‘lower’ part of depth axis. The cross-correlation peak is not observable at this stage position. By translating the stage 100 μm further to position 27.31 mm from the interferometer, the two regions of the auto and cross-correlation terms both appear, as indicated in Fig.7.23(b). Further displacement of the stage away from the interferometer separates the two peaks wider apart, such as illustrated in Fig.7.23(c) where the stage was displaced 90 μm away from position in Fig.7.23(b) to position 27.40 mm. At this position the cross-correlation term occupies around half of the depth range and largely separated from the autocorrelation term, which is an ideal position to start the depth measurement.

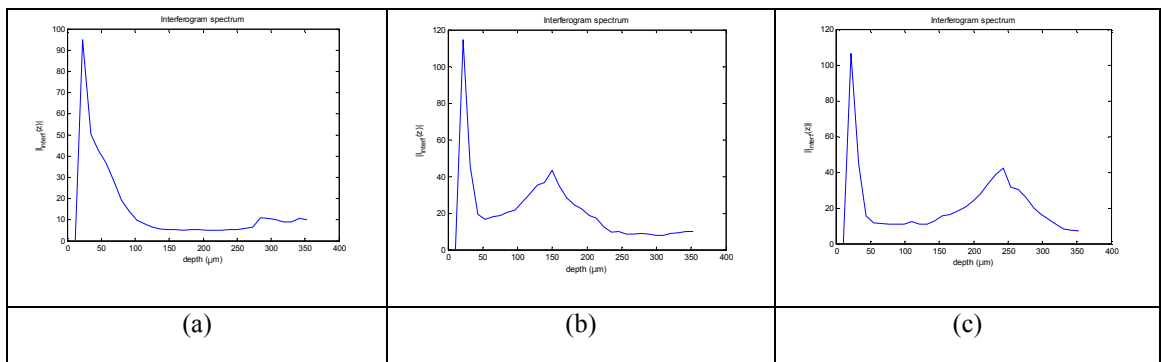


Figure 7.23. Separation of the auto and cross-correlation terms in the depth axis as the stage was translated.

The sample in Fig.7.23 has a 2:1 mass ratio of resin to Cu grains. For the depth measurement experiment, the grain amount was increased to achieve 1 : 1 mass ratio of resin and scattering particles thereby increasing the strength of the back-scattered light. The resulting depth signal (after several stage translations to obtain the best auto and cross-correlation terms separation) is shown in Fig.7.23. The cross-correlation intensity is amplified compared to Fig.7.24 and also higher than that of the auto-correlation term. This sample was later used for the depth measurement experiment reported later in this section.

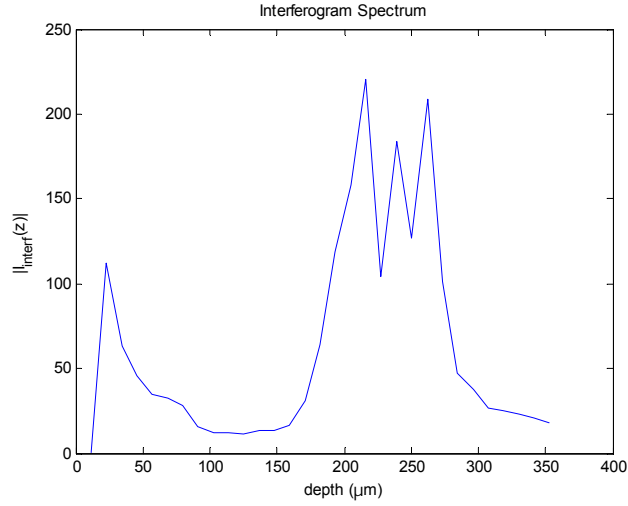


Figure 7.24. The depth distribution of the correlation terms after the grain density in the sample (whose depth intensity shown in Fig.7.23) was increased

The PZT was biased with 10 equal interval voltages from 185 to 800 V. Instead of computing the phase distribution from each individual voltage, phase difference distributions between two interferograms acquired at 2 different voltages were calculated. The interferogram recorded at the first voltage served as the reference, thus the phase difference was calculated between each interferogram, from the 2nd to the 10th voltage, relative to the reference (1st) voltage interferogram. The notation for this phase difference calculation is $\Delta\phi_{i1}$ where the subscripts 'i' and '1' refers to the i^{th} and 1st voltage. Thus $\Delta\phi_{31}$ reads as the phase difference map calculated from the interferograms recorded at the 3rd and 1st voltage values.

The phase difference was calculated using the 'Difference-of-phase' equation [5,35]

$$\Delta\phi_{i1}(z_n) = \tan^{-1} \left\{ \frac{\text{Im}[\tilde{I}_i(z_n)] \text{Re}[\tilde{I}_1(z_n)] - \text{Re}[\tilde{I}_i(z_n)] \text{Im}[\tilde{I}_1(z_n)]}{\text{Re}[\tilde{I}_i(z_n)] \text{Re}[\tilde{I}_1(z_n)] + \text{Im}[\tilde{I}_i(z_n)] \text{Im}[\tilde{I}_1(z_n)]} \right\}, \quad (7-16)$$

where $\text{Im}[\dots]$ and $\text{Re}[\dots]$ are the imaginary and real part, respectively, of $\tilde{I}(x, y, z)$ - the Fourier transform of hyperspectral image volume $I(x, y, k)$, z_n is the n^{th} depth element of $\tilde{I}(x, y, z)$, and the subscript i of $\tilde{I}_i(z_n)$ refers to the i^{th} voltage applied to the PZT. Prior to performing the division, the numerator and denominator of Eq.7-16 was first smoothed by convolving the term with a 3×3 smoothing kernel, similar to the process of smoothing

height map of rough surface in Section 6.4.1. Alternatively, the numerator and denominator can be averaged throughout an entire slice to obtain a single phase change value for a particular depth z_n .

7.8. Results and discussion

Example of the reconstructed phase maps at voltage difference $\Delta\phi_{31}$ (phase difference between V_3 and V_1) is shown in Fig.7.25 (next page). After convolving the phase map with 3×3 smoothing kernel, the phase distribution appears smoother.

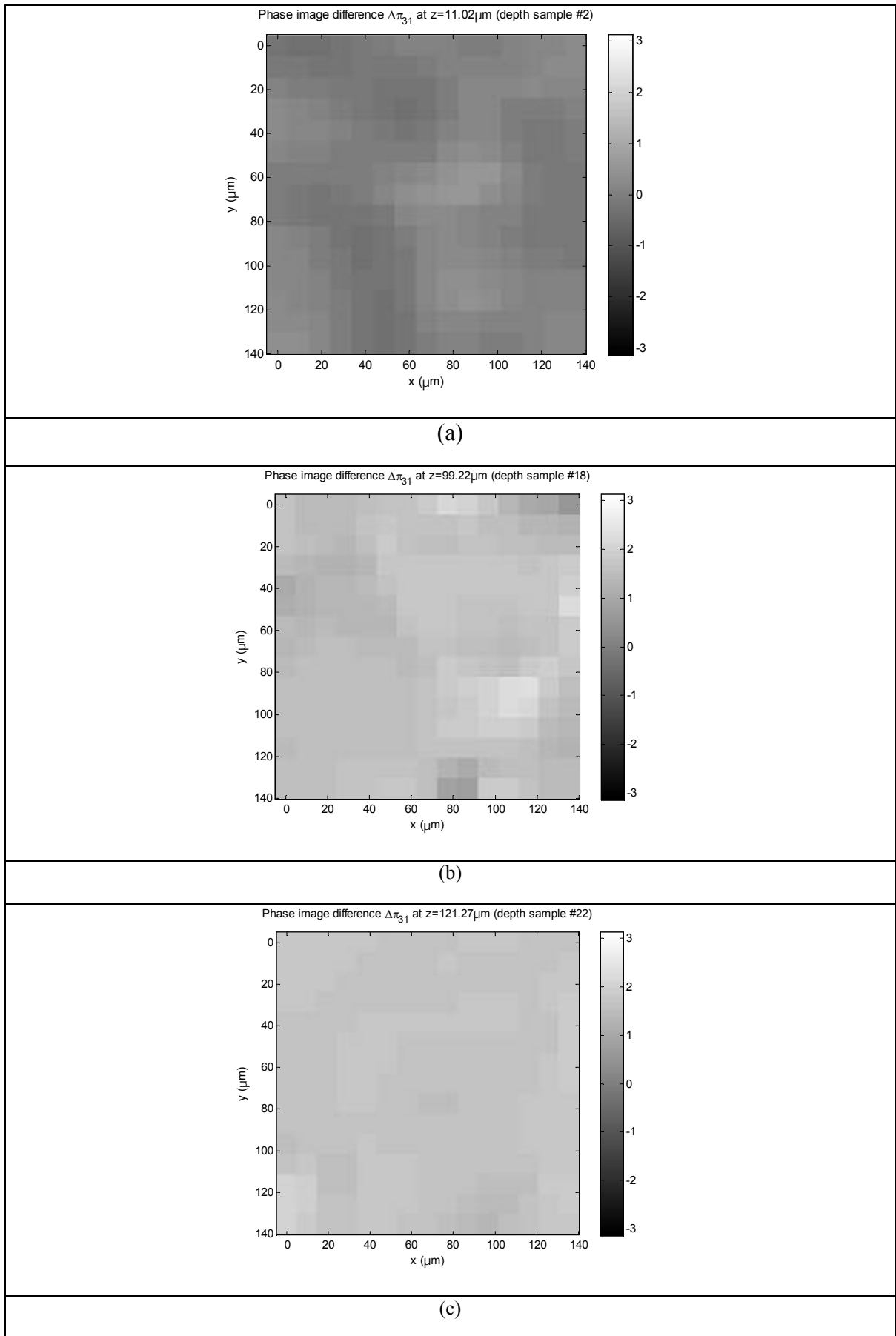


Figure 7.25. Example of the reconstructed phase difference map at a given voltage difference for different depth values.

The results of the phase difference calculation from this experiment is presented in Fig.7.26. The plots in the figure are the phase difference of the interferogram recorded at 2nd to 10th voltages values with respect to the reference interferogram (taken at 1st voltage value), averaged through each slice to increase the SNR. As the voltage increased, the PZT should push further into the sample. The sample thickness in turn should decrease, and the depth layers inside the sample should move closer towards the first layer (the nearest layer to the fixed glass plate). Therefore as the voltage difference becomes higher, the phase difference value should increase as well. If the PZT pushes the sample linearly then so should be the displacement of the depth layers, whence the phase difference should also change linearly. The experimental results in Fig.7.26 however do not show such a trend.

An interesting fact to observe is that (except Fig.7.26.e) the phase difference for the depth roughly between 200 – 300 μm for all voltage differences appears relatively flat. This might be an indication that the displacement of the layers within this depth range is roughly the same, moving en masse with the push from PZT. These layers appear be unable to be compressed by the transducer. On the technical implementation issue, there is also possibility that in fact the PZT was not in full physical contact the pushing glass plate (glass plate 2 in Fig.7.8) so that no or negligible compression took place in the sample. It is also possible that the PZT was not sufficiently constrained so that it was pushed out of the holder as the voltage increased, rather than inducing significant deformation of the sample.

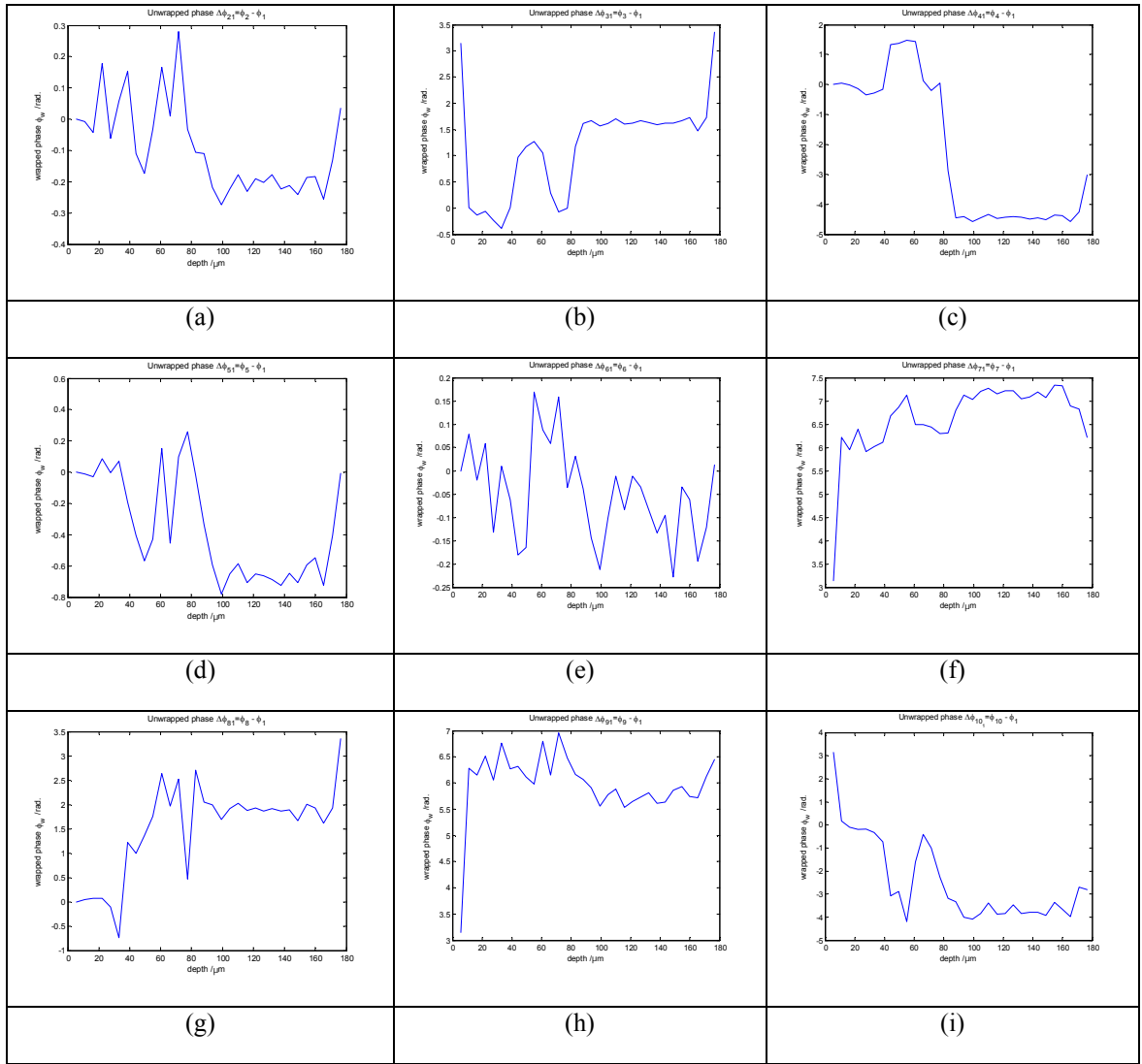


Figure 7.26. The measured phase difference at various voltage difference (a) V2-V1, (b) V3-V1, (c) V4-V1, (d) V5-V1, (e) V6-V1, (f) V7-V1, (g) V8-V1, (h) V9-V1, (i) V10-V1.

Another possibility is that the density of the scattering points is too high so that the light could not penetrate sufficiently deeply into the sample. Therefore even if the deeper layers really moved due to the displacement by the PZT, due to the absence of light, the phase change would not be observed from these layers.

In standard LCI theory it is always assumed the detected signal comes from the interference between the reference and the backscattered light. There is also the possibility that the light undergoes multiple scattering inside the sample thus creating a longer distribution of optical paths than that of direct backscattering. The multiple scattering light will appear as additional higher modulating frequency components (appearing to be from a range of depth values) depending on how far the accrued optical path compares to that of

the desired backscattered component [24]. The high density of the grains inside the sample will inevitably increase the possibility of multiple scattering.

Another possible explanation to the problem is that the grain seeding density does not meet the theoretical requirement as derived in Section 7.3.3.2. If this requirement is not met then the clear areas in a particular depth layer that is bigger than the lateral resolution of the system would not contribute to the modulation information from that depth slice. However, the fact that the data from each slice is averaged to give the plots in Figure 7.26 suggests that, even if some clear regions are present, the data should still be valid provided a few particles are present within each slice.

Although the system appears to be close to providing useful data, the above considerations suggest that some further work is still required in order to show the capability of the HSI system to perform depth-resolved displacement field measurements in a single-shot.

Chapter 8

Conclusions and Future Works

8.1. Summary of the research work

A new approach to the absolute measurement of two-dimensional optical path differences has been presented in this thesis. The method, which incorporates a white light interferometer and a hyperspectral imaging system, is referred to throughout the thesis as Hyperspectral Interferometry. A prototype of the Hyperspectral Interferometry (HSI) system has been designed, constructed and tested for two types of measurement: for surface profilometry and for depth-resolved displacement measurement, both of which have been implemented so as to achieve single shot data acquisition. The surface profilometry system was applied to two types of surface finish: the optically flat and optically rough planes. For depth-resolved displacement field measurement the test object was a scattering translucent material.

The literature and theoretical review presented in Chapter 2 has indicated that the single-shot feature of the system can be implemented by combining a broadband interferometer and the hyperspectral imaging system, from which – as stated above - the prototype name is derived. The combination of the two elements enables the acquisition of the multiple spectral interferograms in a single frame, which provides the key feature of single-shot measurement.

The first design of the prototype involved the use of a microlens array to capture the multiple spectral interferograms. This has been described in detail in Chapter 3. The approach had unfortunately been unable to meet the main condition of a single-shot measurement previously ascribed, as the well-defined multispectral interferogram images were not able to be identified.

Another approach was described subsequently in Chapter 4 on the use of an etalon to spectrally separate the multiple spectral interferograms. This approach has been shown to work well and meet the single-shot measurement condition above. Details of the design of this new approach are also presented in this chapter.

The recorded multiple spectral interferograms are subsequently used to build the Hyperspectral (interferogram) image volume. From this data volume the measurement output data are extracted. Chapter 5 presents the method to construct the hyperspectral

image volume, along with methods of information extraction as well as techniques to suppress unwanted signal that may be present in the recorded data.

Chapter 6 reports the first application of the prototype for 3-D surface profilometry. The prototype has been shown to be capable of performing a single-shot 3-D shape measurement of an optically flat step height sample, with less than 5% difference from the result obtained by a standard optical (microscope) based method. Two main parameters of the prototype, i.e., depth range and depth resolution, have been derived theoretically for the experimental set-up. The HSI prototype has been demonstrated to be able to perform single-shot measurement with an unambiguous 352 μm depth range and a measurement rms error of around 80 nm. An experiment also on surface measurement but with an optically rough surface is also presented in this chapter. Whilst in the smooth surface measurement the recorded interferogram displays clear and well-defined fringes, in the experiment on rough surfaces no clear fringes are observed and only speckles are detected. The intensity level of the light in this measurement is also lower than that of smooth surfaces. The rough surface measurement is therefore more challenging than the optically flat counterpart. The rms error of this measurement was found to increase to around $4 \times$ that of the smooth surface, due to the fact that measured sample is no longer optically smooth.

Finally chapter 7 describes the results of the first tests of the prototype for application to single-shot depth-resolved displacement field measurement. This experiment intrinsically has more challenging aspects compared to that of rough surface profilometry. Not only does the speckle pattern come from the surface, but the depth slices underneath the surface also contribute to the formation of the pattern. Furthermore the detected light is not only coming from direct backscattering, but may also come from multiply-scattered wavefronts inside the material. In this measurement the depth range also halved compared to that of profilometry (i.e., down to 175 μm), making the sample very thin and more difficult to fabricate. The experimental result did not show the expected result of linear phase relation with the displacement provided by the PZT actuator. Analysis of several factors has been carried out with the most plausible reason of excessive scattering particle density inside the sample and the possibility of insignificant deformation of the sample due to insufficient physical contact between the transducer and the sample.

8.2. Further work

An essential issue that needs to be addressed immediately is the automation of the system. Currently all measurements are conducted off-line, and not in real-time. Also the data acquisition was carried out manually i.e. which involved a lot of manual button pressing, clicking and light blocking on the set-up to obtain separate image from the reference and object, instead of one click to do the whole process. As an example, in the depth-resolved measurement experiments, the total amount of time taken to acquire the three images (reference, object and interferogram) and subsequently followed by data processing to obtain the depth-resolved amplitude distribution such as that shown in Fig.7.24, is almost 5 minutes. Recording a number of depth images to position the sample in front of the interferometer (the process illustrated in Fig.7.23) is quite time consuming. If the sample is not entirely stationary during the measurement, for example due to the disturbance from the environment or as the result of the manual activities for light blocking, it can adversely alter the interferogram. This problem could be reduced by employing a brighter light source, or by increasing the efficiency of the optical system, to allow a reduction of the exposure time. On a more technical issue, the final CCD camera performance must also be improved. Whilst inherently the camera used has a high dynamic range (up to 16 bits), due to a technical problem which has not been resolved yet, the analogue-to-digital-conversion (ADC) of the current imager can only sample an image with 8-bit depth, which significantly reduces the dynamic range of the signal. The other issue about the camera is that in real experiments, working with a 20-pixel (or less) wide sub-image is not an easy task. The imaging system unfortunately has no feature to allow magnification of the recorded image, thus the image again must be recorded first and magnified off-line. A significant amount of time would be saved if this facility were available in real time during the data acquisition. Furthermore, a calibration of the sensor camera must be performed to identify and correct for the possibility of spatial variations in pixel sensitivity.

Work on the depth-resolved displacement measurement must be carried out again to evaluate the performance of the prototype for this measurement task. The use of finer grains with lower density to prepare the sample, following the analysis developed in Sect.7.8, could potentially improve the penetration depth of the light and reduce the possibility of the adverse multi-scattering effect inside the sample. In terms of sample preparation, trapped air bubbles were also found inside the sample. Most likely these bubbles were trapped during the mixing of the grains with the resin i.e. the stirring of the grain inside the resin to uniformly mix the scattering particles inside the base material can

trap ambient air inside the sample. Therefore to reduce these undesired particles a continuous, slower, but at constant speed stir to mix the grains must be done, which is difficult to achieve manually. Alternatively, placing the sample in a vacuum chamber after mixing can be effective at removing trapped bubbles.

Further tests on optically rough surfaces also need to be performed. The results presented in Sect.6.4 on a painted surface are not a true representation of rough surface measurements on industrially important surfaces such as machined metal. The use of standard metrology gauge blocks, or roughness standard samples for example, could be good objects to perform this test.

Regarding the HSI prototype system itself, further work could be carried out to improve the performance. For example, another experiment to identify the fringe visibility as function of OPD should be carried out. In smooth object experiments where the light is abundant, the fringe visibility will not be a serious problem. In depth-resolved measurements on random volume scattering particles, however, the speckle intensity level is much lower. If sample was not correctly positioned, the obtained OPD would result in low visibility fringe and degrade the SNR. Also a significant accuracy improvement can be expected to be obtained by employing larger bandwidth light, which will improve the depth resolution and hence the depth accuracy. A more efficient use of the sensor frame to capture more spectral interferograms will improve the depth range.

If those factors above can be improved, it can be expected that the Hyperspectral Interferometry system developed in this research can be potentially be a true single-shot optical system capable of performing both measurement tasks of 3-D surface profilometry and depth-resolved displacement fields, with measurement resolution and range comparable to or better than the conventional systems that can only do the two measurement tasks separately, and which are also inherently prone to environmental disturbance due to the scanning-based mechanisms.

References

- [1] E. Doebelin, *Measurement Systems*. NY: McGraw-Hill, 1990.
- [2] H. J. Tiziani, "Optical metrology of engineering surfaces-scope and trends," in *Optical Measurement Techniques and Applications*, P. K. Rastogi, Ed. Boston: Artech House, 1997, pp. 15.
- [3] R. Jones and C. Wykes, *Holographic and Speckle Interferometry*. Cambridge: Cambridge University Press, 1989.
- [4] J. Schwider, Ed., *Advanced Evaluation Techniques in Interferometry*. Elsevier, 1990.
- [5] J. M. Huntley, "Automated analysis of speckle interferograms," in *Digital Speckle Pattern Interferometry and Related Techniques*, P. K. Rastogi, Ed. Chichester, England: Wiley, 2001, pp. 59.
- [6] P. D. Ruiz, Y. Zhou, J. M. Huntley and R. D. Wildman, "Depth-resolved whole-field displacement measurement using wavelength scanning interferometry," *J. Opt. A: Pure Appl. Opt.*, vol. 6, pp. 679, 2004.
- [7] B. L. Danielson and C. Y. Boisobert, "Absolute optical ranging using low coherence interferometry," *Appl. Opt.*, pp. 2975, 1991.
- [8] T. Y. Liu and J. Cory, "Partially multiplexing sensor network exploiting low coherence interferometry," *Appl. Opt.*, vol. 32, pp. 1100, 1993.
- [9] M. J. Yadlowsky and J. Schmitt, "Multiple scattering in optical coherence microscopy," *Appl. Opt.*, vol. 34, pp. 5699, 1995.
- [10] R. Windecker and H. J. Tiziani, "Optical roughness measurements using extended white-light interferometry," *Opt. Eng.*, vol. 38, pp. 1081, 1999.
- [11] P. De Groot and L. Deck, "Three-dimensional imaging by sub-Nyquist sampling of white-light interferograms," *Opt. Lett.*, vol. 18, pp. 1462, 1993.
- [12] P. De Groot and L. Deck, "Surface profiling by analysis of white-light interferograms in the spatial frequency domain," *J. Mod. Opt.*, vol. 42, pp. 389, 1995.
- [13] P. de Groot, "Vibration in phase-shifting interferometry," *J. Opt. Soc. Am.*, vol. 12, pp. 354, 1995.
- [14] P. A. Flournoy, R. W. McClure and G. Wyntjes, "White-light interferometric thickness gauge," *Appl. Opt.*, vol. 11, pp. 1907, 1972.
- [15] J. Schwider, "White-light Fizeau interferometer," *Appl. Opt.*, vol. 36, pp. 1433, 1997.
- [16] D. Kim, D. Kim, H. J. Kong and Y. Lee, "Measurement of thickness profile of a transparent thin film deposited upon a pattern structure with an acousto-optic tunable filter," *Opt. Lett.*, vol. 27, pp. 1893, 2002.
- [17] I. Verrier, M. Jacquot, G. Brun, C. Veillas and K. B. Houcine, "Imaging through scattering medium by recording 3D "spatial-frequency", " *Opt. Comm.*, vol. 267, pp. 310, 2006.

- [18] M. Kinoshita, M. Takeda, H. Yago, Y. Watanabe and T. Kurokawa, "Optical frequency-domain imaging microprofilometry with a frequency-tunable liquid-crystal Fabry-Perot etalon device," *Appl. Opt.*, vol. 38, pp. 7063, 1999
- [19] A. F. Fercher, W. Drexler, C. K. Hitzenberger and T. Lasser, "Optical coherence tomography-principles and applications," *Rep. Prog. Phys.*, vol. 66, pp. 239, 2003.
- [20] I. Kuwamura S and Yamaguchi, "Wavelength scanning profilometry for real-time surface shape measurement," *Appl. Opt.*, vol. 36, pp. 4473, 1997.
- [21] P. D. Ruiz, J. M. Huntley and A. Maranon, "Tilt scanning interferometry:a novel technique for mapping structure and three-dimensional displacement fields with optically scattering media," *Proc. R. Soc. A*, vol. 462, pp. 2481, 2006.
- [22] D. S. Mehta, M. Sugai, H. Hinosugi, S. Saito, M. Takeda, T. Kurokawa, H. Takahashi, M. Ando, M. Shisido and T. Yoshizawa, "Simultaneous three-dimensional step-height measurement and high resolution tomographic imaging with a spectral interferometric microscope," *Appl. Opt.*, vol. 41, pp. 3874, 2002
- [23] H. -. Wang, J. A. Izatt and M. D. Kulkarni, "Optical coherence microscopy," in *Handbook of Optical Coherence Tomography*, B. E. Bouma and G. J. Tearney, Eds. NY: Marcel-Dekker, 2002, pp. 275.
- [24] P. D. Ruiz, J. M. Huntley and R. D. Wildman, "Depth-resolved whole-field displacement measurement by wavelength-scanning electronic speckle pattern interferometry," *Appl. Opt.*, vol. 44, pp. 3945, 2005.
- [25] M. Wojtkowski, A. Kowalczyk, R. Leitgeb and A. F. Fercher, "Full range complex spectral optical coherence tomography technique in eye imaging," *Opt. Lett.*, vol. 27, pp. 1415, 2002
- [26] M. W. Lindner, P. Andretzky, K. Kiesewetter and G. Hausler, "Spectral radar: Optical coherence tomography in the fourier domain," in *Handbook of Optical Coherence Tomography*, B. E. Bouma and G. J. Tearney, Eds. NY: Marcel-Dekker, 2002, pp. 335
- [27] U. Schnell and R. Dandliker, "Dispersive white-light interferometry for absolute distance measurement with dielectric multilayer systems on the target," *Opt. Lett.*, vol. 21, pp. 528, 1996.
- [28] E. Papastathopoulos, K. Koerner and W. Osten, "Chromatically dispersed interferometry with wavelet analysis," *Opt. Lett.*, vol. 31, pp. 589, 2006
- [29] D. Reolon, M. Jacquot, I. Verrier, G. Brun and C. Veillas, "Broadband supercontinuum interferometer for high resolution profilometry," *Opt. Exp.*, vol. 14, pp. 128, 2006
- [30] T. Widjanarko and R. C. Hardie, "A post-processing technique for extending depth of focus in conventional optical microscopy," *Opt. Laser Technol.*, vol. 34, pp. 299-305, JUN, 2002.
- [31] J. A. Izatt, M. R. Hee, G. M. Owen, E. A. Swanson and J. G. Fujimoto, "Optical Coherence Microscopy in Scattering Media," *Opt. Lett.*, vol. 19, pp. 590-592, APR 15, 1994
- [32] J. A. Izatt, M. D. Kulkarni, K. Kobayashi, M. V. Sivak, J. K. Barton and A. J. Welch, "Optical coherence tomography for biondiagnostics," *Opt. Photon News*, vol. 8, pp. 41, 1997.
- [33] R. Windecker, M. Fleischer, K. Koerner and H. J. Tiziani, "Testing micro devices with fringe projection and white-light interferometry," *Opt. Laser Eng.*, vol. 36, pp. 141, 2001.

- [34] G. S. Kino and S. S. C. Chim, "Mirau Correlation Microscope," *Appl. Opt.*, vol. 29, pp. 3775-3783, SEP 10, 1990.
- [35] M. H. de la Torre-Ibarra, P. D. Ruiz and J. M. Huntley, "Double-shot depth-resolved displacement field measurement using phase-contrast spectral optical coherence tomography," *Opt. Exp.*, vol. 14, pp. 9643, 2006.
- [36] L. Schwider J and Zhou, "Dispersive interferometric profilometer," *Opt. Lett.*, vol. 19, pp. 995, 1994
- [37] De la Torre Ibarra, Manuel H., P. D. Ruiz and J. M. Huntley, "Simultaneous measurement of in-plane and out-of-plane displacement fields in scattering media using phase-contrast spectral optical coherence tomography," *Opt. Lett.*, vol. 34, pp. 806-808, 2009.
- [38] J. M. Huntley, T. Widjanarko and P. D. Ruiz, "Hyperspectral interferometry for single-shot absolute measurement of two-dimensional optical path distributions," *Meas Sci Technol*, vol. 21, pp. 075304, 2010
- [39] D. Briers, "Interferometric optical testing)," in *Optical Measurement Techniques and Applications*, P. K. Rastogi, Ed. Boston: Artech House, 1997, pp. 87.
- [40] D. Post, B. Han and P. Ifju, *High Sensitivity Moire: Experimental Analysis for Mechanics and Materials*. NY: Springer-Verlag, 1994.
- [41] A. Yariv., *Introduction to Optical Electronics*. NY: Holt Rinehart Winston, 1976.
- [42] K. Creath, "Step Height Measurement using 2-Wavelength Phase-Shifting Interferometry," *Appl. Opt.*, vol. 26, pp. 2810-2816, 1987.
- [43] D. J. Bone, "Fourier fringe analysis: the two-dimensional phase unwrapping problem," *Appl. Opt.*, vol. 30, pp. 3627, 1991
- [44] P. de Groot, "What is frequency domain analysis?," R & D technical bulletin, Zygo Corp, Middlefield, Connecticut, September 1993
- [45] O. Sasaki, N. Murata and T. Suzuki, "Sinusoidal wavelength scanning interferometer with a superluminescent diode for step-profile measurement," *Appl. Opt.*, vol. 39, pp. 4589, 2000.
- [46] R. Onedera, H. Wakaumi and Y. Ishii, "Measurement technique for surface profiling in low-coherence interferometry," *Opt. Comm.*, vol. 254, pp. 52, 2005.
- [47] A. R. Somervell and T. H. Barnes, "Fast, accurate measurement of path difference with white light," *J. Mod. Opt.*, vol. 50, pp. 2781, 2003.
- [48] J. W. Goodman, *Introduction to Fourier Optics*. McGraw-Hill, NY, 1996.
- [49] C. Polhemus, "Two-wavelength interferometry," *Appl. Opt.*, vol. 12, pp. 2071, 1973.
- [50] Y. -. Cheng and J. C. Wyant, "Two wavelength phase shifting interferometry," *Appl. Opt.*, vol. 23, pp. 4539, 1984.
- [51] A. F. Fercher, H. Z. Hu and U. Vry "Rough surface interferometry with a two-wavelength heterodyne speckle interferometer," *Appl. Opt.*, vol. 24, pp. 2181, 1985
- [52] S. Kuwamura and Y. Yamaguchi, "Wavelength scanning profilometry for real-time surface shape measurement," *Appl. Opt.*, vol. 36, pp. 4473, 1997

- [53] J. Y. Cheng and J. C. Wyant, "Multiple-wavelength phase shifting interferometry," *Appl. Opt.*, vol. 24, pp. 804, 1985.
- [54] R. D. Alcock and J. M. Coupland, "A compact, high numerical aperture imaging Fourier transform spectrometer and its application," *Meas Sci Technol*, vol. 17, pp. 2861-2868, 2006.
- [55] S. Jorez, A. Cornet and J. - Raskin, "MEMS profilometry by low coherence phase shifting interferometry: Effect of the light spectrum for high precision measurements," *Opt. Comm.*, vol. 263, pp. 6, 2006.
- [56] Z. Duan, Y. Miyamoto and M. Takeda, "Dispersion-free absolute interferometry based on angular spectrum scanning," *Opt. Exp.*, vol. 14, pp. 655, 2006.
- [57] P. Hlubina, "Dispersive white-light spectral interferometry to measure distances and displacements," *Opt. Comm.*, vol. 212, pp. 65, 2002
- [58] B. Bouma, G. J. Tearney (eds.), *Handbook of Optical Coherence Tomography*. NY: Marcel-Dekker, NY, 2002.
- [59] . Yamaguchi, A. Yamamoto and M. Yano, "Surface tomography by wavelength scanning interferometry," *Opt. Eng.*, vol. 39, pp. 40, 2000.
- [60] M. Takeda, H. Ina and S. Kobayashi, "Fourier-Transform Method of Fringe-Pattern Analysis for Computer-Based Topography and Interferometry," *J. Opt. Soc. Am.*, vol. 72, pp. 156-160, 1982.
- [61] M. Hart, D. G. Vass and M. L. Begbie, "Fast surface profiling by spectral analysis of white light interferograms with Fourier transform spectroscopy," *Appl. Opt.*, vol. 37, pp. 1764, 1998.
- [62] P. H. Tomlins and R. K. Wang, "Theory, developments and applications of optical coherence tomography," *Journal of Physics D-Applied Physics*, vol. 38, pp. 2519-2535, 2005.
- [63] Merriam-Webster Inc, *The Merriam-Webster Dictionary*, Merriam-Webster Inc, Springfield, Mass, 2008
- [64] A. F. Fercher, K. Mengedoht and W. Werner, "Eye-length measurement by interferometry with partially coherent light," *Opt. Lett.*, vol. 13, pp. 186, 1988.
- [65] T. Dressel, G. Hausler and H. Venzke, "Three-dimensional sensing of rough surfaces by coherence radar," *Appl. Opt.*, vol. 31, pp. 919, 1992.
- [66] M. Szkulmowski, M. Wojtkowski, T. Bajraszewski, I. Gorczynska, P. Targowski, W. Wasilewski, A. Kowalczyk and C. Radzewicz, "Quality improvement for high resolution in vivo images by spectral domain optical coherence tomography with supercontinuum source," *Opt. Comm.*, vol. 246, pp. 569, 2005.
- [67] P. Targowski, M. Wojtkowski, A. Kowalczyk, T. Bajraszewski, M. Szkulmowski and I. Gorczynska, "Complex spectral OCT in human eye imaging in vivo," *Opt. Comm.*, vol. 229, pp. 79, 2004.
- [68] S. R. Chinn and E. A. Swanson, "Optical coherence tomography for high-density data storage," in *Handbook of Optical Coherence Tomography*, B. E. Bouma and G. J. Tearney, Eds. NY: Marcel-Dekker, 2002, pp. 385.
- [69] J. P. Dunkers, "Applications of optical coherence tomography to the study of polymer matrix composite," in *Handbook of Optical Coherence Tomography*, B. E. Bouma and G. J. Tearney, Eds. NY: Marcel-Dekker, 2002, pp. 421.

- [70] E. Jonathan, "Non-contact and non destructive testing of silicon V-grooves: A non-medical application of Optical Coherence Tomography (OCT)," *Opt. Laser Eng.*, vol. 44, pp. 1117, 2006.
- [71] F. A. Jenkins and H. E. White, *Fundamentals of Optics*. McGraw-Hill, NY, 2001.
- [72] E. Hecht and A. Zajac, *Optics*. Addison-Wesley, Reading, Mass, 2002.
- [73] P. Sandoz, "An algorithm for profilometry by white-light phase-shifting interferometry," *Journal of Modern Optics*, vol. 43, pp. 1545-1554, 1996.
- [74] L. Deck and P. de Groot, "High speed non-contact profiler based on scanning white light interferometry," *Appl. Opt.*, vol. 33, pp. 7334, 1994
- [75] P. De Groot, X. C. de Lega, J. Kramer and M. Turzhitsky, "Determination of fringe order in white light interference microscopy," *Appl. Opt.*, vol. 41, pp. 4571, 2002
- [76] F. T. S. Yu, *Optical Information Processing*. Florida: Krieger Publishing Co. Malabar, 1984.
- [77] M. Born and E. Wolf, *Principles of Optics*. Pergammon Press, London, 1970
- [78] J. A. Izatt and M. A. Choma, "Theory of optical coherence tomography," in *Optical Coherence Tomography: Technology and Applications*, W. Drexler and J. G. Fujimoto (eds.) 2008, pp. 47.
- [79] M. Takeda and H. Yamamoto, "Fourier-transform speckle profilometry: three dimensional shape measurement of diffuse objects with large height step and/or spatially isolated surfaces," *Appl. Opt.*, vol. 33, pp. 7829, 1994
- [80] C. K. Hitzenberger, "Measurement of corneal thickness by low coherence interferometry," *Appl. Opt.*, vol. 31, pp. 6637, 1992
- [81] H. Matsumoto and A. Hirai, "A white-light interferometer using a lamp source and heterodyne detection with acousto-optic modulators," *Opt. Comm.*, vol. 170, pp. 217, 1999
- [82] A. Lulli, P. Zanetta, A. C. Lucia and F. Casagrande, "Contrast variations in white-light speckle interferometry with application to 3D profilometry," *Opt. Comm.*, vol. 124, pp. 550, 1996.
- [83] P. Hariharan and M. Roy, "White-Light Phase-Stepping Interferometry for Surface Profiling," *Journal of Modern Optics*, vol. 41, pp. 2197-2201, 1994
- [84] P. Hariharan and M. Roy, "Interferometric surface profiling with white light: Effects of surface films," *Journal of Modern Optics*, vol. 43, pp. 1797-1800, 1996
- [85] S. S. Helen, M. P. Kothiyal and R. S. Sirohi, "Analysis of spectrally resolved white light interferograms: use of a phase shifting technique," *Opt. Eng.*, vol. 40, pp. 1329, 2001.
- [86] P. Sandoz, G. Tribillon and H. Perrin, "High-resolution profilometry by using phase calculation algorithms for spectroscopic analysis of white-light interferograms," *J. Mod. Opt.*, vol. 43, pp. 701, 1996.
- [87] L. Rovalti, U. Minoni, M. Bonardi and F. Docchio, "Absolute distance measurement using comb-spectrum interferometry," *J. Opt.*, vol. 29, pp. 121, 1998.
- [88] J. E. Calatroni, P. Sandoz and G. Tribillon, "Surface profiling by means of double spectral modulation," *Appl. Opt.*, vol. 32, pp. 30, 1993

- [89] E. Wolf, "Three-dimensional structure determination of semi-transparent objects from holographic data," *Opt. Comm.*, vol. 1, pp. 153, 1969
- [90] P. D. Ruiz, J. M. Huntley, J. M. Coupland, "Depth-resolved imaging and displacement measurement techniques viewed as linear filtering operations", *Experimental Mechanics*, 2010, 13pp. (DOI: 10.1007/s11340-010-9393-8)
- [91] T. Endo, Y. Yasuno, S. Makita, M. Itoh and T. Yatagai, "Profilometry with line-field Fourier-domain interferometry," *Opt. Exp.*, vol. 13, pp. 695, 2005.
- [92] S. Constantino, O. E. Martinez and J. R. Torga, "Wide band interferometry for thickness measurement," *Opt. Exp.*, vol. 11, pp. 952, 2003
- [93] D. Kim, S. Kim, H. J. Kong, Y. Lee and Y. K. Kwak, "Fast thickness profile measurement using a peak detection method based on an acousto-optic tunable filter," *Meas. Sci. Technol.*, vol. 13, pp. L1, 2002.
- [94] D. Kim and S. Kim, "Direct spectral phase function calculation for dispersive interferometric thickness profilometry," *Opt. Exp.*, vol. 12, pp. 5117, 2004
- [95] B. Qi, G. R. Pickrell, J. C. Xu, P. Zhang, W. Peng, Z. Huang, W. Huo, H. Xiao, R. G. May and A. Wang, "Novel data processing techniques for dispersive white light interferometer," *Opt. Eng.*, vol. 42, pp. 3165, 2003.
- [96] P. Sandoz, R. Devillers and A. Plata, "Unambiguous profilometry by fringe-order identification in white-light phase shifting interferometry," *J. Mod. Opt.*, vol. 44, pp. 519, 1997.
- [97] A. Pfoetner and J. Schwider, "Dispersion error in white-light Linnik interferometers and its implications for evaluation procedures," *Appl. Opt.*, vol. 40, pp. 6223, 2001.
- [98] H. Kikuta, K. Iwata and R. Nagata, "Distance measurement by the wavelength shift of laser diode light," *Appl. Opt.*, vol. 25, pp. 2976, 1986
- [99] H. Kikuta, K. Iwata and R. Nagata, "Absolute distance measurement by wavelength shift interferometry with a laser diode: some systematic error sources," *Appl. Opt.*, vol. 26, pp. 1654, 1987.
- [100] M. Suematsu and M. Takeda, "Wavelength-shift interferometry for distance measurements using the Fourier transform technique for fringe analysis," *Appl. Opt.*, vol. 30, pp. 4046, 1991.
- [101] K. Hotate and T. Okugawa, "Selective extraction of two-dimensional optical image by synthesis of the coherence function," *Opt. Lett.*, vol. 17, pp. 1529, 1992
- [102] T. C. Strand and Y. Katzir, "Extended unambiguous range interferometry," *Appl. Opt.*, vol. 26, pp. 4274, 1987.
- [103] B. S. Lee and T. C. Strand, "Profilometry with a Coherence Scanning Microscope," *Appl. Opt.*, vol. 29, pp. 3784-3788, 1990.
- [104] S. C. Chim and G. S. Kino, "Correlation microscope," *Opt. Lett.*, vol. 15, pp. 579, 1990.
- [105] S. C. Chim and G. S. Kino, "Three-dimensional image realization in interference microscopy," *Appl. Opt.*, vol. 31, pp. 2550, 1992.
- [106] H. Saint-Jalmes, M. Lebec, E. Beaurepaire, A. Dubois and A. C. Boccara, "Full-field optical coherence microscope," in *Handbook of Optical Coherence Tomography*, B. E. Bouma and G. J. Tearney (eds.), Marcel-Dekker, NY 2002, pp. 299.

- [107] K. L. Baker and E. A. Stappaerts, "A single-shot pixellated phase-shifting interferometer utilizing a liquid-crystal spatial light modulator," *Opt. Lett.*, vol. 31, pp. 733, 2006.
- [108] M. Sugiyama, H. Ogawa, K. Kitagawa and K. Suzuki, "Single-shot surface profiling by local model fitting," *Applied Optics*, vol. 45, pp. 7999, 2006
- [109] T. Yokota, M. Sugiyama, H. Ogawa, K. Kitagawa and K. Suzuki, "Interpolated local model fitting method for accurate and fast single-shot surface profiling," *Appl. Opt.*, vol. 48, pp. 3497-3508, 2009
- [110] W. -. Su and H. Liu, "Calibration-based two-frequency projected fringe profilometry: a robust, accurate, and single shot measurement for objects with large depth discontinuities," *Opt. Exp.*, vol. 14, pp. 9178, 2006.
- [111] N. I. Toto-Arellano, G. Rodriguez-Zurita, C. Meneses-Fabian and J. F. Vazquez-Castillo, "A single-shot phase-shifting radial-shearing interferometer," *J. Opt. A-Pure Appl. Opt.*, vol. 11, pp. 045704, 2009.
- [112] G. Rodriguez-Zurita, N. I. Toto-Arellano, C. Meneses-Fabian and J. F. Vazquez-Castillo, "Adjustable lateral-shear single-shot phase-shifting interferometry for moving phase distributions," *Meas Sci Technol*, vol. 20, pp. 115902, 2009.
- [113] M. S. Hrebesh, Y. Watanabe and M. Sato, "Profilometry with compact single-shot low-coherence time-domain interferometry," *Opt. Commun.*, vol. 281, pp. 4566-4571, 2008.
- [114] S. Ri, M. Fujigaki and Y. Morimoto, "Single-shot three-dimensional shape measurement method using a digital micromirror device camera by fringe projection," *Opt. Eng.*, vol. 48, pp. 103605, 2009
- [115] E. L. Lago and R. de la Fuente, "Single-shot amplitude and phase reconstruction by diffracted-beam interferometry," *Journal of Optics A-Pure and Applied Optics*, vol. 11, p. 125703, 2009
- [116] Y. Delacretaz, N. Pavillon, F. Lang and C. Depeursinge, "Off-axis low coherence interferometry contouring," *Opt. Commun.*, vol. 282, pp. 4595-4601, 2009
- [117] S. Witte, M. Baclayon, E. J. G. Peterman, R. F. G. Toonen, H. D. Mansvelder and M. L. Groot, "Single-shot two-dimensional full-range optical coherence tomography achieved by dispersion control," *Opt. Express*, vol. 17, pp. 11335-11349, 2009.
- [118] M. Hering, S. Herrmann, M. Banyay, K. Koerner and B. Jaehne, "One-shot line-profiling white light interferometer with spatial phase shift for measuring rough surfaces - art. no. 61880E," *Optical Micro- and Nanometrology in Microsystems Technology*, vol. 6188, pp. E1880-E1880, 2006.
- [119] N. Koukourakis, C. Kasseck, D. Rytz, N. C. Gerhardt and M. R. Hofmann, "Single-shot holography for depth resolved three dimensional imaging," *Optics Express*, vol. 17, pp. 21015-21029, 2009
- [120] L. Martinez-Leon, M. Araiza-E, B. Javidi, P. Andres, V. Climent, J. Lancis and E. Tajahuerce, "Single-shot digital holography by use of the fractional Talbot effect," *Opt. Express*, vol. 17, pp. 12900-12909, 2009
- [121] J. Lawlor, D. W. Fletcher-Holmes, A. R. Harvey and A. I. McNaught, "In vivo hyperspectral imaging of human retina and optic disc," *Invest. Ophthalmol. Vis. Sci.*, Vol. 43, pp. 4350, 2002
- [122] A. R. Harvey, A. Lawlor, A. I. McNaught, J. W. Williams and D. W. Fletcher-Holmes, "Hyperspectral imaging for the detection of retinal diseases," *Proc. SPIE 4816 Imaging*

Spectrometry VIII, pp. 325-335, 2002

[123] Jeremy Allington-Smith, "Basic principles of integral field spectroscopy," *New Astron.Rev.*, Vol. 50, iss. 4-5, pp. 244-251, 2006

[124] F. Melgani and L. Bruzzone, "Classification of hyperspectral remote sensing images with support vector machines", *IEEE Transactions on Geoscience and Remote Sensing*, Vol.42, iss.8,pp.1778-1790, 2004

[125] Robert A. Schowengerdt, "Remote sensing: models and methods for image processing", Academic Press, Burlington, MA, 2007

[126] I. Alabboud, G. Muyo, A. Gorman, D. Mordant, A. McNaught, C. Petres, Y. R. Petillot and A. R. Harvey, "New spectral imaging techniques for blood oximetry in the retina", *Proc.SPIE 6631 Novel Optical Instrumentation for Biomedical Applications III*, art. no. 66310L, 2007

[127] A. R. Harvey, I. Abboud, A. Gorman, A. McNaught, S. Ramachandran and E. Theofanidou, "Spectral imaging of the retina," *Proc.SPIE 6047 Fourth International Conference on Photonics and Imaging in Biology and Medicine*, art. no. 604713, 2006

[128] D. W. Fletcher-Holmes, A. R. Harvey, "Real-time imaging with a hyperspectral fovea", *J.Opt.A-Pure Appl.Opt.*, Vol.7, iss.6, S298-S302, 2005

[129] D. W. Fletcher-Holmes, A. R. Harvey, "A snapshot foveal hyperspectral imager," *Proc.SPIE 4816 Imaging Spectrometry VIII*, pp.407-414, 2002

[130] Y. Inoue, J. Penuelas, " An AOTF-based hyperspectral imaging system for field use in ecophysiological and agricultural applications," *Int. J. Remote Sensing*, Vol.22,iss.18,p.3883, 2001

[131] J. M. Eichenholz, J. Dougherty, " Ultracompact Fully Integrated MegaPixel MultiSpectral Imager," *Proc.SPIE 7218 Integrated Optics: Devices, Materials, and Technologies XIII*, p. 721814, 2008

[132] L. Dubois, A. Vabre, A. C. Boccara and E. Beaufrepaire, "High-resolution full-field optical coherence tomography with a Linnik microscope," *Appl.Opt.*, Vol.41, iss. 4, pp. 805-812, 2002

[133] Y. Chen, S.W. Huang, A. D. Aguirre, J. G. Fujimoto, " High-resolution line-scanning optical coherence microscopy," *Opt.Lett.*, Vol.32, iss.14, pp.1971-1973, 2007

[134] Superlum Diodes Ltd, "Acceptance test report: Superlum BroadLighters S-840-HP-I Fiber Lightsource at 840 nm Serial No.0059", 2008

[135] C. Palmer, "Diffraction Grating Handbook," Thermo Richardson Grating Laboratory, Rochester, NY, 2002

[136] Linos Photonics, " Microlens array, fused silica, type FC-Q-100 Square", Catalog International 2007/2008, Linos AG, 2007

[137] W. Smith, "Basic optical devices," in *Modern Optical Engineering*, Ch.9, McGraw-Hill, NY, 2000

[138] J. M. Huntley, "Laser speckle and its application to strength measurement and crack propagation," *PhD Thesis*, University of Cambridge, 1986

[139] W. Smith, "Stops and apertures," in *Modern Optical Engineering*, Ch.6, McGraw-Hill, NY, 2000

[140] R. Haynes, " Depth of field and depth of view," in *Optical Microscopy of Materials*, Ch.3, International Textbook Company, Glasgow, 1984


- [141] F. Sigernes, D. A. Lorentzen, K. Heia and T. Svenoe, "Multipurpose spectral imager," *Appl. Opt.*, vol. 39, pp. 3143-3153, 2000.
- [142] K. Chuang, H. Wang and F. Yang, "Design of a aberration-corrected VIS–NIR imaging spectrograph," *Opt. Commun.*, vol. 272, pp. 330-335, 2007.
- [143] W. L. Wolfe, *Introduction to Imaging Spectrometers*. Bellingham,WA: SPIE, 1997.
- [144] T. Bajraszewski, M. Wojtkowski, M. Szkulmowski, A. Szkulmowska, R. Huber, A. Kowalczyk," Improved spectral optical coherence tomography using optical frequency comb," *Opt.Exp.*, Vol.16. iss.6, pp. 4163-4176, 2008
- [145] S. J. Lee, B. Widyatmoko, M. Kourog, M, Ohtsu," Ultrahigh scanning speed optical coherence tomography using optical frequency comb generators," *Jpn.J.Appl.Phys.Part 2 - Lett.*, Vol. 40, iss.8B, L878-L880, 2001
- [146] V. Shidlovski, "Superluminescent diodes.application notes.SLD sensitivity to optical feedback," Superlum Diodes Ltd, Moscow, 2006.
- [147] D. Mamedov, "Loss factors," Oct 2008 (*personal communications*).
- [148] D. Mamedov, "Estimation of optical feedback," September 2008 (*personal communications*).
- [149] D. Mamedov, "Characteristics of optical isolators used in BroadLighter type S-840," Superlum Diodes Ltd, Moscow, September 2008.
- [150] J. M. Huntley, "An Image-Processing System for the Analysis of Speckle Photographs," *Journal of Physics E-Scientific Instruments*, vol. 19, pp. 43-49, 1986
- [151] Kaufmann G H, Ennos A, Gale B and Pugh,D.J., "An electro-optic readout system for analysis of speckle photographs," *J.Phys.E: Sci Instrum.*, vol. 13, pp. 579, 1980.
- [152] S. C. Chapra, "Roots:Open methods," in *Applied Numerical Methods with Matlab*, 2nd ed.Anonymous McGraw-Hill, 2008, .
- [153] J. M. Huntley, T. Widjanarko and P. D. Ruiz," Hyperspectral interferometry in rough surafces - results from preliminary study,"*interim report* (unpublished), Loughborough, 2010
- [154] Z. Xu, L. Zhang and G. Chen, "Decay of electric charge on corona charged polyethylene," *J. Phys. D-Appl. Phys.*, vol. 40, pp. 7085-7089, 2007.
- [155] J. D. Kraus,"Polarization," in *Electromagnetics*, Ch.3, McGraw-Hill, NY, 1981
- [156] G. E. Dieter, *Mechancial Metallurgy*. New York: McGraw-Hill, NY, 1989.
- [157] M. H. De la Torre Ibarra. (2010), OCT scatterer test. (*personal communication*)
- [158] A. E. Ennos, "Speckle Interferometry,"in *Laser speckle and related phenomena* (J.W. Goodman ed.), Ch. 6, Springer-Verlag, Berlin, 1975
- [159] J. W. Goodman, "Statistical properties of laser speckle pattern,"in *Laser speckle and related phenomena* (J.W. Goodman ed.), Ch. 2, Springer-Verlag, Berlin, 1975

Appendices

Non-archived reference links

A1. Hyperspectral Imager (Photon etc)

(retrieved from <http://photonetc.com/documents/pdf/HI.pdf> ,on 21 April 2011, 11:01 GMT)




Photon etc

A spectrum of solutions

5795 DE GASPE AVENUE, #222
MONTREAL, QUEBEC, H2S 2X3
CANADA

VIS & SWIR HYPERSPECTRAL CAMERA



Giving complete information on your target with full resolution images at any wavelength, our Widefield HI will change your view of spectral analysis. The Widefield HI delivers a series of monochromatic images. The optimized hyperspectral cube allows for spectral analysis of each and every pixel of a full resolution image, meaning no more fastidious x-y or line scanning. Beside increasing efficiency, the Widefield HI provides data on both spectral and spatial content, allowing you to perform new analyses to push the boundaries of your most demanding applications.


STANDARD PRODUCTS	Spectral Range (nm)	Bandwidth (FWHM) (nm)
V-EDS	400-1000	2
S-EDS	1000-2500	4

TECHNICAL SPECIFICATIONS	
Spectral Window	400 to 2500 nm
Bandwidth (FWHM)	0.3 to 4 nm
Tuning Range	250 to 1300 nm
Peak Transmission	up to 60 %
Damage Threshold	> 100 kW/cm ² average power > 5 GW/cm ² peak power @ 1064 nm, 8 ns
Aperture Diameter	≤ 10 mm
Dimensions (L x W x H)	24" x 12" x 12" 61 cm x 30.5 cm x 30.5 cm
Operating Temperature	10 to 40°C
Storage Temperature	5 to 50°C
Software	PhySpec included or ActiveX drivers
Computer Connection	USB 2.0 (compatible 1.1)
Power Supply	100 - 240 V , 50 - 60 Hz
Absolute Wavelength Precision	0.1 nm (for FWHM = 0.3 nm)
Wavelength Relative Resolution	0.05 nm (for FWHM = 0.3 nm)

www.photonetc.com© 2010 Photon etc. Inc. All rights reserved.

A2. Hyperspectral Imager (Teledyne-Dalsa)

(retrieved from <http://www.dalsa.com/sensors/applications/hyperspectral.aspx> ,on 21 April 2011, 11:05 GMT)



TELEDYNE DALSA
A Teledyne Technologies Company

Log In | Language | Search

Image Sensor Solutions

Home | Company | Products | Applications | Support | News | Careers | Contact

APPLICATIONS

- Professional Photography
- Industrial Imaging
- Medical Imaging
- Aerospace Imaging
 - Multispectral
 - Hyperspectral
 - High Resolution Panchromatic
- Defense and Security Imaging

PRODUCTS

- Sensor Product List

TECHNOLOGY

- CCD Imager Technology
- CMOS Imager Technology
- CCD vs. CMOS Comparison

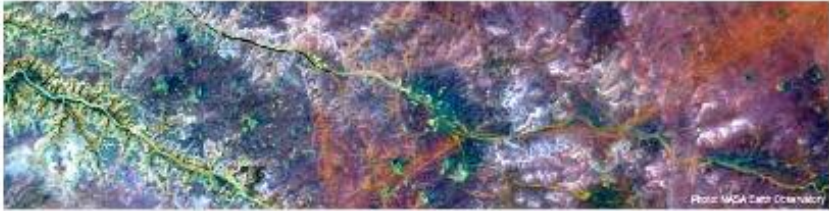


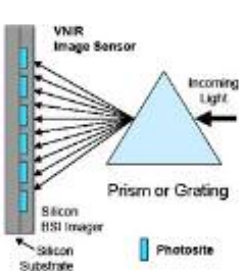
Photo: NASA Earth Observatory

New: Hyperspectral Imaging

Teledyne DALSA is pleased to offer new and expanded VNIR (Visible to Near Infrared) hyperspectral image sensor capability for remote sensing applications, such as environmental observation, defense and security and other earth observation applications.

Capabilities

- Monolithic hyperspectral imagers—multiple different imaging areas on one chip
- "Push-broom" linear and TDI sensors with X resolution to 12000+ pixels and unlimited Y resolution
- Back side illuminated (BSI) options for maximum sensitivity and QE
- Antireflective coatings to optimize QE
- Radiation tolerance/hardness
- Sophisticated packaging experience



Teledyne DALSA's custom products group is able to offer a number of new technologies to enable the latest improvements in hyperspectral imaging. In hyperspectral imaging, the incoming light signal is divided into bands that can span as little as a mere 10nm; the more sensitive the sensor, the greater its ability to produce useful information. More and more critical environmental information is available with the latest sensor technologies available from Teledyne DALSA. Key attributes to developing leading edge hyperspectral imaging are:

- ultra high quantum efficiency, back side thinning, high speed read rates, low defects and advanced packaging techniques.

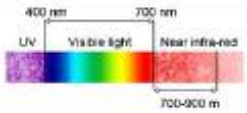
Teledyne DALSA is able to offer both CCD and CMOS detectors. CCDs are ideal where ultra low noise is preferred and CMOS where low power and high data/frame rates are more important. Typical requirements in hyperspectral imaging require back side thinning in order to get the highest quantum efficiency due to the spreading of the incoming light sensor over many pixels. In addition to back side thinning custom anti-reflection coatings further broaden the quantum efficiency in the VNIR (Visible to near IR) range.

With the fabrication possibility of ever smaller pixels (down to 4 microns square) high resolutions are obtainable and advanced architectures like spill frame frame transfer enable high dynamic range with low cross talk or blurring. In CMOS the use of partial region readout can enable the highest in frame scene dynamic range.

Multiple cost effective package choices are available with hermetic sealing. Designs are available for radiation hardness for extreme environments.

For more information email aerospace@dalsa.com.

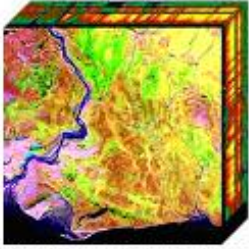
FEATURES



- High sensitivity and dynamic range
- CCD and CMOS solutions
- Extreme high throughput performance
- Linear resolution to 12000+ pixels
- Customizable pixel sizes
- Back side illumination options

MORE INFORMATION

Do you have a multispectral challenge? Let our experienced engineers and application specialists help. [Contact Teledyne DALSA](#) today.



Hyperspectral "cube" layering images with different spectra

A3. Hyperspectral Imager (Brimrose Corp)

(retrieved from http://www.brimrose.com/products/aotf_hyperspectral.html ,on 21 April 2011, 11:07 GMT)

BRIMROSE

[Home](#) [Contact Us](#) [About Us](#) [Products](#) [R&D](#) [Sitemap](#)

- ▶ Acousto Optics
- ▶ AOTF Light Sources
- ▶ AOTF Hyperspectral
- ▶ Fiber Optics
- ▶ NIR-MIR Spectrometers
- ▶ Process Control
- ▶ Laser Vibrometers
- ▶ R&D

The state-of-the-art AOTF devices operate at the heart of Brimrose's optical imaging systems. AOTF microscope and camera telescope video adapters in the visible or range were also designed for imaging and spectroscopy applications.

Application example:
[Brimrose AOTF Hyperspectral Imager for field use in ecophysiological and agricultural applications.](#)

On-line process monitoring and waste material sorting can also be performed with a NIR-MIR macro-spectral imaging system. Our AOTF video adapters can be used for both biomedical and semiconductor applications. Specially designed visible, NIR, and MIR spectral imaging systems have been utilized for environmental monitoring and remote sensing.





[Click here for a Video Presentation on AOTF Imaging System](#)

Our AOTF Hyperspectral Imaging system enhances image quality, enables an image more clear, and there is no image distortion. It has a higher spatial resolution, spectral resolution and equipped with radio-frequency drive software.

You will see some real-time applications using AOTF Hyperspectral Imaging System from this Video Presentation: AOTF Microscope image of pine stem over visible spectrum, AOTF Microscope image of onion epidermis over visible spectrum and AOTF Camera image of different color of letters, etc.

AOTF Camera Video Adapters and AOTF Microscope Video Adapters

Applications

- Laboratory and Industry Applications
- Environmental Science and Remote Sensing
- Biology and Biomedical Research
- Agriculture Monitoring
- Normal, Fluorescence, and Raman Spectral Imaging in Biomedical Industry
- On-Line Quality and Process Control
- Other OEM Applications

Specifications	VA210-.40-0.65	VA210-.55-1.0	VA210-.9-1.7
Device Type	Image Quality AOTF		
Wavelength Range	400-650nm	550-1000nm	900-1700nm
Spectral Resolution	2-6nm		5-20nm
Spatial Resolution	Up to 2560 x 1920 Pixels (6.4x 4.8 mm Camera Sensor Area)		1280 x 960 Pixels
For Camera Sensor Area*	6.4 x 4.8 mm (1/2")		12.8 x 9.6 mm
Field of View for Camera	1.5 - 6.5 deg with Nikon F-Mount Zoom Lens f70-300mm And 5.7 - 13 deg with Nikon F-Mount Zoom Lens f28-80mm		
Field of View for Microscope	1.6 mm with 4x objective lens 0.64mm with 10x objective lens 0.16mm with 40x objective lens		
Magnifications	1x		2x
Connection to Camera**	C-mount		
Lens Mount	C-Mount and F-Mount		
Driving Power	~2 Watts		
RF Connector	SMA		
Weight	< 1.0 kg		
Dimensions	W x H x D: 60 x 70 x 178 mm		

* Other dimensions or sensor area are available upon request.
** Other mounts are available upon request.

AOTF Hyperspectral Imaging

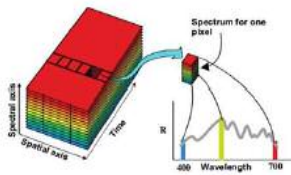
Price, Quoted Literature, Request Form

A5. Hyperspectral Imager (Gilden Photonics)

(retrieved from <http://www.gildenphotonics.com/Products/spectral-imaging/vnir-hyperspectral-imaging.aspx>, on 21 April 2011, 11:19 GMT)



<http://www.gildenphotonics.com>
sale@gildenphotonics.com
tel +44(0)141.952.9475
fax +44(0)141.952.9400



Spectral Imaging - VNIR

Hyperspectral camera operating in the VIS and VNIR ranges of 380-800 nm and 400-1000 nm. With its high spatial and spectral resolution, high image rate, and rugged structure, Spectral Camera, HS is an excellent tool for both industry and science.

Specim's spectral camera is an imaging spectrometer, i.e., an integrated combination of our ImSpector imaging spectrograph and an area monochrome camera. It works as a pushbroom type line scan camera and provides full, continuous spectral information for each pixel.


The Spectral Camera HS consists of ImSpector, V8E or V10E for the wavelength range 380-800 nm or 400-1000 nm, respectively and a sensitive high speed interlaced CCD detector. The transmission diffraction grating and lens optics used in the spectrograph provide a high quality, low distortion image that is designed to fulfill the most demanding specifications. The Spectral Camera HS provides outstanding performance at affordable cost. Spatial resolution of 1600 pixels, image rate up to 120 images/s, and adjustable spectral sampling make it a tool which can meet the highest industrial and scientific hyperspectral imaging requirements.

SPECIFICATIONS

Range (nm)	VIS 380 - 800/VNIR 400 - 1000
Sensor	CCD
V8E/V10E	380 - 800/400 - 1000
Interface	CameraLink
Frame rate (full frame)	33Hz
Pixels in full frame (spatial x Spectral)	1600 x 1200


A6. Hyperspectral Imager (Spectral Imaging Ltd)

(retrieved from http://www.specim.fi/media/pdf/product-brochures/specim_products-ver3-09.pdf, on 21 April 2011, 11:28 GMT)



HYPERSPETRAL IMAGING

SPECIM provides the most comprehensive line of hyperspectral imaging solutions. These products meet the unique requirements of industrial OEM clients and system integrators, as well as science and research customers. SPECIM also provides innovative hyperspectral solutions for remote sensing, military and security applications.




ImSpector V10E

ImSpector imaging spectrographs

SPECIM delivers industry standard spectrographs which employ our unique spectrographic technologies. These nearly polarization independent technologies provide high light throughput, and a high quality aberration-free image, in an extremely rugged device.

PRODUCT RANGE	
Raman	400 to 1000 nm
UV4E	200 – 400 nm
V8, V8E	380 – 800 nm
V10, V10E, Fast10	400 – 1000 nm
N17E	900 – 1700 nm
N25E	970 – 2500 nm
M30M	3000-5000nm
L120M	8000 – 12000 (14000) nm




SWIR Spectral Camera

Spectral Cameras

SPECIM offers a broad range of integrated and calibrated Spectral Cameras for line-imaging. These Spectral Cameras precisely measure all spectral data for each image pixel simultaneously. This push-broom operation is perfect for applications where either the target or camera is in motion.

In addition to providing standard products, system integration projects are often undertaken. At a customer's request, SPECIM is capable of partnering with the customer to develop unique Spectral Camera solutions, which are based on their own detailed requirements specification. Please contact SPECIM for more information.

PERFORMANCE GUIDE			
	Pixels	Spectral resol.	Speed, up to
UV	1000	2 nm	100 Hz
VIS/NIR	640 - 2K	2 - 15 nm	2000 Hz
NIR	320, 640	6 nm	350 Hz
SWIR	320	10nm	250 Hz
LWIR	384	150-400nm	100 Hz



100 channel fiber optical spectrometer

Multiple point spectrometers

Optionally, SPECIM ImSpectors spectrographs and Spectral Cameras may be equipped with multiple fibre optical inputs. The Spectral Camera records the spectrum of the incoming light through each of the fibre optical probes simultaneously, making a Multiple-Point Spectrometer without any moving parts. Up to 100 fibre optic probes can be coupled to a single spectrometer.

SPECIM also provides custom made fibre optical assemblies based on unique customer requirements. Some of the customisable features are:


- number of fibre channels
- length and
- light collection optics

HYPERSPETRAL IMAGING

A7. Hyperspectral Imager (Surface Optics)

(retrieved from http://www.surfaceoptics.net/products_details.php?id=18 , on 21 April 2011, 11:40 GMT)

[Home](#) [Company](#) [Contact Us](#)



SURFACE OPTICS CORP.

[HOME](#)

[MARKETS](#)

PRODUCTS & SERVICES


- [SPECTRAL IMAGING](#)
- [REFLECTOMETRY](#)
- [COATINGS](#)
- [MEASUREMENT SERVICES](#)
- [SOFTWARE](#)
- [DATABASE](#)
- [SERVICES SUPPORT](#)

[RESOURCES](#)


[NEWS & EVENTS](#)

[COMPANY](#)

[CONTACT US](#)



/ HOME / PRODUCT & SERVICES



Model SOC760

[More Info](#)

SOC700HZ / SOC760

STARING REAL-TIME, VIDEO-RATE SPECTRAL CAMERAS

Based on Surface Optics's highly successful SOC700 Visible-Near Infrared(VNIR) system, The SOC760 High-Speed Hyperspectral (HS) Imager is the fastest commercial real-time HS imaging system on the market today. Out of the box, the SOC760 can be used in demanding analysis, quality control and detection work.

Comprising a very high-speed, high sensitivity visible-near IR(VNIR) 512 x 512 pixel Si array, imaging spectrometer, integrated scanning system and vector processor, the SOC760 can acquire and process imagery at a rate of 80 mega-pixels per second at 14-bit resolution. The scan line speed is adjustable from 725 lps (1.5 cubes/sec) to 6700 lps(12 cubes/sec)The system's spectral response covers the visible to near-infrared spectral range from 0.4 – 1.0 microns and comes either as an imager or line scan camera. The spectral resolution is variable 2.8 to 25 nm.

With four programmable filters, three integration channels, on-the-fly dark frame subtraction and calibration, the system can be configured to display color, single-band or any user-specified three band sensor. The internal matched filters can be used to detect or reject with a high degree of confidence up to 4 different spectral fingerprints. The HS cube size is variable from 10 – 90 MB. The SOC760 imager is supported by SOC's custom HSAnalysis3 software with a user-friendly GUI.

Features:

- Sustains the speeds necessary to provide the immediate feedback that is required 50x's faster than conventional system, meeting the demands of time critical industrial applications.
- Low power – 50 watts
- Embedded PC for in camera, real-time HS processing
- Adjustable line scan speed – 725 - 6700/sec

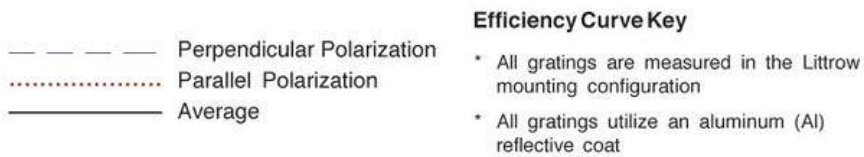
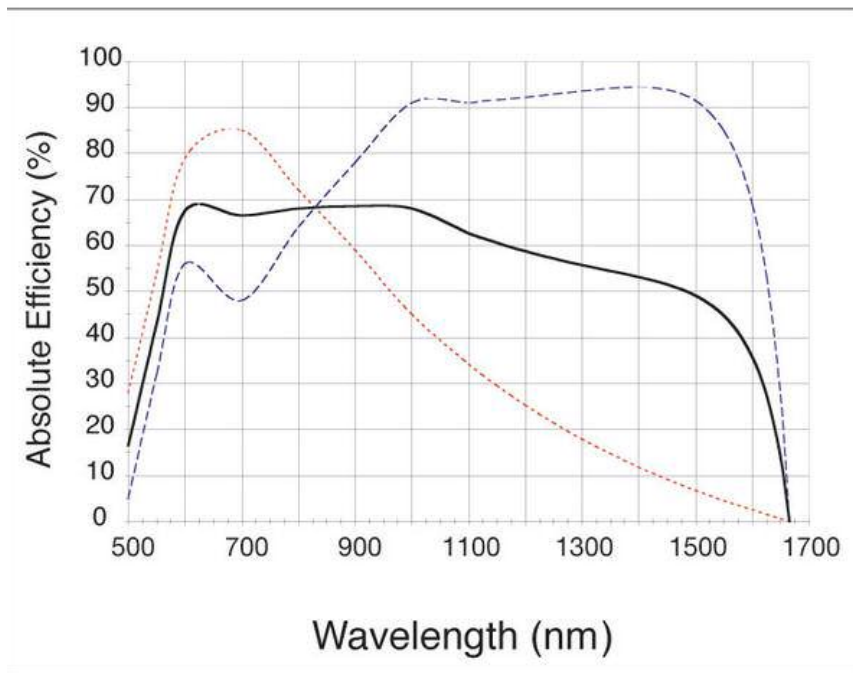
Contact
Phone: (868) 675-7404
Email: markd@surfaceoptics.com

189

A8. Grating efficiency plot


(retrieved from http://www.thorlabs.de/images/tabImages/N_1200Grv_Blz1.0_lrg.jpg on 29 April 2011, 18:17 GMT)

1200 grooves/mm Blazed at 1.0 μm



A9. Peak finding (Matlab) routine

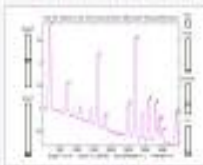
(retrieved from <http://www.mathworks.com/matlabcentral/fileexchange/11755-peak-finding-and-measurement-version-2> , on 22 April 2011, 16:07 GMT)



Search:

File Exchange
Answers
Howgroup
Link Exchange
Blogs
Contact
MathWorks.com

File Exchange



Peak finding and measurement (version 2)

by Tom O'Haver
20 Jul 2005 (Updated 03 Sep 2005)

Function to locate and measure the positive peaks in noisy data sets.

[Watch this file](#)

★★★★★

4.7 | 14 ratings

[Rate this file](#)

173 Downloads (last 30 days)

File Size: 27.73KB

File ID: #11755

Download All

Code covered by the [BSD License](#)

Highlights from Peak finding and measurement (version 2)

- fx* [AmpSlider\(n\)](#)
Changes AmpThreshold when the AmpThreshold slider is moved.
- fx* [BGSlider\(n\)](#)
Called when the BG slider is clicked.
- fx* [FWSlider\(n\)](#)
Changes FWHM when the FWHM slider is moved.
- fx* [Findpeaks\(x,y,SlopeThreshold,...\)](#)
Function
Findpeaks(x,y,SlopeThreshold,AmpThreshold,FWHM,PeakWidth,PeakGroup)
- fx* [FindpeaksSliderRedraw\(x,y,S,...\)](#)
Redraws graph for FindPeakSliders when slider are moved.
- fx* [PeakSlider\(n\)](#)
Changes PeakNumber when the Peak slider is moved.
- fx* [SlopeSlider\(n\)](#)
Changes SlopeThreshold when the SlopeThreshold slider is moved.
- fx* [SmoothSlider\(n\)](#)
Changes SmoothWidth when the SmoothWidth slider is moved.
- fx* [\[index,closestval\]=val2nd\(x,...\)](#)
Returns the index and the value of the element of vector x that is closest to val
- fx* [d=diff\(x\)](#)
First derivative of vector using 2-point central difference.
- fx* [d=secdiff\(x\)](#)
Second derivative of vector using 3-point central difference.

File Information

Description A fast customizable function for locating and measuring the peaks in noisy time-series signals. Adjustable parameters allow discrimination of "real" signal peaks from noise and background. Determines the position, height, and width of each peak by least-squares curve-fitting. It can find and measure 1000 peaks in a 1,000,000 point signal in 8 seconds. Includes two interactive versions, one with mouse-controlled sliders and one with keyboard control, for adjusting the peak-finding criteria in real-time. Self-contained demos show how it works. See <http://www.usm.edu/~toh/pep/run/FindpeaksandMeasurement.htm> for details.

Acknowledgements
This submission has inspired the following:
[Peak Interactive Peak Detector \(Version 1.1\)](#)

MATLAB release MATLAB 6.5 (R13)

Tags for This File

Everyone's Tags: analytical chemistry, chemistry, instrumental analysis, peak detection, physics

Tags I've Applied:


Add New Tags: [Please login to tag files.](#)

Comments and Ratings (21)

20 Aug 2005	Frank Arnold	It is pretty good and easy to use. Yet some commercial software such as origin, can do faster.	★★★★★
24 Aug 2005	Tom O'Haver	Version 1.2, dated August 24, 2005, is even faster than the previous version. It can find and measure 1000 peaks in a 1,000,000 point signal in 13 seconds.	🗨️
15 Sep 2005	K. Tampa	Get EXTREME W in this site and you'll find the ALL peaks (minima and	★★★★☆

A10. Low Density Polyethylene (LDPE) data

(retrieved from <http://www.matbase.com/material/polymers/commodity/ldpe/properties>, on 22 April 2011, 16:42 GMT)



High Density Polyethylene Hdpe suppliers. Wide range of waterproofing membranes. [www.daltech.com](#)
 Extreme Thermal Insulation Insulation board for extreme heat situations up to 1000°C. [www.pipon.com](#)
 Acrylic Products Online - Free Cutting, Great Choice We Won't Be Beaten On Price [www.daltech.com](#)

Home | Columns | News | Events | Forum | Suppliers | Guidelines | Partners

Name » Polymer » Commodity Polymers » LDPE

LDPE

Category	Type	Material
Plastics	Commodity Polymers	ABS Durbane
	General Purpose Polymers	ABS General Purpose
	High Impact Polymers	ABS High Impact
	High Impact Polymers	ABS High Impact
	High Impact Polymers	HDPE
	High Impact Polymers	LDPE
	High Impact Polymers	LLDPE
	High Impact Polymers	MMA
	High Impact Polymers	Polystyrene
	High Impact Polymers	PP (Gen.)
	High Impact Polymers	PP (Gen.)
	High Impact Polymers	PS (Gen.)
	High Impact Polymers	PS (Gen.)
	High Impact Polymers	PVC (Gen.)
	High Impact Polymers	PVC (Gen.)

DATA TABLE FOR: Polymer: Commodity Polymers: LDPE

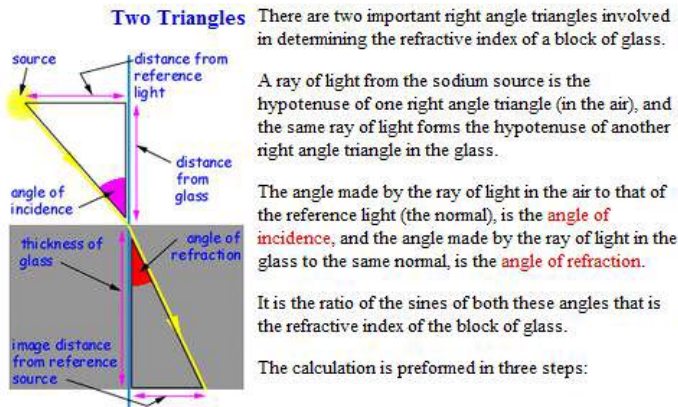
Mechanical Properties		
Quantity	Value	Unit
Young's modulus	200 - 400	MPa
Shear modulus	80 - 150	MPa
Tensile strength	8 - 12	MPa
Elongation	800 - 850	%
Bending strength	10 - 40	MPa
Yield strength	15 - 20	MPa

Physical Properties		
Quantity	Value	Unit
Thermal expansion	100 - 200	µm/mK
Thermal conductivity	0.3 - 0.325	W/m.K
Specific heat	1000 - 2400	J/kg.K
Melting temperature	105 - 120	°C
Glass temperature	-110 - -110	°C
Service temperature	-20 - 70	°C
Density	910 - 920	kg/m ³
Refractivity	1.497 - 1.497	Dimensionless
Breakdown potential	17.7 - 20.4	kV/mm
Dielectric loss factor	0.002 - 0.001	
Friction coefficient	0.3 - 0.5	
Refractive index	1.51 - 1.53	
Shrinkage	1.5 - 3	%
Water absorption	0.005 - 0.015	%

Bookmarks

A11. Simple method for measuring the refractive index of a glass slab

(retrieved from <http://www.brooklyn.cuny.edu/bc/ahp/CellBio/RefIndex/RI.Main.html> , on 29 April 2011 , 15292 GMT)



Step One: The first calculation determines the actual distance traveled by the ray of light in the air and in the glass. This is the hypotenuse of the two right angle triangles.

Once again, a table makes the calculation easier.

Distance traveled by ray in air

distance from reference light	(distance from reference light) ²	distance from glass	(distance from glass) ²	(distance from reference light) ² + (distance from glass) ²	square root of (distance from reference light) ² + (distance from glass) ²
DR	(DR) ²	DC	(DC) ²	(DR) ² + (DC) ²	sqrt [(DR) ² + (DC) ²]
20	400	34	1156	1556	39.446
					distance travelled by ray of light in the air